Measurement of the $D^{\pm}$ Meson Cross Section in DIS with the H1 Detector at HERA

Dissertation

zur Erlangung des Doktorgrades
des Department Physik
der Universität Hamburg

vorgelegt von
PHILIPP PAHL
aus Berlin

Hamburg
2014

Gutachter der Dissertation	Prof. Dr. Eckhard Elsen
	PD Dr. Thomas Schörner-Sadenius
Gutachter der Disputation:	Prof. Dr. Eckhard Elsen
	Prof. Dr. Johannes Haller
Datum der Disputation:	7. April 2014
Vorsitzender des Prüfungsausschusses:	Dr. Georg Steinbrück
Vorsitzende des Promotionsausschusses:	Prof. Dr. Daniela Pfannkuche
Dekan der MIN Fakultät:	Prof. Dr. Heinrich Graener
Leiter des Department Physik:	Prof. Dr. Peter Hauschildt

Abstract

The inclusive production of $D^{\pm}$ mesons in deep inelastic scattering at $\sqrt{s} = 318\,\mathrm{GeV}$ at HERA is studied using data taken with the H1 detector during the high energy measurement period in the years 2006 and 2007 corresponding to an integrated luminosity of $202.6\,\mathrm{pb}^{-1}$. The visible phase space is defined by $5 < Q^2 < 100\,\mathrm{GeV}^2$, $0.05 < y < 0.6$, $1.5 < p_T(D^{\pm})$ and $-1.5 < \eta(D^{\pm}) < 1.5$, where Q^2 is the photon virtuality, y is the inelasticity and $p_T(D^{\pm})$ and $\eta(D^{\pm})$ are the transverse momentum and rapidity of the $D^{\pm}$ meson. Charm production events are identified by the reconstruction of the $D^{\pm} \to K^{\mp}\pi^{\pm}\pi^{\pm}$ decay channel. The sample is enhanced by the application of a multi-variate analysis technique using a multilayer perceptron. The input variables of the classifier are based on the specific energy loss of the kaon decay particle candidate and the reconstructed decay length of the $D^{\pm}$ meson. The single and double differential cross sections are compared to leading and next-to-leading order QCD predictions.

Zusammenfassung

Die inklusive Produktion von $D^{\pm}$-Mesonen in tiefunelastischer Streuung bei $\sqrt{s} = 318\,\text{GeV}$ bei HERA wird untersucht. Es werden Daten verwendet, die während der Messperioden mit hohen Schwerpunktenergien in den Jahren 2006 und 2007 mit dem H1-Detektor gemessen wurden. Die Datenmenge entspricht einer integrierten Luminosität von $202,6\,\text{pb}^{-1}$. Der sichtbare kinematische Bereich wird durch $5 < Q^2 < 100\ \text{GeV}^2$, $0,05 < y < 0,6$, $1,5 < p_T(D^{\pm})$ und $-1,5 < \eta(D^{\pm}) < 1,5$, definiert, wobei Q^2 dem quadratischen Viererimpulsübertrag, y der Inelastizität und $p_T(D^{\pm})$ und $\eta(D^{\pm})$ dem Transversalimpuls und der Rapidität des $D^{\pm}$-Mesons entsprechen. Ereignisse mit Charmbeitrag werden mit Hilfe der Rekonstruktion des Zerfallskanals $D^{\pm} \to K^{\mp}\pi^{\pm}\pi^{\pm}$ identifiziert. Die Messdaten werden durch eine multivariate Analysemethode angereichert, die ein mehrlagiges künstliches neuronales Netz als Klassifikator beinhaltet. Die Eingangsgrößen des Klassifikators basieren auf dem teilchenabhängigen Energieverlust des als Kaon angenommenen Zerfallsteilchens und der Rekonstruktion der Zerfallslänge des $D^{\pm}$-Mesons. Die einfach- und doppeltdifferentiellen Wirkungsquerschnitte werden mit QCD-Vorhersagen führender und nächstführender Ordnung verglichen.

Contents

Chapter 1

Introduction

In elementary particle physics the interaction between the fundamental particles is described within the framework of the Standard Model of Particle Physics (SM). The SM consists of the three gauge theories which underly the strong, weak and electromagnetic interaction. The fundamental particles consist of six leptons, six quarks and their charge conjugates. The *up, down* and *strange* quark are the light quark, whereas the heavy quarks *charm, bottom* and *top* have considerably higher masses. The interactions are mediated by the exchange of gauge bosons: The W and Z boson for the weak force, the γ for the electromagnetic interaction and the gluons for the strong interaction.

Deep Inelastic Scattering (DIS) [29] provides a tool for the investigation of the hadron structure and the underlying physics model of the strong force. In DIS leptons such as electrons or positrons are brought into collision with hadrons. HERA[1] is a world-wide unique electron-proton collider and was in particular built to test the proton structure. It allowed the access of much higher energy regimes compared to fixed target experiments, corresponding to a photon virtuality Q^2 of up to $\approx 30,000\,\mathrm{GeV}^2$ and a spatial resolution of $\approx 10^{-18}\,\mathrm{m}$, which corresponds to

[1] **H**adron-**E**lektron-**R**ing**a**nlage, English: Hadron-Electron Ring Accelerator

$1/1000$ of the proton size.

The calculation of QCD processes faces various peculiarities. The renormalization introduces a scale dependence of the strong coupling constant α_s. Also, perturbative methods are only applicable at small values of α_s. At small energies the values become large and the next higher order might still be non-negligible. Another scale dependence is introduced by the factorization of the short distance perturbative effects and the long distance non-perturbative effects. The long distance effects are absorbed into the *Parton Density Functions* (PDF). PDFs can be evolved to the scale in question by evolution equations once they are known at a certain scale. The PDFs can only be determined experimentally and are derived by fits of parametrized PDFs to globally available experimental data. The derivation relies, amongst others, on the theoretical treatment of charm quark production in DIS. Since the gluon distribution appears in the initial production process of heavy quarks, the production provides a direct probe. A precise knowledge about the PDFs is essential for the LHC[2] where two protons are brought into collision.

For both the evolution of the coupling constant and the derivation of the PDFs a heavy flavor mass scheme has to be chosen which is valid for a certain scale. The $D^{\pm}$ production cross section data in the phase space region of this analysis provides a scale which is in between the two different schemes where either the charm quark is treated massless or massive.

This thesis provides the measurement of the charmed hadron, namely $D^{\pm}$ production cross section which is compared to next-to-leading order QCD calculation and discussed with respect to the aforementioned issues. The measurement can be used for future extraction of the charm contribution to the structure functions and derivation of the PDFs. Furthermore it is utilized to further understand regions of the phase space where previous measurements have observed an excess compared

[2] **L**arge **H**adron **C**ollider

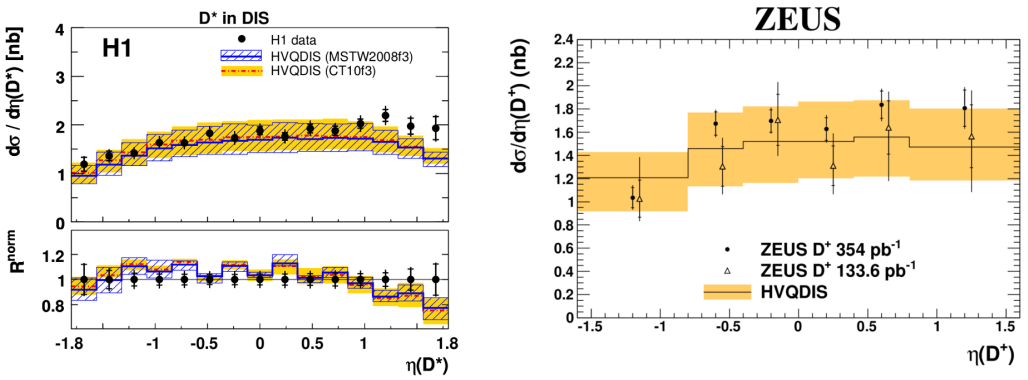

Figure 1.1: The published cross section as function of the rapidity η

to the predictions, e.g. for large rapidities. Figure 1.1 shows recently published results of the H1 D^* and ZEUS $D^{\pm}$ measurement.

Organization of this thesis In chapter 2 an overview over DIS and the basic theoretical concepts is given. In the successive chapter 3 the leading-order and next-to-leading order event generators which are used in this analysis are discussed. The experimental setup, the apparatus, the HERA collider, the H1 detector and its relevant components for this analysis are presented in chapter 4. The on- and off-line run and event selection this measurement is based on is discussed in chapter 5. Chapter 6 presents the reconstruction chain of the $D^{\pm}$ mesons. The sample is enhanced by the application of a multilayer perceptron based classifier (section 6.5). The input variables which enter the multivariate classifier are based on the specific energy loss of the kaon (section 6.2) and the $D^{\pm}$ decay length reconstruction (section 6.3). In chapter 7 the cross section determination and especially the correction of the reconstruction inefficiency is discussed. A detailed discussion and derivation of systematic uncertainties is presented in chapter 8. Special attention is paid to systematic studies of the particle reconstruction (sec 8.1). Finally the cross section results are discussed and compared to leading and next-to-leading

order calculations (chapter 9)

Chapter 2

Deep Inelastic Electron Proton Scattering and Charm Production

2.1 Deep Inelastic Scattering

Deep inelastic scattering (DIS) is the process by which the structure of hadrons is studied. Hadrons like protons or neutrons are probed by electrons, muons or neutrinos. The electroweak force is mediated by the exchange of the photon γ or the Z^0 boson for the neutral current or the $W^{\pm}$ boson for the charged current process. Figure 2.1 shows the Feynman diagrams of the leading order processes. The negative four-momentum transfer squared $-q^2 = Q^2$ is referred to as virtuality. Due to the large masses of the $W^{\pm}$ and Z^0 bosons, contributions from the weak force are strongly suppressed and negligible for $Q^2 \ll m^2(W^{\pm}, Z^0)$.

QED Corrections in DIS The two higher order QED processes shown in figure 2.2 involve the real next-to-leading order corrections. QED correction at one loop level are included in the running of the electromagnetic coupling α_{em}. The running of α_{em} is discussed in section 2.6.

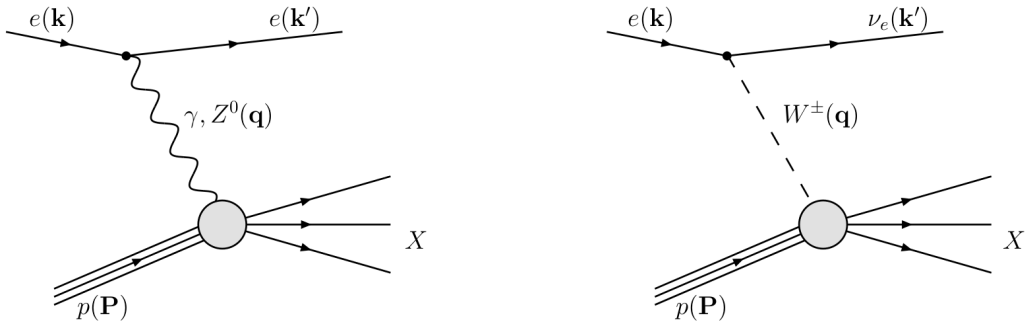

Figure 2.1: The leading order Feynman diagrams for *ep* scattering. The force is mediated by a photon γ or Z^0 (neutral current, left) or a $W^{\pm}$ boson (charged current, right).

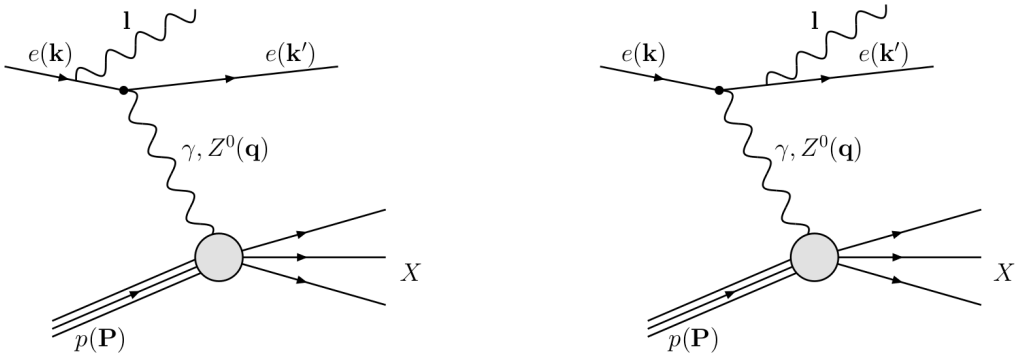

Figure 2.2: Next-to-leading order QED processes. Left: Initial state radiation (ISR). Right: Final state radiation (FSR).

Figure 2.2 shows the initial state radiation (ISR) and the final state radiation (FSR). ISR originates from the incoming electron and therefore lowers the energy which is available for the scattering process. This effect has to be taken into account for the determination of the cross section and is discussed in section 7.3.

FSR denotes the radiation off the outgoing electron. In that case the radiated photon is often detected together with the electron in a merged state since the photon is almost collinear to the electron and cannot be distinguished experimentally from non-radiative events.

2.2 Kinematics

The kinematic of the scattering process $e + p \to e(\nu_e) + X$ is described by means of Lorentz-invariant kinematic variables. The frequently used variables are the negative four-momentum squared Q^2, the Bjørken scaling variable x, the inelasticity y and the center-of-mass energy $\sqrt{s}$. The four-momenta of the scattering process are depicted in figure 2.1.

Q^2 is defined by the difference of the incoming and outgoing four-momenta of the electron:

$$Q^2 := -\mathbf{q}^2 = -(\mathbf{k} - \mathbf{k}')^2 \tag{2.1}$$

The dimensionless scaling variable Bjørken x can be interpreted as the fractional momentum of the proton carried by the struck quark:

$$x := \frac{Q^2}{2(\mathbf{P} \cdot \mathbf{q})}, \quad 0 < x < 1 \tag{2.2}$$

For $x \to 1$ the process approaches elastic scattering. The inelasticity y describes the relative energy loss of the electron in the proton rest frame, i.e. the

energy fraction carried by the photon:

$$y := \frac{\mathbf{P}\cdot\mathbf{q}}{\mathbf{P}\cdot\mathbf{k}}, \quad 0 < y < 1 \tag{2.3}$$

Neglecting the rest masses the variables are related by

$$Q^2 = sxy, \tag{2.4}$$

where s is the squared center-of-mass energy:

$$s = (\mathbf{k}+\mathbf{P})^2. \tag{2.5}$$

2.3 The Inclusive ep Cross Section

For $Q^2 \ll m_Z^2$ the scattering process is entirely dominated by the electromagnetic force and can be described by Quantum Electro Dynamics (QED). A general structure can be derived by exploiting Lorentz invariance and electromagnetic current conservation [29]:

$$\frac{\partial^2}{\partial x \partial Q^2}\sigma^{NC}(x,Q^2) = \frac{2\pi\alpha_{em}^2}{xQ^4}\left(F_2(x,Q^2) - \frac{y^2}{1+(1-y)^2}F_L(x,Q^2)\right) \tag{2.6}$$

The cross section is parametrized by the two proton structure functions $F_2(x,Q^2)$ and $F_L(x,Q^2)$. The structure functions describe the inner structure of the proton. They cannot be derived perturbatively and have to be determined experimentally. The contribution of the longitudinal structure function F_L is suppressed by a factor of $\frac{y^2}{1+(1-y)^2}$ and only contributes marginally in the phase space region of this analysis. F_L describes the contribution to the cross section which originates from photons which are longitudinally polarized.

2.4 The Quark Parton Model

Early deep inelastic scattering measurements were explained in the framework of the naïve quark parton model (QPM). In the QPM the proton is viewed as being composed of non interacting constituents called partons. Each parton carries a fraction $\xi < 1$ of the longitudinal momentum of the proton, while its transverse momentum is neglected. The cross section 2.6 consists of the incoherent sum of the individual partons and their interactions:

$$\frac{\partial^2}{\partial x \partial Q^2}\sigma^{NC}(x,Q^2) = \sum_i \int_0^1 \mathrm{d}\xi\, f_i(\xi) \cdot \frac{\partial^2}{\partial x \partial Q^2}\sigma^{NC}(\frac{x}{\xi},Q^2)\Big|_{eq_i \to eq_i} \tag{2.7}$$

In this expression $f_i(\xi)$ describes the Parton Density Function (PDF) of the ith parton. In the simplified QPM the proton consists of three non interacting point-like fermions, the valence quarks, namely two up and one down quark. Consequentially the cross section for each parton in leading order is calculated by means of QED as:

$$\frac{\partial^2}{\partial x \partial Q^2}\sigma^{NC}(\frac{x}{\xi},Q^2)\Big|_{eq_i \to eq_i} = \frac{2\pi\alpha_{em}^2[1+(1-y)^2]}{Q^4} \cdot e_i \delta(\frac{x}{\xi}-1)\,, \tag{2.8}$$

from this follows that the structure function F_2 is

$$F_2(x,Q^2) = \sum_i e_i^2 x f_i(x) \tag{2.9}$$

The independence of Q^2 is known as scaling [17] and is related to the point-like behavior of the constituent of the proton. The Callan-Gross relation manifests itself in

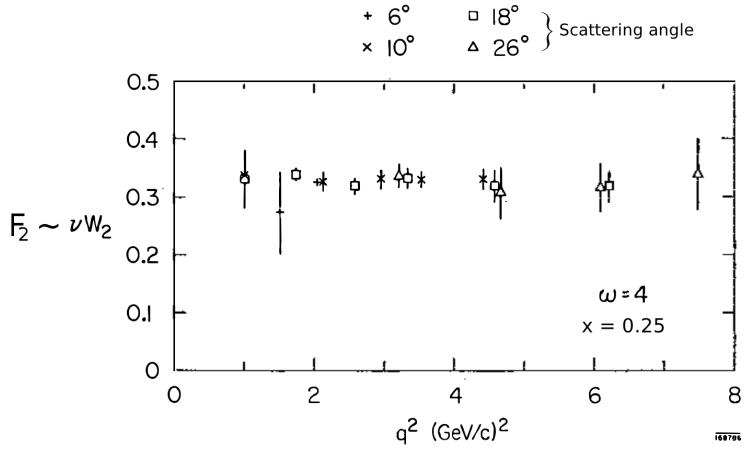

Figure 2.3: One of the first measurements of F_2 from fixed target experiments [34] at a fixed value of $x = 0.25$.

$$F_L(x, Q^2) = 0 \tag{2.10}$$

and reflects the fermionic nature of the partons and the vanishing longitudinal structure function. Both features were predicted and 1972 experimentally confirmed within the precision of the measurement. (cf. figure 2.3)

2.5 Quantum Chromo Dynamics

Non interacting partons inside the nucleon as postulated in the QPM can only be an approximate description. Only shortly after the first measurements violations of the scaling have been found [33]. The interactions between the constituent of hadrons are described within the theory of Quantum Chromo Dynamics (QCD) [35, 74, 41]. QCD was initially introduced to describe the asymmetric wave function of the Δ^{++} particle which required an additional degree of freedom. This additional degree of freedom is called color, which is the charge of the strong force which drives QCD. QCD is a Yang-Mills theory based on the SU(3) symmetry

group. The generators of the SU(3) form an octet of color-anticolor states; these mediators of the strong force are called gluons. The fact that both quarks and gluons carry color charge results in emissions of gluons from quarks and from other gluons, the splitting into quark-antiquark pairs and the gluon self-interaction. Because of the non zero probability that a quark emits a soft gluon the perfect scaling behavior is broken as higher Q^2 terms resolve more and more partons. Additionally gluons can split into $q\bar{q}$ pairs enhancing the quark content at small x. The scaling violations as measured at HERA are depicted in figure 2.4. The reduced cross section for neutral current DIS ep scattering is shown which is proportional to the neutral current cross section apart from a kinematic factor.

2.6 Renormalization and the Running of the Couplings

Any physical field theory must be renormalizable in case of the appearance of divergences. In quantum field theories (QFT) divergences occur if an integration over all momenta in closed loops is performed. Renormalization can be seen as the replacement of a bare charge and consequently the bare coupling by a physical observable quantity.

The coupling in the lowest order is modified by higher order corrections of the propagator. This correction results in a so-called UV-divergence. In QED closed fermion loops emerge, whereas in QCD in addition to the fermion loops the gluon loops contribute (cf. figure 2.5).

There are different possibilities to account for and remove divergences. The different schemes are called renormalization schemes. The minimal subtraction scheme ($\overline{\text{MS}}$) [72] is the most commonly used renormalization scheme in DIS. In the $\overline{\text{MS}}$ scheme dimensional regularization is utilized to factor out and absorb

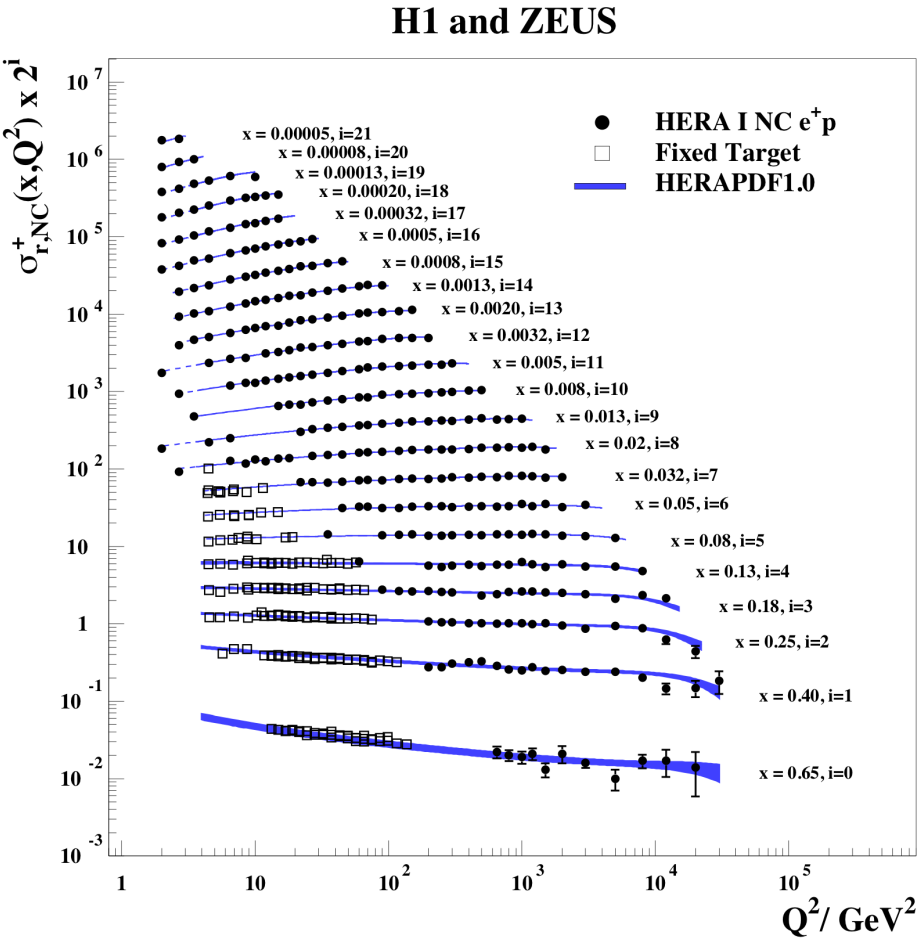

Figure 2.4: H1 and ZEUS combined structure function data from e^+p neutral current DIS scattering.

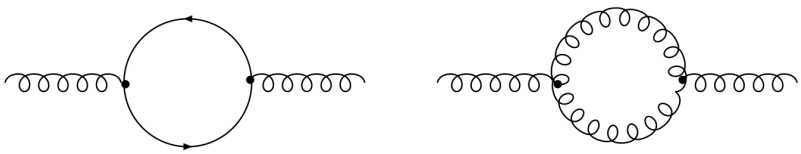

Figure 2.5: Loop contributions to the gluon propagator in QCD. Left: Fermion loop. Right: Gluon loop.

divergences in the definition of the coupling. Another scheme is the DIS scheme. In the DIS scheme all gluon contributions are absorbed into the quark distribution, whereas in the $\overline{\text{MS}}$ scheme only the collinear divergence is factored out. The renormalization removes the divergence, though a scale at which the subtraction is performed is introduced.

Nevertheless physical observables must not depend on the scale parameter. This condition leads to the renormalization group equations (RGE). The RGE contain the scale dependence of the *running coupling* α_s*:*

$$\mu_r^2 \cdot \frac{\partial \alpha_s(\mu_r)}{\partial \mu_r^2} = \beta(\alpha_s(\mu_r)) \tag{2.11}$$

at which the strong coupling constant $\alpha_s(\mu_r)$ at an arbitrary scale μ_r is given by

$$\alpha_s(\mu_r^2) = \frac{1}{\beta(\alpha_s) \cdot \ln(\mu_r^2/\Lambda_{QCD}^2)} \tag{2.12}$$

and $\beta(\alpha_s)$ is given by

$$\beta(\alpha_s) = -\alpha_s \sum_{n=0}^{\infty} \beta_n \left(\frac{\alpha_s}{4\pi}\right)^{(n+1)} \tag{2.13}$$

The coefficients β_n currently have been calculated up to fourth order allowing an iterative determination of α_s [26]. Λ_{QCD} refers to the asymptotic scale parameter which determines the behavior of α_s. From $\mu_r \to \infty$ it follows $\alpha_s(\mu_r) \to 0$. This phenomenon is known as *asymptotic freedom.* At large energies, or correspondingly at small distances the quarks and gluons can be seen as quasi free particles. As μ_r approaches Λ_{QCD}, α_s becomes large. This behavior is known as *confinement* and implies that free colored objects are not observable, since the perturbative expansion breaks down in the small energy regime.

2.7 Perturbative QCD

An observable R can be written in terms of a series expansion,

$$R = \sum_{n=0}^{\infty} c_n(\mu_r)\alpha_s(\mu_r)^n,$$

where the coefficients $c_n(\mu_r)$ can be calculated by the evaluation of Feynman diagrams. Due to the small size of the strong coupling constant $\alpha_s(\mu_r)$ at large scales, R can be approximated by the first n terms of the expression. This approach is called perturbative QCD (pQCD) and is valid at $\mu_r \gg \Lambda_{QCD}$ where terms of order $\alpha_s(\mu_r)^{n+1}$ can be neglected. From the derivative of the observable R by the renormalization scale μ_r

$$\frac{\mathrm{d}}{\mathrm{d}\,\ln(\mu_r)} \sum_{n=0}^{N} c_n(\mu_r)\alpha_s(\mu_r)^n \sim \mathcal{O}(\alpha_s(\mu_r)^{N+1})$$

and $\alpha_s(\mu_r) < 1$ for sufficiently large μ_r it follows that the observable R will depend less on the choice of μ_r the more terms are included in the perturbation series. [71]

2.8 Factorization Theorem and DGLAP Evolution

In the QPM the proton structure is absorbed in the PDF. It is shown that this concept is also applicable in the framework of QCD in which quarks and gluons are interacting with each other. The concept of the PDFs is based on the separation of short distance perturbative effects and long distance non-perturbative effects. A qualitative motivation for the validity as well as a proper mathematical elaboration is provided in [28]:

"To be specific, consider inclusive electron-hadron scattering by virtual pho-

ton exchange at high energy and momentum transfer. Consider how this scattering looks in the center-of-mass frame, where two important things happen to the hadron. It is Lorentz contracted in the direction of the collision, and its internal interactions are time dilated. So, as the center-of-mass energy increases the lifetime of any virtual partonic state is lengthened, while the time it takes the electron to traverse the hadron is shortened. [...] When the latter is much shorter than the former the hadron will be in a single virtual state characterized by a definite number of partons during the entire time the electron takes to cross it."

Although the rigorous proof of the factorization theorem exists only for a few processes, it is assumed that factorization also holds for other processes. Again the factorization has to be performed at a specific scale μ_f, the factorization scale. For practical reasons in most applications the factorization and renormalization scale are set to the same values $\mu = \mu_r = \mu_f$.

DGLAP Evolution Equation Physical observables must not depend on the choice of the factorization scale, which again leads to renormalization group equations, also known as evolution equations. Once a PDF is known at a given scale the evolution equations provide a prescription to evolve parton densities to an arbitrary scale. The evolution is described by coupled integro differential equations, the so-called DGLAP equations [30, 40, 10]

$$\frac{\partial q_i(x,Q^2)}{\partial \ln Q^2} = \frac{\alpha_s(Q^2)}{2\pi} \cdot \int_x^1 \frac{d\xi}{\xi} \left[P_{qq}\left(\frac{x}{\xi}\right) q_i(\xi,Q^2) + P_{qg}\left(\frac{x}{\xi}\right) g(\xi,Q^2) \right]$$

$$\frac{\partial q_i(x,Q^2)}{\partial \ln Q^2} = \frac{\alpha_s(Q^2)}{2\pi} \cdot \int_x^1 \frac{d\xi}{\xi} \left[P_{gq}\left(\frac{x}{\xi}\right) q_i(\xi,Q^2) + P_{gg}\left(\frac{x}{\xi}\right) g(\xi,Q^2) \right]$$

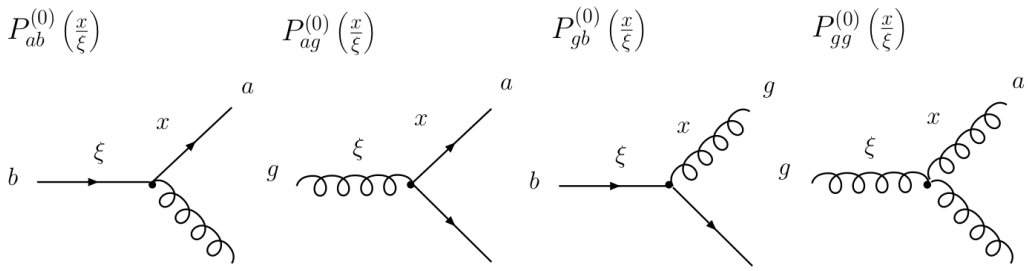

Figure 2.6: Splitting functions and the corresponding Feynman graphs.

$P_{ab}(x/\xi)$ denote the splitting functions as depicted in figure 2.6. The splitting functions give the probabilities for an incident parton b with momentum fraction ξ to radiate a new parton a with momentum fraction x. The splitting functions are calculated perturbatively.

2.9 Heavy Quark Production in DIS

Heavy quark production in DIS at HERA is dominated by the boson-gluon-fusion (BGF) process. BGF describes the interaction between the virtual photon of the electron and a gluon of the proton. The lowest order Feynman diagrams of the BGF process $\gamma g \to c\bar{c}$ are depicted in figure 2.7a)[1]

The upper left figure represents the direct BGF process, which corresponds to a next-to-leading order process in inclusive DIS. The other diagrams of figure 2.7a) are the diagrams which take into account the so-called hadronic component of the photon. The resolved contribution only emerges at small photon virtualities. It is highly suppressed for the phase space region of this analysis and negligible [9].

The proof of hard scattering factorization with the inclusion of heavy quark masses is given in [27]. The factorization theorem has the following form:

[1] In the following only c-quarks are mentioned, although the theoretical concept is applicable for b-quarks as well.

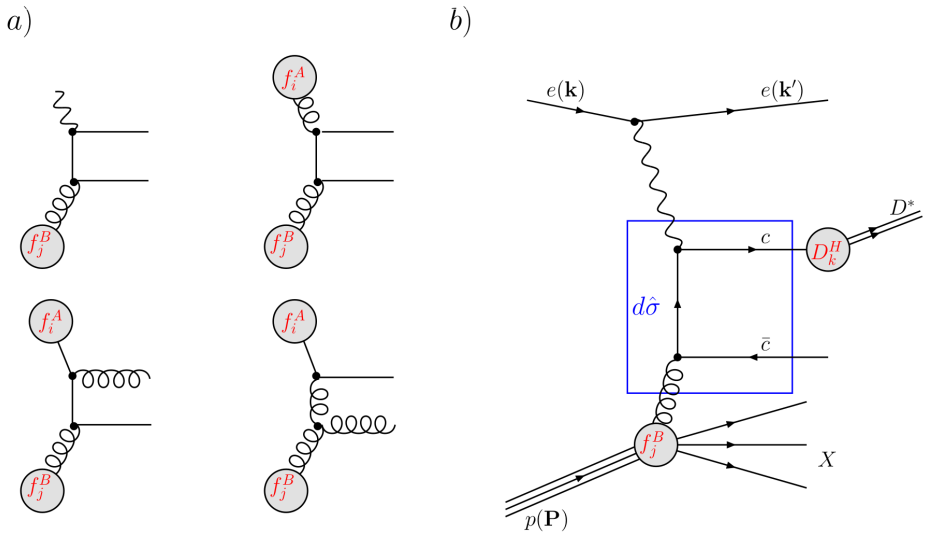

Figure 2.7: The heavy quark boson-gluon fusion processes in leading order. a) The upper left shows the direct process. Additionally the resolved processes are shown. b) Detailed graph of the direct BGF.

$$d\sigma = \sum_{i,j} f_i^A(x_1,\mu_f) \otimes f_j^B(x_2,\mu_f) \otimes d\hat{\sigma}_{ij\to kX}(\mu_f) \otimes D_k^H(z,\mu_f) \tag{2.14}$$

Figure 2.7b) shows the direct process of charm production and illustrates the ingredients of the theoretical treatment and the factorization with its components:

- $d\hat{\sigma}(\mu_f, \alpha_s(\mu_r), \left(\frac{m_c}{p_T}\right))$ element of the hard scattering process of the partons i and j. $d\hat{\sigma}$ can be perturbatively computed at the scale μ_f. The mass is treated in a certain mass scheme as discussed in the next paragraph

- $f_i^A(x_1,\mu_f)$ denotes the photon PDF, $f_j^B(x_2,\mu_f)$ the proton PDF, respectively. The universal PDFs give the probability to find the corresponding partons i and j. The photon PDF only occurs in the resolved case. Otherwise simply the photon exchange is involved. Figure 2.8 shows the proton PDFs measured by H1 and ZEUS.

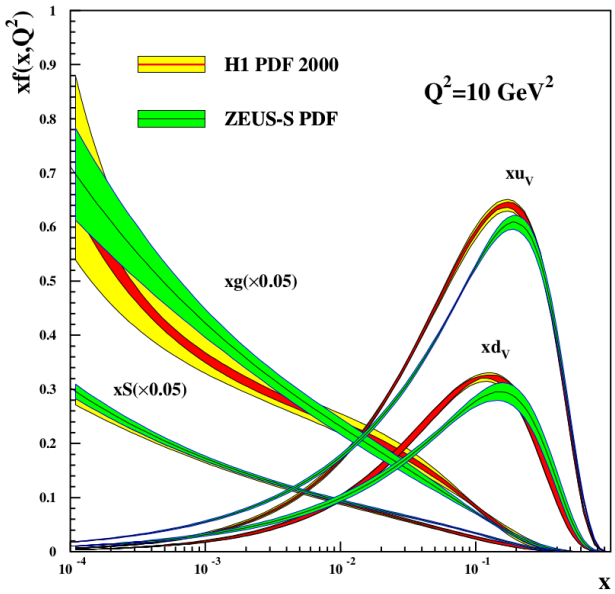

Figure 2.8: The parton density functions [8].

- The fragmentation function $D_k^H\left(z,\mu_f\right)$ gives the probability to produce a colorless hadron H from the produced quark k with a relative momentum z.

Heavy Flavor Mass Schemes In heavy flavor production processes several hard scales $(Q^2, p_{\mathrm{T}}, m_c)$ occur. Depending on the scale involved different schemes exist for the calculation of the process. Within the different schemes the heavy flavor masses are treated differently. The schemes are briefly summarized in the following

FFNS In the fixed flavor number scheme (FFNS) only the light quarks u, d, s and the gluons contribute to the dynamic structure of the proton. The massive charm quark is produced perturbatively as indicated in figure 2.9a).

All calculations are performed in fixed order perturbation theory, which leads to remaining large terms of the form $log^n(Q^2/m_c^2)$ at the order n of the perturbation series. Therefore the FFNS is expected to describe data at a scale in the vicinity of the charm mass.

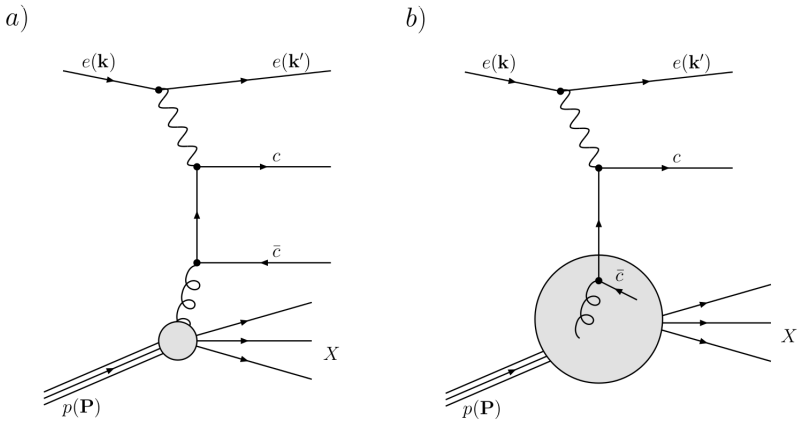

Figure 2.9: Left: Perturbative production graph of massive charm quarks. Right: Production of massless charm quarks.

ZM-VFNS For $\mu \to \infty$ the zero mass variable flavor number scheme is applicable [24, 15]. In the ZM-VFNS light and heavy quarks are treated as massless partons. This implies that the aforementioned large logarithms are absorbed into charm parton distributions and fragmentation functions at a scale close to m_c, which can be re-summed to all orders by DGLAP evolution. This case is depicted in figure 2.9b). The ZM-VFNS represents the common method for conventional QCD parton model calculations. Flavors above $n_f = 3$ are added if Q^2 exceeds the corresponding mass. The only hard scale left is Q^2, which leads to discontinuities at scales of the size of the mass of the heavy quark.

GM-VFNS For completeness the general mass variable flavor number schemes (GM-VFNS) are mentioned. In the mixed schemes both a massive treatment at threshold and a massless treatment at high scales is done. Oversimplified the idea is to sum over the massive FFNS-term and the massless ZM-VFNS-term and to account for the overlap term in a correct way.

2.10 Hadronization

States which are physically observable must be color neutral states due to the phenomenon of confinement. Partons which originate from the hard interactions undergo a cascade of soft interactions which is known as hadronization or fragmentation process and leads to the formation of detectable hadrons. Because the hadronization occurs at a scale at which perturbation theory is not applicable it must be described by phenomenological models. The hadronization of light quarks is based on the Lund string model [11, 14]. In the Lund string model the color field between a massless quark anti-quark pair is modeled by a massless and relativistic string. The string has a tension, which gives a linear potential similar to the QCD potential. When the quarks move apart, the string stretches and the potential increases until the splits up into two color-singlets systems. If the invariant mass of the sub-systems is sufficiently high, further breaks can occur until only on-mass-shell hadrons are left.

Phenomenological models for charm fragmentation are the Peterson, Kartvelishvili and Bowler models [65, 51, 21] whose fragmentation functions are given by:

$$\begin{aligned} \text{Peterson:} \quad & D_H^{\varepsilon}(z) \propto \frac{1}{z \cdot (1 - 1/z - \frac{\varepsilon}{1-z})^2}, \\ \text{Kartvelishvili:} \quad & D_H^{\alpha}(z) \propto z^{\alpha} \cdot (1-z), \\ \textit{Bowler}: \quad & D_H^{\alpha}(z) \propto \frac{1}{z^{1+\beta r_Q m_Q^2}} \cdot (1-z)^{\alpha} \cdot \exp\left(\frac{\beta M_T^2}{z}\right). \end{aligned} \tag{2.15}$$

The fragmentation functions are described by the momentum fraction z which the produced hadron inherits from the initial partons. The Bowler parametrization contains the two free parameter α and β and $r_Q$which is set to 1 by default. The Kartvelishvili parametrization contains the free parameter α. m_Q denotes the mass

of the heavy quark, $M_T = \sqrt{M_H^2 + p_{\mathrm{T}}^2}$ denotes the transverse mass.

2.11 Properties of the Charmed Mesons

In this section the properties of the charmed mesons relevant for this analysis are illustrated. Approximately 23% of the produced charm quarks fragment into $D^{\pm}$ mesons. The decay mode under investigation (cf. chapter 6) is

$$D^{\pm} \overset{(9.13\pm0.19)\,\%}{\longrightarrow} K^{\mp}\pi^{\pm}\pi^{\pm} \tag{2.16}$$

The branching ratio of this channel amounts to $(9.13 \pm 0.19)\,\%$. Because of the weak, flavor changing decay the D meson has a relatively long lifetime of the order of several hundred micrometers, which allows for the charm tagging technique to be applied.

The doubly Cabibbo-suppressed decay (cf. 6.6) has a branching ratio of $(5.27 \pm 0.23) \times 10^{-4}$

$$D^{\pm} \overset{(5.27\pm0.23)\times10^{-4}}{\longrightarrow} K^{\pm}\pi^{\mp}\pi^{\pm} \tag{2.17}$$

And hence is suppressed by a factor of ≈ 200.

Furthermore the $D^{*\pm}$meson and its decay in the *golden* decay channel is analyzed for systematic studies.

$$D^{*\pm} \overset{(67.7\pm0.5)\,\%}{\longrightarrow} D^0\pi^{\pm}_{\mathrm{slow}} \overset{(3.87\pm0.05)\,\%}{\rightarrow} \rightarrow K^{\pm}\pi^{\mp}\pi^{\pm}_{\mathrm{slow}} \tag{2.18}$$

The relevant information is summarized in table 2.1.

	$D^{\pm}$	$D^*(2010)^{\pm}$	D^0
Mass m [MeV]	1869.57 ± 0.16	2010.22 ± 0.14	1864.8 ± 0.14
$I(J^{Parity})$	$\frac{1}{2}(0^-)$	$\frac{1}{2}(1^-)$	$\frac{1}{2}(0^-)$
Mean lifetime τ	$(1040 \pm 7) \times 10^{-15} s$		$(410.1 \pm 1.5) \times 10^{-15} s$
$c\tau$	$311.8\,\mu$m		$122.9\,\mu$m
$f(c \to DX)$	$(23 \pm 0.85)\,\%$	$(23.4 \pm 0.8)\,\%$	$(58.5 \pm 1.9)\,\%$
Quark content	$(c\overline{d}) + c.c.$	$(c\overline{d}) + c.c.$	$(c\overline{u}) + c.c.$

Table 2.1: Properties of the D mesons relevant for this analysis. All but one number taken from[61]. The relative fragmentation probability for $D^{\pm}$ is taken from [59].

Chapter 3

Event Generators

Event generators simulate the physics processes which underly ep scattering. Their computation is based on random number generation and the sampling of possible processes and final states. From the accumulated samples a prediction for the resulting cross section is derived. Section 3.1 discusses leading-order (LO) generators which include parton hadronization and allow for simulation. The events are subsequently passed to the detector simulation and yield fully reconstructed events. These generators are so-called Monte Carlo (MC) event generators. In this thesis leading-order MC events are used for detector efficiency correction and as input data for the training of the neural network based event classifier (cf. 6.5). Section 3.2 introduces next-to-leading-order (NLO) event generators which also take into account corrections to the order α_s^2 BGF process and calculate cross sections on parton level without parton showering.

3.1 Leading Order Event Generators

The `RAPGAP` package is used for the detector efficiency correction (cf. 7.1) and provides the signal events for the training of the neural network (cf. 6.5) which

is applied for particle candidate classification. The second generator package is DJANGOH which provides the background particle candidates for the classifier training set. Candidates of both generators are used to estimate the model dependency (cf. 8.2) and their cross sections are compared to the measured cross sections. (cf. chapter 9)

The process of the event generation begins with the electron-proton interaction, i.e. the application of the factorization theorem as discussed in section 2.8. First the hard subprocess is calculated at the given factorization scale by the exact calculation of the matrix element in leading order perturbation theory. The matrix element which belongs to the hard subprocess is convoluted with the proton PDF. The PDF is evolved to the desired scale by application of the parton evolution. The scale is given by the factorization scale usually defined by the hardest scale of the process, e.g. the virtuality Q^2. Next the initial and final state partons from the hard interaction are subject to the parton showers which are performed with the help of the DGLAP evolution. The parton evolution terminates when only partons on the mass shell from the initial virtual partons are left. Afterwards the still colored particles undergo the hadronization process. At the end of the generation process all particles have a lifetime $\tau > 10^{-8}$ s. The four-vectors are then provided for the detector simulation, which is described in section 4.8. In the following paragraphs the MC generators used in this analysis are presented.

RAPGAP RAPGAP[50] generates ep events by evaluating the BGF process with leading order matrix elements. The matrix elements are matched to LO parton showers for which the DGLAP evolution is used. The factorization scale is chosen to be $\mu^2 = Q^2 + p_T^2 + 4m_c^2$. The heavy quarks are treated as massive with a charm mass of $m_c = 1.5\,\text{MeV}$. RAPGAP is interfaced to HERACLES [56]. HERACLES generates next-to-leading order QED corrections as explained in paragraph 2.1. The

Lund fragmentation is utilized for the light quark flavors and the Bowler fragmentation function for heavy quark fragmentation. The fragmentation function is parametrized after Bowler, derived from the ALEPH tune [53]. The proton PDF used for the particle generation is CTEQ6L [68] and reweighted to H1PDF2009 [2, 32].

DJANGOH The DJANGOH [69] software package also generates events in deep inelastic scattering including parton showers and hadronization. LEPTO[48] is used for the hard scattering process and ARIADNE [12, 43] for parton showering, which is an implementation of the color dipole model for parton cascades. For the fragmentation the JETSET[70] package is applied, which implements the Lund string model. Also DJANGOH is interfaced to HERACLES in order to account for radiative corrections.

3.2 Next-to-Leading Order Calculations

Next-to-leading order calculations are expected to provide more reliable results as they account for the presence of hard parton emissions. In the DIS regime the HVQDIS [44] program implements QCD predictions for heavy quark production. The calculations include the α_s^2 corrections to the leading order α_s BGF process as depicted in figure 3.1.

Unfortunately a NLO hard subprocess can not be directly supplemented with parton showers because of double counting problems. The treatment of the fragmentation process is discussed in the next paragraph. HVQDIS uses the FFNS heavy flavor mass scheme (cf. 2.9). To cancel collinear and soft divergences the modified subtraction renormalization scheme is used. More details on the calculation can be found in [45]. The configuration for the NLO calculation is taken from the $D^{\pm}$ cross section measurement at ZEUS [57] and adapted to the phase

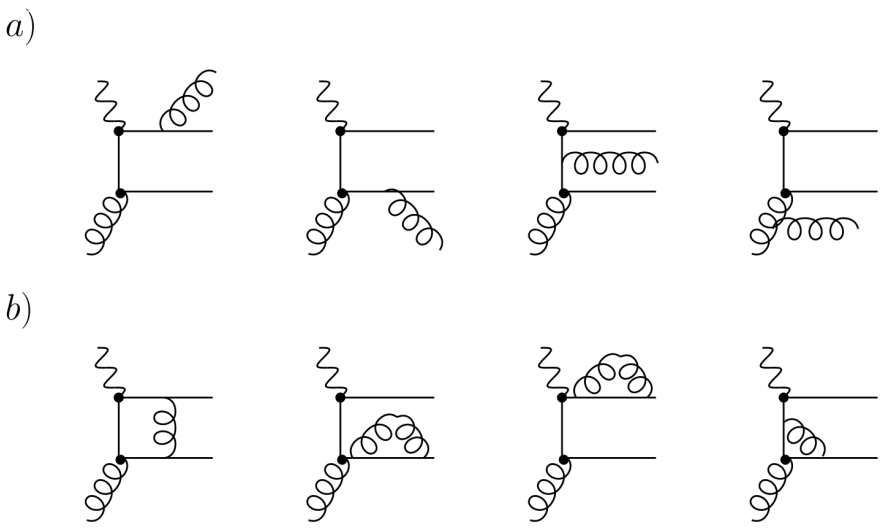

Figure 3.1: A selection of the real corrections (a) and of the virtual corrections of the order α_s BGF process.

space of this analysis. This allows a comparison to the NLO calculation as well as an indirect comparison to the ZEUS measurement. In the following the settings are summarized:

- The charm mass is set to $m_c = 1.5\,\text{GeV}$. For the estimation of the theory uncertainty the value of m_c was varied by 0.15 GeV up and down. Simultaneously with the charm quark mass in the matrix element, the value used in the PDF fit was varied.

- Renormalization and factorization scale were set to $\mu_R = \mu_F = \sqrt{Q^2 + 4m_c^2}$. To estimate the theory uncertainty based on the scale definition, they were varied independently by a factor of 2 up and down.

- The PDFs were extracted from the ZEUS-S NLO PDF fit [25] in the 3-flavor FFNS with the charm masses mentioned above. Unfortunately for the central value of the charm mass only fits with a different choice for the scales exist ($\mu_R = \mu_F = Q^2$). A check in [57] demonstrates that the effect is

small and can be neglected.

- α_s was calculated at NLO with 3 active flavors and $\Lambda_{QCD} = 363\,\text{GeV}$

In order to derive the total theory uncertainty the single contributions are summed in quadrature.

Fragmentation process

As mentioned earlier `HVQDIS` calculates events on parton level only. It uses the Kartvelishvili [51] parametrization for the fragmentation function (cf. 2.10). In [57] a detailed study of the charm fragmentation modeling was performed: The approach was to fit the α parameter of the fragmentation function (eq. 2.15) as a function of an energy scale to the HERA data. Figure 3.2 shows the fit result as function of $\hat{s}$, the center of mass energy of the hard subprocess. While the fragmentation function is normalized to unity, the total probability for a certain meson to be produced in a given fragmentation process is given by the fragmentation fractions $f(c \to D^{\pm}) = 0.2297 \pm 0.0085$ and $f(c \to D^{*}) = 0.234 \pm 0.008$ [59].

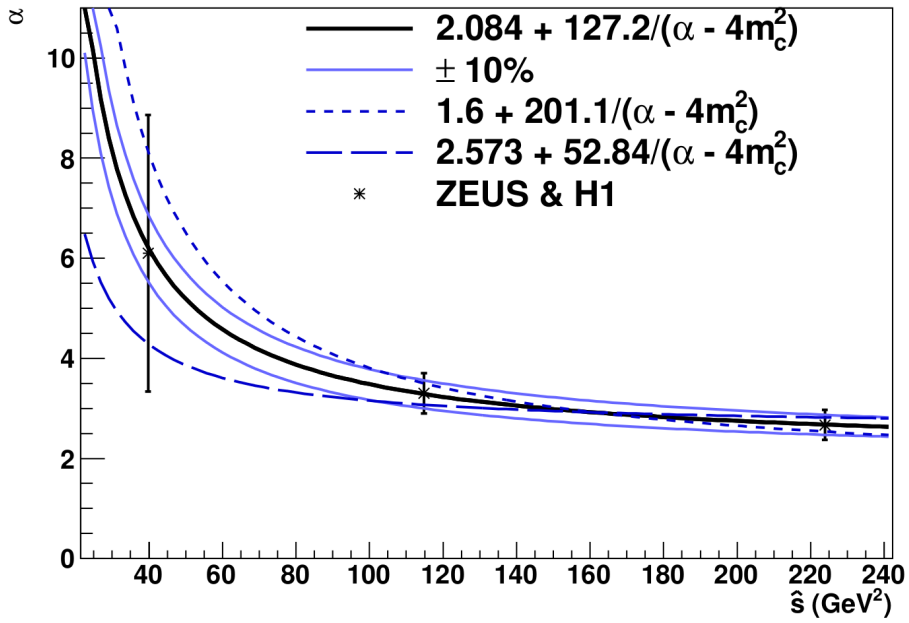

Figure 3.2: A fit of the measured values of the Kartvelishvili parameter α as a function of $\hat{s}$ to ZEUS and H1 data. For details see [57]

Chapter 4

Experimental Setup

4.1 HERA

HERA[1] was an electron proton collider at the research institute DESY[2] located in Hamburg, Germany. It was constructed and operated as a double ring collider for the collision of protons and leptons. The lepton beam consisted of either electrons or positrons[3]. HERA started operation in 1992. After a successful operation until the year 2000 a major upgrade has been performed to increase the luminosity. This running phase is termed HERA I, whereas HERA II refers to the second running period during 2002-2007.

Figure 4.1 shows the HERA storage ring with its 6.3 km circumference and its pre-accelerators. Before the injection into HERA the particles were accelerated by different linear accelerators, synchrotrons and the storage ring PETRA. The injection energies were 14 GeV for electrons and 40 GeV for protons. The beams entered in separate bunches with a distance of 28.8 m between successive bunches, corresponding to a bunch crossing time of 96 ns and a collision rate of

[1] **H**adron-**E**lektron-**R**ing**a**nlage, English: Hadron-Electron Ring Accelerator
[2] **D**eutsches **E**lektronen **Sy**nchrotron
[3] The term electrons will be used throughout the text representing both kinds of leptons

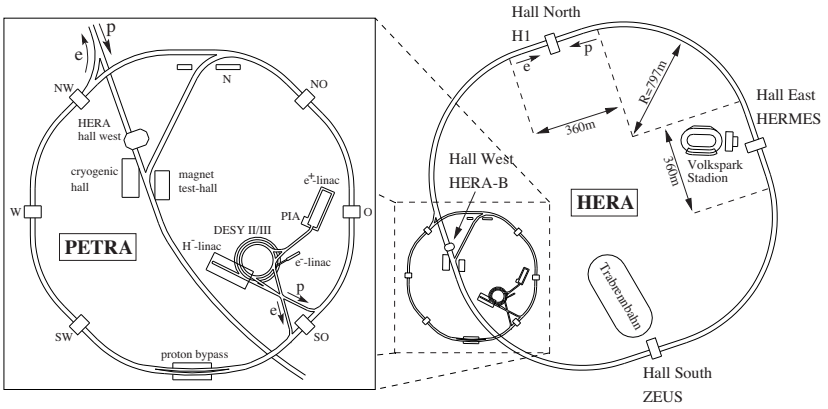

Figure 4.1: The HERA storage ring with its pre-accelerator chain and the four experiments H1, ZEUS, HERMES and HERA-B.

10.4 MHz. The particles were then further accelerated to their nominal beam energies of 27.6 GeV for electrons and 920 GeV for protons. At the four different interaction points (IP) four experiments were located (figure 4.1). The two multi purpose experiments H1 and ZEUS as well as the fixed target experiments HERMES and HERA-B. HERMES made use of the polarized electron beam, which was brought into collision with a gas target to investigate the spin structure of the proton. HERA-B made use of the proton beam halo on a wire target between 1998 and 2003 to study CP violation in decays of B mesons.

From the beam parameters the luminosity can be derived and is defined as

$$\mathscr{L} = \frac{N_P N_e n_b f_0}{4\pi\sigma_x\sigma_y} \tag{4.1}$$

in units of $\mathrm{cm}^{-2}\ \mathrm{s}^{-1}$. $N_{P/e}$ is the number of particles in each bunch, n_b denotes the number of colliding bunches and f_0 the revolution frequency. $\sigma_{x/y}$ denotes the width of the interaction region as illustrated in figure 4.2: During the traversal of the two bunches the distribution of the particles in the projection onto the transverse plane follows a normal distribution with corresponding widths.

The integrated luminosity

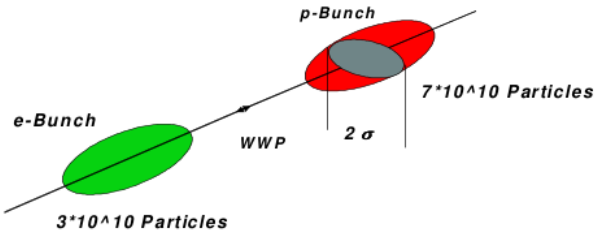

Figure 4.2: Proton and electron bunch penetrating each other. The particles are normally distributed inside the bunches with widths $\sigma_{x/y}$ in the transverse plane.

$$L = \int \mathscr{L} \, \mathrm{d}t \tag{4.2}$$

is directly proportional to the expected number of events for a specific process with interaction cross section σ

$$N = L\sigma. \tag{4.3}$$

At the end of HERA I the machine parameters reached their performance limits. Given the luminosity formula, an upgrade to further improve the performance required mainly a smaller size of the two beams at the interaction point. During a shutdown period in the years 2000-2002 the interaction region was redesigned and the focusing structure was revised in order to provide a stronger focusing and a smaller β function at the interaction points. The upgrade project was based on faster beam separation, i. e. the separation of the low energetic beam and guidance into its own magnetic lattice before the focusing of the proton beam. The focusing structure was based on a doublet focusing in the case of the protons and a triplet for the electron beam. Table 4.1 summarizes the beam parameters for the HERA I and HERA II period as well as for the different e^+/e^- running modes. The decrease of the beam size is clearly visible. σ_x is determined experimentally (cf. 6.3) whereas the ratio $\sigma_x/\sigma_y = 4$ has been derived from the focusing structure

	HERA I		**HERA II**			
	e^-	p	e^-	p	e^+	p
Beam energy E [GeV]	27.5	920	27.5	920	27.5	920
Current I [A]	45	100	58	140	58	140
Particles per bunch N [10^{10}]	3.5	7.3	4.0	10.3	4.0	10.3
Number of beam bunches	189	180	189	180	189	180
Beam widths $\sigma_x \times \sigma_y$ [μm]	190×50		112×30		130×33	
Synchrotron radiation at IP [kW]	6.9		25			
Luminosity [$cm^{-2}s^{-1}$]	$1.4 \cdot 10^{31}$		$7 \cdot 10^{31}$			

Table 4.1: The beam parameters of the HERA collider, before and after the luminosity upgrade and for the $e^-$and e^+mode.

geometry.

Figure 4.3 shows the accumulated luminosity vs. days of running for the two run periods HERA I and HERA II. The upgrade resulted in a factor of 5 of increase in luminosity. During their total time of operation both experiments H1 and ZEUS collected data corresponding to an integrated luminosity of $L \approx 500$ pb^{-1}.

4.2 H1 Detector

The H1 detector is a multi purpose high energy physics detector that was built to observe particles and their properties which were produced during the ep collision process. The detector with its dimensions of approximately $12\,\text{m} \times 10\,\text{m} \times 15\,\text{m}$ and its weight of roughly 2800 tons almost covers the full solid angle. Figure 4.4 shows a schematic drawing of H1. The figure also illustrates the orientation of the right-handed coordinate system that is commonly used at H1. The positive z-axis coincides with the proton flight direction and is referred to as forward direction. The x-axis points in the direction of the center of the HERA storage ring. Due to the different beam energies the center of mass is boosted towards the forward direction. The asymmetric design and geometry as well as a higher granularity in

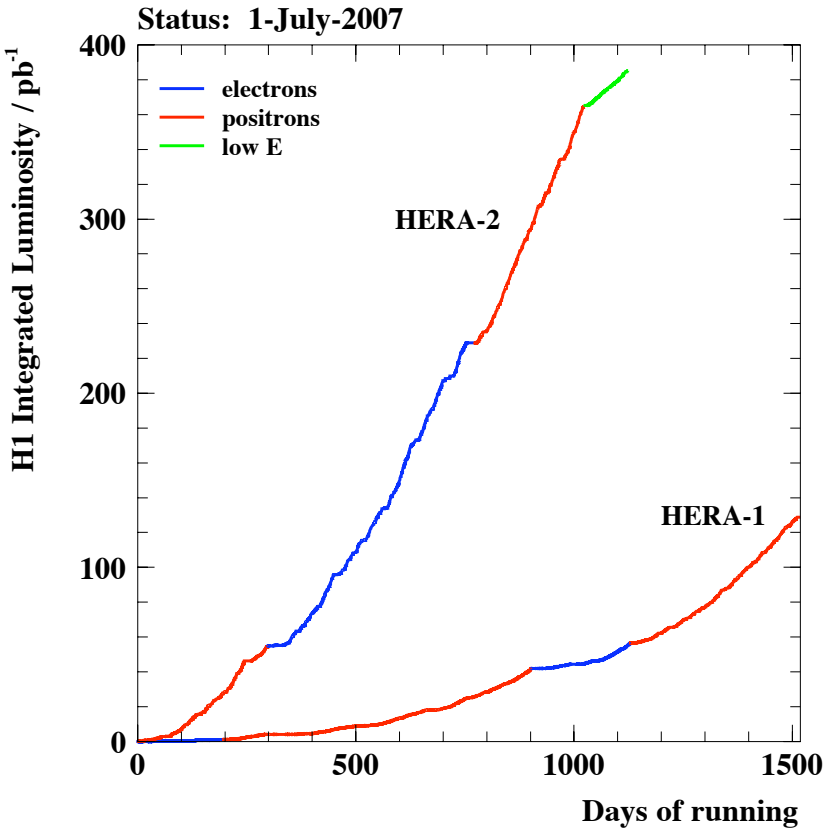

Figure 4.3: Integrated luminosity at the end of HERA operation.

forward direction account for this.

The H1 detector consists of multiple sub-detectors which are arranged around the interaction point in several layers. The beam pipe is surrounded by the central and forward tracking detectors. The trackers are enclosed by the liquid argon calorimeter (LAr) which consist of an electromagnetic and hadronic part. The LAr is surrounded by a superconducting coil which provides the axial field of 1.15 T. The instrumented iron yoke also functions as muon detector and catches hadronic showers that escape the LAr. The forward muon detector covers small angles in the forward direction. Very forward and backward directions are covered by the PLUG calorimeter and the backward calorimeters. A detailed description of the H1 detector can be found in [6]. In the following sections the detector components relevant for this analysis are discussed. Especially emphasized are the Central Tracking Detector which is relevant for the reconstruction of the D meson candidates and the backward calorimeter which plays a crucial role for the reconstruction of the event kinematics.

4.3 Tracking Detector

The H1 Tracking detector consists of several sub-components. The central part combined to the **Central Tracking Detector** (CTD) consists primarily of the two concentric drift chambers CJC1 and CJC2 (Central Jet Chamber), which are described in more detail in section 4.4. The main component of the CTD is supported by several components for dedicated tasks. (cf. figures 4.5 and 4.6) The two thin proportional chambers CIP and COP (Central Inner/Outer Proportional Chamber) are mainly used for triggering purposes. The COZ (Central Outer z-Chamber) is a thin drift chamber with sense wires perpendicular to the beam axis, that account for a z resolution of $\sigma_z \approx 300\,\mu$m and the consequential improvement of the polar

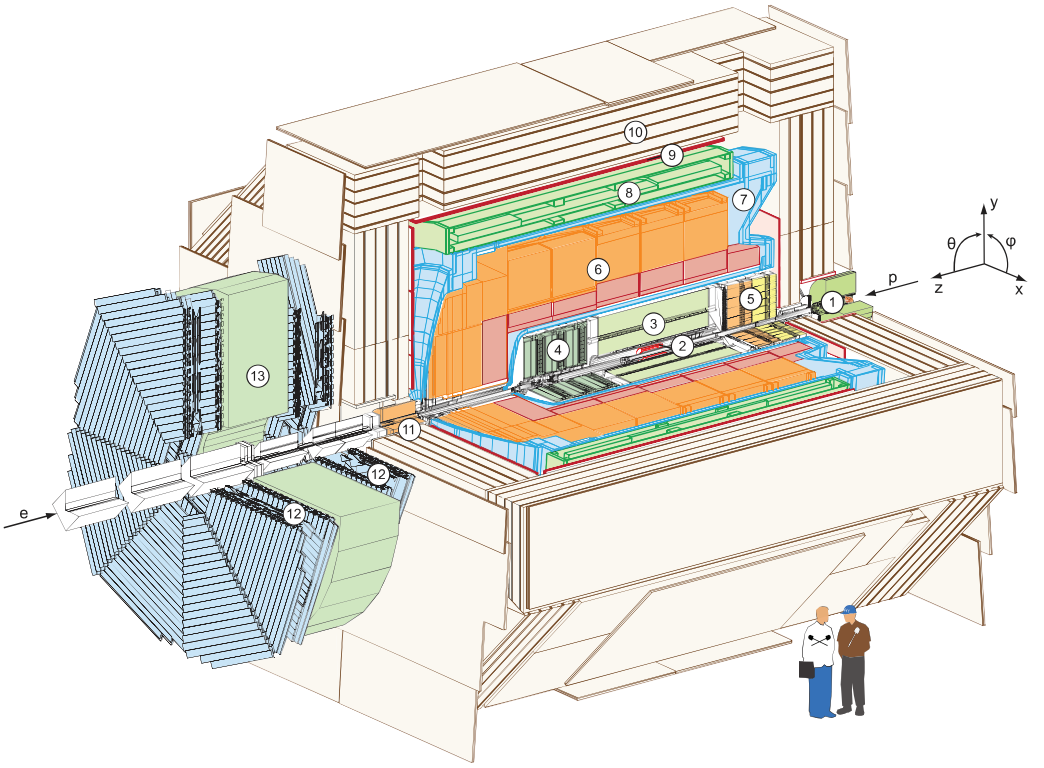

1. Beam pipe and beam magnets
2. Silicon tracking detector
3. Central tracking detector
4. Forward tracking detector
5. Spacal calorimeter (em and had)
6. Liquid Argon calorimeter (em and had)
7. Liquid Argon cryostat
8. Superconductiong coil
9. Muon chambers
10. Instrumented iron (streamer tube detectors)
11. Plug calorimeter
12. Forward muon detector
13. Muon toroid magnet

Figure 4.4: Schematic drawing of the H1 detector. The H1 coordinate system is shown on the right. The protons are entering from the right, electrons from the left.

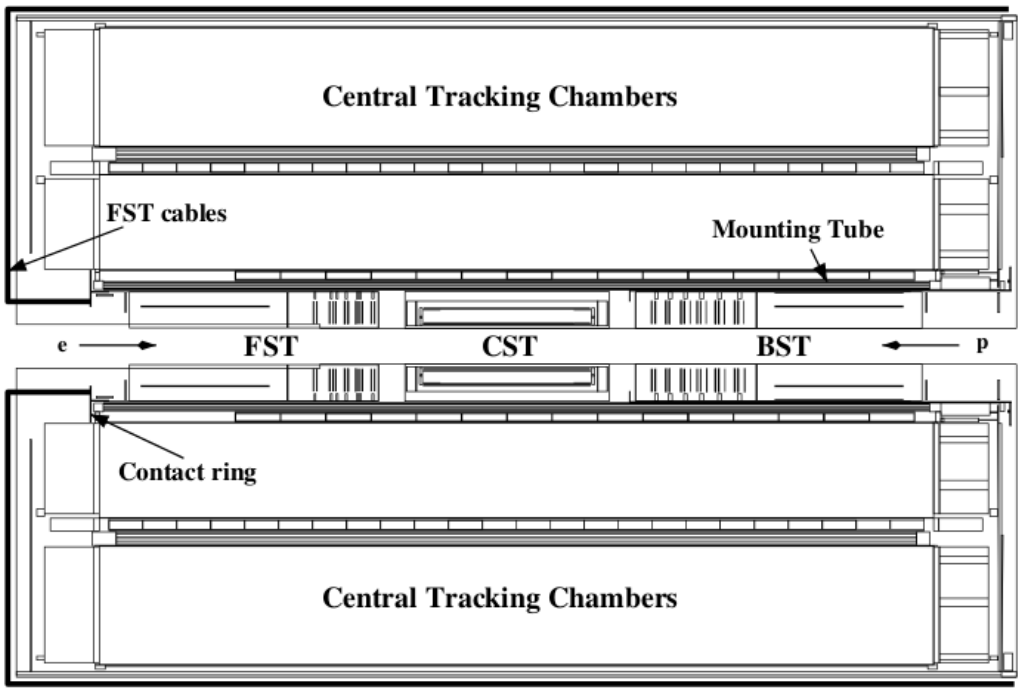

Figure 4.5: Schematic view of the H1 Central Tracking Detector (CTD).

angle measurement of the tracks. The θ coverage of the COZ is $25^\circ < \theta < 156^\circ$.

The **Forward Track Detector** (FTD) extends the polar coverage of the track reconstruction to $5^\circ < \theta < 25^\circ$. It consists of three super-modules with several drift chambers and different wire geometries. The single hit resolution is of the order of $\sigma_{r\phi} \approx 210\,\mu$m in $r\phi$ with a radial resolutions of $\sigma_r \approx 3\,$cm. The momentum resolution takes values of $\sigma_p/p^2 \approx 0.1 - 0.02\,\text{GeV}^{-1}$ according to the track length and its polar angle. The **Backward Proportional Chamber** is located in front of the backward calorimeter and provides an improved position measurement of particles entering the calorimeter. The BPC consists of six wire layers, which have three different azimuthal orientations. For charged particles the spatial resolution in the $r\phi$-plane is $\sigma_{r\phi} \approx 1\,$mm.

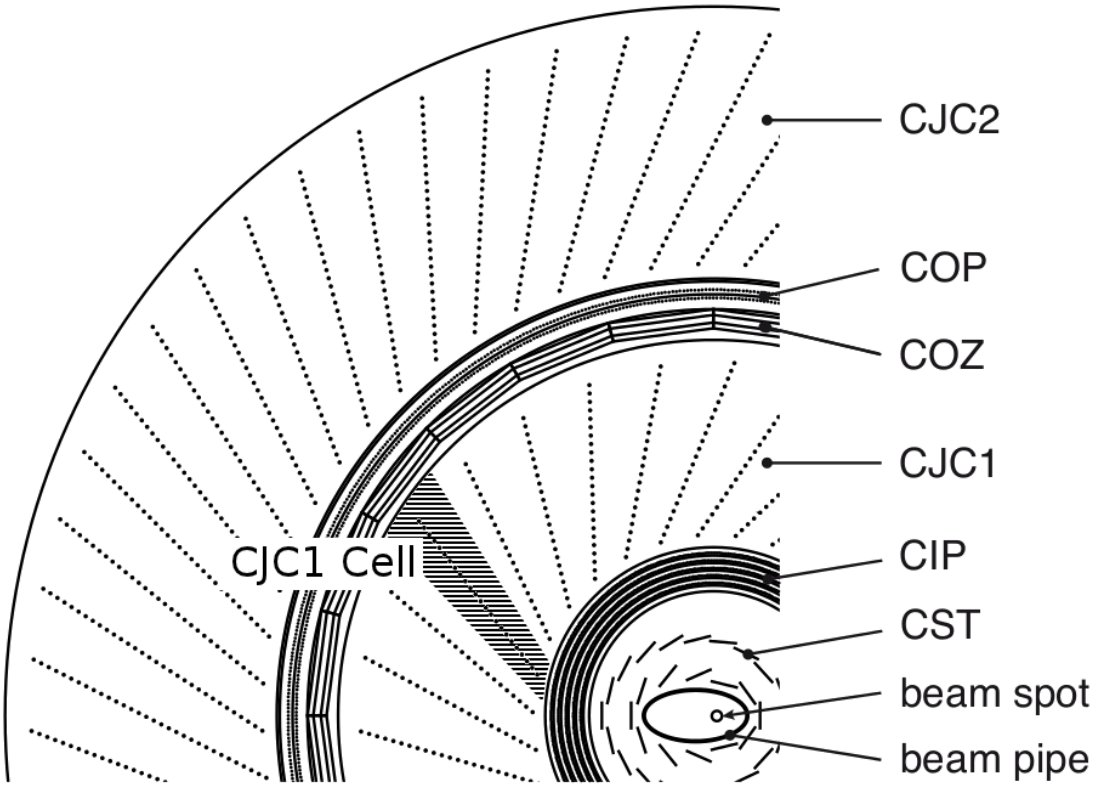

Figure 4.6: Radial view of the Central Tracking Detector (CTD). The sense (anode) wires of the CJC are stretched parallel to the beam pipe and depicted as points. The area between two cathode planes is defined as cell. The cathode wires are not displayed.

Silicon Trackers The silicon trackers have been built to provide vertex information from precision measurements of charged particle tracks close to the interaction point. In order to reduce the lever arm of the track to the interaction point the silicon trackers are placed as close as possible to the beam pipe and have a distance to the IP of 5-10 cm. The central barrel part, the CST (Central Silicon Tracker) consist of two layers of double-sided silicon strip detectors [58]. In the course of the HERA upgrade the mechanical arrangement of the individual sensors was changed to account for the new, elliptical BeAl beam pipe (cf. figures 4.6 and 4.7). Each individual sensor has a size of 5.9×3.4 cm^2. The p side has strips parallel to the z axis with a readout (strip) pitch of 50 μm (25 μm). The n side measures the z coordinate with a strip pitch of 88 μm, without any intermediate strips; a second metal layer contains the readout lines. Six sensors are daisy-chained to form a ladder, with a readout hybrid for 2 x 640 channels (p and n side) at either end. Carbon fiber strips glued to both sides of the ladder provide the mechanical support. The ladders are cylindrically arranged in two layers around the beam pipe such that particle trajectories origination at the IP are perpendicular to the silicon ladders (cf. figure 4.6). 32 ladders are used in total, 12 in the inner and 20 in the outer layer. The polar angle coverage is $30^\circ < \theta < 150^\circ$. The ladders are screwed to rigid carbon fiber end plates, forming a self-supporting structure with minimal dead material: the total thickness of the CST in its central region is 0.40 g/cm^2, corresponding to 1.4% X_0. By the interpolation of the measured hits the achieved intrinsic point resolutions are 12 μm in $r\phi$ and 22 μm in the z direction. The lightweight design and the high intrinsic resolution yields an impact parameter resolution of $20\,\mu\text{m} \oplus 70\,\mu\text{m/p}$ and provides the required precision for the accurate vertex reconstruction.

In the forward and backward region the FST (Forward Silicon Tracker) and the BST (Backward Silicon Tracker) are mounted to complement the CST and to

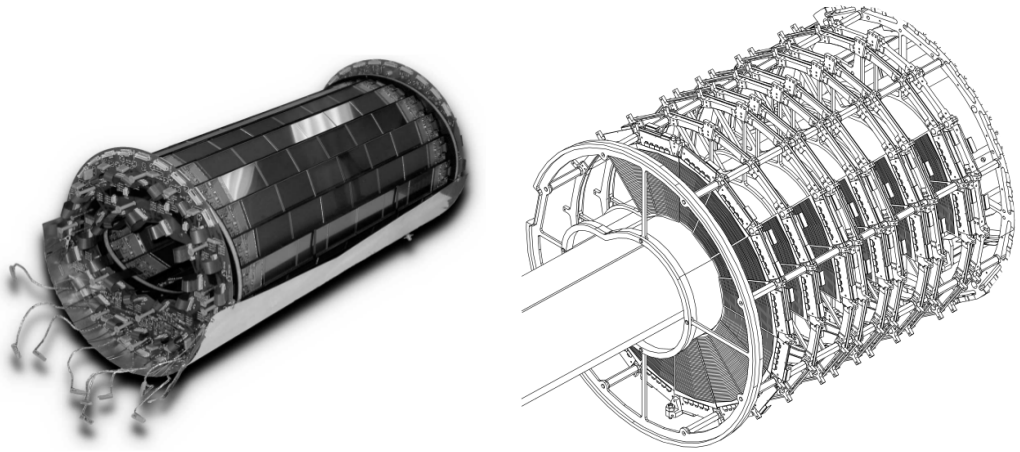

Figure 4.7: Left: The central, barrel part of the H1 silicon tracker (CST). Right: Detail drawing of the Forward Silicon Tracker (FST) showing the wedge-shaped sensors partially inserted constituting the disk layout.

extend the θ coverage [63]. The FST covers the angular region of $6.7^\circ < \theta < 18.8^\circ$ and the BST $163^\circ < \theta < 176^\circ$. Both detectors are disk detectors made up of wedge-shaped sensors (cf. figures 4.7 and 4.5) grouped in several wheels. The BST reaches a transverse momentum resolution of $\sigma_{p_T}/p_T^2 \approx 4\%\,\mathrm{GeV}^{-1}$ and a single track impact parameter resolution of $130\,\mu$m.

4.4 Central Jet Chambers

The main component of the central tracking system is the CJC, consisting of the chambers CJC1 and CJC2, as depicted in figure 4.6. Between the two chambers the COZ is located. Die CJC covers a polar angle of $15^\circ < \theta < 165^\circ$ and the full azimuthal angle. It is filled with a gas mixture of ethane and argon. The electric field which induces the electron drift is caused by potential differences of gold wires spanning the drift chamber. The inner cylinder, the CJC1 consists of 30 drift cells. The cells are delimited by the cathode wire planes. Each cell contains one anode (sense) wire plane (cf. figure 4.6). All wires run parallel with

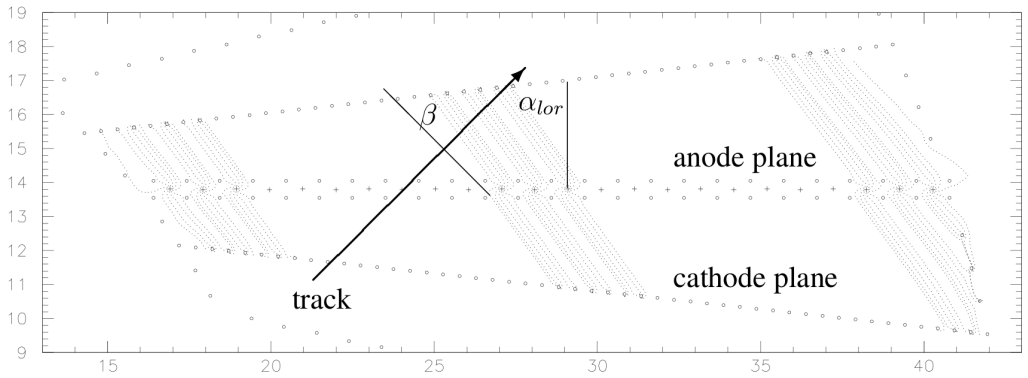

Figure 4.8: CJC1 cell: The anode wires are represented by crosses and the potential and cathode wires by circles. For some inner, central and outer anodes the field (drift) lines from the cathodes to the anodes are shown. The angles between drift direction and the normal to anode plane α_{lor} and the normal to the track direction β are indicated.

respect to the beam axis. In CJC1 there are 30 drift cells each composed of 24 sense wires. CJC2 comprises 60 cells with 32 sense wires each. The drift cells are inclined by about 30° with respect to the radial direction. Taking into account the curvature of a track caused by the magnetic field, the tilt of the cells results in trajectories approximately perpendicular to the electric flux lines for a wide range of momenta. Hence the electron drift direction is roughly orthogonal to the trajectory. Furthermore the curved tracks cross the cell boundaries at least once, which ensures a measurement based on at least two cells. One cell of the CJC showing the arrangement of all kinds of wires is depicted in figure 4.8. The planes of the sense wires alternate with the cathode planes. Furthermore the field wires which surround the sense wires are shown. The field wires are jointly responsible for the parallel geometry of the field. Hardly visible in the figure is the staggering of the signal wires with respect to the anode layer by 160 μm to resolve the drift side ambiguity. From the time difference of the event t_0 and the arrival of the signal the drift duration is deduced. With the knowledge of the drift velocity and the angle regarding the magnetic field α_{lor} (Lorentz angle) the distance between

	CJC1	CJC2
Total length	2.5 m	
Active length	2.5 m	
Inner radius	203 mm	530 mm
Outer radius	451 mm	844 mm
Number of cells	30	60
Number of sense wires	720	1920
Sense wire distance	10.16 mm	
Resolutions:		
Spatial resolution in the $r\phi$-plane $\sigma_{r\phi}$	$130\,\mu$m	
Spatial resolution in the z direction σ_z	$2-10$ cm	

Table 4.2: Technical parameters of the central jet chambers CJC1 and CJC2.

hit and wire can be determined. Figure 4.9 shows the signal after digitization. The amount of deposited charge on the wire is measured on both wire ends and digitized with an 8bit Flash-ADC sampling at 104 MHz. From drift time measurement a single hit resolution in the $r\phi$-plane of $\sigma_{r\phi} = 130\,\mu$m is obtained. The z coordinate is determined by means of charge division. A precision of 1% of the wire length can be achieved: σ_z= 2.2 cm. Table 4.2 summarizes geometrical and technical parameters of the drift chambers.

Measurement of the Particle Energy Loss in the CJC A particle which traverses the CJC ionizes the gas and loses energy. This energy loss can be measured and used for particle identification (cf. 6.2). For this purpose the total charge which is collected on the considered wire is determined from the integral of the charge distribution (cf. figure 4.9).

The energy loss is related to the density and the atomic charge of the chamber gas. The chambers are filled with argon and ethane at a ratio of 50:50 at atmospheric pressure. Argon has a atomic-number-to-weight ratio of $\frac{Z}{A} = 0.450589$ and a density of $\rho = 1.782 \cdot 10^{-3}$g/cm^3. The corresponding characteristics of ethane are $\frac{Z}{A} = 0.59861$ and $\rho = 1.356 \cdot 10^{-3}$g/cm^3. The resulting mean value

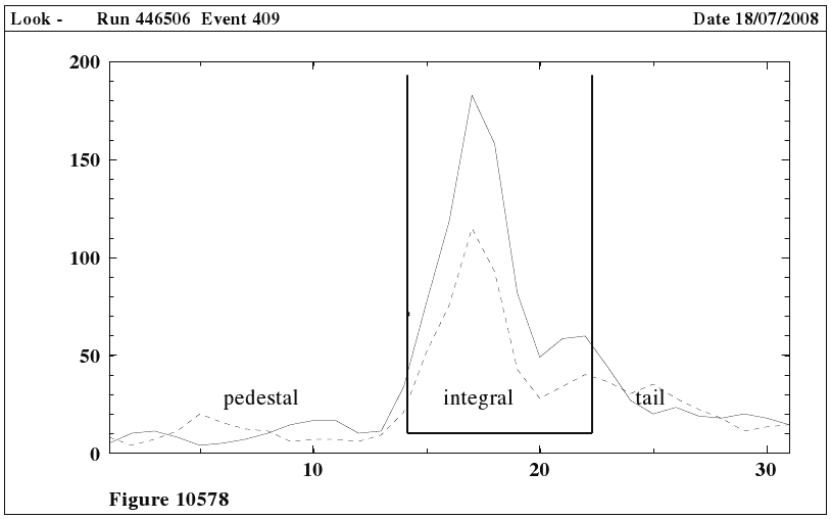

Figure 4.9: Signal after digitization by FADC. The linearized amplitude (in FADC units) is shown as function of time (in 9.6 ns bins) for both wire ends (full, dashed line). The integration interval is indicated.

for the mixture of the chamber gas amounts to $\langle \rho \frac{Z}{A} \rangle = 0.807 \cdot 10^{-3} \mathrm{g/cm}^{-3}$. The charge which is produced during the ionization process is proportional to the energy loss $(dE/dx)_{BB}$ of the particle

$$Q_{prim} = C\rho_{gas} \left(\frac{\mathrm{d}E(\beta\gamma)}{\mathrm{d}x} \right)_{BB} \Delta x \,.$$

The constant C depends on the mixing ratio of the gas and Δx corresponds to the length of the traversed particle path.

4.5 Backward Calorimeter

The backward calorimeter covers the backward region ($153^\circ \leq \theta \leq 174^\circ$). It consists of the electromagnetic and the hadronic part. The electromagnetic part is built-up of single cells of dimension $4.05\,\mathrm{cm} \times 4.05\,\mathrm{cm} \times 25\,\mathrm{cm}$. Each single cell consists of 2340 longitudinally aligned scintillating fibers embedded in

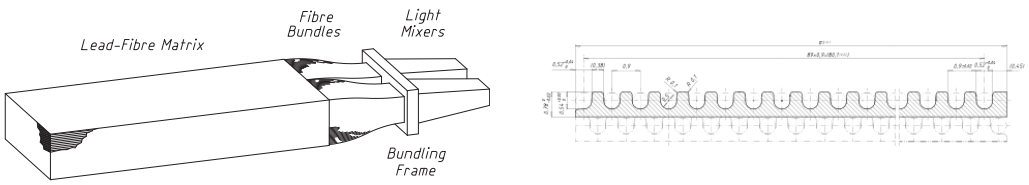

Figure 4.10: Cell of the electromagnetic SpaCal (left). It consists of 2340 longitudinally aligned scintillating fibers embedded in a lead matrix (right)

a lead matrix (cf. figure 4.10) which lead to the denotation "Spaghetti" calorimeter (SpaCal). 16 cells are compiled to form a 4×4 structure called super-module (cf. 4.11). The SpaCal is a sampling calorimeter, which consists of active and absorption material in a sandwich structure (cf. figure 4.10) The scintillating fibers (active material) are embedded in z direction in small notches in the absorption material lead. The fiber diameter is 0.5 mm and the lead-to-fiber ratio is 2.3:1. At the end of the cells photo-multiplier tubes are mounted to collect the light signal from the showers. The electromagnetic SpaCal has an energy resolution of

$$\frac{\delta E_{elm}}{E_{elm}} \simeq \frac{7\%}{\sqrt{E_{elm}/\mathrm{GeV}}} \oplus 1\%$$

The spatial resolution was determined with test beams at CERN and DESY [62, 13] and amounts to

$$\delta_{xy} \simeq \frac{4\,\mathrm{mm}}{\sqrt{E_{elm}/\mathrm{GeV}}} \oplus 1\,\mathrm{mm} \tag{4.4}$$

4.6 Luminosity Detector

At H1 the luminosity is determined by photons which are detected in the photon detector (PD). In the Bethe-Heitler process $ep \to ep\gamma$ bremsstrahlung photons are produced and emitted at very small angles. Because only the electrical form factor

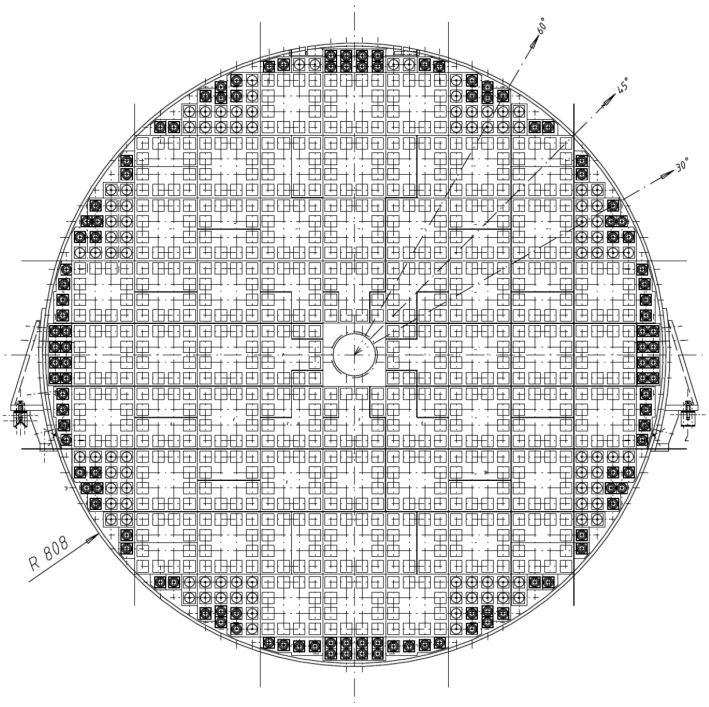

Figure 4.11: Outline of the electromagnetic backward calorimeter. The individual cells are grouped into 4×4 super-modules.

is involved in the calculation of the process the production rate is known to high precision. The photon detector is a Cerenkov sampling calorimeter with tungsten absorbers and mounted at $z = -102.9\,\mathrm{m}$ [6]. Background events mainly arise due to beam-gas interaction and pile-up of multiple interactions per bunch crossing. The off-line reconstruction of the luminosity accounts for these background sources as well as for the acceptance of the photon detector.

Furthermore a precision measurement of the QED Compton (QEDC) process [4] is performed. QEDC events are characterized by two back-to-back deposits regarding the azimuthal angle ϕ in the electromagnetic part of the SpaCal. The QEDC measurement is exploited as independent measurement of the integrated luminosity. The result yields a small positive correction in comparison to the Bethe-Heitler measurement.

4.7 Trigger System

The bunch crossing rate amounts to 10.4 MHz. The H1 data acquisition is capable to handle data at a rate of 50 Hz. Therefore the rate of data recording has to be reduced by the H1 trigger by 6 orders of magnitude. The trigger is built in several stages [6, 31]. During the HERA upgrade the Fast Track Trigger (FTT) was installed in order to cope with the increased luminosity. The FTT is integrated in the first three of the four trigger levels and provides enhanced selectivity for events, especially for photoproduction events in which no scattered electron can be reconstructed. The FTT is able to compute invariant masses on-line. For more details see appendix of [49]. Figure 4.12 gives a schematic overview of the trigger system and its different trigger levels. The first three levels are synchronous with the HERA clock which is in phase with the crossing particle bunches corresponding to intervals of 96.5 ns.

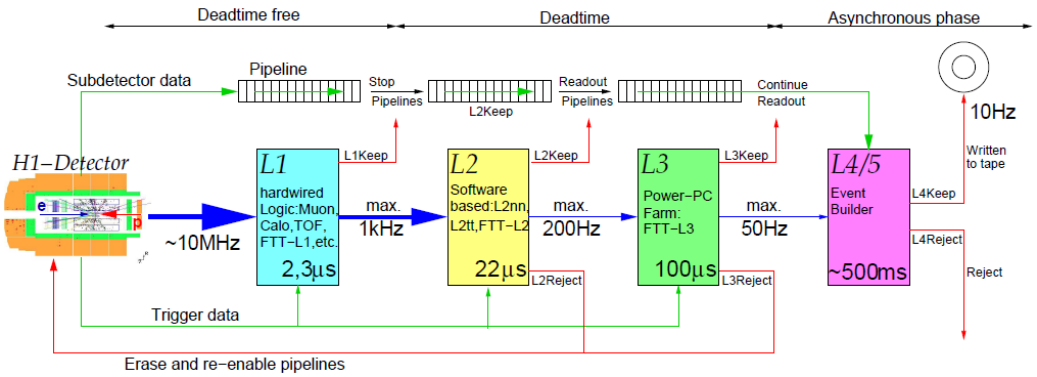

Figure 4.12: Schematic overview of the H1 trigger.

Trigger Layout The **level one** system is a dead time free trigger stage with a pipeline of 2.3 μs depth. The L1 trigger is implemented as hardware system. The trigger signals delivered by the sub-detectors are called trigger elements (TE). The trigger elements are logically combined to sub-triggers "s1" to "s128" in order to select physics channels of interest.

A signal from one of the subtriggers induces a positive level one trigger decision (L1Keep). If the event is kept the front-end pipelines are stopped and the dead time starts. The level one output rate is $\mathcal{O}(1\,\mathrm{kHz})$. The level one trigger decision is refined by the **second level** of the trigger which arrives 23 μs after the bunch crossing. In the second level the trigger elements of the sub-detectors are combined by means of topological correlations (L2TT trigger [16]), by neural networks (L2NN trigger [55]) or track based quantities. The track based quantities are evaluated by the software based FTT L2 system [75]. The L2 decision (L2Keep) causes the readout of the front-end and takes about 1.4 to 2 ms from which the level two rate of $\mathcal{O}(200\,\mathrm{Hz})$ follows. The **level three** decision happens during the readout and is performed by the third level of the FTT (FTT L3). FTT L3 additionally exploits information from the calorimeter and the muon system. Within the time frame of 100 μs a level 3 reject decision (L3Reject) can be fanned

out. A L3Reject aborts the readout and leads to a level 3 rate of $\mathcal{O}(50\,\mathrm{Hz})$. After the level 3 phase the data is transferred to the event builder of the **fourth trigger level**. The event builder rejects remaining background events from beam-gas or beam-wall interactions and classifies all events according to physics finders. Every event is sorted by the physics finder to different physics classes. This final step takes about 500 ms and reduces the rate to 10 - 20 Hz.

4.8 Detector Simulation

The simulation of the H1 detector is based on the GEANT3 [23] software package. The four vectors of the particles which are generate by the MC generators (cf. chapter 3) are made available to the simulation. The passage of the particles and in flight decays are simulated. During the transition of the simulated detector material multiple scattering and nuclear interaction are taken into account. In the process the cross sections which correspond to the material are used. The H1 detector simulation accounts for both the correct geometry of the detector components and the correct material composition. The simulation has been verified with various test beam measurements with prototype detectors and has been monitored and improved to high accuracy. Especially the correct description of multiple scattering is crucial for this analysis in order to retrieve reliable reconstruction efficiencies. After the simulation process the software simulation GEANT produces the detector signals. The signals are in the same format as genuine events and are passed on to the same reconstruction software H1REC.

Chapter 5

Run and Event Selection

5.1 Run selection

This analysis is based on HERA II high energy data recorded in the years 2006 and 2007. Earlier HERA II data is omitted due to CST inefficiencies. This section outlines the run selection criteria. H1 data taking took place in so-called luminosity runs lasting for approximately 8 hours. During this time the run conditions might vary and the data taking was subdivided into several "recorded runs". The recorded runs last for about one hour to assure stable running conditions. The runs are categorized as good, medium or bad, depending on the status of the detector components and the beam quality. In case an essential sub-detector is not fully functional, e.g. the drift chamber of the main calorimeter, the run is labeled as "bad". Bad runs are not taken into account in this analysis. Furthermore the following detector components have to be operational and in the read-out: CJC1 and CJC2, the central silicon tracker, the backward calorimeter, the liquid argon calorimeter, the time of flight and VETO system and the luminosity system. In addition the following criteria have to be fulfilled

- The run exceeds an integrated luminosity of 0.1 nb^{-1}

Year	**Lepton type**	**Luminosity** $L[\mathrm{pb}^{-1}]$
2006	electron	55.1
2006	positron	88.4
2007	positron	47.5

Table 5.1: The luminosity for the run periods of the data of this analysis.

- The trigger system is in phase 2, i.e. in the luminosity run phase to ensure stable running conditions.
- The sub-trigger s61 is switched on and in the read-out
- The z position of the vertex is located within 30 cm around the nominal interaction point

The luminosity of the individual run periods is summarized in table 5.1.

5.2 On-line Event Selection

During the HERA operation the event selection was performed by several triggers (cf. 4.7). The events of this analysis are selected by sub-trigger 61 (s61). A typical DIS event which contains a charmed meson is illustrated in figure 5.1. The event contains a high track multiplicity and a cluster in the backward calorimeter. s61 was initially designed for the selection of D^* events in DIS which have an event topology with high track multiplicity and a distinct energy cluster from the scattered electron. This event topology however holds for all charmed meson decays.

The explicit trigger conditions are (SPLe_IET $> 2\,||\,$SPCLe_IET_Cen_e) which corresponds to an isolated energy deposition in the backward calorimeter with an energy above 9 GeV. Secondly a track condition is determined by the FTT. The condition FTT_mul_Td > 0 corresponds to the occurrence of at least one track

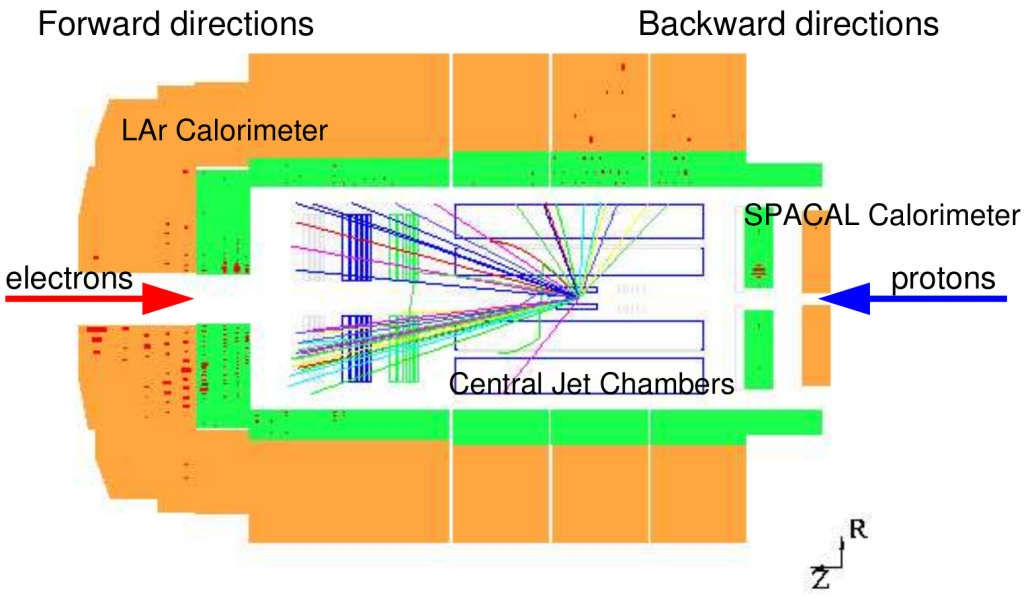

Figure 5.1: Event display of an event triggered by subtrigger 61. It shows the event signature with a high track multiplicity and a cluster in the backward calorimeter.

with a p_T threshold of 900 MeV. In addition veto conditions are implemented on trigger level one to avoid background events from non ep scattering. Subtrigger 61 does not use any conditions from level two or three since the trigger rate is comparably low with stable trigger rates of approximately 12 Hz [42].

5.3 Event Kinematics Reconstruction

This section discusses the experimental reconstruction of the event kinematics. Because of the determination of the scattered electron and the hadronic final state (HFS) the measurement is over-constrained. It can be based on the exclusive reconstruction of the electron final state (electron method), the HFS (Σ-method) or on a method which exploits information of both measurements. The latter is used in this analysis. It has been shown that the $e\Sigma$-method provides the best resolutions, purities and efficiencies in the phase space region of this analysis

[49].

eΣ-method In the $e\Sigma$-method the combined information for $y_{e\Sigma}$ of the electron method at high $y_{e\Sigma}$ and information from the Σ-method at low $y_{e\Sigma}$ are used in order to retrieve the most precise information over the whole kinematic range. $Q^2_{e\Sigma}$ equals Q^2_e and solely uses information of the scattered electron, whereas $x_{e\Sigma}$ exploits the measurement of the HFS. The kinematic variables derived by the $e\Sigma$-method are defined as:

$$Q^2_{e\Sigma} = Q^2_e = 2E^{Beam}_e E_{e'} \cdot (1+\cos(\theta_{e'})) \tag{5.1}$$

$$y_{e\Sigma} = \frac{2E^{Beam}_e \Sigma}{(\Sigma + E_{e'} \cdot (1-\cos\theta_{e'}))^2} \tag{5.2}$$

$$x_{e\Sigma} = x_\Sigma = \frac{E^2_{e'} \sin(\theta_e)}{s \cdot y_\Sigma (1-y_\Sigma)}\,, \tag{5.3}$$

where y_Σ is given by

$$y_\Sigma = \frac{\Sigma}{\Sigma + E_{e'}(1-\cos(\theta_{e'})} \tag{5.4}$$

$$\text{with}\,\Sigma = \sum_a (E - p_{z,a}) = \sum_a E_a \cdot (1-\cos_a)\,,$$

where the summation is performed over all hadronic final state particles.

Backward Calorimeter Calibration and Double Angle Method Yet another reconstruction method is the double angle method which was used for the calibration of the backward calorimeter. The double angle method only relies on the hadronic angle γ_h and the angle of the scattered electron and therefore is independent of the electron energy. The hadronic angle γ_h is defined as

$$\tan\left(\frac{1}{2}\gamma_h\right) := \frac{(E-p_z)_{HFS}}{(p_T)_{HFS}}, \tag{5.5}$$

γ_h can be interpreted as the polar angle of the scattered parton. y, $E_{e'}$, and Q^2 can then be determined with γ_h and the scattered electron angle:

$$y \simeq y_{DA} = \frac{\tan\left(\frac{1}{2}\gamma_h\right)}{\tan\left(\frac{1}{2}\gamma_h\right)+\tan\left(\frac{1}{2}\theta_e\right)} \tag{5.6}$$

$$E_{e'} \simeq E_{DA} := E_e^{Beam} \cdot \frac{1-y_{DA}}{\sin^2\left(\frac{\theta_e}{2}\right)} \tag{5.7}$$

$$Q^2 \simeq Q^2_{DA} := 2E_{DA}E_e^{Beam} \cdot (1-\cos\theta_e). \tag{5.8}$$

The calibration is done using the double angle method which compares the reconstructed energy E_{DA} with the raw cluster energy E_e^{raw}.

From the comparison a correction prescription is derived to correct the cluster energy $E_e^{raw} \rightarrow E_e$ and subsequently to derive a correction factor for each cell. Since a single cluster extends over several SpaCal cells the calibration procedure has to take into account a prescription for the single cell correction as well as a prescription for the cluster position and the energy distribution within a cluster [1].

The double angle method relies on the precision of the measurement of the angles $\theta_e$and γ_h. For that reason a special data set is selected for the calibration procedure. The electron energy is in the range of the kinematic peak $20 < E_{e'} < 32\,\text{GeV}$ and the electron cluster radius $R_{e'}^{cluster} > 4\,\text{cm}$. Furthermore the hadronic angle is in a well resolved range of $15^\circ < \theta_{HAD} < 80^\circ$. Figure 5.2 shows the ratio of E_{DA} and the electron energy $E_{e'}$ reconstructed in the SpaCal after the calibration. The distribution is shown for data and simulated data. The left plot

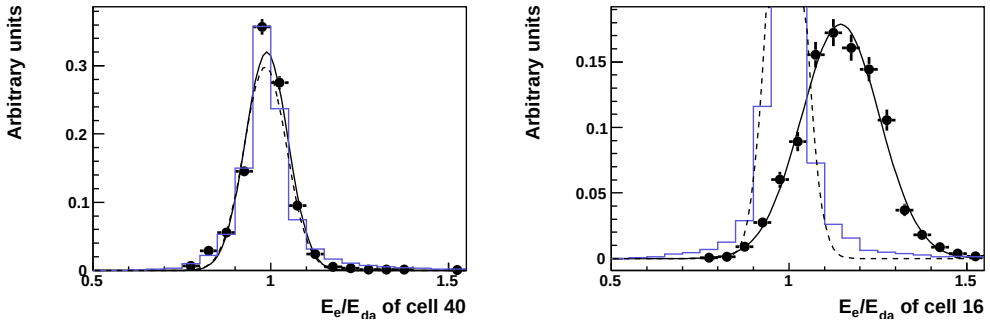

Figure 5.2: Electron energy ratio for events of the SpaCal calibration sample.

shows the result for a cell located in a well resolved area of the SpaCal. The entries scatter around one and the data distribution is well reproduced by the simulation.

In order to retain as many events as possible it is desirable to reconstruct events even for smallest scattering angles down to the inner edge of the SpaCal. In the HERA I period a veto layer was mounted between the SpaCal and the beam pipe. This veto layer enabled the rejection of events in which to much energy of a cluster remained undetected due to leakage. The veto layer was removed for HERA II operation in order to install the focusing magnet structure as close as possible to the interaction point. The missing veto layer results in undetected energy if a cluster position is located to close to the beam pipe and subsequently in an incorrect determination of the calibration constants since all events which have a center of gravity of the cluster in a specific cell are considered. On the other hand these events have a different amount of leakage, depending on the cluster position. Figure 5.2 (right) shows the energy ratio of a cell at the inner edge of the SpaCal. In this cell the electron energy is systematically too high for data. This behavior is not described by the simulation.

The energy ratio distributions are fit with a Gaussian distribution and the mean values for data and simulated data are compared. Figure 5.3 (right) shows the result of the double ratio of the mean values for data and simulated data. The

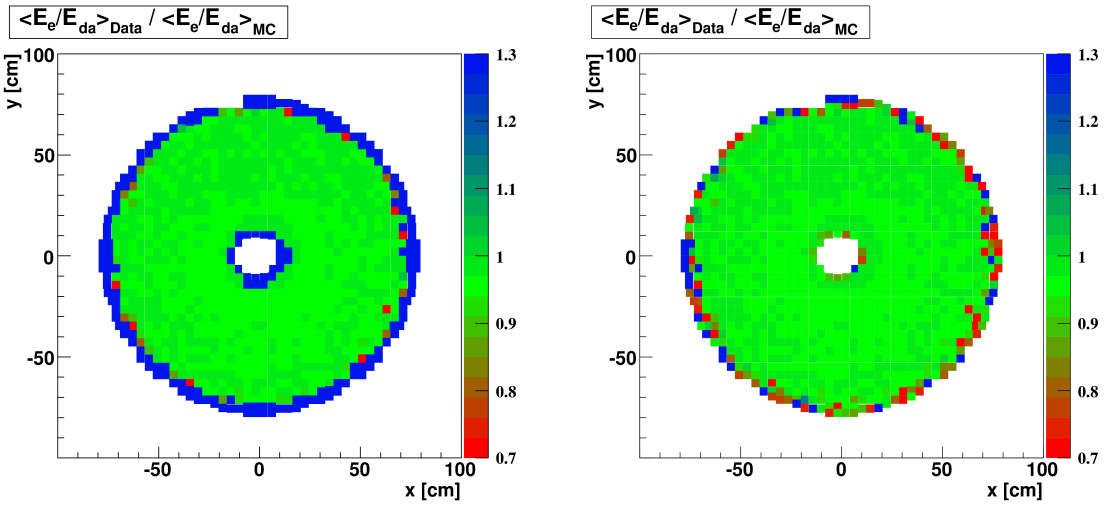

Figure 5.3: Double ratio of the electron energy in the SpaCal for each cell.

outer cells show fluctuations due to low statistics at large radii.

For this analysis events are rejected for which the center of gravity of the cluster of the scattered electron is located in one of the rejected cells which show a bad description by the simulated data. Additionally a radius cut $R_{SpaCal} < 72\,\text{cm}$ is performed. The excluded cells (blue) are shown in figure 5.3 (left).

5.4 Off-line Event Selection

The off-line event selection criteria for the deep inelastic events of this analysis are summarize in table 5.2. The cut on the electron energy is motived by the threshold of the trigger condition. The trigger efficiency drops for small $E_{e'}$ [20]. The electron cluster radius cut rejects hadronic background.

Photon virtuality	$5\,\mathrm{GeV}^2 < Q^2 < 100\,\mathrm{GeV}^2$
Inelasticity	$0.05 < y < 0.6$
Electron Energy	$E_{e'} > 11\,\mathrm{GeV}$
$\sum E_i - p_{z;i}$	> 35
Electron cluster radius	$R_{cluster} < 4\,\mathrm{cm}$
z vertex position	$-30\,\mathrm{cm} < z_{vtx} < 30\,\mathrm{cm}$

Table 5.2: Off-line event selection criteria.

Chapter 6

D Meson Reconstruction

This chapter covers the $D^{\pm}$ and $D^{*\pm}$ meson reconstruction. Firstly the decay channel $D^{\pm} \to K^{\mp}\pi^{\pm}\pi^{\pm}$ for which the production cross sections are derived is discussed. Secondly the reconstruction of decays of the so-called golden decay channel $D^{*\pm} \to K^{\mp}\pi^{\pm}\pi^{\pm}_{slow}$ is described. The D^{*} decays are used for systematic studies because of the similar behavior and low combinatorial background. The mesons under investigation decay inside the uninstrumented vacuum of the beam pipe and are detected by means of their decay particles. The decay particle type is not explicitly identified, nor can a common production vertex be determined with certainty.

The reconstruction method can be summarized as follows: Three tracks with a correct charge combination are selected and treated as decay particle candidates. From these particles a D meson candidate is reconstructed by summing the four-momenta of the decay particles. From the entirety of the reconstructed D meson candidates the amount of signal events is statistically determined with the help of the reconstructed mass spectrum. The masses of real D meson particles cluster around their nominal value.

The sample is enhanced to improve the statistical uncertainty and extend the

accessible phase space. The enhancement is achieved by the reconstruction of several signal classifier and the training and evaluation of a neural network.

The chapter starts with the particle track reconstruction in section 6.1. Section 6.2 treats the specific energy loss of particles which traverse the central jet chamber. The specific energy loss is mass dependent and provides a probability for a particle type at a given momentum. This probability is exploited for corrections during the track reconstruction and as classifier for the enhancement of the sample. In section 6.3 the fit of the decay particle tracks to a common vertex is discussed. From the vertex fit the decay length, the uncertainty on the decay length as well as the χ^2 probability of the fit are derived and provided for the neural network. The application of the neural net is discussed in section 6.5. After the reconstruction of the particle candidates the signal fraction is determined by a fit to the reconstructed mass spectrum. This is discussed in section 6.6.

6.1 Track Reconstruction

In the following the track reconstruction at H1 is described. The parametrization of trajectories traversing the detector is introduced as well as the hit pattern recognition and the initial track finding. Based on these tracks various improvements are implemented which in particular account for the correction of multiple scattering and energy loss and result in improved track parameters and track parameter uncertainties.

Track parametrization The idealized track of an electrically charged particle in a homogeneous magnetic field is described by a helical trajectory, which is defined by 5 parameters $(\kappa, \phi_0, \theta, d_{ca}, z)$. The projection of the helix onto the $r\phi$-plane defines a circle and is parametrized by

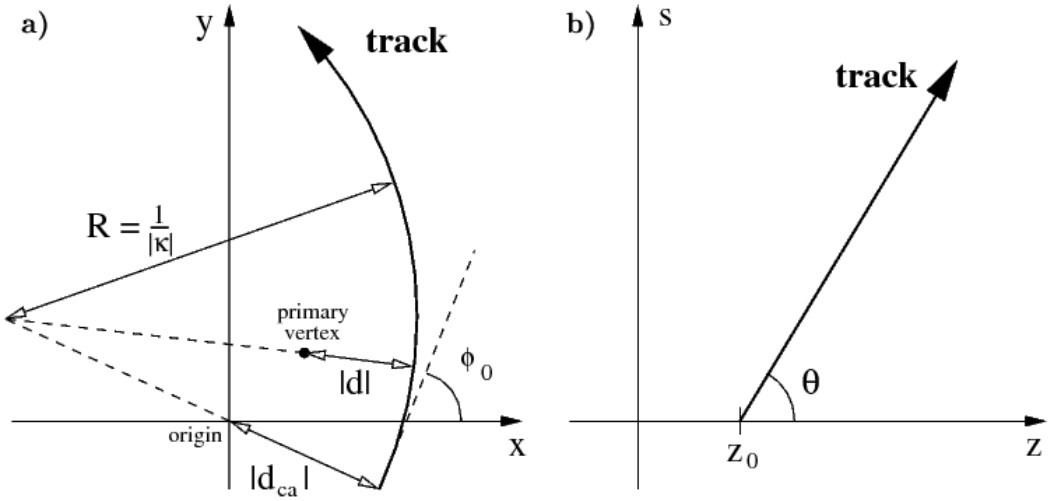

Figure 6.1: Left: Track and its parameters in the $r\phi$-plane. Right: Track in the zs-plane.

$$\frac{1}{2}\kappa(x^2+y^2+d_{ca}^2)-(1+\kappa d_{ca})(x\sin\phi_0-y\ \cos\phi_0)+d_{ca}=0.$$

The parametrization in the zs-plane is given by

$$z=z_0+(\tan\lambda)s,$$

where s is the arc-length for a given value of a corresponding (x,y)-coordinate of the track. The geometrical meaning is depicted in figure 6.1. The transverse momentum can be derived from the curvature κ:

$$p_T=\frac{0.3\cdot B_z}{\kappa}\,[\mathrm{GeV}/c] \tag{6.1}$$

The absolute value of the curvature κ equals the inverse bending radius R, its sign is chosen opposite to the electric charge of the particle. The point of closest approach to the z-axis is defined as starting point of the trajectory $(s=0)$. The absolute value of d_{ca} corresponds to the distance of closest approach. The sign of

d_{ca} is chosen equal to the sign of κ if the circle contains the origin, otherwise the sign is chosen opposite. The azimuthal angle ϕ_0 is the angle between the tangent to the trajectory and the x-axis at $s = 0$. z_0 corresponds to the z coordinate at $s = 0$. In the zs-plane the track forms a straight line with a z-axis intercept of z_0 and a slope $\cot\theta$.

Initial track finding The track reconstruction is based on the hit measurement in the central jet chambers (cf. 4.4). At first short track elements (curvature negligible) are searched independently in the CJC cells with 24 (CJC1) and 32 (CJC2) wires. At this stage the track finding is based almost exclusively on drift time data in the $r\phi$-plane and includes removal of outliers. Within angular sectors the initial track-element finding does not depend on parameters like the Lorentz angle or the drift velocity. The first step involves the search for track elements defined by three hits within angular cells found on three wires with a wire distance of two. The algorithm starts combining all pairs of hits at wires $n \pm 2$ (n = wire index). Possible values of drift distances $\overline{d^n}$ at the wire n are calculated by $\overline{d^n} = |d_i^{n-2} - d_k^{n+2}|/2$ (i,k =hit indices) and stored in a list if the potential direction of the pair does not deviate too much from the radial direction. This list is then compared with the measured values d_j^n and for small differences $|d_j^n - \overline{d^n}|$ the indices of the hits at the three wires are stored as possible track elements. If a specific wire is known to be non-functioning the procedure accounts for that and allows to incorporate the consecutive wire. From these hit triplets the curvature κ and the angle ϕ are determined with sufficient accuracy assuming $d_{ca} \equiv 0$. At this stage the drift sign ambiguity is not resolved. Triplets with a compatible, i. e. not too large value for $|\kappa|$ are kept and used as seeds for the further track reconstruction. Track segments in the cells of each ring are matched separately. Triplets compatible with the fit model are connected to track segments. Compatible hits are continuously added

and the fit procedure is repeated. This procedure is repeated until no further hits are found. After the successful reconstruction in the two CJC rings separately the algorithm tries to combine the track segments. The last step of the $r\phi$ reconstruction adds remaining unlinked hits along the track. After the track reconstruction with the CJC additional hits from the COZ, CIP and CST are added and the track fit is repeated.

The fit of a single helix is an approximation for the ideal case in which the particle traverses the detector without disturbances in a perfect homogeneous magnetic field. Certainly this is not the case and causes an imperfect track parameter determination. The track parameters obtained are used as starting values in a broken-helix fit to acquire corrections due to multiple scattering, the inhomogeneity of the magnetic field and energy loss of the particle when it traverses the detector material. Multiple scattering (MS) accounts for the biggest distortion. MS gives a description of the elastic scattering of charged particles in the Coulomb field of the nuclei of the penetrated material. If the material thickness increases and the number of interactions is sufficiently high the angular distribution can be considered as Gaussian with a mean deflection angle of zero and a variance V. The mean scattering in a material with radiation length X_0 is given by [61]

$$\sigma_\theta = \frac{13.6\,\mathrm{MeV}}{\beta \cdot \gamma} \cdot \sqrt{\frac{L_{eff}}{X_0}} \cdot [1 + 0.038 \cdot \ln(\frac{L_{eff}}{X_0})],$$

where L_{eff} is the length of the path inside the material traversed by the particle. The radiation length is a property of the material. A list all material constituting the H1 detector can be found in [37].

Figure 6.2 depicts the “random walk” of a particle traversing the detector material. For a given σ_θ the covariance matrix for the slope and the angle θ can be determined. By means of the propagation of the uncertainty at the position Δs it is given by

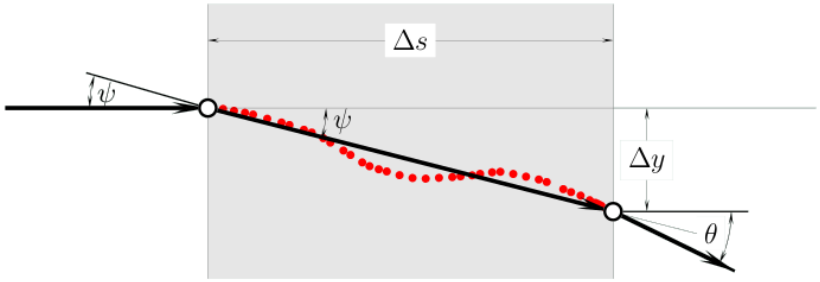

Figure 6.2: Multiple scattering in a material of thickness Δs.

$$V(\Delta s) = \left[\begin{pmatrix} 1 & \Delta s \\ \Delta s & \Delta s^2 \end{pmatrix} + \begin{pmatrix} 0 & 0 \\ 0 & \Delta s^2 \end{pmatrix} \right] \sigma_\theta^2$$

The broken-helix fit The broken-helix fit accounts for multiple scattering at the passage of the material between the outer and inner drift chamber. The fit takes into account two helices simultaneously which are being fit with corresponding curvature and allows for multiple scattering in the COZ. The COZ material is treated as an effective scatterer at the center of gravity s_{cog} of the material at radius $R = 49$ cm. The derived standard deviation of the scattering angle is applied as $\sigma_\theta/2$ at $s_{cog} \pm \Delta s/2$. The uncertainty is propagated to the covariance matrix of the track fit and induces the possibility of a scattering angle and a displacement between the two helices at either side of the COZ.

After the broken helix fit also the multiple scattering which occurs during the passage of other detector components is treated. The multiple scattering angle variances for every detector volume are calculated and propagated to the covariance matrix of the track parameters with regard to κ and ϕ [38].

Energy loss correction A particle loses energy when it traverses the detector material which results in a decrease of the curvature. The energy loss and inho-

mogeneities of the magnetic field are corrected simultaneously by the application of segmented helices. The energy loss is parametrized by the Bethe-Bloch curve [61]:

$$-\frac{dE}{dx} = K \cdot \frac{Z}{A} \cdot \frac{1}{\beta^2} \cdot \left[\frac{1}{2} \cdot \ln \left(\frac{2 \cdot m_e \cdot \beta^2 \cdot \gamma^2 \cdot T_{max}}{I^2} \right) - \beta^2 \right], \tag{6.2}$$

with $K = 0.307\,\mathrm{MeV} \cdot \mathrm{cm}^2/\mathrm{mol}$. β is the velocity of the incident particle, $\gamma = (1-\beta^2)^{-1/2}$, Z and A are the atomic charge and atomic mass of the absorber, m_e is the electron mass. I represents the mean excitation energy and T_{max} is the maximum energy transfer per single collision.

$$T_{max} = \frac{2 \cdot m_e \cdot \beta^2 \cdot \gamma^2}{1 + 2 \cdot \gamma \cdot m_e/m + (m_e/m)^2}.$$

with m denoting the mass of the particle. The mean energy loss ΔE of the particle is then given by $\Delta E = -\mathrm{d}E/\mathrm{d}x \cdot \rho \cdot L_{eff}$. The knowledge of the dependence of the change of the curvature on the change of the energy $\Delta\kappa(\Delta E)$ allows for the deduction of an additional contribution to σ_κ. The uncertainties are taken into account for the individual helix segments.

Since the correction depends on the particle mass a particle identification has to be carried out. The particle type hypothesis is determined by taking the measurement of the specific energy loss in the CJC gas. The procedure is described in more detail in section 6.2. If the probability does not exceed 1% for any considered hypotheses no particle identification takes place. Otherwise if the condition for the weighed likelihood ratio is fulfilled:

$$\frac{w \cdot \mathscr{L}(\text{particle})}{\sum_{\text{All hypotheses}} w_i \cdot \mathscr{L}(\text{particle}_i)} > 0.9,$$

the corresponding mass is assumed. In case the criterion is not met for any hypothesis the mass of a pion is assumed.

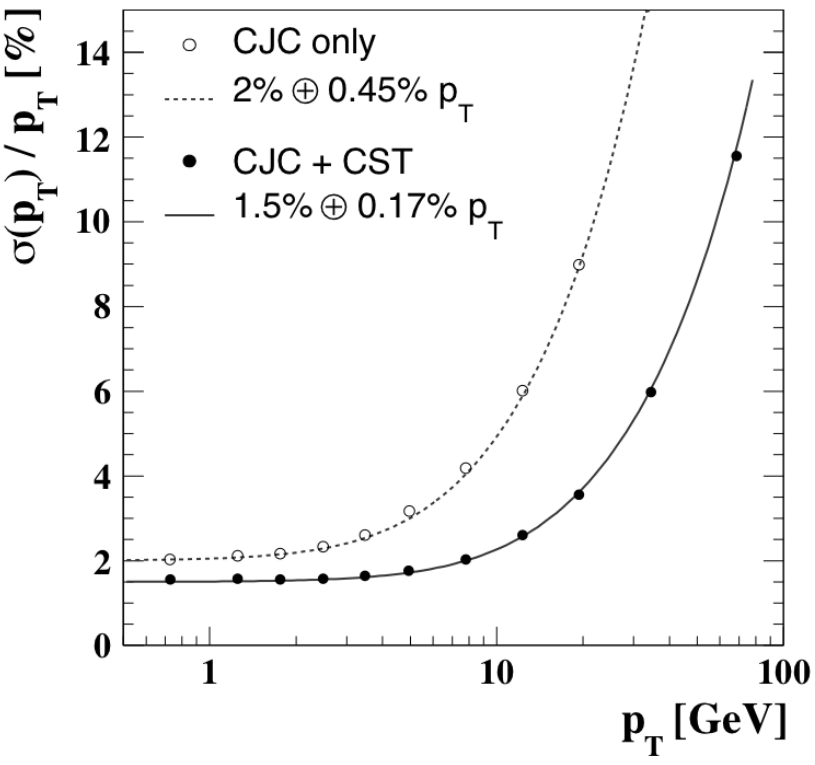

Figure 6.3: H1 central tracker momentum resolution. From [67].

After all corrections have been applied a resolution of $1.5\% \oplus 0.17\% \cdot p_T$ for central tracks is achieved. Figure 6.3 shows the resolution which is derived from an analysis of cosmic particles.

Primary Vertex and Primary Vertex Fitted Tracks An event z-vertex based on the information of the event timing T_0 and the tracks from all silicon vertex detectors is determined. Therefore in the first step a common vertex from all CJC tracks in the $r\phi$ plane is fitted. If the χ^2 probability is smaller than 10^{-4} the track with the biggest χ^2 is removed and the track fit is repeated. Afterwards the z coordinate information of all CJC and silicon tracks with acceptable d_{ca} and compatible timing are used to calculate a weighted average to obtain the z coordinate of the primary vertex [19].

Finally all tracks which originate from the primary vertex are refitted with a vertex constraint. These tracks are referred to as primary vertex fitted tracks. Primary vertex fitted tracks have an improved p_T and θ resolution.

6.2 Specific Energy Loss

The measurement of the specific energy loss in the CJC can be exploited to identify the particle type of a traversing particle. In general charged particles lose energy during material passage due to e. g. nuclear losses, radiative effects and ionization. In case of the CJC and the interaction with the CJC gas ionization is the dominant effect. The energy loss is described by the Bethe-Bloch curve and depends on $\beta\gamma = \frac{p}{m}$, i. e. the ratio of momentum and mass. The Bethe-Bloch curve is depicted in figure 6.4. It describes a μ^+ which traverses copper. The curve has a minimum at $\beta\gamma \approx 2.5$, a steep rise towards smaller values and increases slowly towards higher values.

If the momentum of a given particle is determined it is possible to compare the specific energy loss for a specific mass hypothesis with the predicted one. Subsequently a probability for the particle hypothesis can be derived. In order to calculate a prediction the most probable value of $\mathrm{d}E/\mathrm{d}x$ and its resolution for a given p/m value must be known.

The original Bethe-Bloch curve needs corrections to describe the situation at H1 correctly. In the following the determination of the value and the resolution for a given p/m of the specific energy loss is described. This must be corrected for data as well as for simulated data in order to derive the correct reconstruction efficiencies for both cases and to avoid systematic uncertainties.

The specific energy loss is reconstructed from the deposited charge at the wire ends. This amount of charge cannot be transformed into $\mathrm{d}E/\mathrm{d}x$ directly since

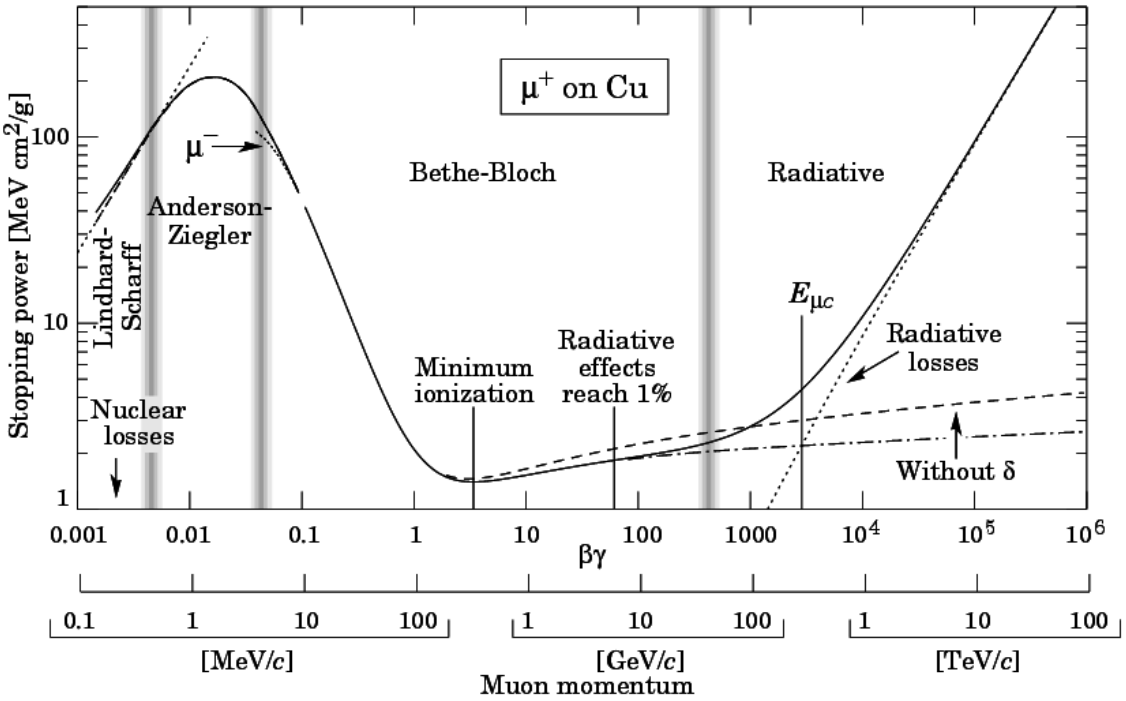

Figure 6.4: Stopping power for positive muons in copper. The $\beta\gamma$ range of 0.1 - 300 is described by the Bethe-Bloch formula.

various detector effects which influence the measurement have to be taken into account. The specific energy loss is proportional to the charge per path length $Q_{prim}/\Delta s$, which is produced in the ionization process during the transition of the chamber. A minimum ionizing particle produces about 100 free electrons in approximately 35 collisions traversing 1 cm of gas. The distribution of $Q_{prim}/\Delta x$ follows a Landau distribution with a long tail. The transformed value $1/\sqrt{Q_{prim}\Delta s}$ on the other hand is Gaussian distributed and therefore used for all applications. In order to derive the primary charge Q_{prim} from the measured deposited charge several calibration steps are performed which result in the calibrated charge Q_{cal}. The calibrated charge is then corrected for several effects. Corrections are first performed on hit level, with which subsequently a mean value is calculated which represents the mean energy loss for the track. At the end, based on the calibrated and on hit level corrected charge the specific energy loss is determined by

$$\frac{\mathrm{d}E(\beta\gamma)}{\mathrm{d}x} = \left(\frac{1}{N_{hit}} \sum_{N_{hit}} \frac{1}{\sqrt{Q_{cal} c_{hit} c_{track}/\Delta s}} \right)^{-2} \tag{6.3}$$

where c_{hit} and c_{track} are the correction factors. The track level correction $c_{track}(p/m, \theta)$ is only applied on analysis level since it depends on the particle type and the polar angle of the track. For the calibration of the charge various gains are taken into account. A global gas gain for each chamber and for measured data in addition gains accounting for the difference of each anode wire and the difference of the two wire ends. This accounts for spatial variations, difference in temperature, electric and magnetic fields, wire diameter and the electronics between the anodes.

Correction on hit level The measured charge depends on the angle γ_{dEdx} between the drift direction of the ionized electrons and the flight direction of the traversing particle. The angle influences the time interval between the arrival

of the first and the last contributing electrons. The length of the time interval consequently influences the width of the FADC signal and the amount of ADC counts inside and outside of the integration interval. Furthermore the staggering effect must be taken into account because the amount of deposited charge depends on whether the drift electrons traversed the anode plane or not in order to reach the sense wires. The correction factor $c_{hit}(\gamma_{dEdx})$ which corrects these effects is parametrized by 5 parameters which are determined for data and MC separately.

Correction on track level The correction on track level can only be applied on analysis level since it depends on the particle type hypothesis and the polar angle. For data three contributions are taken into account, the threshold and saturation effect as well as the electronic gain. Some hits are not detected because the charges do not reach the threshold of the charge integration code. This effect is called threshold effect and turns out to be more significant at low values for the energy loss. A correction is applied which is derived from a comparison of the mean and the median values of the $\mathrm{d}E/\mathrm{d}x$ for the different hits along a track. The correction parameters are determined separately for data and Monte Carlo. Furthermore even after the correction a dependence on the polar angel θ is found for Monte Carlo events. Also this dependence is corrected by the application of a charge dependent parametrized correction curve. The saturation effect takes into account that electrons which reach the wires first create secondary electrons which results in a self screening effect. The effect and the electronic gain are corrected in data exclusively.

Parametrization Even after all applied corrections the curve of the specific energy loss does not follow the initial Bethe-Bloch curve. An additional parameter is introduced which accounts especially for the low momentum behavior:

$$\frac{\mathrm{d}E(p/m)}{\mathrm{d}x} = \mathrm{d}E/\mathrm{d}x|_{\mathrm{MIP}}\,\xi\,z^2\frac{1}{\beta^n}[K+\ln(\beta^2\gamma^2)-\beta^2-\delta,$$

the $\frac{1}{\beta^n}$ dependence is introduced instead of the $\frac{1}{\beta^2}$ dependence. Afterwards in total 5 parameters which define the Bethe-Bloch curve are determined for data and Monte Carlo separately. An overall good agreement is found between data and MC for the derived parameters. [46]

To exploit the specific energy loss as classifier the measured value is compared to the prediction by calculating the χ^2 and the corresponding χ^2 probability P_{dEdx}. For this reason the resolution of the $\mathrm{d}E/\mathrm{d}x$ is determined:

$$\delta(\mathrm{d}E/\mathrm{d}x) = \frac{(\mathrm{d}E/\mathrm{d}x)_{\mathrm{Measured}} - (\mathrm{d}E/\mathrm{d}x)_{\mathrm{Expected}}}{(\mathrm{d}E/\mathrm{d}x)_{\mathrm{Expected}}} \tag{6.4}$$

A reasonable agreement of the resolutions for data of $47\%/\sqrt{N_{\mathrm{Hit}}}$ and for MC $52.7\%/\sqrt{N_{\mathrm{Hit}}}$ is achieved [52, 46]. However, the expected scaling of the resolution with $1/\sqrt{N_{\mathrm{Hit}}}$ is not found for simulated events (cf. figure 6.5). This deficiency is corrected by means of a correction factor $c_{\delta(\mathrm{d}E/\mathrm{d}x)}$ which is parametrized by two parameters. The $\chi^2_{\mathrm{d}E/\mathrm{d}x}$ is then calculated as

$$\chi^2_{\mathrm{d}E/\mathrm{d}x} = \frac{[(\mathrm{d}E/\mathrm{d}x)_{\mathrm{Measured}} - (\mathrm{d}E/\mathrm{d}x)_{\mathrm{Expected}}]^2}{\delta(\mathrm{d}E/\mathrm{d}x)^2 \cdot c^2_{\delta(\mathrm{d}E/\mathrm{d}x)}} \tag{6.5}$$

6.3 Secondary Vertex Fit

In a χ^2 vertex fit procedure the significance of the decay length, the uncertainty on the decay length and the χ^2 probability are derived and later on used as classifiers to enhance the sample. The classifier distributions and benefits of the application are discussed in section 6.5. The following section describes the fitting requirements and technique.

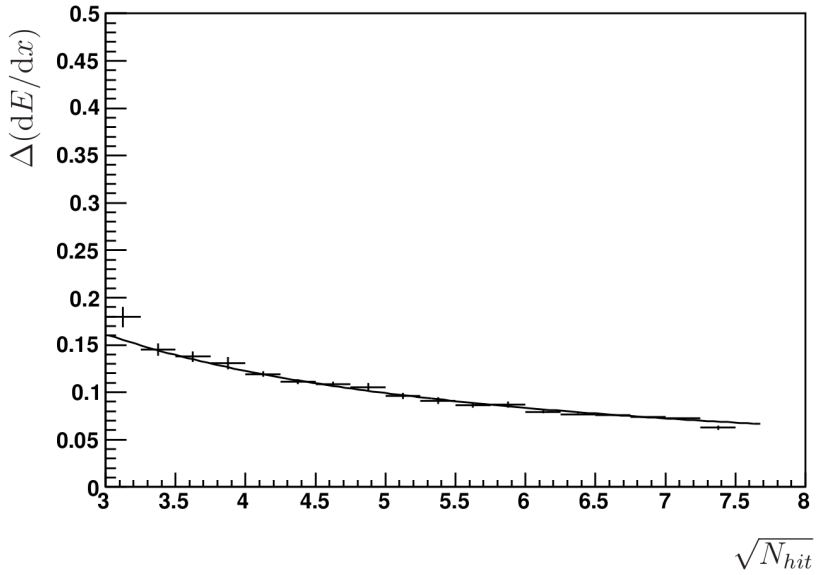

Figure 6.5: Specific energy loss resolution as function of $\sqrt{N_{\mathrm{Hit}}}$ for simulated data. The curve indicates the parametrization used for the correction. From [46].

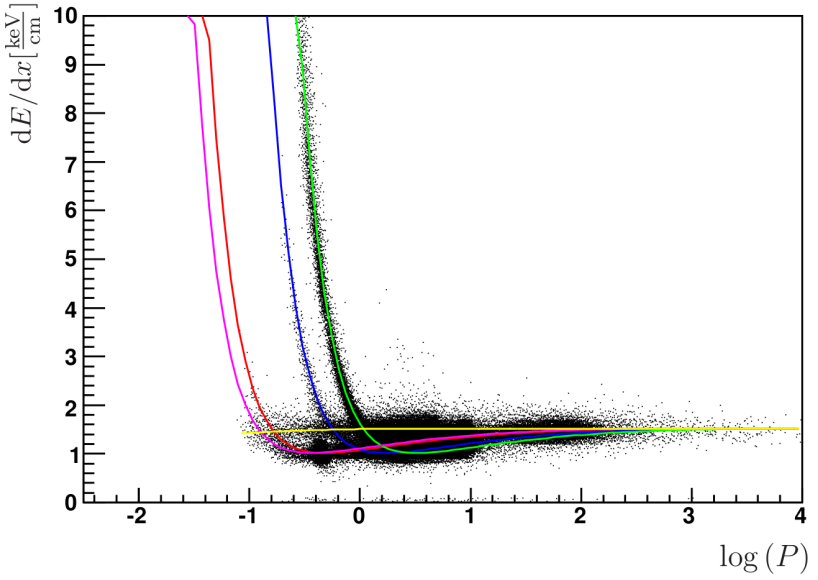

Figure 6.6: Specific energy loss for Monte Carlo Events and the reference curves for electrons (yellow), protons (green), kaons (blue) and muons (pink). From [46].

Parameters which enter the fit procedure are the parameters of the tracks of the decay particles and their uncertainties as well as the interaction point with its uncertainty. The position of the interaction point is derived from the beam trajectory and the z-vertex position [64]. A simultaneous fit calculates the most probable values for the primary vertex $\vec{r}_{PV}$ and the secondary vertex $\vec{r}_{SV}$. The fit is performed in the $r\phi$ plane only for which only the track parameters $(d_{\mathrm{ca}}, \kappa, \phi)$ are needed. $(d_{\mathrm{ca}}, \kappa, \phi)$ define the track in the $r\phi$ plane and are significantly better resolved than the z related components. The decay topology is depicted in figure 6.7. The decays take place in the uninstrumented vacuum of the beam pipe. Therefore the trajectories must be extrapolated to the inner detector. The closest detector component, the CST is $5-10$ cm away from the interaction point.

Taking into account the resolutions of the track parameters and the beam spot which were discussed in earlier chapters it has been shown that an unconstrained fit to the decay vertex $\vec{r}_{SV}$ yield a mean resolution of $\sigma_x \approx 130\ \mu$m in horizontal direction and $\sigma_y \approx 150\ \mu$m in vertical direction [37]. The different resolutions in x and y result from the flat beam spot. An improvement in the resolution can be achieved by constraining the direction of the vectored decay length $\vec{l} = \vec{r}_{SV} - \vec{r}_{PV}$ to the direction of the reconstructed momentum of the D meson. The direction of the momentum is significantly better resolved. The resolutions are improved by $\approx 10\%$. The horizontal component of the primary vertex resolution is even improved by $\approx 30\%$.

The fit is performed by minimizing the corresponding χ^2 function and the constraint is implemented by means of Lagrangian multipliers. A detailed description of the vertex fit can be found in [37]. The fit result provides the best values for the vertex positions and their uncertainties. The directional decay length is then defined as

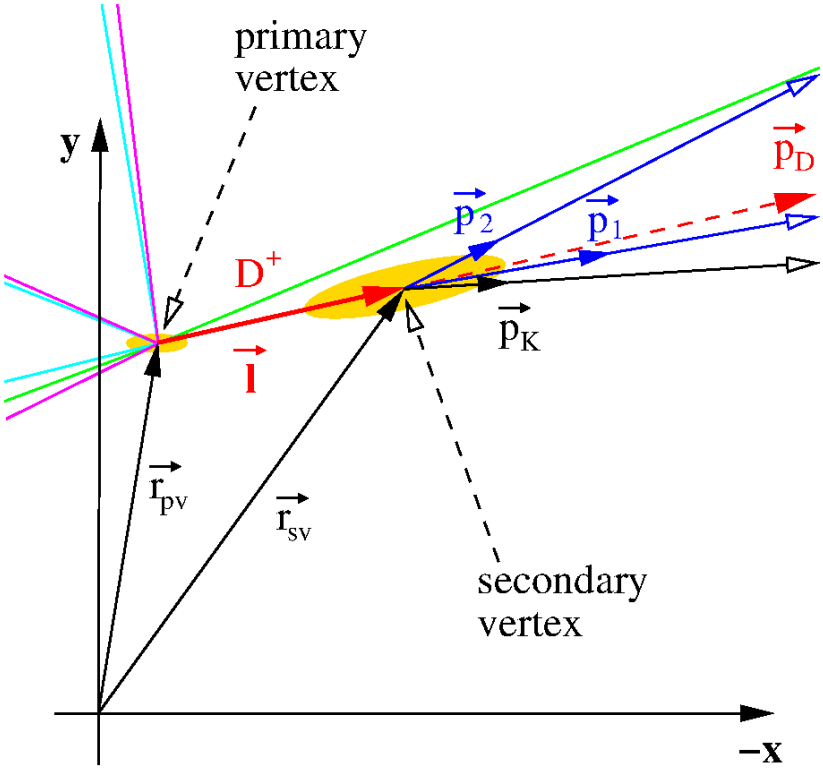

Figure 6.7: The topology of a $D^{\pm} \to K^-\pi^+\pi^+$decay.

$$l = \begin{cases} |\vec{l}| & \text{if } \frac{\vec{p}}{|\vec{p}|} = \frac{\vec{l}}{|\vec{l}|} \\ -|\vec{l}| & \text{if } \frac{\vec{p}}{|\vec{p}|} = -\frac{\vec{l}}{|\vec{l}|} \end{cases} \tag{6.6}$$

and can take negative values if the vectored decay length points opposite to the momentum vector. The vertex fit further provides the corresponding uncertainty on the decay length and the probability P_{Vtx} of the χ^2 result. The significance S_l of the decay length is defined as the ratio of the decay length and its uncertainty:

$$S_l = \frac{l}{\sigma_l} \tag{6.7}$$

6.4 Particle Candidate Selection

This section discusses the D meson candidate selection. The candidates are directly reconstructed from its presumed decay products. Three tracks are selected from which the invariant mass of a potential mother particle is derived. The four momenta of the individual decay particles are reconstructed, which are deduced from the track parameters and the assigned mass hypothesis. The combined tracks form a decay candidate. Afterwards the combinatorial background is subtracted. Combinatorial background consists of tracks which have not been produced in the analyzed decay channel, but originate from other production processes. The fraction of combinatorial background is significant, especially at low transverse momenta. The background subtraction is treated in section 6.6. In this section the reconstruction of the $D^{\pm}$ meson decay is discussed, which is of primary interest because it is the channel for which the production cross sections are derived. Furthermore the D^{*} decay into the golden channel is treated since it is used for systematic studies.

$D^{\pm}$ candidate selection For the $D^{\pm}$ reconstruction all central tracks which have a length above 10 cm and a transverse momentum above 0.3 GeV are taken into account. From these tracks all triple with a net charge of ± 1 are selected. The track charge signature of the decay $D^{+} \to K^{-}\pi^{+}\pi^{+}$ is $(-,+,+)$, whereas in case of $D^{-} \to K^{+}\pi^{-}\pi^{-}$ it corresponds to $(+,-,-)$. The identical particle selection which would result from the exchange of the two likewise charged particles is not taken into account. The kaon hypothesis is applied to the particle whose charge only occurs once. The pion hypothesis is applied to the other tracks correspondingly. Then the secondary vertex fit is carried out and provides improved parameters for p_{T} and ϕ (cf. 6.3). Furthermore the polar angle is taken from the corresponding primary vertex fitted track in case a successful primary vertex fit

has been performed for the track in question (cf. 6.1). With the improved track parameters the mass of the D meson candidate is derived from the four-vectors p_i of the decay particles:

$$p_i = \begin{pmatrix} E_i \\ \vec{p}_i \end{pmatrix} = \begin{pmatrix} \sqrt{m_i^2 + \vec{p}_i^2} \\ p_{T;i}\cos\phi_i \\ p_{T;i}\sin\phi_i \\ p_{T;i}\cot\theta_i \end{pmatrix} \tag{6.8}$$

where m_i is mass corresponding to each decay particle hypothesis. The four-vector of the mother particle is the sum of the four-vectors p_i:

$$p(D^{\pm}) = \sum_{Decay\,particles} p_i$$

and the invariant mass is derived by $m(D^{\pm}) = p^2(D^{\pm})$.

Besides the correct charge combination a so-called **wrong charge decay** is reconstructed. The net charge of a triple is ± 1 as well and the exactly same combinatorics is regarded. However the first two particle hypothesis are interchanged. This would describe the non resonant doubly Cabibbo suppressed decay $D^{\pm} \to K^{\pm}\pi^{\mp}\pi^{\pm}$ (cf. 2.11). The reconstructed mass spectrum consists mainly of combinatorial background and is exploited to determine the background parameter as described in section 6.6.

D* particle selection The $D^{*\pm}$ mesons are reconstructed in the "golden decay channel": $D^{*\pm} \to D^0\pi^{\pm}_{\text{slow}} \to K^{\mp}\pi^{\pm}\pi^{\pm}_{\text{slow}}$. To resemble the $D^{\pm}$ selection as close as possible the same quality criteria with respect to the track selection is performed as for the $D^{\pm}$ candidates. Only the transverse momentum of the π_{slow} is allowed to be as low as 0.1 GeV. In order to reconstruct the full decay chain first the D^0 decay into kaon and pion: $D^0 \to K^{\mp}\pi^{\mp}$ is reconstructed by selecting two oppositely

charged particles and applying the particle hypotheses. Thereafter the vertex fit is performed and the improved track parameters are assigned, analogous to the $D^{\pm}$ reconstruction. The invariant mass of the D^0 is derived and the candidate is kept if the mass difference of the reconstructed D^0 mass and the nominal mass is less than 0.16 GeV: $|m_{D^0} - m(K\pi)| < 0.16\,\text{GeV}$. Subsequently the tracks are combined with the third track of a potential π_{slow} which carries the same charge as the other pion. This combination is referred to as correct charge. The mass difference of the reconstructed D^* and D^0, $\Delta m = m(D^*) - m(D^0)$ is then calculated. The nominal mass difference Δm amounts to only 145.4 MeV which is only slightly above the pion mass of $m(\pi) = 139.57$ MeV. This results in a restricted phase space and implies very low momenta of the π_{slow}. The advantage of this method is the low combinatorial background and the good resolution of the mass difference Δm compared to the individual masses of the D^* and D^0. The low background allows the reconstruction of signals even if no enhancement to the sample is performed. This allows the use of the D^* sample for systematic studies.

Additionally also in the case of the D^* a **wrong charge sample** is reconstructed to help understand the combinatorial background. The wrong charge decay is selected from the decay $D^{*\pm} \to D^0\pi^{\mp}_{\text{slow}} \to K^{\pm}\pi^{\pm}\pi^{\mp}_{\text{slow}}$. This decay does not show a resonance in the Δm distribution.

6.5 Neural Network Candidate Classification

The particle candidates are classified with the help of a neural network (NN). In general a neural network is a non-linear mathematical function, which maps multiple input variables onto a real valued output variable. In high energy physics a typical application is the mapping of the features of an event or particle candidate onto a probability which indicates the probability to find a signal or background

event. The NN is a supervised learning algorithm which uses simulated data to train the model parameter and subsequently predict the outcome of unknown input variables. This is used to enhance the data sample and to optimize the signal to background ratio. The classical approach of the enhancement of the analyzed data set is the application of straight line cuts. Straight line cuts reject an event in case a parameter exceeds a certain threshold. The drawback of this procedure is the same behavior over the whole phase space which is usually sub-optimal. Furthermore the application of more than one straight line cut does not take into account the correlation of the parameters.

The neural network is able to evaluate several input parameters simultaneously. The reconstructed information of a decay, e.g. the decay length and the specific energy loss are exploited to achieve an optimal signal and background separation. Based on several significant classifiers an estimate of the signal probability is calculated. In the calculation in particular the correlations of the classifiers are taken into account. A predefined behavior of the dedicated training sample is adopted by supervised learning. Afterwards this "learned" behavior is applied to new unknown cases. In the case of this analysis the desired behavior is derived from simulated events for which it is known whether the event is a true signal event or not. After the training the network predicts signal weights for data events.

The neural network takes into account the different behavior in different areas of the phase space. An intuitive motivation for the consideration of a phase space dependent approach are the significance of the decay length and the specific energy loss of the kaon decay particle candidate. While the specific energy loss has more prediction power at low transverse momenta the decay length significance plays a more significant role at larger p_{T}. The importance of different "selection strengths" in different phase space areas is especially important for small

transverse momenta of the $D^{\pm}$ meson, for which the combinatorial background is significant and critical.

In the course of this section the classifier which are used for the training and evaluation of the network are discussed and motivated. The design of the neural net which is used in this analysis is discussed as well as the training and the evaluation.

The Classifier The classifier which enter the neural network separate signal and background events on a statistical level. The classifier involvement improves the signal but cannot differentiate signal and background on an explicit event level. Also is it not possible to completely eliminate the background. Considering a classifier distribution one would find a different shape for signal and background events which results in a signal probability for an explicit value of the classifier. Figure 6.8(a) shows the normalized distribution of the decay length significance and illustrates this behavior: E.g. for $S_l \approx 5$ the signal probability is much higher compared to $S_l \approx 0$. Nonetheless one has to keep in mind that the background distribution in this illustration is strongly downscaled and there is still a good chance to find a background event with $S_l \approx 5$. The discriminating power of the input variables further increases if they are evaluated simultaneously.

Figure 6.8 shows the distributions of the variables which have been derived from the secondary vertex fit: l, σ_l and S_l. The background distribution contains the events from the inclusive `DJANGOH` sample (cf. 3.1). It is apparent that the decay length is well suited to enhance the charm sample. Charmed mesons decay weakly and therefore have a longer lifetime. The decay length is the product of lifetime and momentum. Especially at large transverse momenta the decay length is significantly larger for signal events than for combinatorial background. At the same time the uncertainty on the decay length σ_l is taken into account.

σ_l is the propagated uncertainty from the uncertainties of the track parameters and the uncertainty of the primary vertex. From figure 6.8(c) it can be seen that σ_l is slightly smaller on average. The discriminating power on the other hand is not as significant as the decay length. σ_l does not depend on the transverse momentum, therefore the ratio of l and σ_l, i.e. the significance S_l is the most significant classifier, especially at medium and high p_{T}. The classifier provided for the neural network are S_l and σ_l.

In addition the χ^2 probabilities of the vertex fit P_{Vtx} and of the specific energy loss of the kaon P_{dEdx} (cf. equation 6.5) are used as classifiers for the neural network. The distribution of P_{Vtx} (figure 6.9) illustrates the tendency to larger probabilities for signal events. P_{Vtx} describes the probability to actually find the vertex with the parameters derived from the fit. In this case it also means to find the vertex at the given location with the given track parameters. Hence it takes into account geometrical relations. E.g. the vertex location does not fit the direction of the momentum P_{Vtx} would decrease. P_{Vtx} likewise with σ_l does not strongly depend on the magnitude of the transverse momentum. The background distribution for P_{Vtx} clearly peaks at very small values and decreases strongly towards more likely values.

Finally the distribution of P_{dEdx} is shown in figure 6.9(b). The difference of the shapes for signal and background events is most pronounced for this classifier. Additionally the signal events are relatively evenly distributed as expected. The uniform distribution indicates a correct description of the resolution of the specific energy loss in the simulation.

The Multi Layer Perceptron The neural network which is used is a multi layer perceptron (MLP), which is a special kind of artificial neural networks (ANN). ANN are mathematical models following the function of biological neural net-

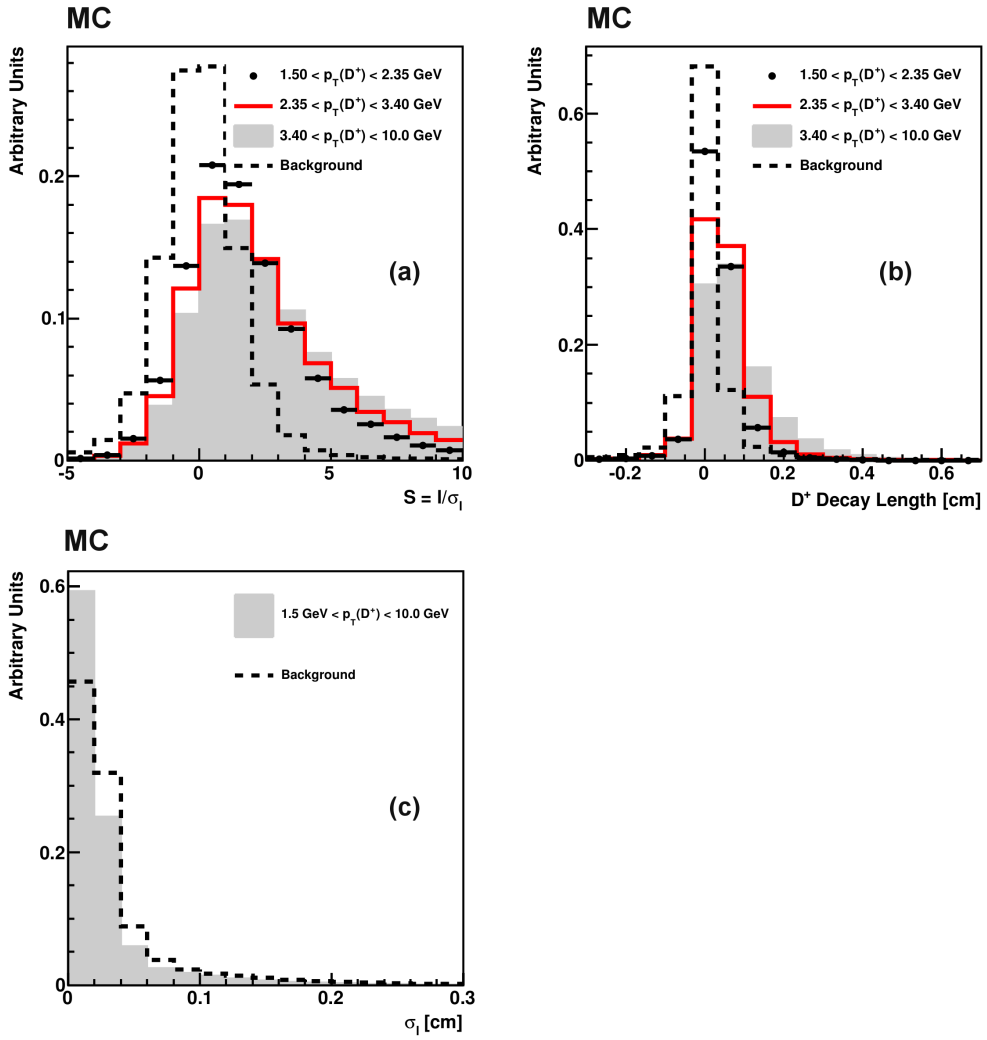

Figure 6.8: Normalized distributions of the significance of the decay length, the decay length and the decay length error. Signal and background distributions are shown for different ranges of the transverse momentum. The signal events originate from the RAPGAP Monte Carlo, the background candidates from the inclusive DJANGOH sample.

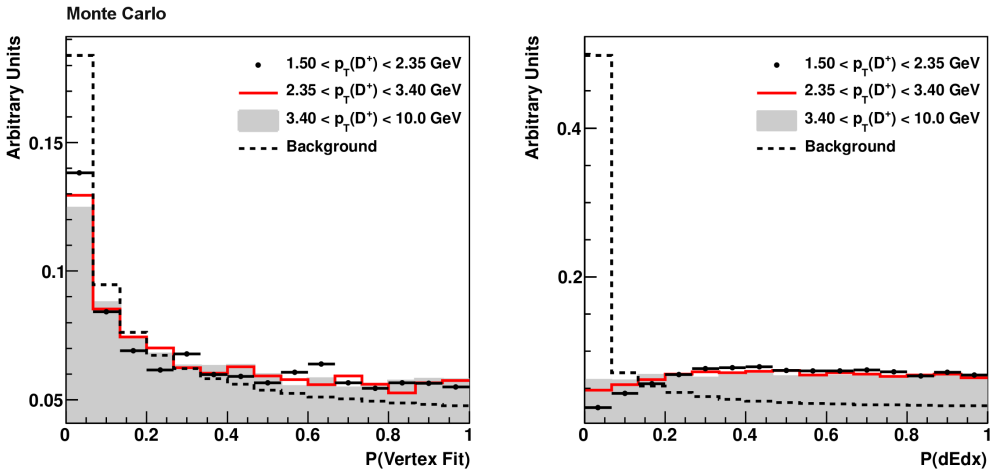

Figure 6.9: Normalized distributions of the $\mathrm{d}E/\mathrm{d}x$ and vertex fit probabilities as function of p_{T}

works. They are based on the linking of neurons and in principal can have any topology. Multi layer perceptrons on the other hand are composed of several layers of neurons of which only neurons of neighboring layers can communicate.

In general a MLP is a non-linear map $F_{NN} : X \rightarrow Y$, where an element of the input data X is mapped onto the set Y of appropriate output. In case of event classification in high energy physics the input usually consists of a set of discriminating parameters which have been directly measured or reconstructed. The output is a single real number equivalent to a signal probability. In figure 6.10 the design of a MLP is illustrated. It consists of the input layer, followed by k hidden layers and finally the output node. The hidden layer then again can consist of arbitrarily many nodes. The calculation of the output follows the feed forward paradigm. The neurons of the leftmost layer are simply the values of the input variables $x_1^0, ..., x_N^0$. Thereafter the value of each node is calculated from the results of the neurons of the preceding layer. The jth neuron of layer l is calculated as:

$$x_j^l = A(\sum_{m=0}^{M_{l-1}} w_{mj}^{l-1} \cdot x_m^{l-1}) = A(w_{0j}^{l-1} + \sum_{m=1}^{M_{l-1}} w_{mj}^{l-1} \cdot x_m^{l-1}), \tag{6.9}$$

From this expression the output is derived recursively. The weights w_{mj}^l are the parameters of the network which defines its behavior. Every connection of two nodes is characterized by its own weight. $A(x)$ is the activation function $A(x) = \frac{1}{1+e^{-x}}$. Its functional form is depicted in figure 6.11. The application of $A(x)$ "activates" a neuron smoothly. If the value which enters a node is small the node is "deactivated" and "switched on" for larger values. Furthermore there are the so-called bias nodes x_0^l which are set to 1. The corresponding weights w_{0j}^l determine the "activation-level" of every single node.

Training of the MLP The behavior of the MLP is specified by the weights. The weights are supposed to be determined such that the net describes the features of a dedicated training sample. For the weight determination MLPs follow a supervised learning paradigm. Supervised learners are trained with a set of training data of which the behavior is supposed to be adapted. The MLP is trained with Monte Carlo data. In total 60.000 events are used, 30.000 $D^{\pm}$ decays used as signal events and 30.000 events of non $D^{\pm}$ decay candidates, i.e. combinatorial background. Whether or not a candidate of the training sample is an actual $D^{\pm}$ decay is explicitly determined with the help of generator information. The signal events are taken from the `RAPGAP` sample, whereas the background is taken from the inclusive `DJANGOH` sample.

The properties of the N training events $(x_1,...,x_N)$ are propagated back to the weights $\mathbf{w}$ by means of an error function $E(x_1,...,x_N,\mathbf{w})$, which is supposed to be minimized:

$$E(x_1,...,x_N,\mathbf{w}) = \sum_{a=1}^{N} \frac{1}{2}(y_{NN,a}(\mathbf{w}) - \hat{y}_a)^2 \tag{6.10}$$

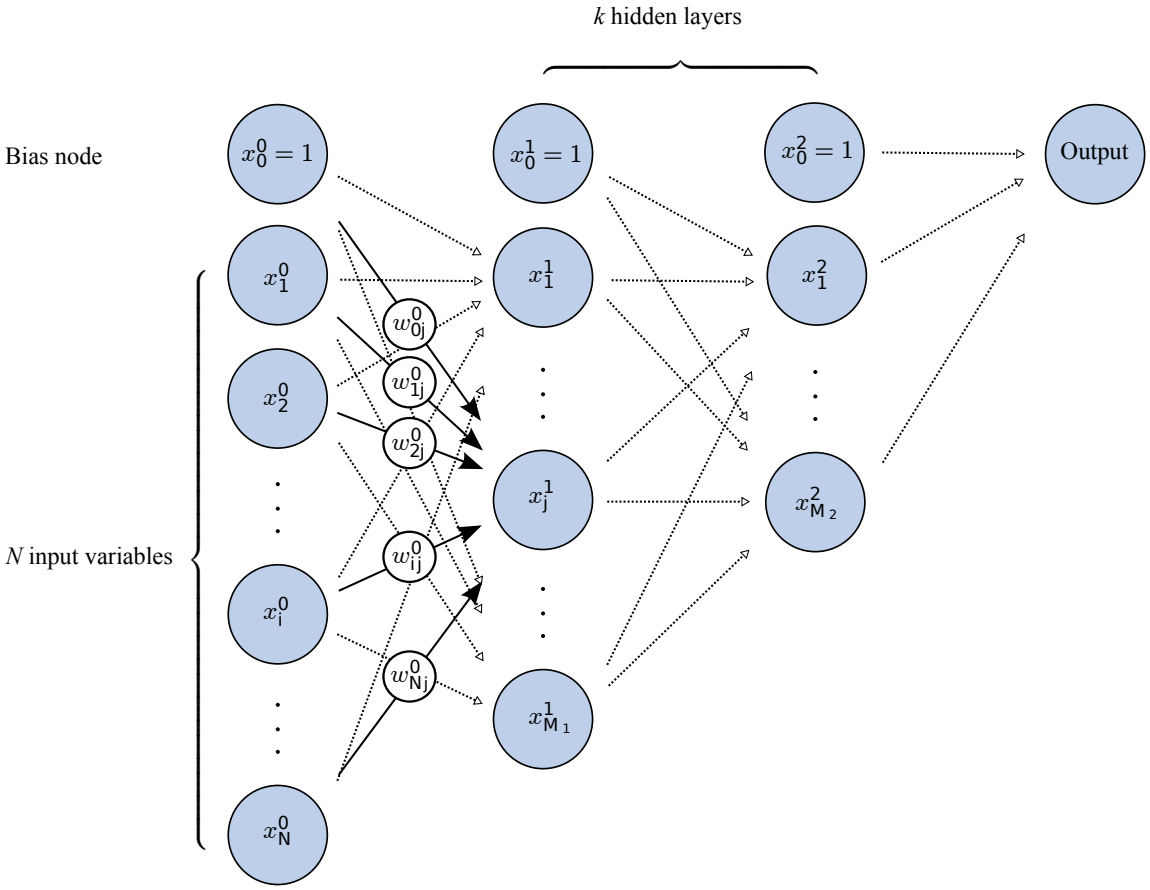

Figure 6.10: Graphical representation of a MLP. The calculation of the *Output*-node follows the rules of feed forward networks. Weights w_{ij}^{l} are only shown as examples. In principal every connecting line is correlated to a weight.

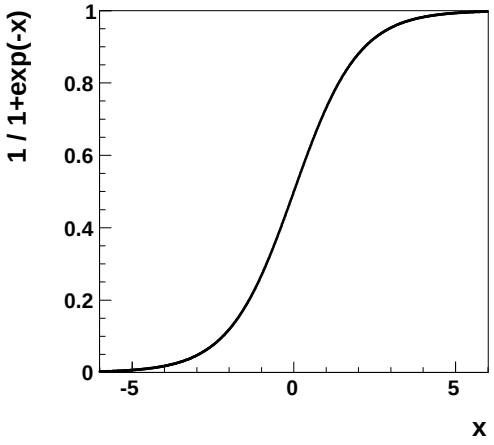

Figure 6.11: Activation function $A(x) = \frac{1}{1+e^{-x}}$.

$y_{NN,a}(\mathbf{w})$ is the output of the neural network for the event a. $\hat{y}_a$ corresponds to the desired output. The desired output in case of this analysis is 0 for a background event and 1 for a signal event. A fit of the weights is performed by starting from a random set of weights $\mathbf{w}^j$. The weights are updated by moving into the direction of steepest descent in the $\mathbf{w}$ space.

$$\mathbf{w}^{(j+1)} = \mathbf{w}^j - \eta \nabla_{\mathbf{w}} E$$

This method is denoted as bulk learning. An alternative method is the so-called on-line learning, where the weights are updated at each event. The TMVA framework [47], which is used in this analysis applies on-line learning.

Layout of the MLP The network used in this analysis consists of 7 input nodes, one node for each of the classifiers S_l, σ_l, P_{Vtx}, $P_{dEdx}(Kaon)$. Additionally the p_{T} of the tracks are fed into the network to account for the dependency of the classification on the transverse momentum. Furthermore the training events are weighted with $p_{\mathrm{T}}^2(D^{\pm})$ to take into account the descending p_{T} distribution and

the low statistics at larger p_{T}. The first hidden layer of the network consists of 15 nodes, the second layer of 7 nodes. Extensive studies have been performed to find an optimal layout of the MLP. The layout is flexible enough to reach the best possible performance, i.e. the highest classification power. At the same time it is kept as small as possible in order not to run the risk to over-train the network and to keep a smooth behavior.

In the low p_{T} range the signal-to-noise ratio (SNR) is significantly worse because of the much higher combinatorial background. But even for low p_{T} a SNR which allows the fit to the mass distribution and a reliable signal extraction is required. The quadratic p_{T} weight achieves the best result in the sense that enough background events are rejected at low p_{T} and at the same time the maximum amount of signal events over the whole phase space is preserved. Without the application of the event weight or an event weight with a smaller exponent the neural net would mainly focus on the optimal behavior at low p_{T}. The signal at larger p_{T} would as well strongly decrease. On the other hand a weight with an exponent larger than two would result in a strong emphasis of the NN on events with large p_{T} and would not reduce enough background at low p_{T} to allow a reliable signal extraction.

Results of the Training Figure 6.12 shows the distribution of the MLP response $F_{NN}(x_1^0,...,x_N^0)$ for signal and background events. The figure shows the training sample and an independent test sample. The results cluster at small values near 0 for background events and near 1 for signal events, which corresponds to the intended behavior. The comparison of the training data with the independent test sample demonstrates the general applicability of the event classification and the fact that the network is not over-trained. The term “over-training” indicates that the weights which were found during the training phase specifically describe the

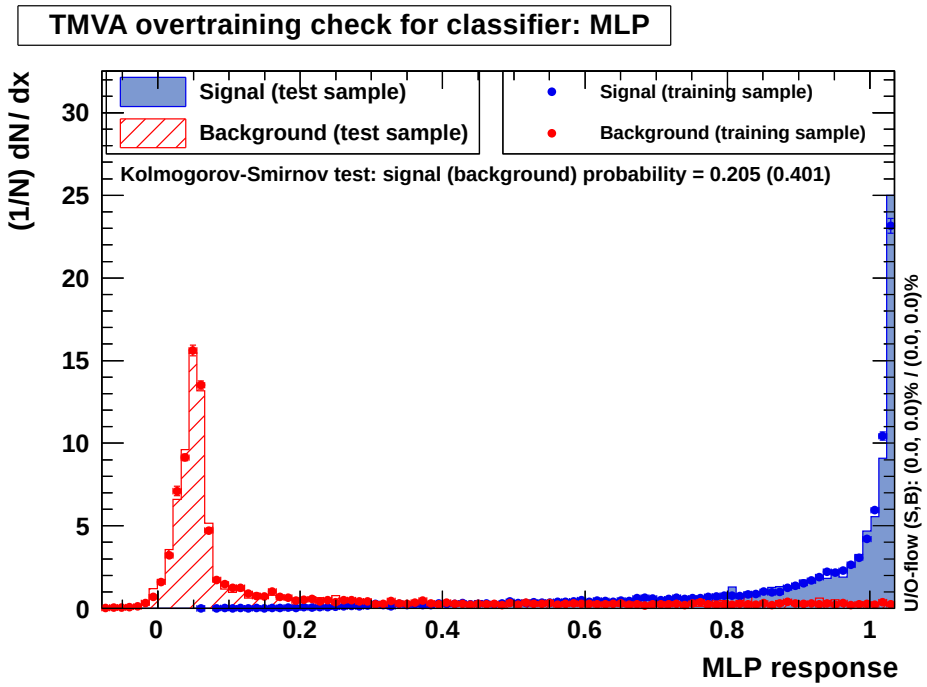

Figure 6.12: MLP response F_{NN} of signal and background events for the training and test sample

features of the training sample, but are not generally applicable.

Figure 6.13 shows the receiver curve, the background rejection versus the signal efficiency. In this analysis a cut on $F_{NN} > 0.6$ is applied, which corresponds to a total background rejection of 0.86 and a signal efficiency of 0.9. But signal and background events cannot be separated over the full phase space as the figure suggests. Figure 6.13 refers to the momentum weighed events, for low transverse momenta the signal efficiency is lower in comparison to the high p_{T} region. See figure 6.14 for the $D^{\pm}$ yield. Figure 6.15 shows the distribution of the significance S_l and indicates the selection behavior of the neural network and the signal loss in several p_{T} ranges. Events with negative values for the significance are almost completely rejected. Before the selection the significance distributions are similarly shaped among the different p_{T} ranges. The F_{NN} selection tends to smaller S_l for low p_{T} events. It is owed to higher decay lengths at boosted high p_{T} events and therefore a higher classification power even at low values of S_l.

Figure 6.16 shows the signal to background ratio of events with a mass in a 3 sigma mass window: $M_{D^+} - 3\sigma < m_{D^+} < m_{D^+} + 3\sigma$. In principle a higher statistical significance could be achieved if a stronger cut on F_{NN} would be applied. On the other hand as many signal events as possible have to be kept to avoid to lose signal events in regions of very low efficiency (cf. figure 7.1). At very low p_{T} the reconstruction efficiency amounts to only 7% which results in very large extrapolation factors and potentially large extrapolation uncertainties.

6.6 Signal Extraction

The previous sections describes the determination of D meson candidates which still contain a large fraction of combinatorial background. This section describes the extraction of the signal, i.e. the fraction of signal events from the entirety of

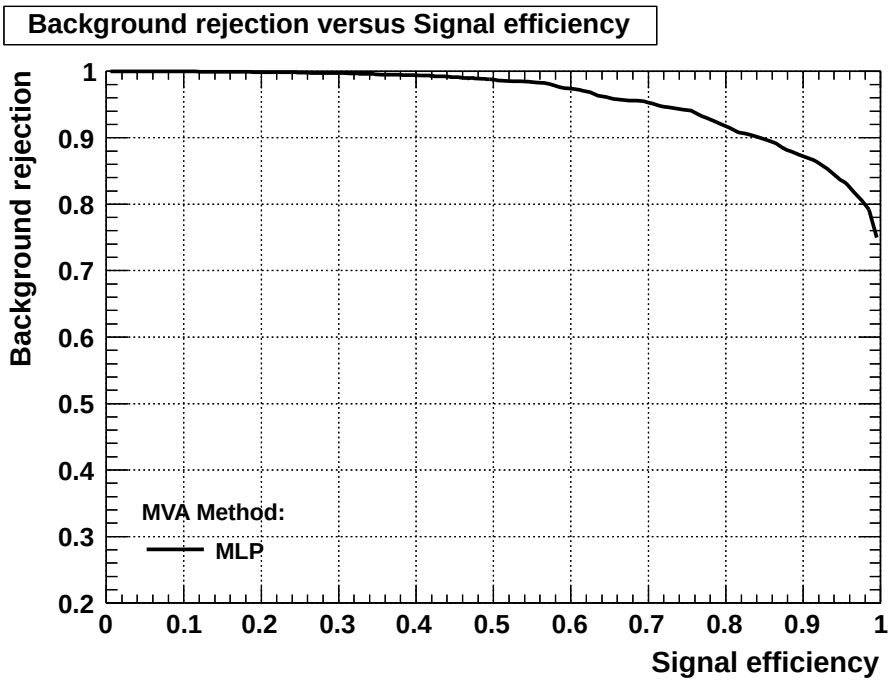

Figure 6.13: Background rejection versus signal efficiency of the MLP.

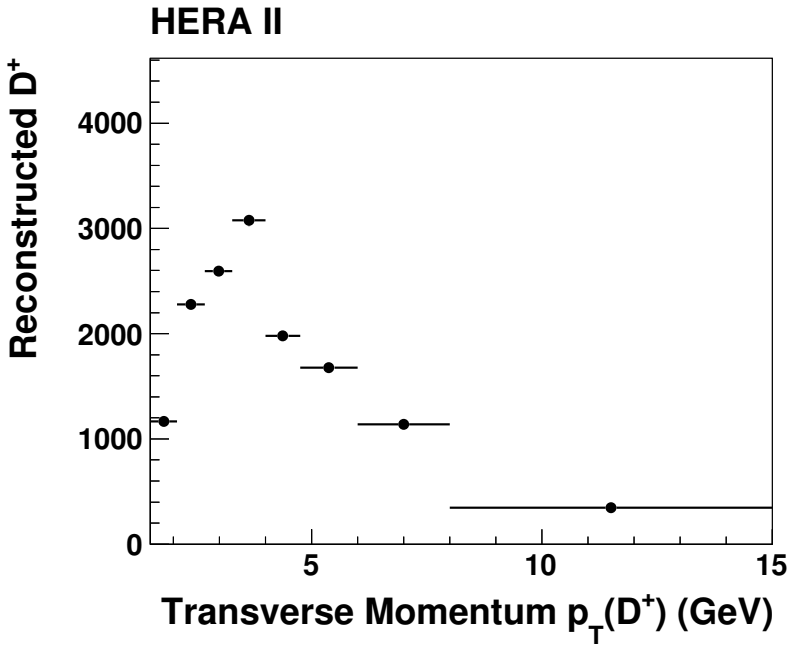

Figure 6.14: The number of reconstructed $D^{\pm}$ as function of the transverse momentum p_{T}. The result is derived from data events of the HERA II period.

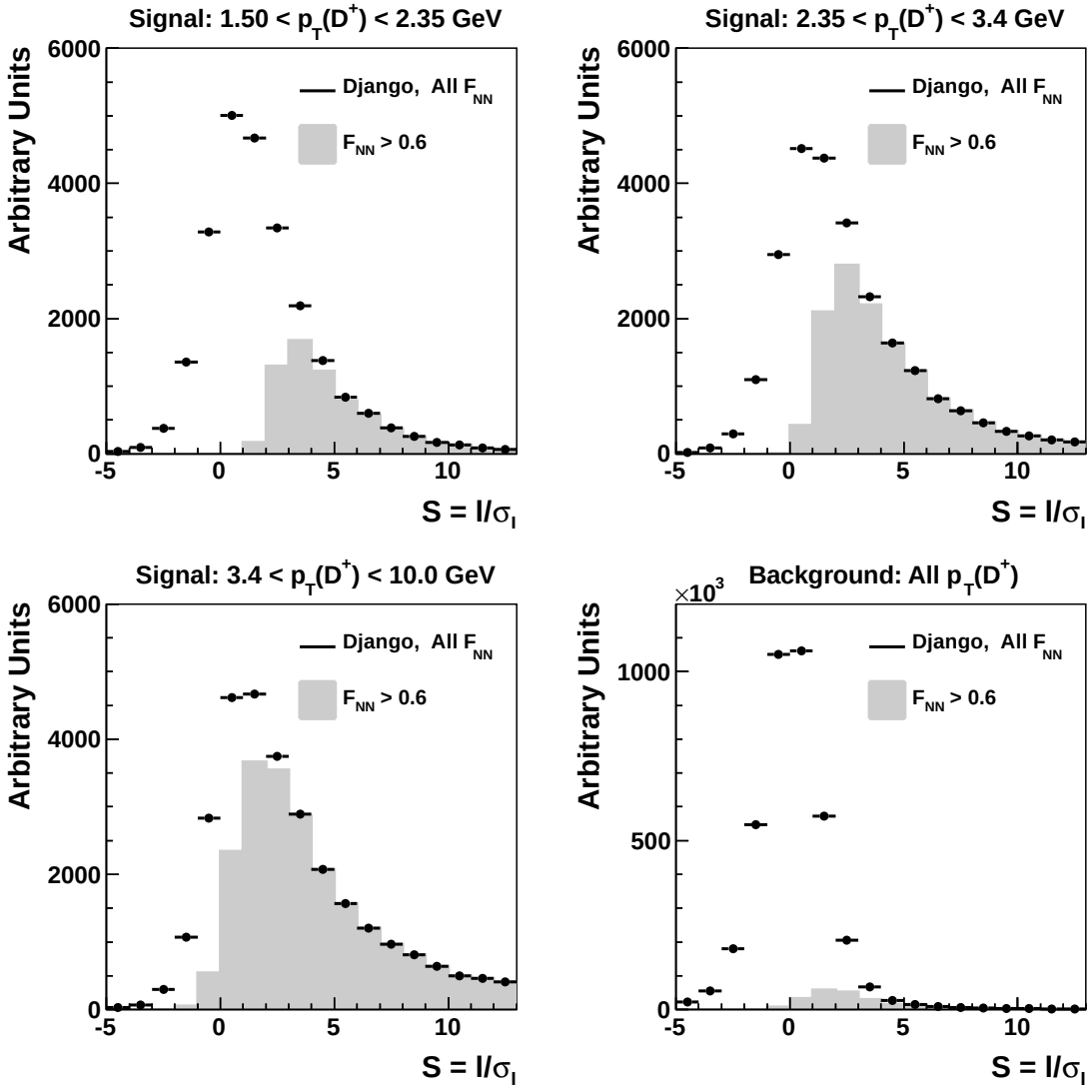

Figure 6.15: Significance distribution as function of S_l before and after the cut on the MLP output $F_{NN} > 0.6$.

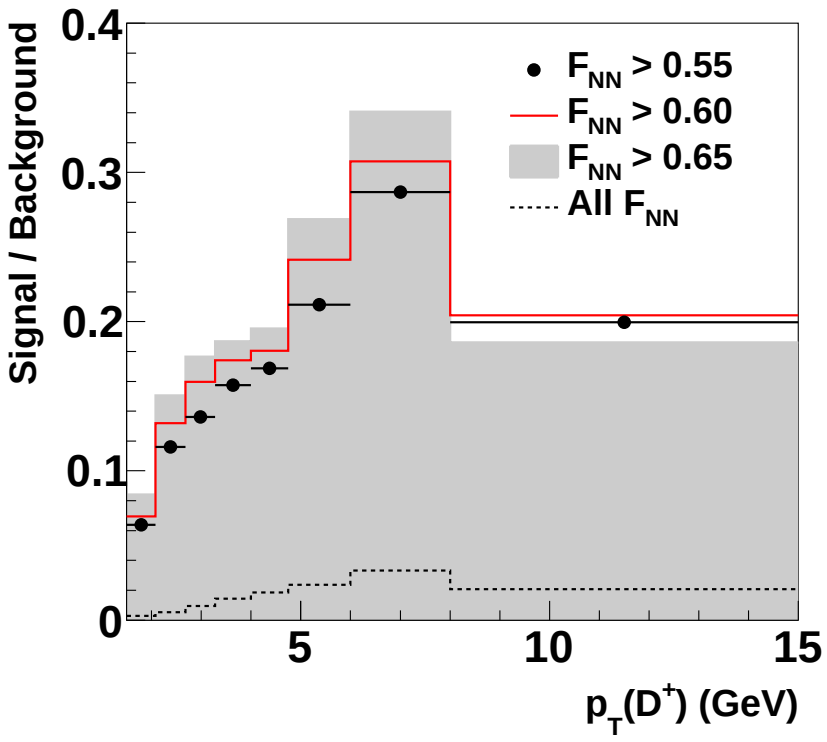

Figure 6.16: Signal to background ratio of events in a 3 sigma mass window.

candidates. The background events are subtracted on a statistical basis. In the course of this analysis three different methods are applied. The $D^{\pm}$ mass distribution fit is used to extract the signal for $D^{\pm}$ mesons. The method is based on the reconstructed mass spectrum of the $D^{\pm}$ sample. Signal events cluster around the nominal mass of the $D^{\pm}$. The distribution is then fit to a function which contains a signal and background part. From the proportion of the contributions the signal fraction is deduced.

The second method is applied to derive the D^{*} signal. The method also makes use of the reconstructed mass spectrum. In contrast to the $D^{\pm}$ method the reconstructed mass of the $D^{\pm}$ is not used directly. The mass difference of the the D^{*} and the D^{0} candidate is evaluated. Again the mass difference clusters at the nominal value. The distribution is then fit to a corresponding model of signal and background. This method is used for systematic studies. The third method is used to generate control distributions of the D^{*} sample. The method exploits the wrong charge D^{*} sample. To plot a control distribution the wrong charge distribution is subtracted from the corresponding right charge distribution. This results in the signal distribution of the control variable.

D$^{\pm}$ Mass Distribution Fit The $D^{\pm}$ signal is extracted by a fit procedure to the reconstructed mass spectrum. The mass distribution is modeled by the sum of a signal part and a background part. The signal is described by a Gaussian distribution $G(m)$. The width of the Gaussian distribution corresponds to the detector resolution, which is determined from MC for each bin and subsequently fixed to the corresponding value. It is of the order of 20 MeV. The background is represented by orthogonal second order Chebyshev polynomials of the first kind $C(m, \vec{p_{bg}})$. The slope and the curvature $\vec{p}_{bg}$ are treated as free parameters. The mass distribution is then parametrized by $l(m) = f \cdot G(m) + (1-f) \cdot C(m|\vec{p_{bg}})$, where f denotes

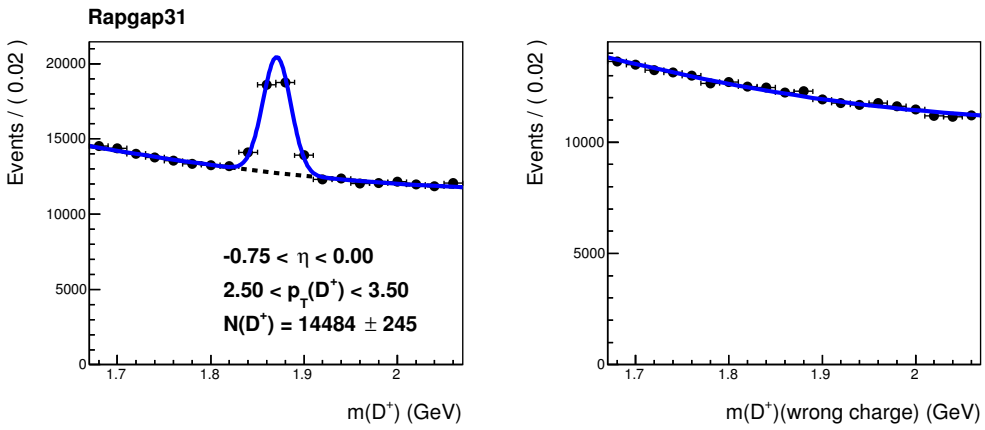

Figure 6.17: Exemplary $D^{\pm}$mass distribution and fit result with a pronounced signal for the right charge (left) and wrong charge sample (right).

the fraction of signal and background.

The `RooFit` [73] software package is used to perform an unbinned maximum likelihood fit. The unbinned likelihood fit maximizes the use of available information to obtain the shape of a distribution and avoids a systematic bias due to a certain binning. `RooFit` automatically normalizes the distributions in the considered intervals. In the procedure simultaneously the background distribution $l_{bg} = C(m, \vec{p_{bg}})$ is fit to the wrong charge background (cf. 6.4). Taking into account the wrong charge distribution in the fit procedure stabilizes the fit result and reduces the statistical uncertainty. The fitter maximizes the composite likelihood for all right and wrong charge particle candidates $N_{rc} + N_{wc}$ $L = \prod_{i=1}^{N_{rc}} l(m_i|f, \vec{p_{bg}}) \cdot \prod_{i=1}^{N_{wc}} l_{bg}(m|\vec{p_{bg}})$ with respect to the parameters f and $\vec{p}_{bg}$. After the fit procedure the signal s is obtained as the signal fraction f multiplied by the number of right charge candidates $s = f \cdot N_{rc}$.

D* Mass Distribution Fit Detailed information on the fit procedure and corresponding systematic studies can be found in [49, 20]. The key features are summarized in the following paragraph. For the D^* signal extraction not the re-

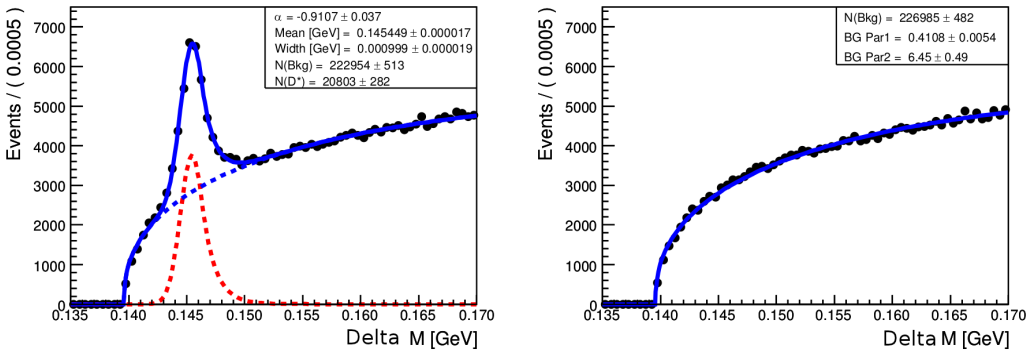

Figure 6.18: Δm distribution and fit result for signal events and the non resonant wrong charge background. From [49]

constructed mass directly is considered, but the difference of the D^*mass and the mass of the decay particle D^0: $\Delta m = m(D^*) - m(D^0)$. Here, too the Δm distribution is fit by the sum of a signal and a background function. The signal is then deduced from the ratio of the signal and background part.

For the background the Granet parametrization is applied [39]. The shape of the signal is asymmetric. Therefore the asymmetric Crystal Ball parametrization [36] is applied. `RooFit` is used to perform an unbinned likelihood fit of the parameters to the right charge and non resonant wrong charge Δm distribution simultaneously. The result of the fit is illustrated in figure 6.18.

D* Wrong Charge Subtraction Method The statistical subtraction method is applied for the determination of control distributions. The method follows the idea of subtracting a wrong charge background distribution from a signal distribution such that the distribution of the D^* meson signal candidates remains. A cut on the mass difference Δm of ± 0.002 GeV is applied in order to reduce as much background as possible. The procedure is illustrated for the energy of the scattered electron in figure 6.19. For further details see [49]. The subtraction method is less accurate than the fit method. On the other hand distributions of higher granularity

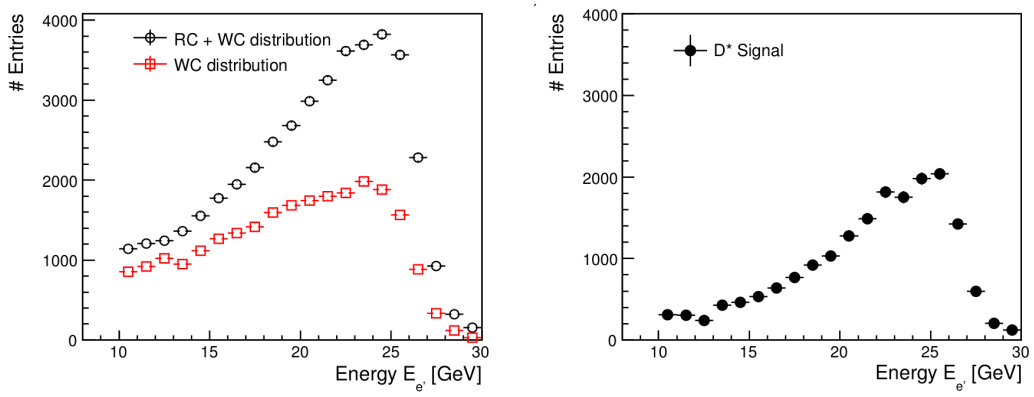

Figure 6.19: $E_{e'}$ distribution of all D^* candidates, the wrong charge background events (left). After the subtraction (right) only signal events remain.

Transverse momentum of the initial tracks	$p_{\mathrm{T}}(Track) > 0.3\,\mathrm{GeV}$
Track length	$l(\mathrm{Track}) > 10\,\mathrm{cm}$
Probability of the $\chi^2$of the vertex fit	$P_{Vtx} > 0.4\%$
Evaluation of the neural network	$F_{NN} > 0.6$

Table 6.1: Selection criteria for $D^{\pm}$ candidates.

can be extracted, which would otherwise not be possible due to too few signal events per bin.

6.7 Summary of the Particle Selection Criteria

Table 6.1 summarizes the selection criteria of the $D^{\pm}$ candidates. The minimal value on the transverse momentum of a single track is owed to the detector acceptance. Also tracks of length below 10 cm are rejected, because of large track parameter uncertainties. The cut on the probability of the vertex fit is motivated by the strong accumulation of background events at very small values. The peak structure would result in a strong accentuation on the background events.

Chapter 7

Cross Section Determination

To derive the production cross section from the number of reconstructed particles several effects have to be taken into account. There are detector effects, such as a limited geometrical acceptance, reconstruction deficiencies due to particle-detector interactions or the trigger efficiency. The effects and their treatment are discussed in the following sections. Furthermore the measurement is corrected for NLO QED contributions to derive the Born cross section.

The total visible $D^{\pm}$ meson production cross section is defined as:

$$\sigma_{tot}^{vis}(ep \to eD^{\pm}X) = \frac{N(D^{\pm})}{L \cdot B(D^{\pm} \to K^{\mp}\pi^{\pm}\pi^{\pm}) \cdot \varepsilon \cdot A^{det} \cdot (1+\delta_{rad})} , \qquad (7.1)$$

where $N(D^{\pm})$ is the number of reconstructed D mesons in the visible range (cf. chapter 6), L is the luminosity (cf. 5.1), $B(D^{\pm} \to K^{\mp}\pi^{\pm}\pi^{\pm})$ is the branching ratio [61], ε corresponds to the total reconstruction efficiency, including detector efficiency ε^{rec} and trigger efficiency ε^{trig} (cf. 7.1), A^{det} is the detector acceptance (cf. 7.1) and $(1+\delta_{rad})$ is the correction for radiative effects as explained in section 7.3. The above mentioned formula for the cross section defines the total cross

section in the visible range. In addition single and double differential cross sections are derived as functions of the particle properties $p_{\mathrm{T}}(D^{\pm})$ and $\eta(D^{\pm})$ as well as the kinematic variables Q^2 and y.

7.1 Correction of Detector Effects

The measurement suffers from limited detector acceptance, reconstruction deficiencies and resolution effects. Migrations caused by resolution effects result in the reconstruction of events in neighboring bins. For the cross section determination these effects have to be corrected. Mathematically this behavior is described by the detector "response matrix" R:

$$y_i = \sum_j R_{ij} x_j$$

where y_i denotes the reconstructed result in bin i and x_j the true result in bin j. The true results can be deduced from the measured ones by the application of unfolding. In case of the full matrix unfolding first the matrix R is determined from simulated data and inverted afterwards. However the problem is ill posed: A whole class of possible solutions for the matrix inversion exists which would result in different results of the true distribution. In order to derive a meaningful inverse matrix the statistically relevant part has to be determined. For this several regularization methods exist [18, 32]. This analysis applies a simplified method for the determination of the true result, the so called bin-by-bin method. In the bin-by-bin method the matrix R is replaced by an "effective" correction factor a^{bbb} for each bin. The correction factor for bin i is connected to the matrix by:

$$a_i^{bbb} = \frac{N_i^{rec}}{N_i^{gen}} + \frac{N_i^{smear}(\mathrm{in}) - N_i^{smear}(\mathrm{out})}{N_i^{gen}},$$

where the contributions of the off-diagonal matrix elements, i.e. $\sum_{j|j\neq i} R_{ij}x_j$ are compiled in N_i^{smear}. $N_i^{smear}(\text{in})$ denotes the number of events which have migrated into bin i, corresponding to positive values of $R_{ij|i\neq j}$. In contrast to $N_i^{smear}(\text{out})$, which denotes the number of events which migrate from bin i into other bins and correspond to negative values of $R_{ij|i\neq j}$. The measured value y_i is then given by:

$$y_i = a_i^{bbb} x_i$$

The bin-by-bin method requires a significant part of the result originating from the same bin in which it has been reconstructed. In this analysis the migration effects are small because of relatively wide bins, which need to be chosen wide enough to derive a signal from the fit to the mass distribution. Figures 7.3 and 7.4 depict purity and stability of the reconstructed mesons. Purity and stability are characteristics of the migration and discussed in the next paragraphs. The high purities indicate low migrations. The result which is extracted by the bin-by-bin method is the same as the one derived from a full matrix unfolding. On the other hand the propagation of the uncertainties is not fully correct. For this analysis the effect is small and neglected. The migrations are discussed quantitatively in the next paragraphs.

Detector Acceptance and Reconstruction Efficiency In this paragraph the two components of the corrections factor a_i^{bbb} are discussed. a_i^{bbb} can be seen as the product of the detector acceptance A^{det} and the efficiency ε. The quantities and the corresponding ranges which define the detector acceptance and hence the visible range are summarized in table 7.1.

The angular constraints of the central tracks and the scattered electron are introduced due to geometrical limitations. The limit on the transverse momentum

$p_T(\text{track})$	0.3 GeV
$\theta(\text{track})$	$20^\circ < \theta < 160^\circ$
Energy of the scattered electron	$E_{e'} > 11\,\text{GeV}$
Polar angle of the scattered electron	$153^\circ < \theta_{e'} < 177^\circ$

Table 7.1: Detector acceptance cuts.

is required for a reliable track reconstruction. Furthermore a reliable energy measurement in the SpaCal requires a sufficiently high energy of the scattered electron. The acceptance describes the fraction of particle candidates in the visible range:

$$A_i^{det} = \frac{N_i^{gen} \,\&\&\, N_i^{acc}}{N_i^{gen}} \tag{7.2}$$

$N_i^{gen} \,\&\&\, N_i^{acc}$ is the number of particles which are generated in bin i and fulfill the acceptance criteria on generator level in bin i.

The efficiency refers to the particles in the visible range and is defined by:

$$\varepsilon_i = \frac{N_i^{rec}}{N_i^{gen} \,\&\&\, N_i^{acc}}\,, \tag{7.3}$$

where N_i^{rec} is the number of reconstructed particles. On reconstruction level the acceptance cuts have been performed on the reconstructed quantities. N_i^{rec} contains both the particles which have been generated in bin i and the ones which migrated into it. Migration effects are discussed in the next paragraph.

The single differential result for acceptance and efficiency is shown in figure 7.1, whereas figure 7.2 shows the double differential results. Most notably is the drop of both efficiency and acceptance for low transverse momenta.

Migration Effects The migration effects are quantified by purity and stability. The purity is the fraction of particles which have been reconstructed and generated in the same bin i and the number of particles which have been reconstructed in bin

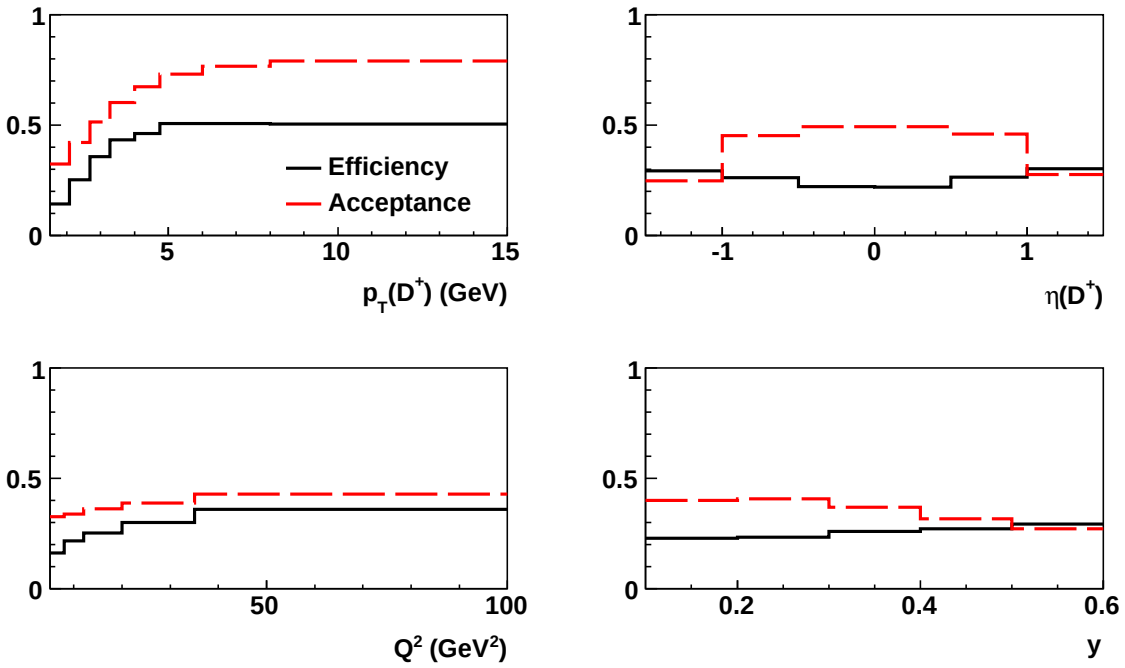

Figure 7.1: Single differential detector acceptance and reconstruction efficiency.

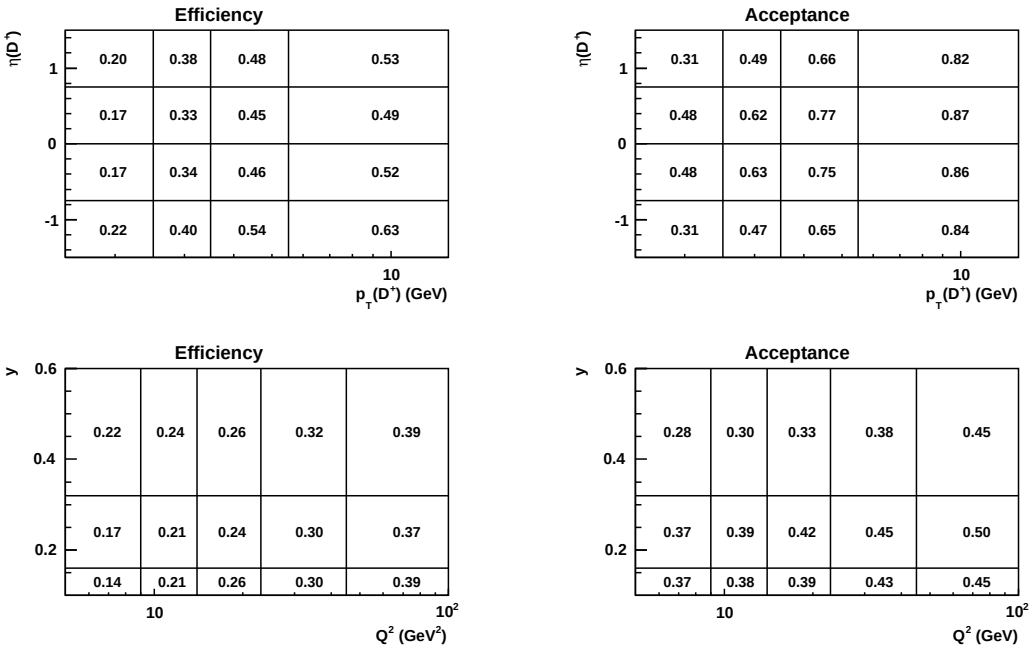

Figure 7.2: Double differential detector acceptance and reconstruction efficiency.

i. The purity is a measure for migration of events into the bin, since the purity gets low the more events from neighboring bins impurify the number of reconstructed events.

$$p = \frac{N_i^{gen} \&\& N_i^{rec}}{N_i^{rec}} \tag{7.4}$$

The stability describes the fraction of the number of particles which have been generated and reconstructed in a certain bin and the number of particles which have been generated in the corresponding bin and are in the visible range. The stability is a measure for the emigration from a certain generator level bin.

$$s = \frac{N_i^{gen} \&\& N_i^{rec}}{N_i^{gen} \&\& N_i^{acc}} \tag{7.5}$$

Figures 7.3 and 7.4 show the purity and stability single and double differentially. The purities are close to one, whereas the stabilities are small due to the reconstruction inefficiencies, i.e. many events which are generate are not reconstructed at all. The comparison between the efficiencies and stabilities show that the migration effects are small.

7.2 Trigger Efficiency

Besides the reconstruction efficiency the trigger efficiency contributes to the total reconstruction efficiency $\varepsilon = \varepsilon^{rec} \cdot \varepsilon^{trig}$. The trigger efficiency is determined from data. The $D^{\pm}$ events selected by the subtrigger used for this analysis (s61, cf. 5.2) are logically combined (logic AND link) with an independent reference subtrigger.

$$\varepsilon^{trig} = \frac{N^{s61}(D^{\pm}) \&\& N^{ref}(D^{\pm})}{N^{ref}(D^{\pm})} \tag{7.6}$$

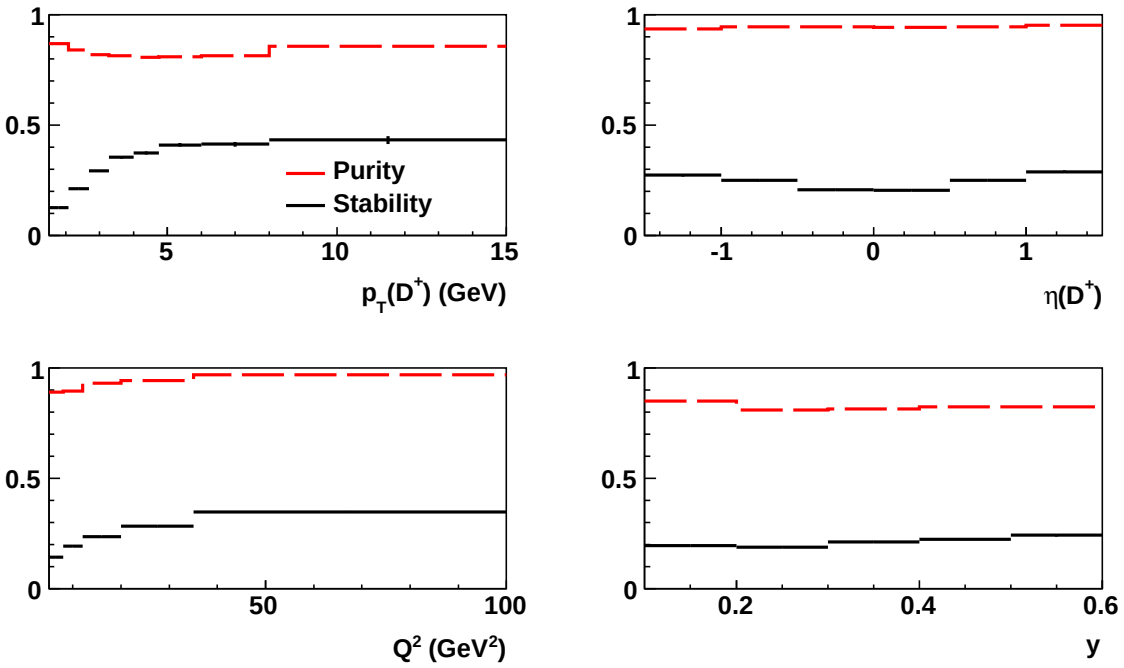

Figure 7.3: Single differential purity and stability.

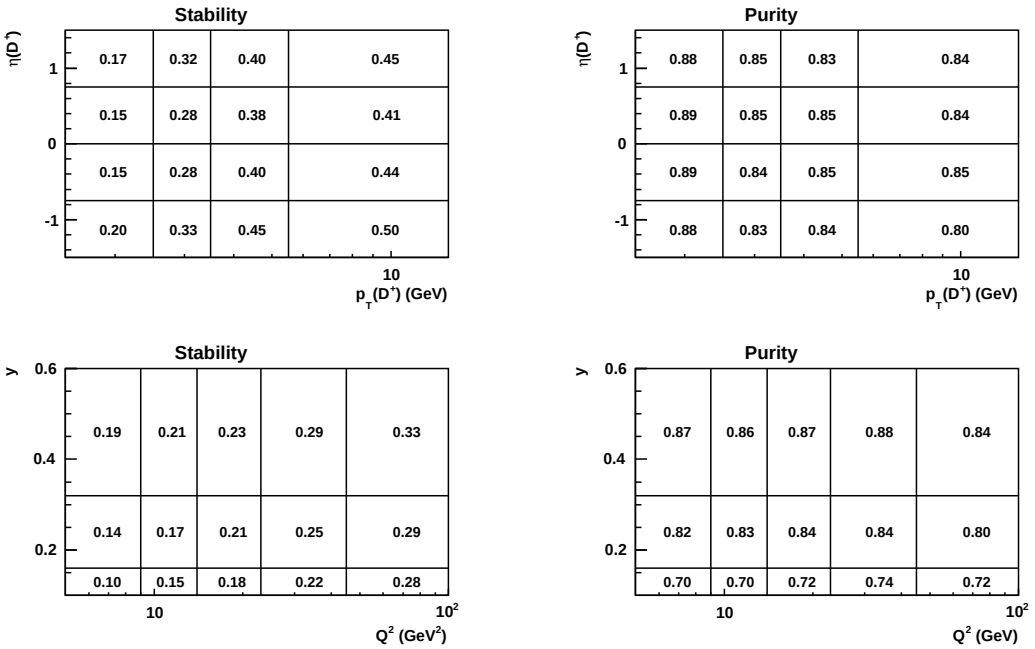

Figure 7.4: Double differential purity and stability.

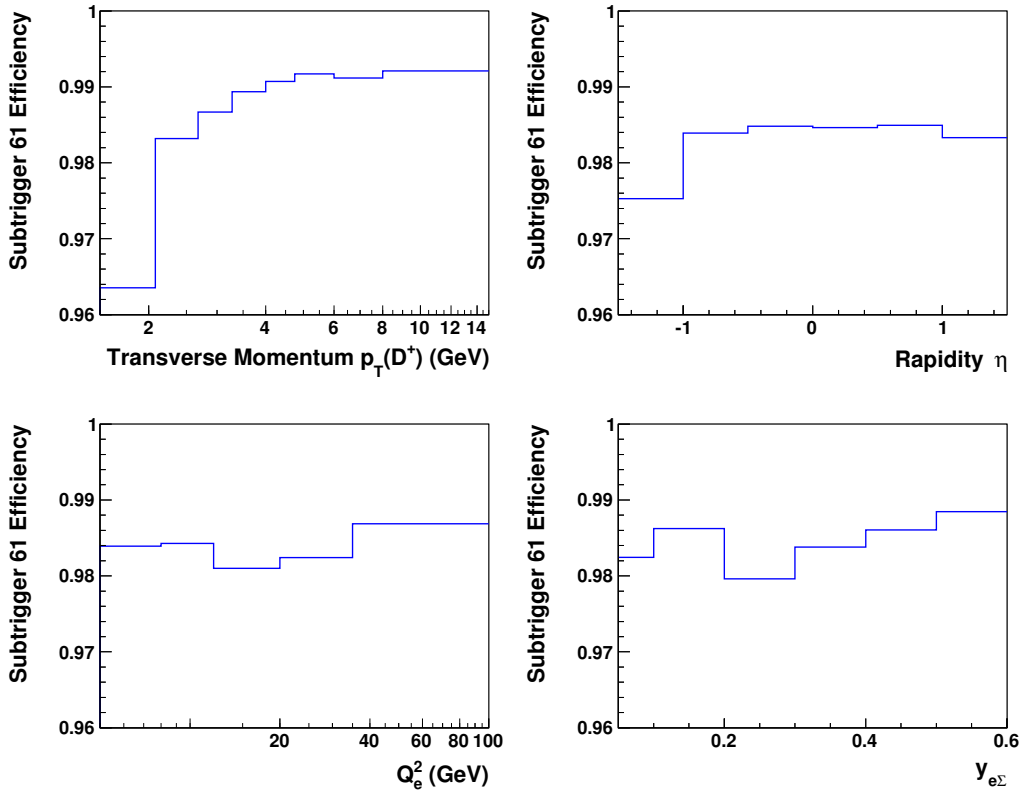

Figure 7.5: Single differential subtrigger 61 efficiency.

The independent reference triggers s0, s3 and s9 are solely based on calorimeter information and therefore independent of the track based subtrigger s61.

The $D^{\pm}$ selection requires a particle candidate which fulfills the quality criteria as defined in 6.7. The trigger efficiencies are shown in figures 7.5 and 7.6. They are derived from the full data sample and show values of the order of 98 to 99%. Only the lowest p_{T} range shows efficiencies as low as 97%. For the cross section measurement they are applied as bin wise corrections to the data. For more information on the reference triggers and trigger studies see [49, 60].

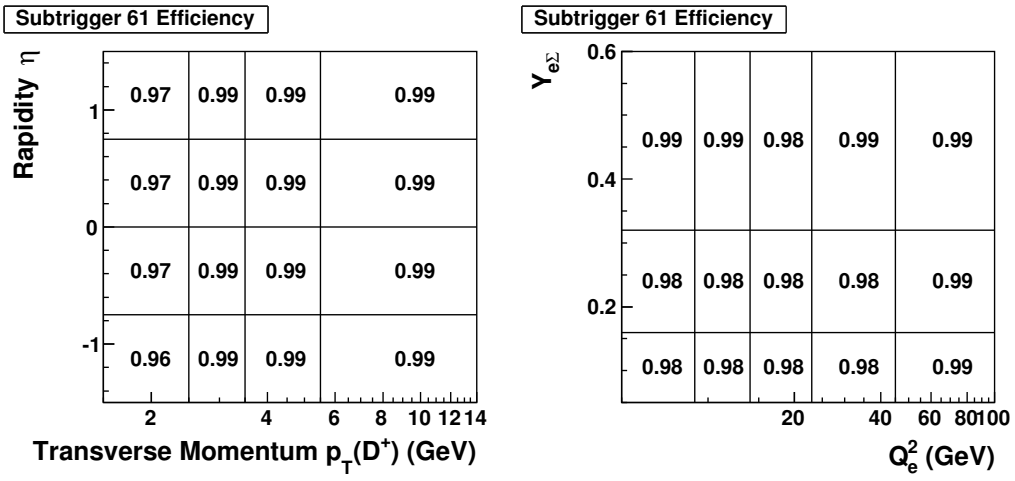

Figure 7.6: Double differential subtrigger 61 efficiency.

7.3 NLO QED Contributions

In order to convert the measured $D^{\pm}$ cross section to the Born level, i.e. the one photon exchange cross section (cf. 2.1) a correction factor is applied. The NLO contribution corrections are mainly a question of initial state radiation from the lepton. The virtual NLO QED corrections are included in the running of the electromagnetic coupling constant. The final state radiation almost always is merged with the electron cluster and subsequently taken into account by the energy measurement of the SpaCal. The correlation between the measured cross section and the Born level cross section is expressed by means of the fractional difference δ_{rad}:

$$\sigma_{Born+NLO} = (1 + \delta_{rad}) \cdot \sigma_{Born} \tag{7.7}$$

To determine the correction factor the cross sections σ_{Born} and $\sigma_{Born+NLO}$ are derived from radiative and non radiative MC simulations. The radiative MC sample is interfaces with HERACLES as described in section 3.1. From the two samples the cross sections $\sigma_{rad} = \sigma_{Born+NLO}$ and $\sigma_{non-rad} = \sigma_{Born}$ in the visible range

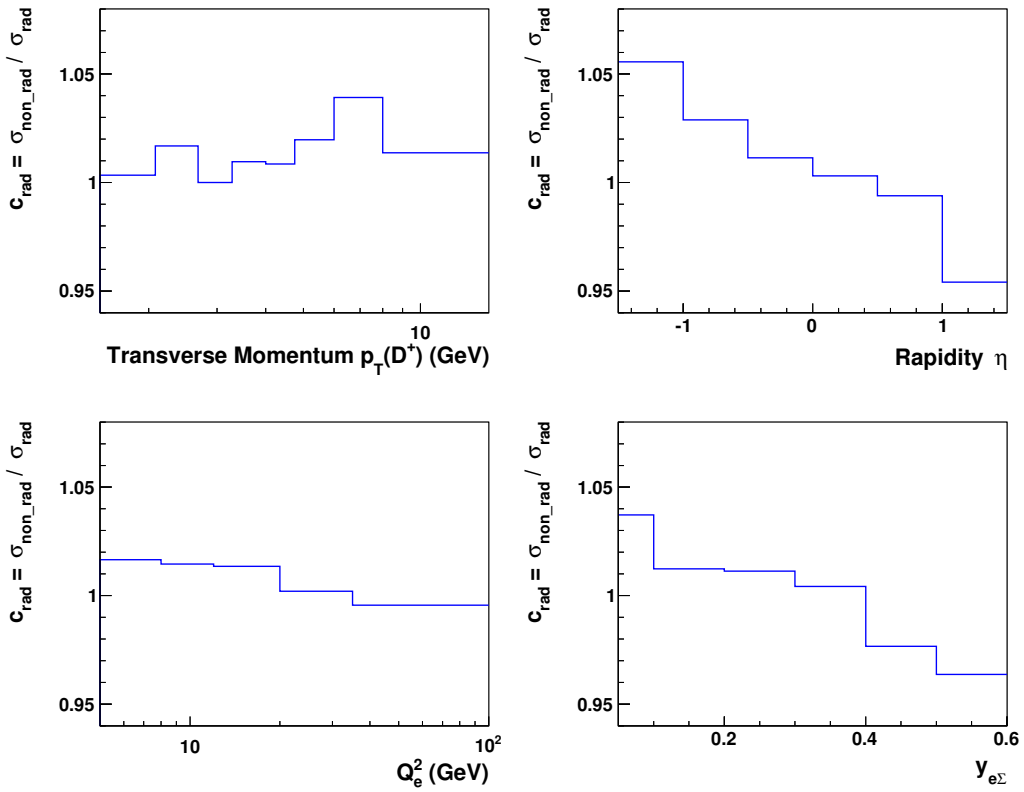

Figure 7.7: Single differential NLO QED contributions as function of the measured variables.

are derived. The correction factor applied for the cross section determination then reads: $(1+\delta_{rad})^{-1} = \sigma_{non-rad}/\sigma_{rad}$. The results are displayed in figures 7.7 and 7.8.

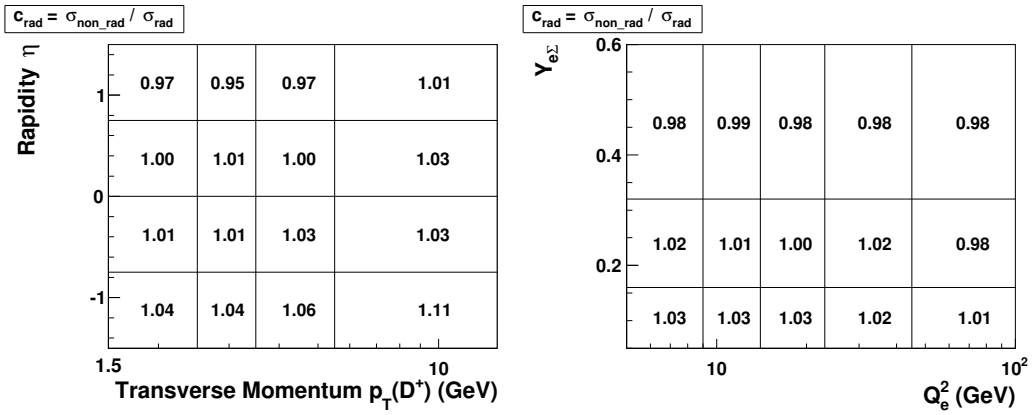

Figure 7.8: Double differential NLO QED contributions as function of the measurement variables.

Chapter 8

Systematic Uncertainties

In this chapter the systematic uncertainties of the cross section measurement are discussed. The different components of the cross section (cf. 7.1) contain different sources of systematic uncertainties. In the first part of this chapter the uncertainty of the particle reconstruction efficiency ε^{rec} is discussed. ε^{rec} itself is a composite quantity. It depends on the behavior of the neural network particle selection which in turn depends on the input classifier. The strategy of the derivation of the uncertainty of the reconstruction efficiency is to derive the uncertainties of the classifier and subsequently convolute them through the neural network. Furthermore an uncertainty of the used model of the simulated data is derived to take into account an uncertainty of the detector acceptance (8.2). In section 8.3 studies on the reconstruction of the event kinematics regarding the uncertainty of the energy scale of the SpaCal and the angle of the scattered electron are performed. In the last section of this chapter other contributions to the uncertainty, i.e. the trigger, luminosity measurement, branching ratio, the mass distribution fit and radiative corrections are discussed. The different contributions to the systematic uncertainties amount of up to 3% with the exception of the uncertainty of the particle reconstruction efficiency influenced by the decay length error. In this case the ef-

ficiency uncertainty goes up to 9%. In the course of this chapter it is shown that the different contributions to the total uncertainty are not correlated and can be summed up in quadrature.

8.1 Particle Reconstruction

Particles which undergo the full reconstruction chain as discussed in chapter 6 only have a certain probability of passing all reconstruction steps and selection criteria and being counted in the final mass distribution. Therefore the reconstruction efficiency ε^{rec} was introduced and corrects for this effect to obtain the cross section. The differential reconstruction efficiencies are shown in section 7.1. They are below 50% throughout the whole phase space and reach their maximum at high transverse momenta. Typical values are of the order of $20-30\%$.

The correction factor is derived from simulated data, therefore the systematic uncertainty on the reconstruction efficiency $\delta(\varepsilon^{rec})$, i.e. the uncertainty on the number of reconstructed particles for simulated data arises solely from the imperfection of the detector simulation. $\delta(\varepsilon^{rec})$ is the biggest contribution to the systematic uncertainty and reaches $\approx 9\%$ for low p_{T}. Its determination is difficult because it itself consists of several contributions, which are not necessarily independent. The reconstruction deficiencies originate mainly from the misclassification of the signal candidates. There is a small contribution from the track reconstruction deficiency, which is neglected in the analysis.

The reconstruction procedure runs through various steps from the very basic detector signals to the reconstructed tracks and finally to the reconstruction of the composite particle candidates with its neural network response. The network response in turn depends on the correct reconstruction of its input parameters and these in turn depend on the correct reconstruction of the underlying tracks. Ergo,

the most fundamental source of the reconstruction efficiency uncertainty is on the detector hit level, e.g. uncertainties on the hit efficiency of the tracking detector. Another source of uncertainties is the imperfect description of the material distribution and composition of the detector in the simulation. Material distribution and composition influence multiple scattering (cf. 6.1) and nuclear interactions. Nuclear interactions may result in secondary interactions and the break up of particle trajectories, which in turn can end up in different track reconstruction efficiencies. Differences in the behavior of multiple scattering result in different resolutions of the track parameter and influence the track reconstruction efficiency. Differences in the track reconstruction efficiencies may lead to a different number of reconstructed particles. The analysis of the quality of the track reconstruction (cf. 8.1.1) demonstrates the very precise description of the track reconstruction efficiency and the track properties in general. The track reconstruction efficiency is not considered as source of uncertainty. Differences in the track properties and resolutions may lead to different neural network responses an subsequently to a different number of reconstructed particles. Figures 8.2 and 8.3 show the track properties of kaons and pions from the reconstruction of D^* decays. The D^* sample is used because of its lower statistical background. The track parameters are described by the simulated data within the statistical uncertainty, which in turn does not allow a direct deduction of the uncertainty on the track parameters. There would not be a prescription of how to exactly convolute the uncertainties on track parameters to the uncertainties on the classifier anyways. In the remainder of this section an uncertainty on ε^{rec} is derived from the convolution of the uncertainties of the classifier through the neural network. In principle the difference of the full distributions of the classifier would have to be considered and convoluted, which is not determinable because of insufficient statistics. The first moment, i.e. the mean value, which is the best approximation to the distribution are studied and

compared for data and simulated data. The difference of these values is taken as approximation to the uncertainty of the classifier. Furthermore the uncertainties of the classifiers are derived globally and not in dependence of the measured variables, e.g. p_{T}, which is an additional approximation. Afterwards the uncertainties are propagated through the neural network. This procedure is described in more detail in section 8.1.4. The procedure also describes why it is possible to separately derive $\delta_i(\varepsilon^{rec})$ for each classifier and retrieve the total uncertainty by adding them up in quadrature. Since S_l and σ_l are naturally correlated the decay length l is considered for the derivation of the uncertainty instead of S_l. Also P_{Vtx} and P_{dEdx} are substituted by their corresponding χ^2 values which have a one-to-one correspondence. This is done because the probability distributions are flat and inappropriate to derive an uncertainty from the difference between the data and simulated data distributions. This means in the course of the derivation of the uncertainty on the reconstruction efficiency the efficiency is treated as a function of the substituted neural network classifier: l, σ_l, χ^2_{Vtx}, χ^2_{dEdx}.

8.1.1 Track Reconstruction Quality

For pions and kaons the track reconstruction efficiency for the p_{T} range of this analysis is described within the limit of the statistical uncertainty. This has been studied in [22]. Figure 8.1 shows the reconstruction efficiency for pions based on an analysis of D^0_S decays. The track reconstruction efficiency as source of a systematic uncertainty is neglected.

Figures 8.2 and 8.3 show the distributions of the track properties for D^*-tagged pions and kaons for data and simulated data. The distributions were reconstructed by means of the D^* wrong charge subtraction method as explained in section 6.6. The data distribution of the number of hits in the CJC is narrower in the peak region of around 50 hits. Also the peak position is shifted towards higher values,

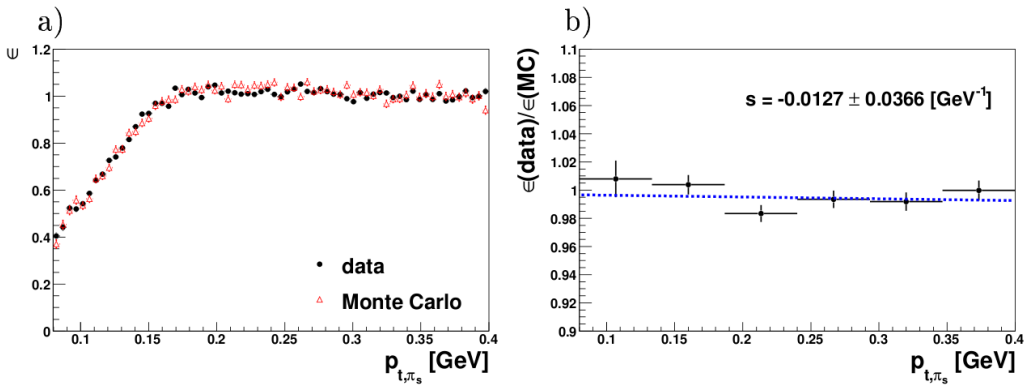

Figure 8.1: a) Pion track reconstruction efficiency as function of transverse momentum for data and MC. b) Ratio of the efficiencies. From [22]

i.e. tracks in data produce more hits in the central jet chamber. The difference in the number of hits can be explained by a narrower pulse height spectrum of the simulated data [66]. More important for the vertex resolution is the CST hit efficiency. The CST hit distributions is well described, still the number of CST hits of the kaons is slightly higher for data compared to the simulated data. The third figure shows the track length of the particles. As expected from the bias in the number of CJC hits the data tracks are slightly longer. The number of hits and the track length influences the pattern recognition, the track fit and subsequently the track parameters and its resolutions. Especially the uncertainty on the track parameter resolutions convolute to the calculated decay length error. The overall description of the simulated data is good, especially the d'_{ca} is well described, which plays a crucial role for the vertex fit and the decay length resolution. For κ the data distribution is steeper than the MC distribution. The ϕ distributions are compatible within the limits of the statistical accuracy.

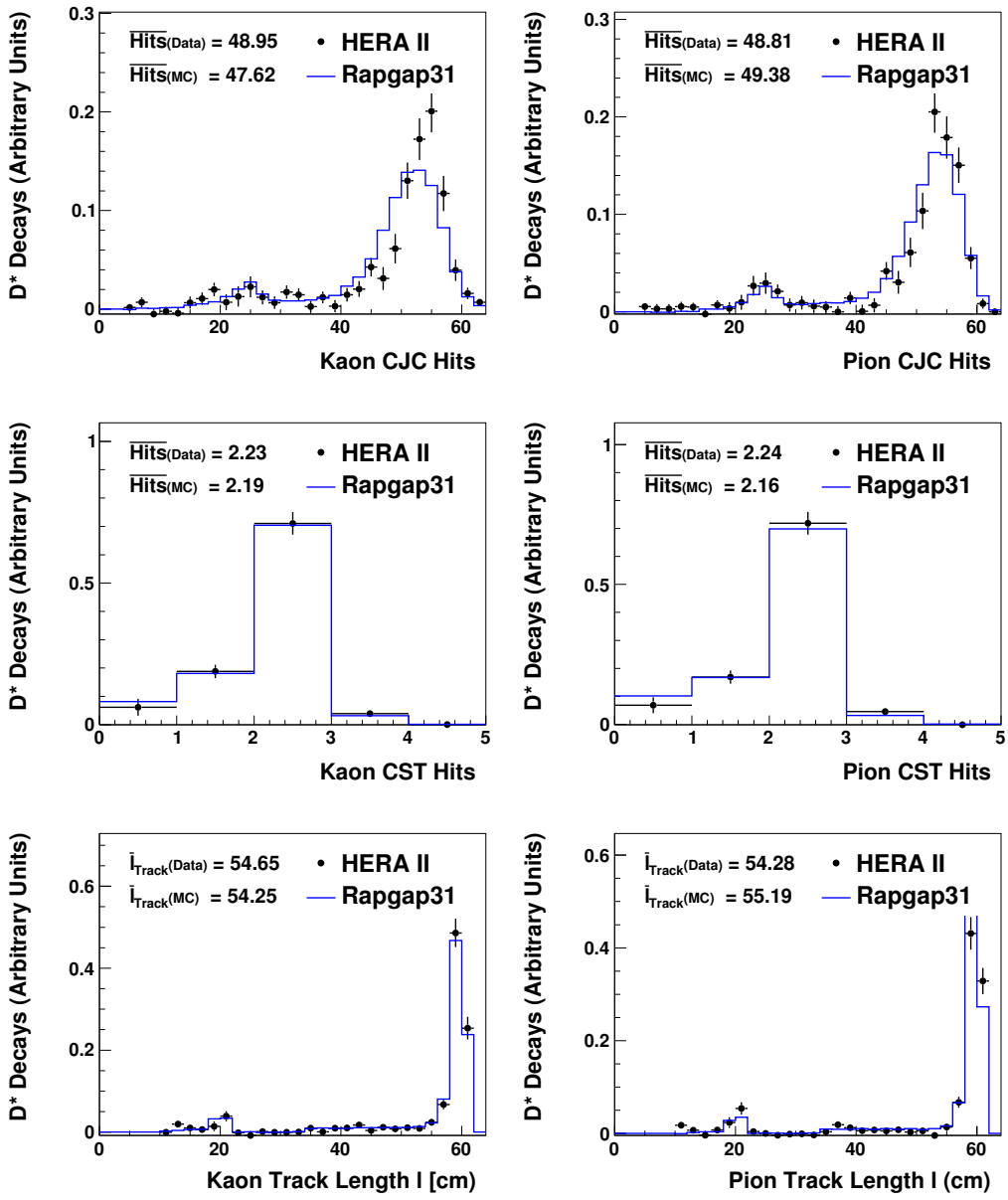

Figure 8.2: Number of track detector hits and track length of D^*-tagged kaon and pion tracks.

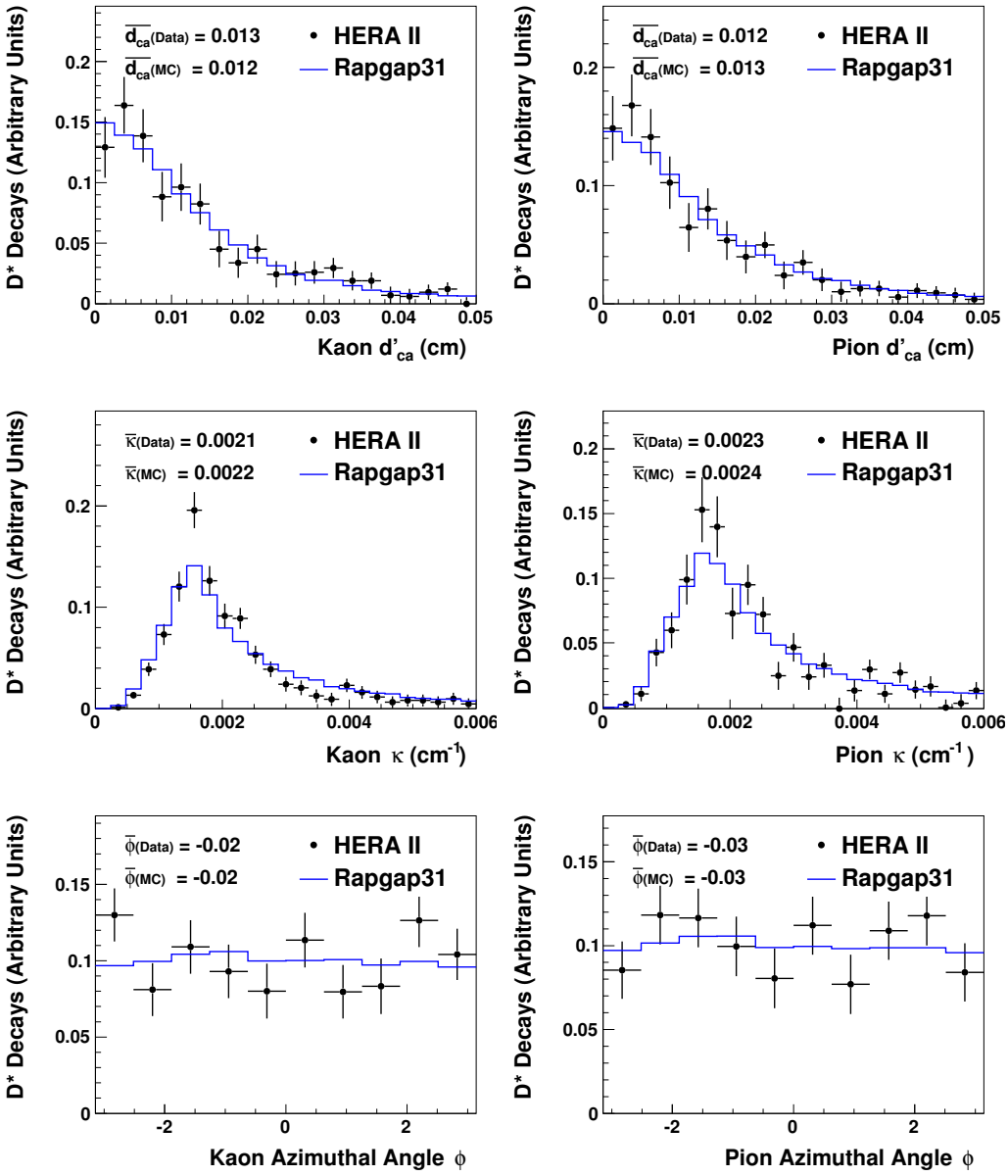

Figure 8.3: $r\phi$-track properties of D^*-tagged kaon and pion tracks.

8.1.2 Classifier Correlations

In the course of this section the correlations of the classifiers are studied and it is shown that it is a valid approximation to treat the classifier as independent variables which allows the quadratic summation of the different contributions to the total uncertainty. As previously mentioned the classifier of the neural network S_l, σ_l, P_{Vtx}, P_{dEdx} are replaced for the derivation of the uncertainties. The more suitable classifier l, σ_l, χ^2_{Vtx}, χ^2_{dEdx} which have a one-to-one relation to the original classifiers are used to avoid the apparent correlation of S_l and σ_l and the flat distributions of P_{Vtx} and P_{dEdx}. It is assumed that parameters derived from the vertex fit and the χ^2_{dEdx} probability of the specific energy loss are not correlated. In order to demonstrate the correlation properties of the vertex fit related properties first the mutually combined variables are plotted against each other. Figure 8.4 shows the distributions of reconstructed $D^{\pm}$ signal events from the simulated data sample and their corresponding correlation coefficients. The vertex fit likelihood P_{Vtx} does not show a correlation to neither one of the other variables. The decay length and the decay length uncertainty show a small positive correlation which corresponds to a correlation factor of $\rho(l,\sigma_l) = 0.25$. Correlations significantly smaller than 0.5 are treated as non-correlated.

The vertex fit related variables are not strongly correlated. On the other hand systematic uncertainties can arise from imperfect simulation and description of the hit efficiency, intrinsic detector resolution or the material distribution. These effects can induce correlated shifts of l, σ_l, and P_{Vtx}. In order to study the behavior of the vertex fit variables under the change of the track parameters, κ and d'_{ca} have been shifted for each track preceding the full reconstruction chain. Figures 8.5 and 8.6 show the distributions of the differences of the vertex fit variables for shifts of $\Delta d_{\mathrm{ca}} = 2\,\mu\mathrm{m}$ and $\Delta\kappa = 0.0002\,\mathrm{m}^{-1}$.

The values for Δd_{ca} and $\Delta\kappa$ are derived from the uncertainties on theses val-

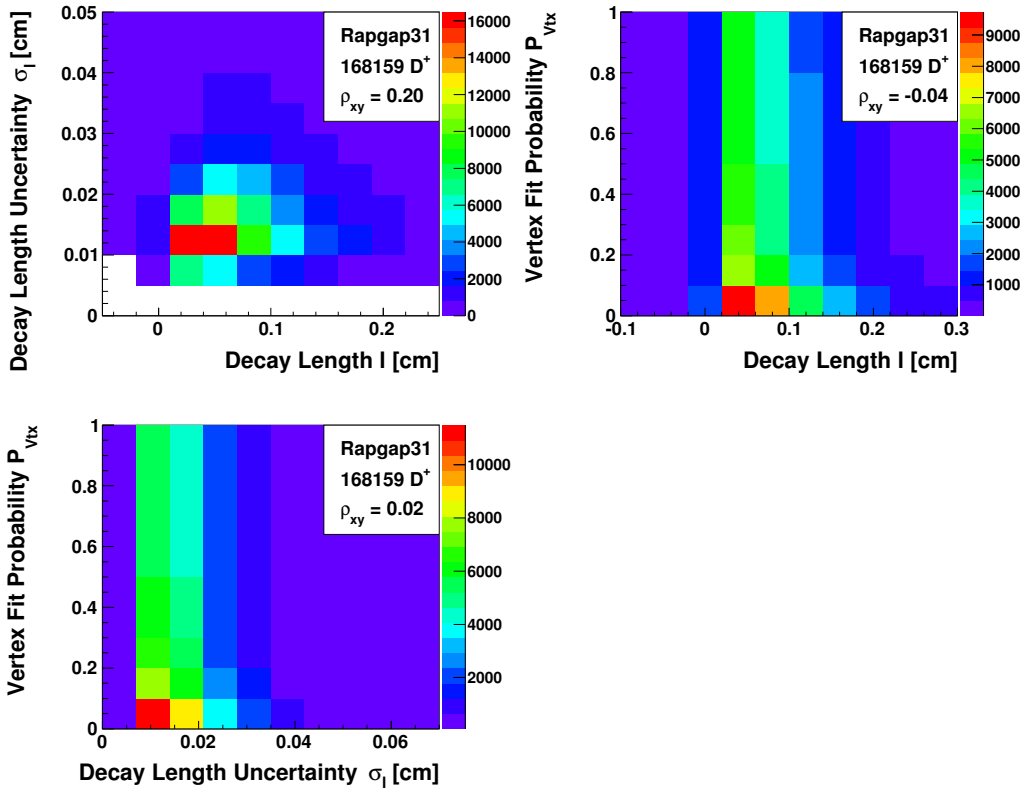

Figure 8.4: Two-dimensional distributions of the vertex fit related variables l, σ_l, P_{Vtx}.

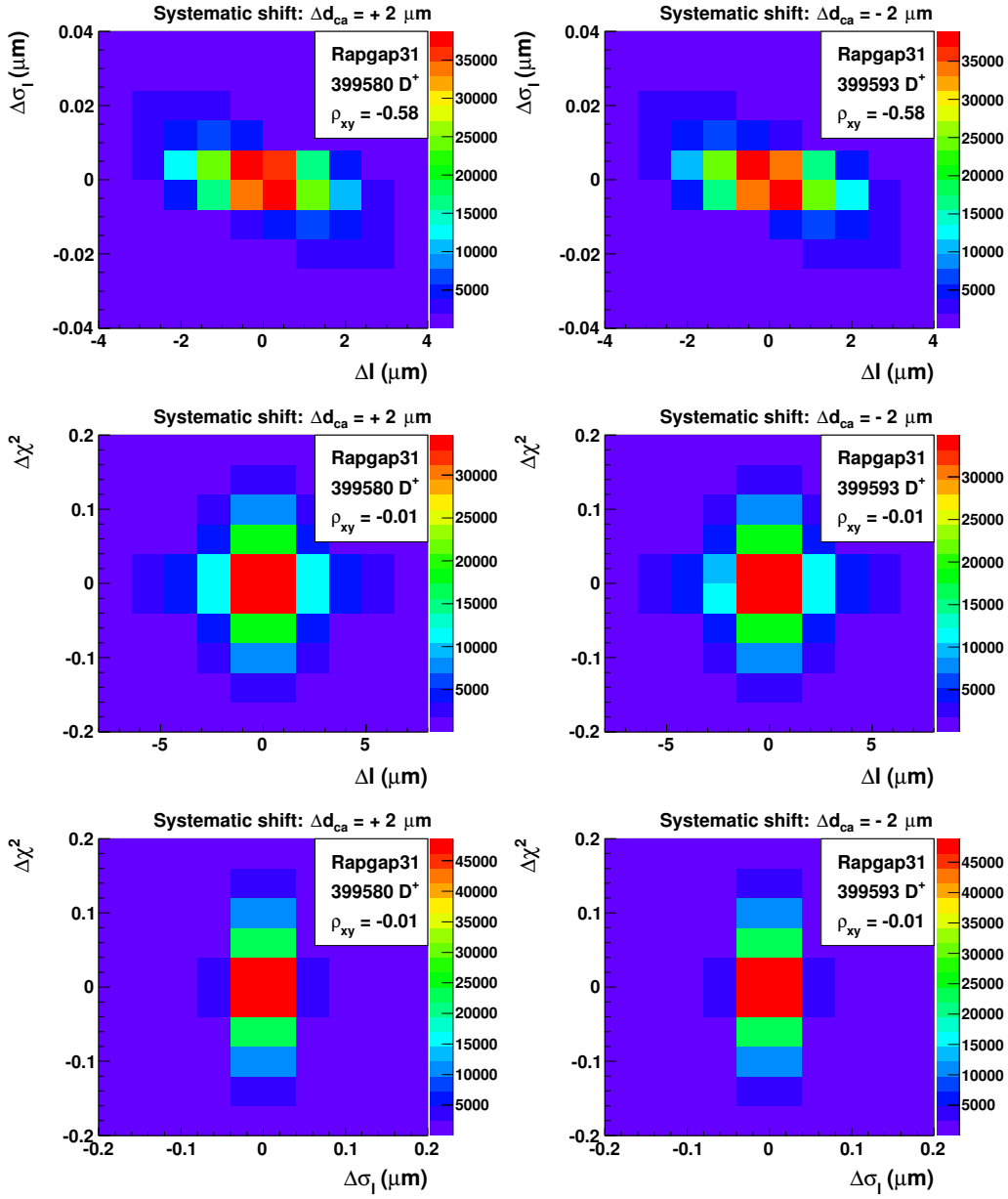

Figure 8.5: Correlations of the vertex fit quantities after the variation of the track parameter d_{ca}.

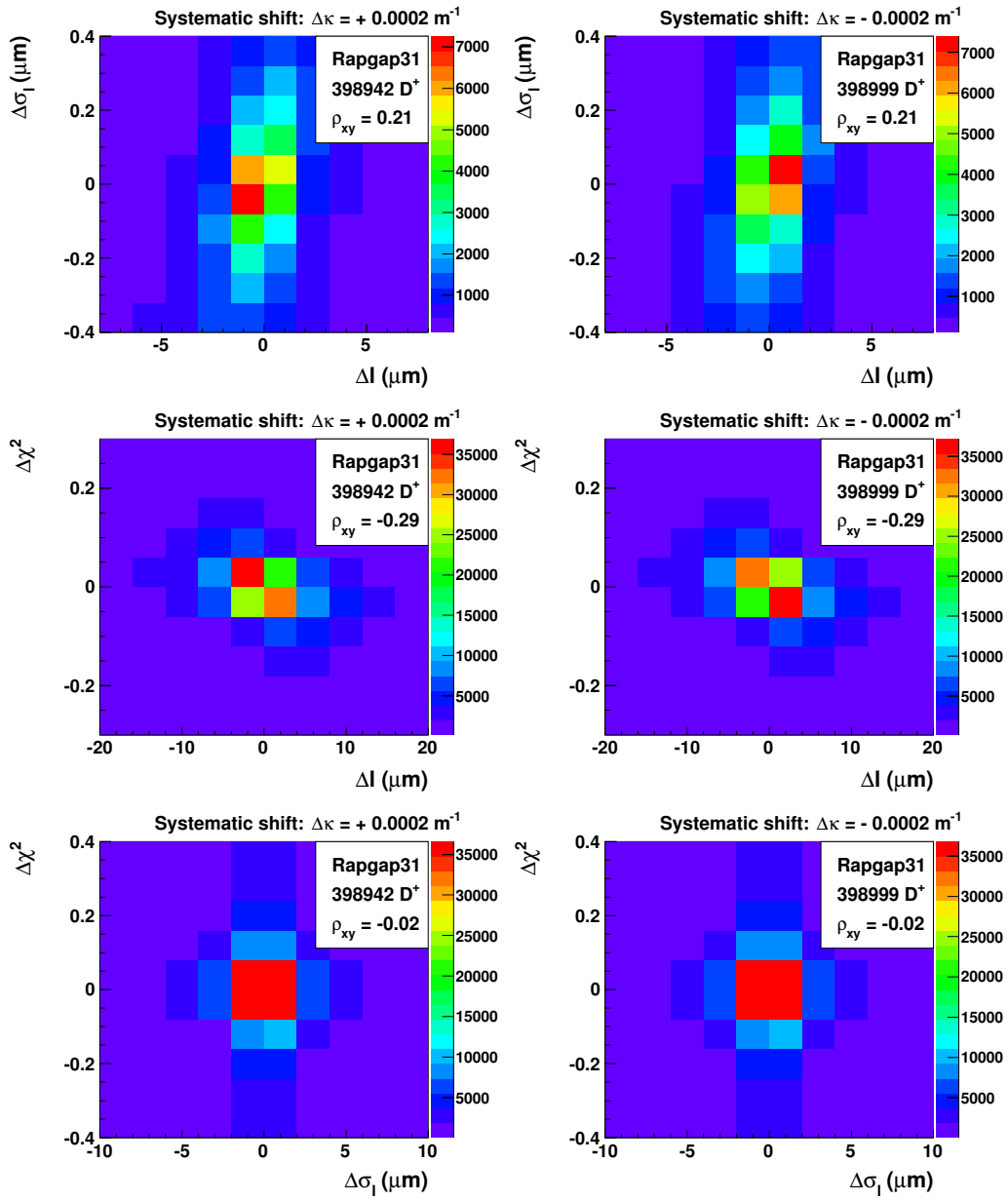

Figure 8.6: Correlations of the vertex fit quantities after the variation of the track parameter κ.

ues derived from the D^*-tagged events (cf. 8.3). The strongest correlation are seen in the decay length and the decay length error after the shift of d_{ca}. They are anti-correlated with a correlation factor of $\rho(\Delta l, \Delta\sigma_l) = -0.58$. Nonetheless are these variables treated as non-correlated variables in the course of the derivation of the uncertainty of the reconstruction efficiency because of the insignificant change in σ_l of $\mathcal{O}(10\,\mathrm{nm})$, which is three orders of magnitude smaller than the applied uncertainty on σ_l (cf. table 8.1). In other words the uncertainty on d_{ca} is not considered as source of the uncertainty on the decay length error. The other variables do not show a correlation with the exception of a small anti-correlation for Δl and $\Delta\chi^2$ in case of the κ shift. As $\rho(\Delta l, \Delta\chi^2) = -0.29$ is still significantly lower than 0.5 it is not considered as correlated. Without showing the corresponding distribution for the shifted track parameter ϕ it is worth mentioning that the vertex fit variables show a random behavior under the variation of ϕ not leading to a correlation.

8.1.3 Classifier Uncertainties

This chapter consists of two parts, in the first part a study on the decay length resolution is discussed, whereas in the second part the uncertainties of the classifiers are derived. All results in this section are derived from D^* decays. Unfortunately it is not possible to use $D^{\pm}$ decays for systematic studies directly due to the statistical background and the resulting large statistical uncertainties. The D^* results are used as approximation to the classifier uncertainties afterwards.

Decay length resolution This paragraph discusses a study on the decay length resolution. A good description of the decay length resolution is crucial because of the two overlapping effects of multiple scattering and the track bending. Both effects depend on the transverse momentum and influence the way the vertex is

determined counteracting. At low p_T multiple scattering is the dominant effect, on the other hand the track is strongly curved which improves the vertex fit. At high p_T it is the other way around. The decay length resolution is especially sensitive to multiple scattering and therefore a crucial test of the material distribution in the detector simulation. Different resolutions for data and MC would lead to systematic biases due to binning effects or geometrical cut-off effects. The decay length resolution has been derived for data and simulated data by the following prescription:

Generally the decay length distribution consists of the convolution of the exponential lifetime distribution, the momentum distribution and the resolution. The model taking into account the convolution of the three contributions was elaborated in [64]. The free parameters of the model are the mean lifetime and the detector resolution. The p_T distribution is divided into three ranges, which are chosen such, that every range contains approximately the same number of events. Since the p_T bins are relatively narrow the weighted mean of p_T is used instead of the full distribution. The mean lifetime is also fixed and set to the value of the world average. Then the only free parameter of the model is the detector resolution. A fit of the model parameter to the data leads to the resolution.

The D^0 decay length distribution is reconstructed from D^* decays as described in section 6.4. Figure 8.7 shows the decay length distribution and the corresponding detector resolutions for different p_T for data and simulated data.

The decay length is well resolved with a mean resolution of about 180 μm in comparison to typical decay lengths of 370 μm. The resolution is well described by the simulation within the statistical accuracy for the whole p_T range. In the lowest p_T range the data resolution of 172 μm is slightly better than the MC resolution of $\sigma_l(MC) = 201\,\mu$m. For the other p_T ranges the MC gives an excellent description. Figure 8.8 shows the resolution of the decay length as function of

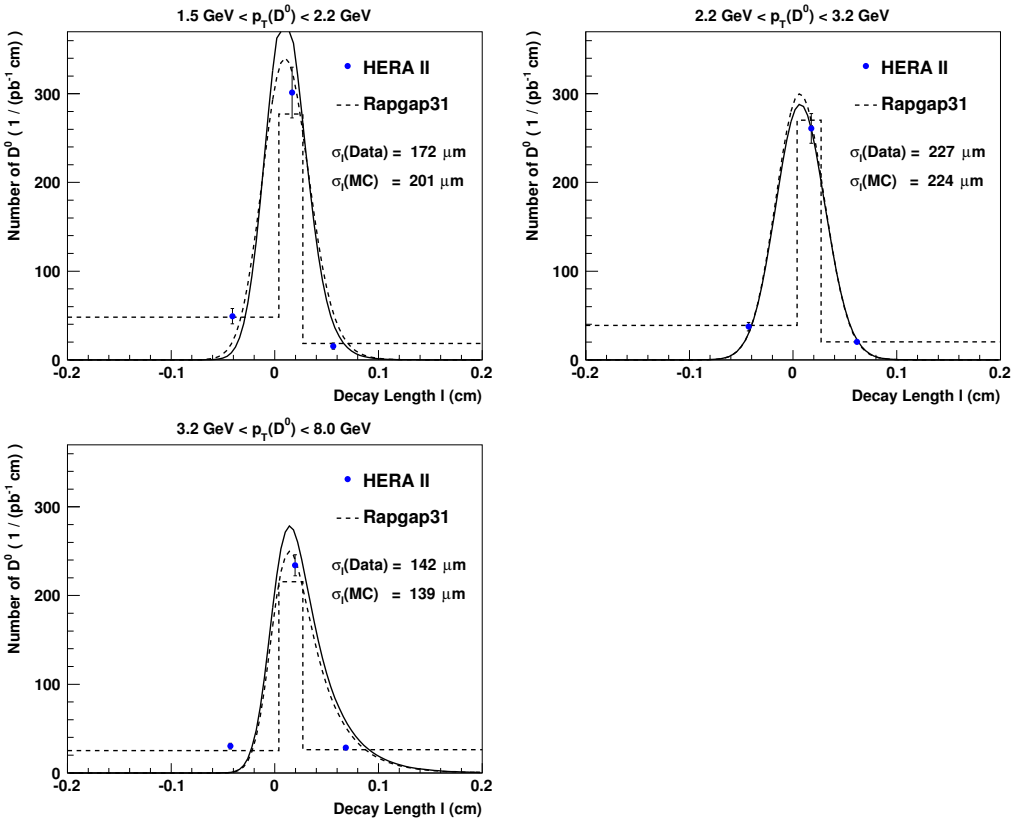

Figure 8.7: D^0 decay length distribution for data and RAPGAP for low, medium and high p_T. The dots and the dashed line of the histogram indicate the number of reconstructed D^0 for data and Monte Carlo. The solid and the dashed lines of the curves illustrate the lifetime distribution model with the fitted resolution.

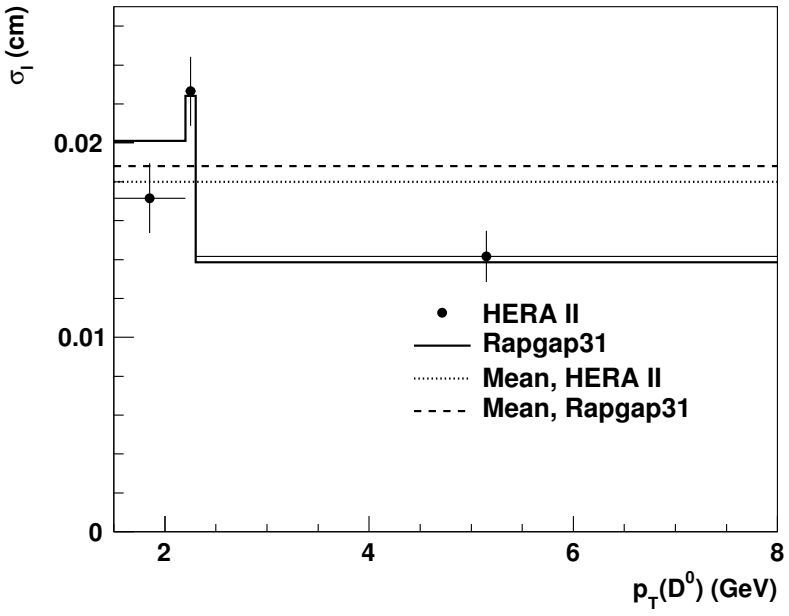

Figure 8.8: D^0 decay length resolution vs. p_{T}

the transverse momentum. There is no p_{T} dependence on the discrepancy. The difference of the mean values amounts to $8\,\mu$m. It is of the same order as the uncertainty of the decay length and calculated decay length uncertainty, which is derived in the course of this section.

Determination of the uncertainty on the classifiers In this paragraph the distributions of the substituted classifiers are shown. As discussed earlier the uncertainties on the classifiers are derived by means of the difference of the mean values of the distributions derived from D^* decays for data and simulated data. The distributions as shown in figures 8.9 are derived by means of the wrong charge subtraction method (cf. 6.6). All classifier are described well within their statistical precision. As summarized in table 8.1 even the mean values of the distributions of the decay length and decay length uncertainty are described within their statistical accuracy. Table 8.1 outlines the results, the differences of the means and

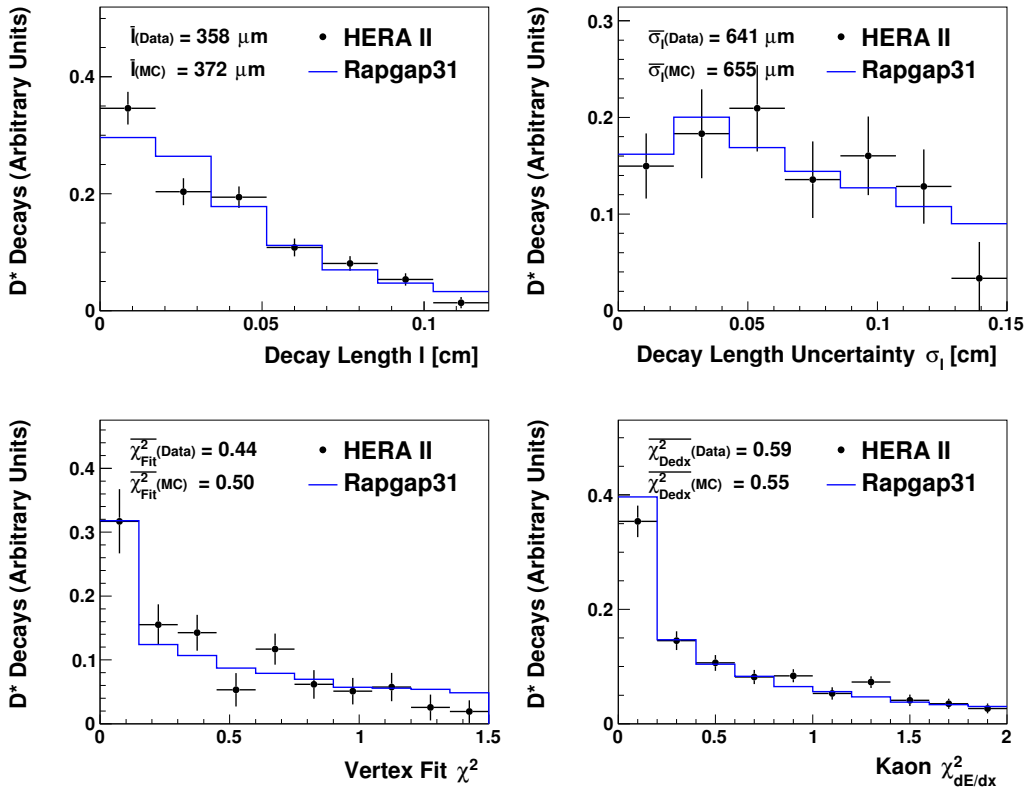

Figure 8.9: Distributions of decay length l, decay length uncertainty σ_l,χ^2 of the vertex fit and the specific energy loss of D^*-tagged D^0 event for data and RAPGAP.

the applied shifts for the derivation of the reconstruction efficiency uncertainty. The shifts correspond to the differences of the mean values except for the decay length l. In that case the difference of the means is smaller than the statistical precision and an average of the difference and the statistical uncertainty is chosen to be applied as shift.

8.1.4 Neural Network Error Propagation

After the derivation of the uncertainty on the classifier the uncertainties are convoluted through the neural network. From the convolution the relative uncertainty on the reconstruction efficiency is derived and applied to the final result. The ef-

Classifier	Mean value for HERA II	Mean value for Rapgap31	Difference of mean values	Applied shifts
Decay Length l	$370 \pm 7\,\mu$m	$372 \pm 2\,\mu$m	$1.8 \pm 3.6\,\mu$m	$3\,\mu$m
Decay Length Error	$644 \pm 20\,\mu$m	$655 \pm 4\,\mu$m	$11 \pm 10\,\mu$m	$11\,\mu$m
$\chi^2_{Vertex\,fit}$	0.48 ± 0.02	0.5 ± 0.004	0.026 ± 0.01	0.026
$\chi^2_{\mathrm{d}E/\mathrm{d}x}$	0.57 ± 0.01	0.55 ± 0.003	0.024 ± 0.007	0.024

Table 8.1: Mean values of neural network classifier reconstructed from tagged D^0 decays.

ficiency is a function of the number of reconstructed particles N, which in turn depends on the distributions of the associated classifier of the candidates. In the following only one component of the input vector $\vec{x}$, namely x of the neural network is considered. This can be done without loss of generalization, since the classifier are treated as uncorrelated variables.

N is expressed as:

$$N = \sum_P \tilde{F}(x),$$

where P are the candidates of the bin and $\tilde{F}(x)$ is a step function related to F_{NN} in the following way:

$$\tilde{F}(x) = \begin{cases} 1 & \text{if } F_{NN}(x) > c \\ 0 & \text{otherwise} \end{cases} .$$

In the approximative case of a large number of particles N can be rewritten by means of a particle density $p(x)$. The integrability of $\tilde{F}$ follows from the smooth-

ness of F:

$$N \approx \int_B dx\, p(x)\, \tilde{F}(x)\,.$$

Let $\tilde{p}(x) = p(x)\,\tilde{F}(x)$. According to the error propagation δN is then defined as

$$\delta N = \int \tilde{p}(x+\Delta x)\, dx - \int \tilde{p}(x)\, dx,$$

which is a valid approximation in case of a linear dependence of $\tilde{p}$ on x. For small variations $\tilde{p}(x)$ depends linearly on x since $p(x)$ is smooth and can be treated as constant in comparison to F_{NN}. The step function $\tilde{F}_{NN}$ is linear if the same holds for F_{NN}. The linearity of F_{NN} is demonstrated in the next paragraph for the scale of the applied shifts. Again, in principle Δx depends on x, but for the derivation of the systematics uncertainty the best approximation of the distribution, i.e. the first moment which corresponds to the mean value is used. The total uncertainty $\delta N/N$ is then defined as the squared sum of the single contributions of each classifier and corresponds to the total uncertainty of the reconstruction efficiency $\delta\varepsilon/\varepsilon$.

Linearity of the neural network on the scale of the variations The requirement for the convolution of the uncertainties of the classifiers through the neural network is the linearity of F_{NN}. By definition F_{NN} is smooth and differentiable. Therefore the linear approximation is valid up to a certain scale. In the following it is shown that this assumption still holds on the scale of the applied variations. Therefore the differential quotient as a function of the classifiers is studied. The full phase space of l, σ_l,χ^2_{Fit}, χ^2_{dEdx} and the transverse momenta of the decay particles is discretized in 15 grid points in each dimension. The ranges and point differences Δx for the calculation of the differential quotients are derived from the extraction of the uncertainties of the classifier and shown in table 8.2.

Classifier	Range	Δx
Decay Length l	$[0-1.5]\,c$m	$3\,\mu m$
Decay Length Error	$[10^{-8}-2]\,c$m	$11\,\mu m$
$\chi^2_{Vertex\,fit}$	$[0-1.5]$	0.026
$\chi^2_{\mathrm{d}E/\mathrm{d}x}$	$[0-2]$	0.024

Table 8.2: Ranges for the classifier used for the calculation of the differential quotients.

With $D(x,\Delta x) = (F_{NN}(x+\Delta x) - F_{NN}(x))/\Delta x$ being the differential quotient, $\delta(dF_{NN}/dx)$ serves as a figure of merit for the linearity of the neural network. It is defined as

$$\delta(dF_{NN}/dx) = \frac{D(x,\Delta x) - D(x,\Delta x/10)}{D(x,\Delta x)}.$$

$\delta(dF_{NN}/dx)$ compares the differential quotient at a certain phase space point to the differential quotient at the same point with a point difference of $1/10$ compared to the other one. The differential quotient with the smaller point difference can be viewed as the nominal value. The relative differences are shown in figures 8.10. The distributions are relatively narrow apart from the distribution of the specific energy loss of the kaon χ^2_{dEdx}. They are distributed around 0 with mean value shifts below 1%. The neural network is considered linear on the scale of the applied variations for the derivation of the systematic uncertainties. The wideness of the χ^2_{dEdx} distribution is not critical because the contribution to the uncertainty of the reconstruction efficiency is negligible. It is derived in the following section (cf. figure 8.14).

8.1.5 Particle Reconstruction Efficiency Uncertainty

In this section the results for the relative reconstruction efficiency uncertainty are presented. They are displayed in figures 8.11 - 8.14. The most significant contri-

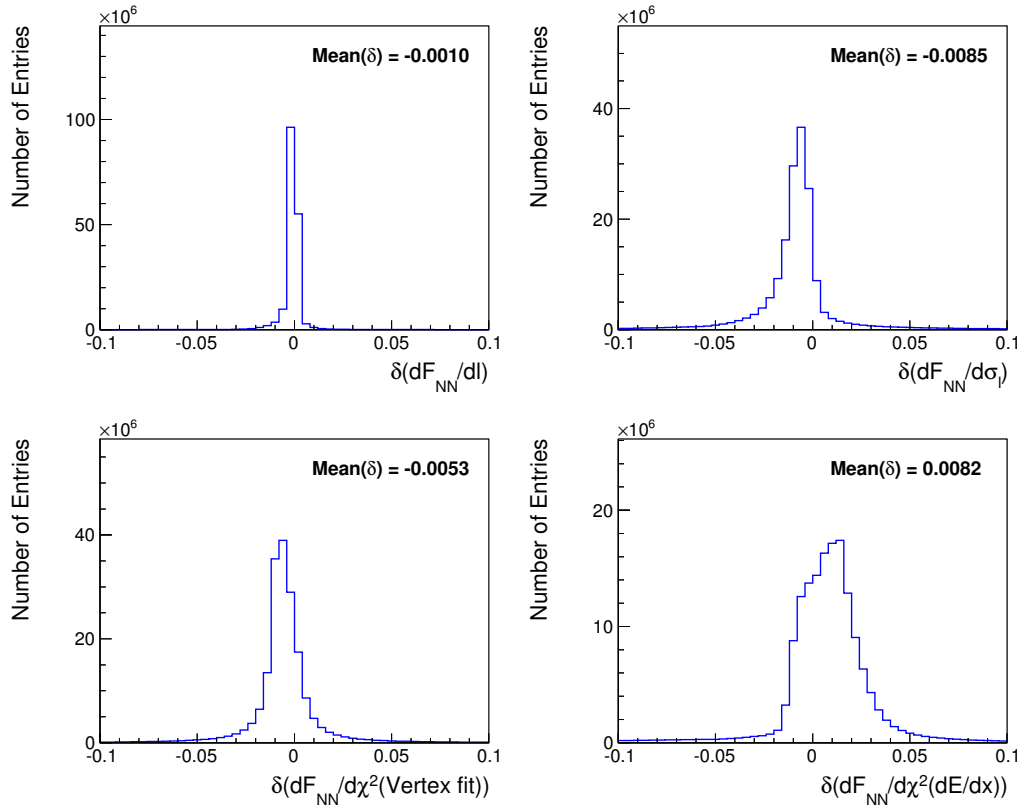

Figure 8.10: Relative difference of the differential quotients of F_{NN} regarding the classifier.

bution arises from the decay length error uncertainty. The shift in the decay length uncertainty results in migrations which are most significant for small transverse momenta. The resulting uncertainty for low p_{T} goes up to 9% and vanishes for $p_{\mathrm{T}} > 4\,\mathrm{GeV}$. The distributions for the other variables are relatively flat. The small Q^2 region also has a slightly larger uncertainty because of the Q^2 and p_{T} correlation. The dependency on the uncertainty of the decay length is biggest for small transverse momenta. On the other hand the overall influence is small and only amounts to uncertainties up to 1%. As expected also in case of the double differential distribution the uncertainties for low p_{T} are biggest, but extend over the range of the rapidity. Figures 11.2 and 11.1 show the double differential results. The uncertainties due to the χ^2 of the vertex fit and the specific energy loss are small and negligible.

8.2 Model Uncertainty

As discussed in section 7.1 the measurement suffers from a limited detector acceptance. The limited detector acceptance as source a systematic uncertainty is two-fold. Imperfection of the detector simulation may lead to a systematic uncertainty. An incorrect description of the acceptance can also arise in case the MC does not describe the data perfectly. The influence of the first source, i.e. the influence of detector simulation with respect to the acceptance is neglected. The dependency on the generator model is derived by the comparison of the detector acceptance derived from the two Monte Carlo samples used in this analysis, namely `RAPGAP` and `DJANGOH` (cf. 3.1).

Figures 8.15 show the results of the relative difference of the acceptance:

$$\Delta A = \frac{A^{det}_{\texttt{DJANGOH}} - A^{det}_{\texttt{RAPGAP}}}{A^{det}_{\texttt{RAPGAP}}}$$

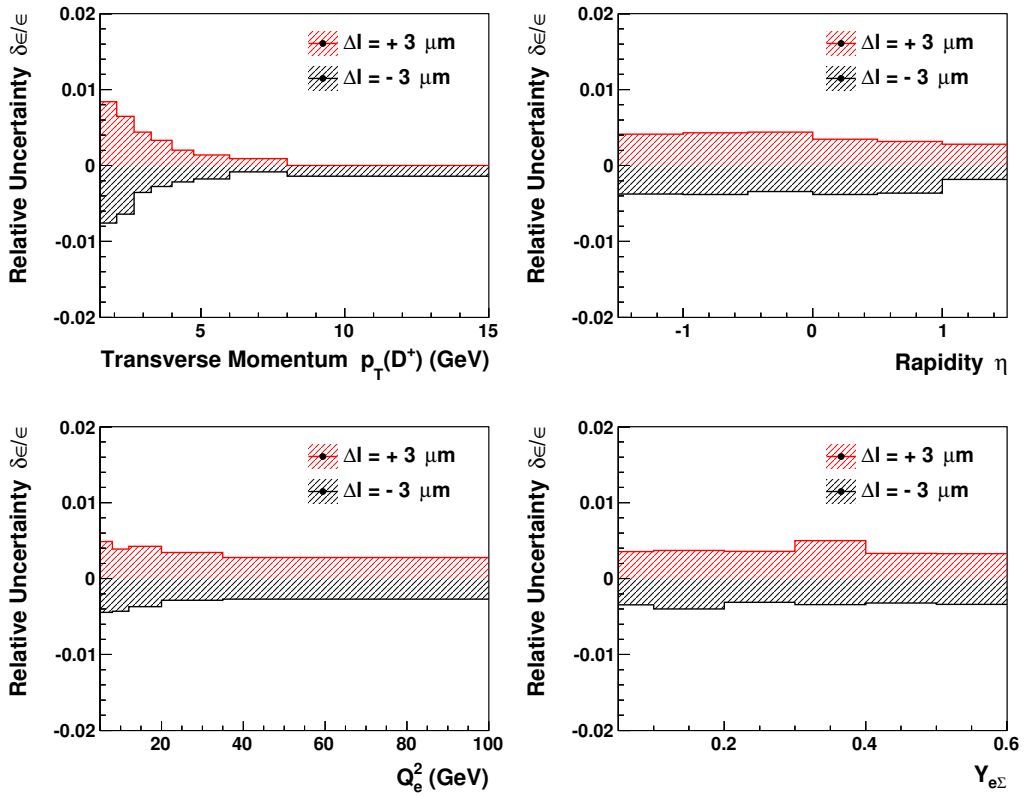

Figure 8.11: Relative uncertainty of the reconstruction efficiency due to the decay length uncertainty.

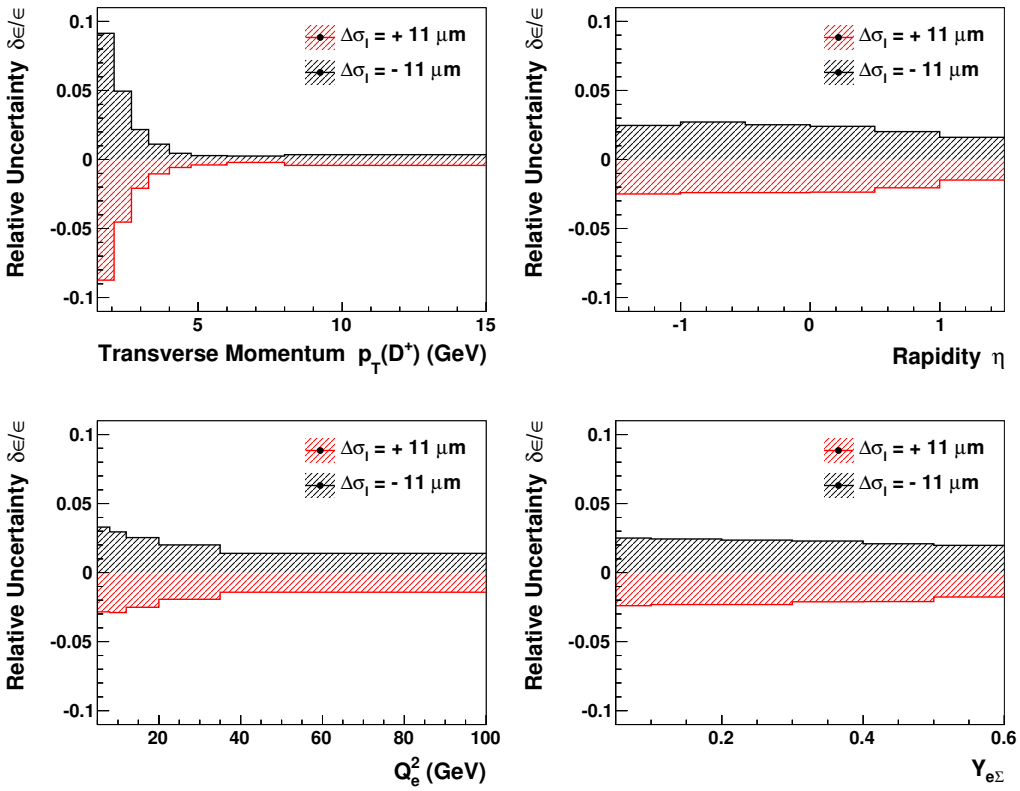

Figure 8.12: Relative uncertainty of the reconstruction efficiency due to the decay length error uncertainty.

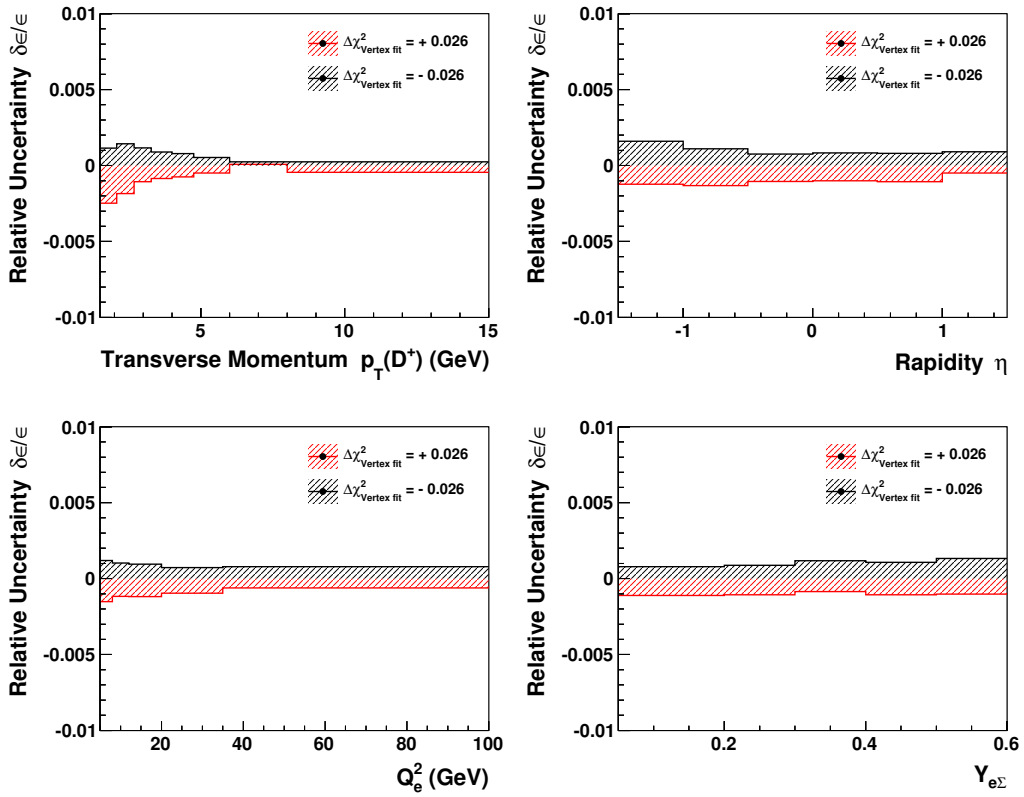

Figure 8.13: Relative uncertainty of the reconstruction efficiency due to the χ^2_{Vtx} uncertainty.

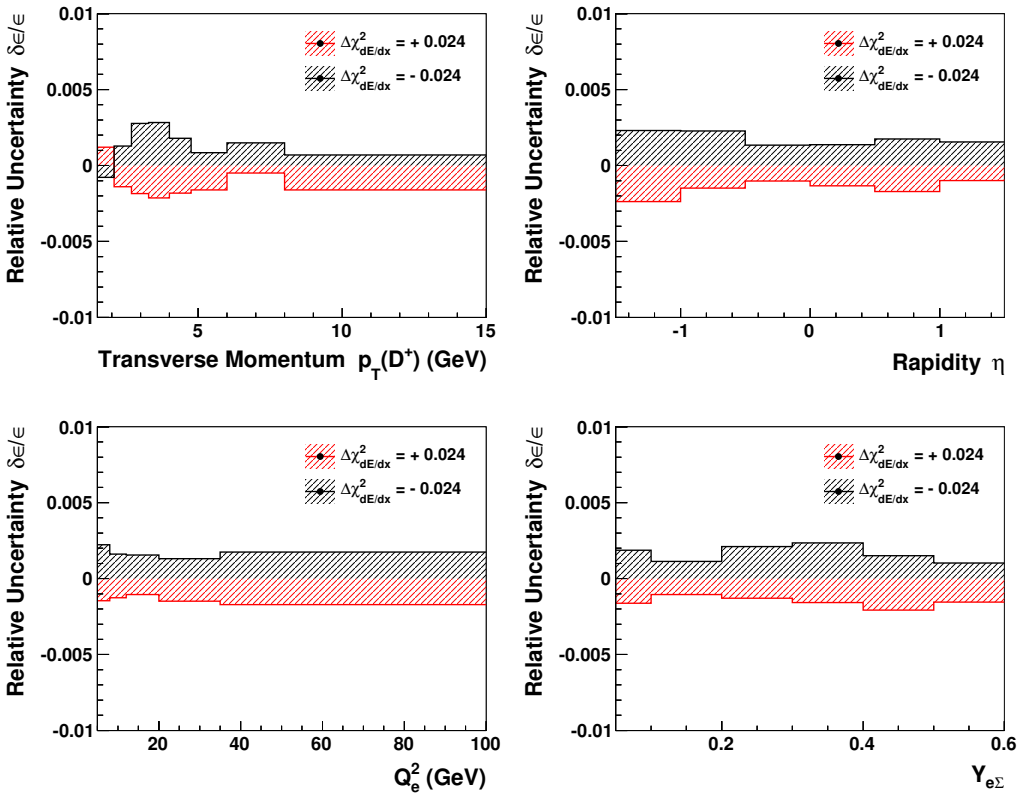

Figure 8.14: Relative uncertainty of the reconstruction efficiency due to the χ^2_{dEdx} uncertainty.

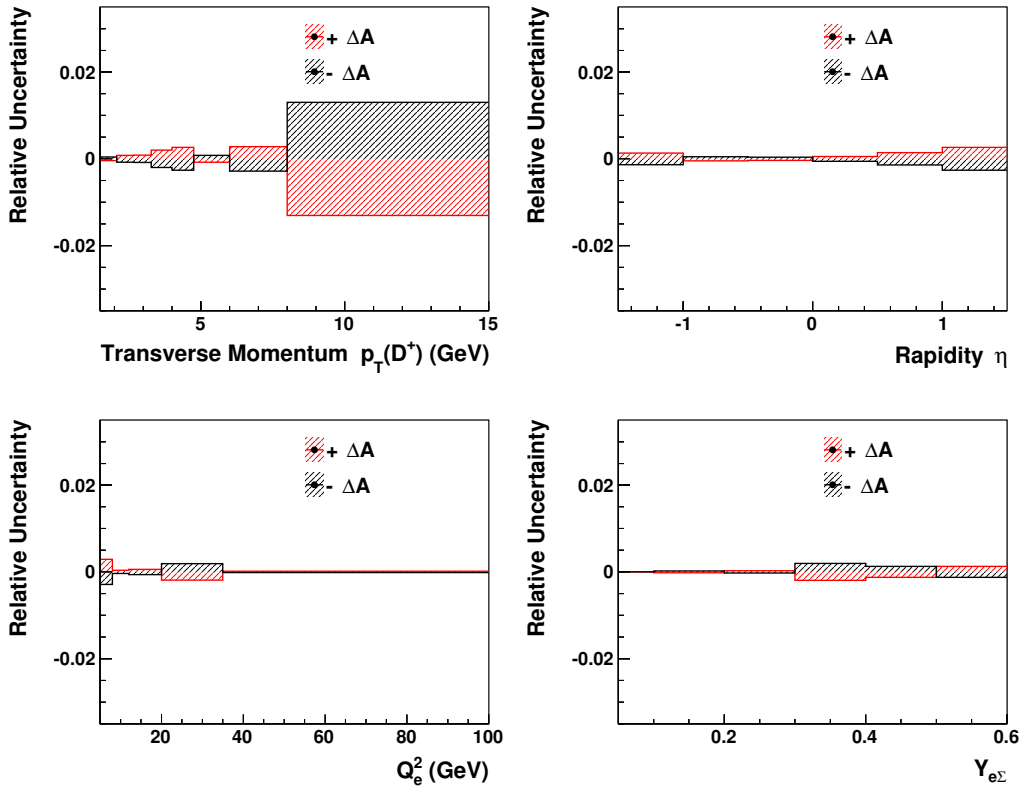

Figure 8.15: Model uncertainty derived from the detector acceptance of the two different models RAPGAP and DJANGOH.

The derived relative uncertainty is symmetrically applied upwards and downwards to the measured result. The overall uncertainty is small and flat with the exception of the high $p_{\mathrm{T}}(D^{\pm})$ region for which the uncertainty reaches values of the order of 1.8%.

8.3 Event Reconstruction Uncertainty

In this section the uncertainty on the reconstruction of the event kinematics is discussed. This analysis makes use of the $e\Sigma$-method which minimizes uncertainties on the event reconstruction [49]. Uncertainties arising from the electromagnetic

scale of the backward calorimeter and the angle of the scattered electron are discussed. Although the hadronic part of the calorimeter is also used for the derivation of the event kinematics, the hadronic energy scale is not considered as source of uncertainty. It only has a small contribution, especially since the calibration has been significantly improved [54]. The uncertainty of the electromagnetic scale and the electron angle are used to estimate the influence on the measurement of the $D^{\pm}$ meson production. The systematic uncertainty of the electromagnetic energy calibration has been measured to be 1%. The angular precision of the SpaCal is about 1 mrad. Scale variations are applied to the simulated data. The relative uncertainty u is calculated from the difference of the nominal cross section compared to the cross section values after a scale variation:

$$u = \frac{\sigma(variation) - \sigma(nominal)}{\sigma(nominal)}$$

The derived uncertainties are displayed in figures 8.16 and 8.17. The resulting uncertainties are reasonably small and flat. Only for large rapidities under the influence of the electromagnetic scale variation the uncertainty reaches its maximum value of 2%. The results are applied to the result of the measured cross sections. The numbers for the double differential uncertainties can be found in the tables of section 11.3.

8.4 Other Contributions to the Uncertainty

Branching ratio uncertainty The systematic error on the branching ratio of the $D^{\pm}$ decaying into $K^{\mp}\pi^{\pm}\pi^{\pm}$ amounts to 2.08% [61].

Luminosity measurement uncertainty As discussed in section 4.6 the measurement of the integrated luminosity is improved by the measurement of QED

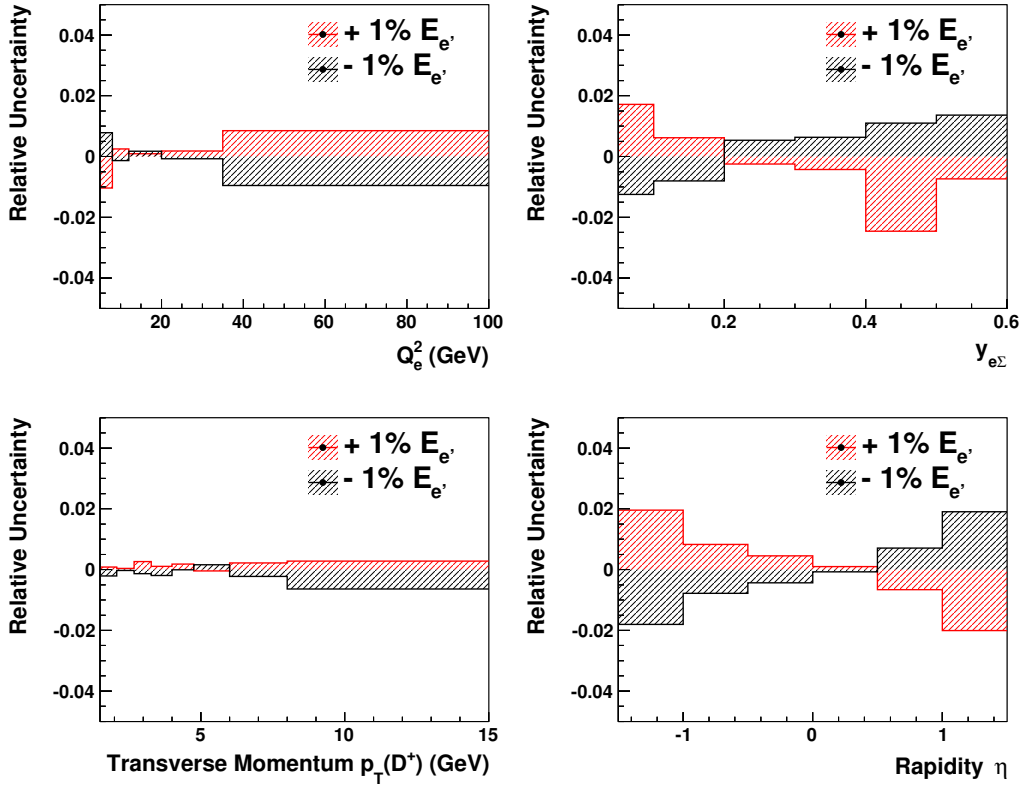

Figure 8.16: Event reconstruction uncertainty due to the scale uncertainty of the electromagnet part of the SpaCal.

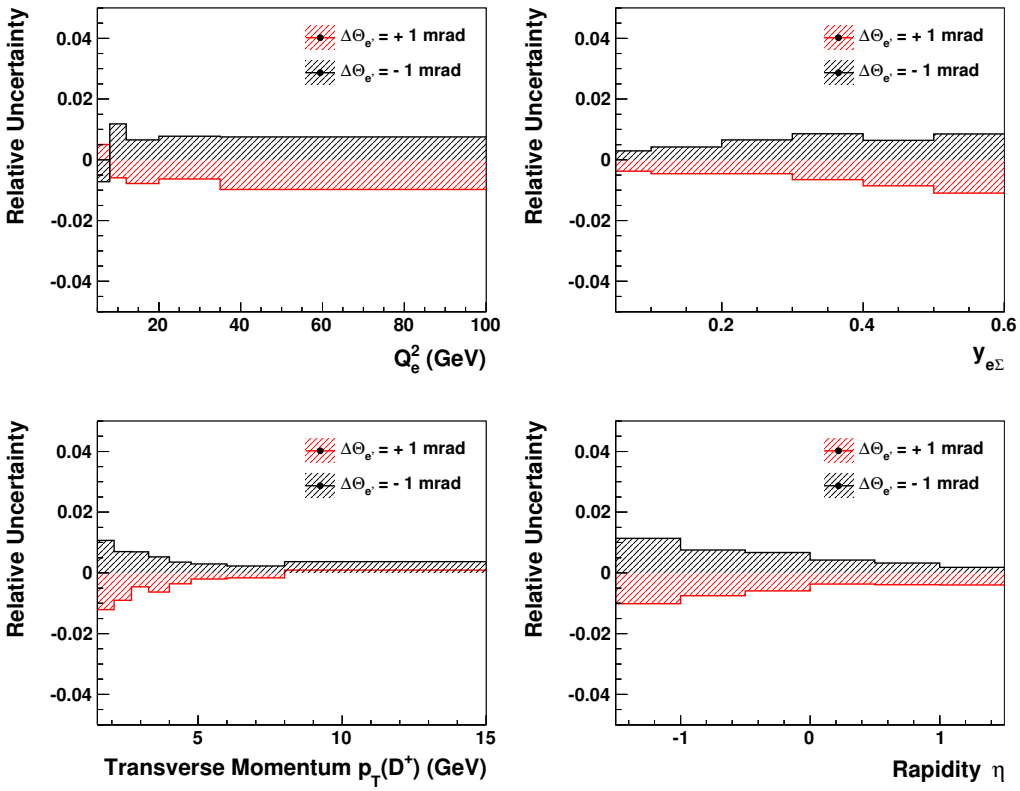

Figure 8.17: Event reconstruction uncertainty due to the uncertainty of the angle of the scattered electron.

Compton events. The measurement is limited by systematic uncertainties of the SpaCal energy scale and resolution, non-elastic QEDC background and theory uncertainties from missing higher orders. [4]. The total systematic uncertainty amounts to 2.3%.

Trigger efficiency uncertainty The estimation of the uncertainty of the two trigger conditions (cf. 4.7) is 1% per condition. Thus a systematic uncertainty of 1.4% covers the trigger uncertainty of s61 and is applied to the measurement. The trigger efficiency uncertainty is taken from [49].

Radiative correction uncertainty The measured cross section is corrected for NLO QED contributions. As explained in 7.3 the correction factors are derived by the comparison of radiative to non-radiative simulated data in which the HERACLES package is used. The corrections are of the order of 3.0%. A more detailed study and comparison to different programs like HECTOR has not been performed, since the contribution to the total uncertainty is small. A more detailed study has been done in [3] and concludes an uncertainty of 2.0%, which has been adopted for this analysis.

Beauty contributions The measured $D^{\pm}$ cross section includes decays from B hadrons to D mesons. The contribution is expected to be small for this analysis and phase space. More extensive studies have been performed in [3, 57]. An uncertainty of 2.0% is assigned.

Mass distribution fit Since the non-Gaussian shapes of the signal distribution are covered in the detector efficiency and the widths of the signal part of the mass distribution are derived from simulated data a systematic uncertainty would only arise from imperfect description by the Monte Carlo. Detailed studies have been

performed in [64]. It has especially been shown that the number of signal events is not sensitive to small changes of the width. An uncertainty of 3.0% on the fit to the mass distribution is assigned.

Chapter 9

Cross Section Results

In this chapter the results of the production cross section of $D^{\pm}$ mesons are presented. The cross section is derived from the $D^{\pm} \to K^{\mp}\pi^{\pm}\pi^{\pm}$ decay channel. The data was accumulated during the HERA II high energy data acquisition period in the years 2006 and 2007 and corresponds to an integrated luminosity of $L = 202.6\,\text{pb}^{-1}$. The run and event selection is described in section 5.1 and summarized in table 5.2. The particle candidate selection is described in chapter 6 and is summarized in table 6.1. Owed to the limited detector acceptance the cross section is derived in a visible range. The definition of the visible cross section is given in equation 7.1 and the kinematic range is summarized in table 9.1. The number of D mesons is derived by a fit to the reconstructed mass spectrum (cf. 6.6). The signal shape is considered Gaussian, whereas the background is described by second order Chebyshev polynomials. The mass spectrum and the fit

Virtuality	$5\,\text{GeV}^2 < Q^2 < 100\,\text{GeV}^2$
Inelasticity	$0.05 < y < 0.6$
Transverse momentum	$p_{\text{T}}(D^{\pm}) > 1.5\,\text{GeV}$
Rapidity	$\lvert\eta(D^{\pm})\rvert < 1.5$

Table 9.1: Definition of the kinematic range of the visible cross section.

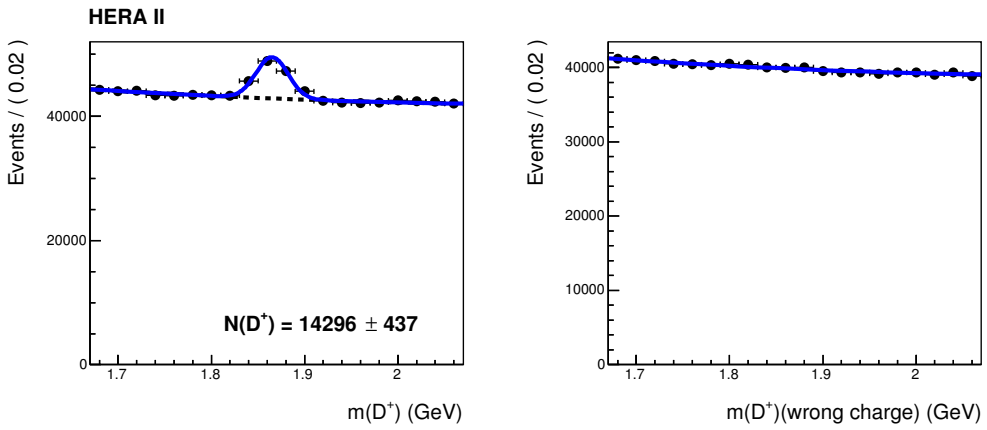

Figure 9.1: The mass distribution of the full data set of all selected candidates in the visible range. The signal is obtained by a fit of the sum of a Gaussian signal and second order Chebyshev polynomial background function to the data.

result of the particles corresponding to the total cross section is depicted in figure 9.1.

9.1 Total Visible Cross Section

The results of the total cross section measurement in the visible range is:

$$\sigma_{vis}^{tot}(ep \to eD^{\pm}X) = 4.82 \pm 0.15(\text{stat.}) \pm 0.28(\text{syst.})\,\text{nb} \tag{9.1}$$

The statistical uncertainty amounts to 3.1% which is about half the systematic uncertainty of 5.8%. The main contributions to the systematic uncertainty originate from the reconstruction efficiency, the branching ratio and the luminosity measurement. Table 9.2 summarizes the results of the total cross sections for each run period in the years 2006 and 2007 and the different lepton modes. The results for the single periods are compatible with the total cross section for HERA II. Considering the statistical uncertainties of the single results, the weighted average corresponds to $\tilde{\sigma}_{vis}^{tot} = 4.83 \pm 0.15\,\text{nb}$ and is therefore in agreement with the afore-

Year	Lepton type	Cross section $\sigma_{vis}^{tot}(ep \to eD^{\pm}X)\,[nb]$
2006	electron	$4.80 \pm 0.30(\text{stat.}) \pm 0.28(\text{syst.})$
2006	positron	$4.93 \pm 0.21(\text{stat.}) \pm 0.29(\text{syst.})$
2007	positron	$4.65 \pm 0.30(\text{stat.}) \pm 0.27(\text{syst.})$

Table 9.2: Total $D^{\pm}$ production cross sections for the different run periods.

mentioned total production cross section. The total cross section prediction of the simulated data sample of the RAPGAP generator (cf. 3.1) is $\sigma_{vis}^{tot}(\texttt{RAPGAP}) = 4.90$ nb which describes the measurement well within the uncertainties. The second model prediction by DJANGOH tends to be too low with a total production cross section $\sigma_{vis}^{tot}(\texttt{DJANGOH}) = 4.21$ nb.

9.2 Single Differential Cross Sections

Single differential cross sections are measured as function of the kinematic variables Q^2 and y and as function of the $D^{\pm}$ meson properties p_{T} and rapidity η. Figures 9.2 - 9.5 show the results of the measurement and the comparison to the results of the leading order MC generators RAPGAP and DJANGOH. The inner error bars represent the statistical uncertainty. The outer error bars indicate the total uncertainties, including the systematic errors. For the exact numbers see the tables in section 11.3. The statistical uncertainties are in the range of $6-13\%$, whereas typical values of the systematic uncertainties are of the order of $6-10\%$. The largest contribution to the systematic uncertainty arises from the uncertainty of the decay length error and subsequently on the transverse momentum.

Underneath the cross section results the ratio R is shown. For a measured variable Y it is defined as:

$$R = \frac{\frac{1}{\sigma^{calc,Y}_{tot,vis}} \cdot \frac{d\sigma^{calc}}{dY}}{\frac{1}{\sigma^{data,Y}_{tot,vis}} \cdot \frac{d\sigma^{data}}{dY}} \cdot \tag{9.2}$$

The ratio facilitates the comparison of the shapes of the normalized generated distributions to the measurement. Systematic errors which are only relevant to the normalization are excluded in this visualization.

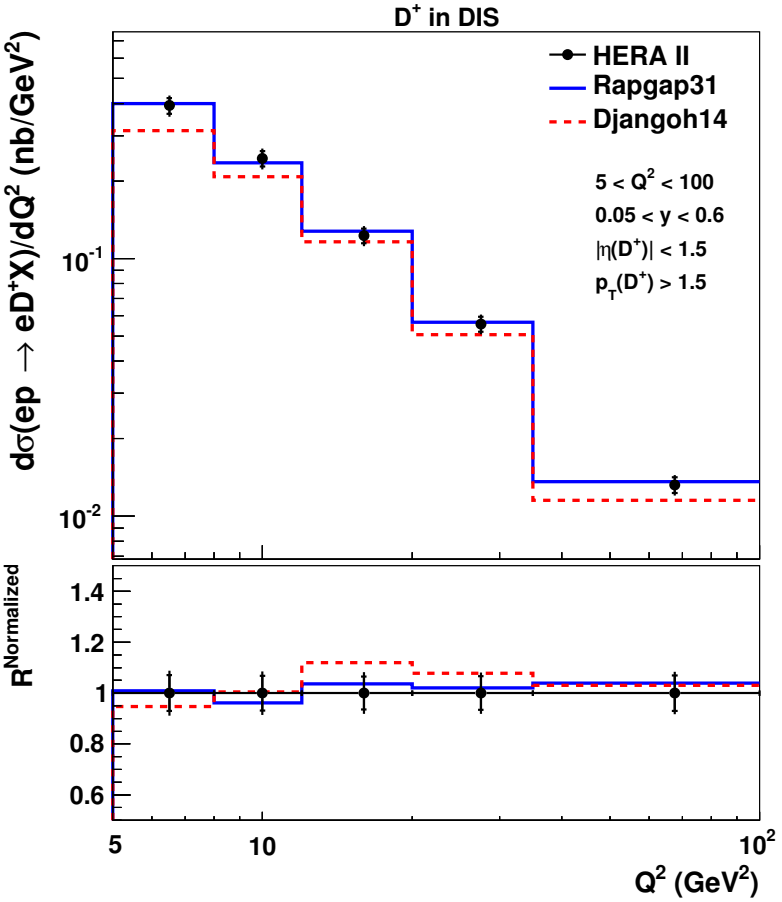

Figure 9.2: Differential cross section as function of Q^2 in the visible range (cf. table 9.1). The measurements are given as black circles. The inner error bar corresponds to the statistical uncertainty of the measurement. The outer error bars correspond to the total uncertainty, including the systematic uncertainty. The measurement is compared to the prediction of the Leading order MC generators RAPGAP and DJANGOH.

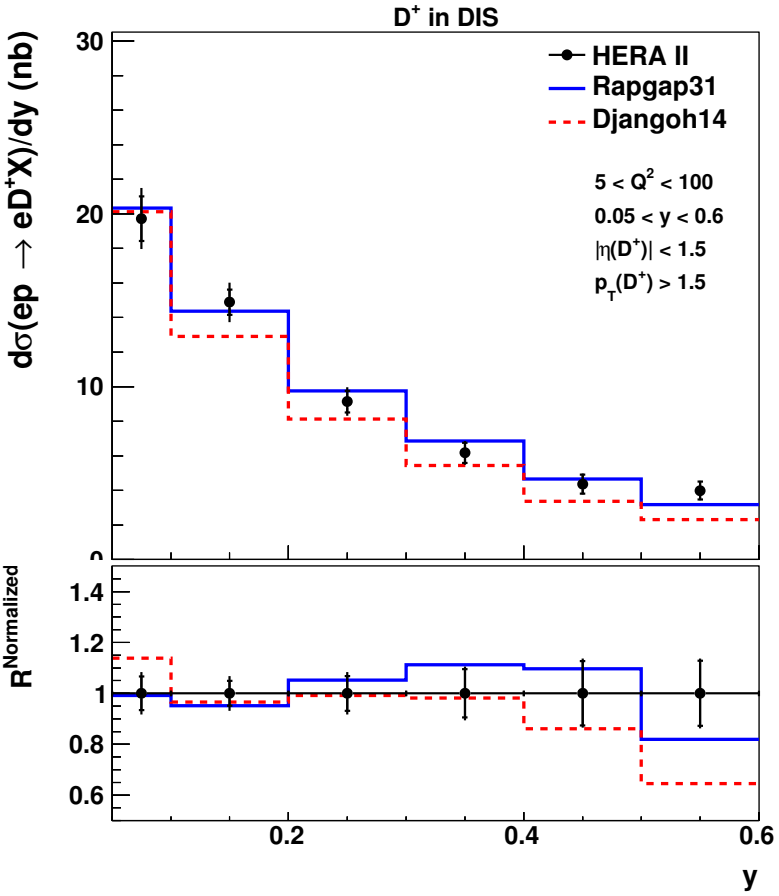

Figure 9.3: Differential cross section as function of inelasticity y in the visible range (cf. table 9.1). The measurements are given as black circles. The inner error bar corresponds to the statistical uncertainty of the measurement. The outer error bars correspond to the total uncertainty, including the systematic uncertainty. The measurement is compared to the prediction of the Leading order MC generators RAPGAP and DJANGOH.

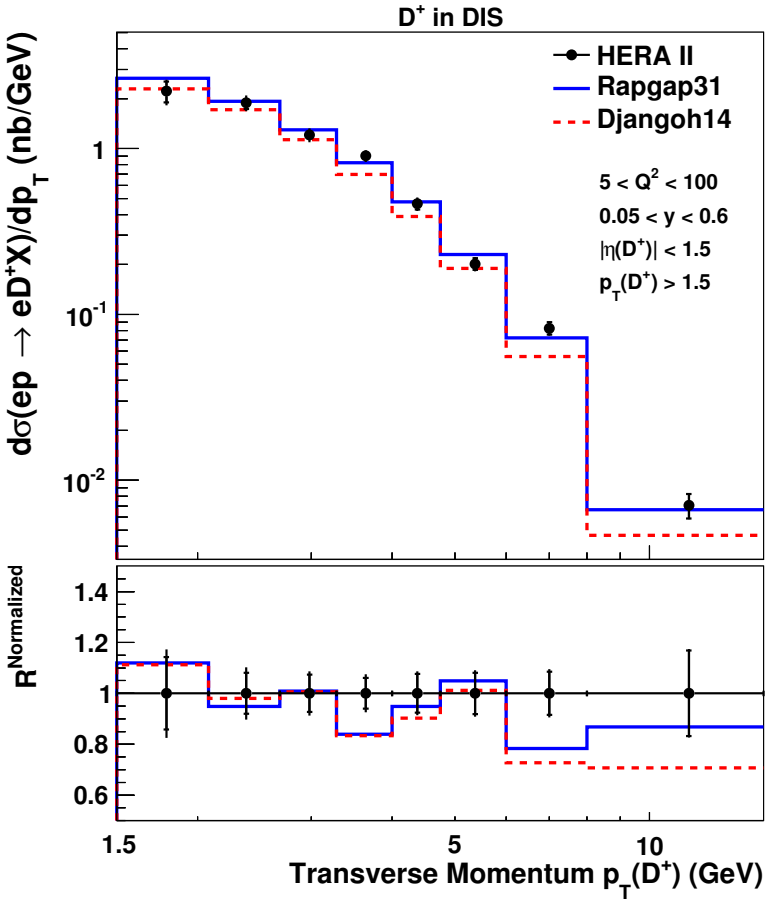

Figure 9.4: Differential cross section as function of $p_{\mathrm{T}}(D^{\pm})$ in the visible range (cf. table 9.1). The measurements are given as black circles. The inner error bar corresponds to the statistical uncertainty of the measurement. The outer error bars correspond to the total uncertainty, including the systematic uncertainty. The measurement is compared to the prediction of the Leading order MC generators RAPGAP and DJANGOH.

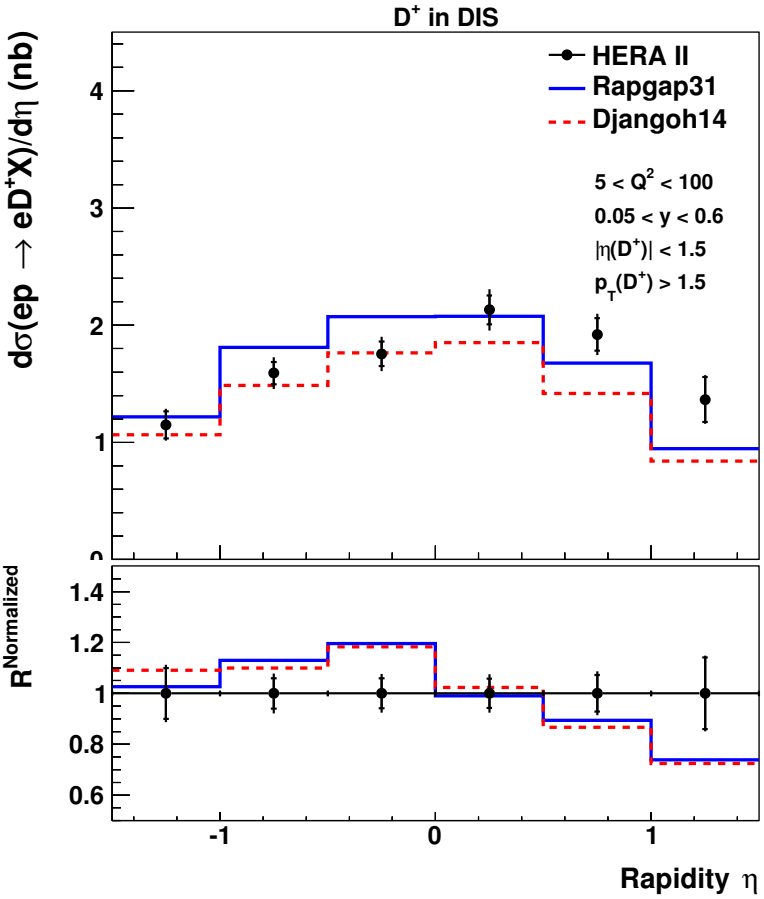

Figure 9.5: Differential cross section as function of rapidity $\eta(D^{\pm})$ in the visible range (cf. table 9.1). The measurements are given as black circles. The inner error bar corresponds to the statistical uncertainty of the measurement. The outer error bars correspond to the total uncertainty, including the systematic uncertainty. The measurement is compared to the prediction of the Leading order MC generators RAPGAP and DJANGOH.

In the following the results of the single differential cross section measurements are discussed in more detail. Figure 9.2 depicts the differential cross section as function of Q^2. RAPGAP gives an excellent description of the Q^2 distribution, whereas DJANGOH describes the data reasonably well, but mostly undershoots the data. The total cross section for DJANGOH is 13% below the data, which becomes apparent when looking at the differential cross section, whereas the shape of the

Variable	Cross section $\sigma_{vis}^{tot}(ep \to eD^{\pm}X)\,[nb]$
Q^2	4.83 ± 0.15(stat.)
y	4.84 ± 0.15(stat.)
$p_{\mathrm{T}}(D^{\pm})$	4.61 ± 0.22(stat.)
$\eta(D^{\pm})$	4.96 ± 0.16(stat.)

Table 9.3: Total $D^{\pm}$ production cross sections derived from the integral over the single differential cross section distributions as function of Q^2, y, p_{T} and $\eta(D^{\pm})$. Only the statistical uncertainties are shown.

distribution is well described as seen in the normalized ratio.

The RAPGAP description of the cross section as function of the inelasticity y (cf. figure 9.3) is worse compared to the Q^2 distribution but still within the uncertainties of the measurement. Only in the last y bin the models undershoot the data. Nevertheless it is not obvious whether this is a feature of the model or a statistical fluctuation of the data. The shape of the DJANGOH sample on the other hand shows a slight tendency to fall towards higher values of y.

The overall description of the cross section in dependence of the transverse momentum of the $D^{\pm}$ meson $p_{\mathrm{T}}(D^{\pm})$ by the leading order MC samples is good within the uncertainties as seen in figure 9.4. The two different models show similar behavior as function of p_{T}. In the last two bins the model shows a too soft $D^{\pm}$-spectrum and undershoots the data.

Table 9.3 summarizes the total cross sections obtained by integrating over the differential cross sections. The integral over the p_{T} distribution tends to be low, compared to the total cross section result. The result is 4% lower than the total visual cross section, although the number of particles in the single differential measurement is determined to be identical to the number of reconstructed particles in the measurement of the total visible cross section. A more detailed investigation shows that the data point of the first bin, which corresponds to a p_{T}-range of 1.5 to 2.08 GeV tends to be too low and the data point in the fourth bin (p_{T}: 3.28 to

4.0 GeV) tends to be too high. Because of the increasing reconstruction efficiency (cf. figure 7.1) and hence the decreasing correction factor towards higher values of p_T the statistical down-fluctuation for low p_T therefore has an increased impact on the total cross section. The purities are of the order of 90% and therefore a faulty description of the migrations by the Monte Carlo is unlikely. Hence, the discrepancy between the integrated total cross section to the measured total cross section originates from statistical fluctuations.

The model description of the rapidity $\eta(D^{\pm})$ tends to be above the data for small η and below the data for larger values of η, where DJANGOH tends to describe the negative rapidity region and RAPGAP favors the larger rapidity regions. Also in case of the rapidity the integrated cross section does not correspond to the total visual cross section, but is approximately 3% higher. This is caused by the falling detector acceptance towards higher rapidities. Especially in the highest rapidity bin of 1.0 - 1.5 the Monte Carlo result is below the corresponding data point and therefore disproportionately taken into account for the correction.

9.3 Double Differential Cross Sections

Besides the single differential cross section measurements visible cross sections for $D^{\pm}$ production are also measured double differentially, once as function of the neutral current kinematic variables and once as function of the $D^{\pm}$ properties.

Figure 9.6 shows the double differential cross section in dependence of the inelasticity y for five ranges in Q^2. Numerical values are given in table 11.6. The uncertainties are dominated by the statistical uncertainties, which are of the order of 7 - 21%, whereas the systematic uncertainties account for approximately 6%. The data are compared to predictions from the leading-order MC generators. Overall a good description is observed within the experimental uncertainties both

for the shape and the normalization of the distributions.

Double differential visible cross sections for $D^{\pm}$ production as function of the rapidity $\eta(D^{\pm})$ for four ranges in p_{T} are displayed in figure 9.7. The statistical uncertainty is the dominant contribution to the total uncertainty. The values range from 7 - 17% and two points having higher statistical uncertainties of about 30%, however the systematic uncertainties account for 5 - 9%.

As already seen in the single differential measurement as function of $\eta(D^{\pm})$ the MC predictions undershoot the data for large values of η. This is observed for all p_{T} ranges. The second data point of the lowest p_{T} bin corresponding to an η range of -0.75 to 0.0 and a p_{T} range of 1.5 to 2.5 GeV is considered to be a statistical down-fluctuation of the data. This data point shows a reasonable mass fit as seen in figure 11.11.

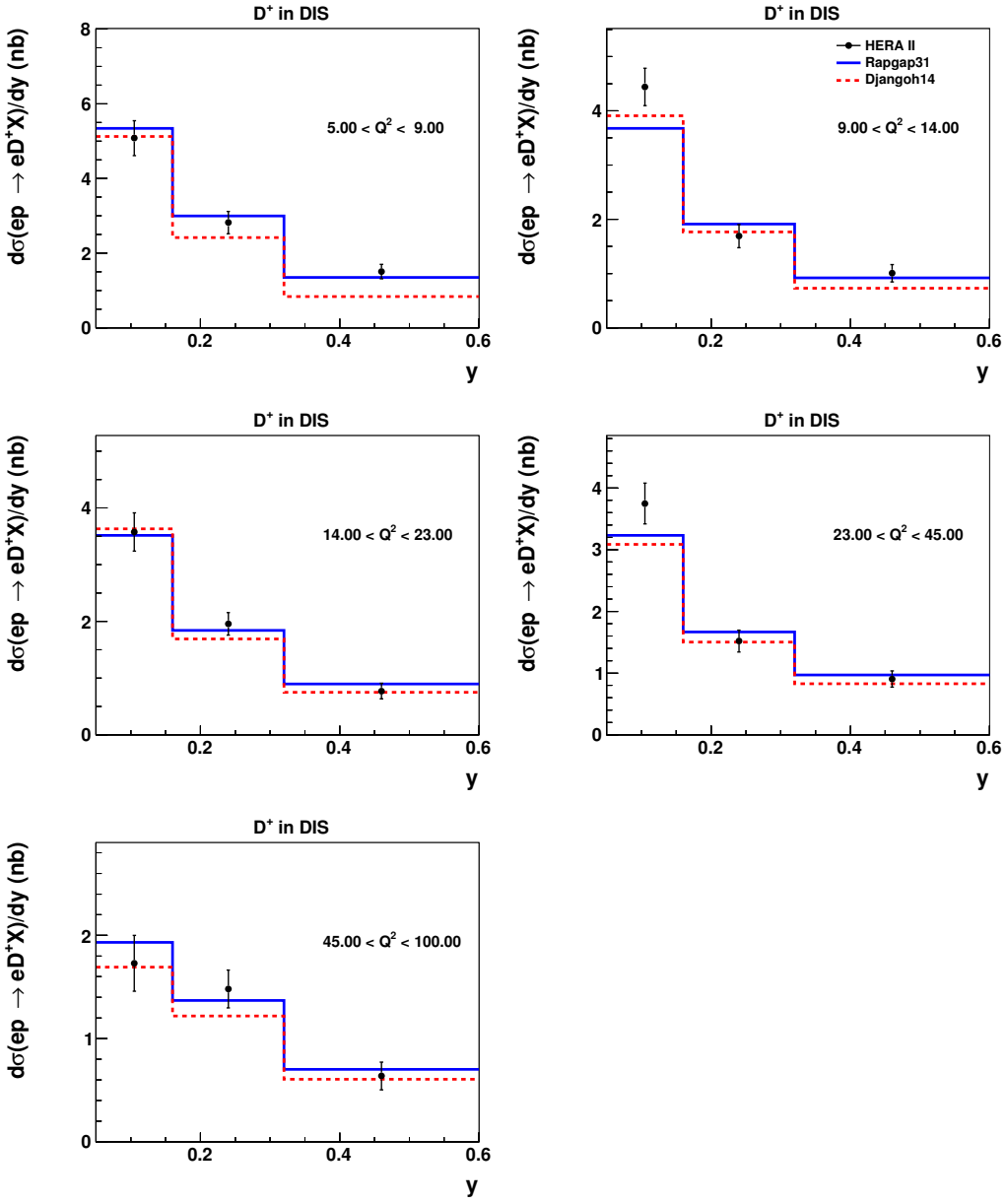

Figure 9.6: The double differential cross section as function of inelasticity y and photon virtuality Q^2 in the visible range (cf. table 9.1). The measurements are given as black circles. The inner error bar corresponds to the statistical uncertainty of the measurement. The outer error bars correspond to the total uncertainty, including the systematic uncertainty. The measurement is compared to the leading order MC RAPGAP and DJANGOH.

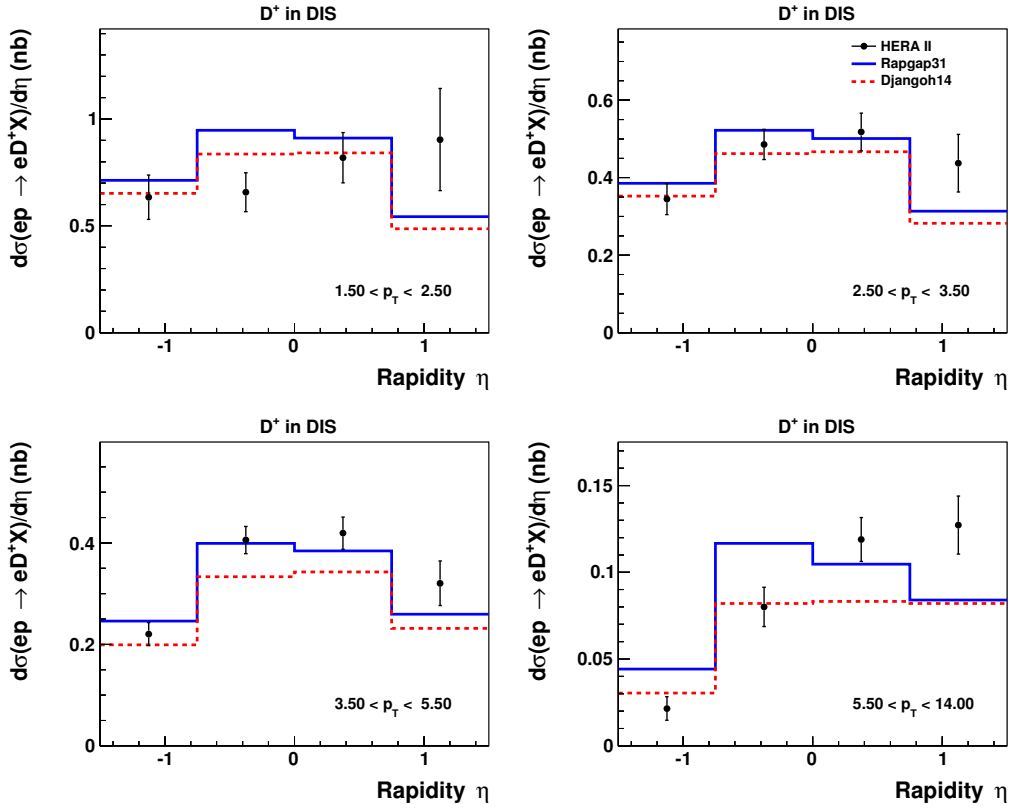

Figure 9.7: The double differential cross section as function of the rapidity η and transverse momentum p_{T} of the $D^{\pm}$ meson in the visible range. Numerical values are given in table 9.1. The measurements are given as black circles. The inner error bar corresponds to the statistical uncertainty of the measurement. The outer error bars correspond to the total uncertainty, including the systematic uncertainty. The measurement is compared to the leading order MC RAPGAP and DJANGOH.

9.4 Comparison to NLO QCD Calculations

In this section the measured cross sections are compared to the NLO QCD predictions calculated by HVQDIS. It is expected that the NLO calculation gives a better description of the measurement because it accounts for the emission of hard partons in the matrix element.

The total visible cross section of the HVQDIS calculation amounts to $3.61\,^{+0.60}_{-0.88}$ nb,

Parameter	Variation	Cross section $\sigma_{vis}^{tot}(ep \to eD^{\pm}X)\,[nb]$	Relative Change [%]
m_c	$-0.15\,\mathrm{GeV}$	3.28	-10.1
	$+0.15\,\mathrm{GeV}$	3.94	8.4
μ_r	$\times 0.5$	4.14	12.8
	$\times 2.0$	3.23	-11.8
μ_f	$\times 0.5$	3.04	-18.8
	$\times 2.0$	3.96	8.8

Table 9.4: Total $D^{\pm}$ production cross sections for the HVQDIS NLO QCD prediction after variation of the central values of the charm mass, renormalization scale and factorization scale.

which is 25% below the measurement. The uncertainty is calculated from a squared sum of the single theory uncertainties. As described in section 3.2 the charm mass m_c, the renormalization scale μ_r and the factorization scale μ_f are varied in order to estimate this uncertainty of the model prediction. Table 9.4 denotes the results of the total visible cross section after the variation of the parameters and the relative change in comparison to the nominal value. The relative changes are of the order of 10%. The largest upscale by 12.8% is caused by the reduction of the renormalization scale μ_r. The largest downscale of -18.8% is caused by the reduction of the factorization scale μ_f. The theoretical uncertainties from the variation of the renormalization and the factorization scale are expected to be reduced significantly as soon as NNLO calculations become available.

Since the total visible cross sections are underestimated by the NLO calculation mainly the shapes of the differential distributions are discussed in the following. Figures 9.8-9.9 show the single differential cross section as function of the NC DIS kinematic variables Q^2 and y. The measurements of the $D^{\pm}$ meson properties $p_{\mathrm{T}}(D^{\pm})$ and η are compared to NLO predictions in figure 9.10 and 9.11, respectively. The prediction of the differential cross section as function of the virtuality Q^2 describes the data within the uncertainty of the measurement. The

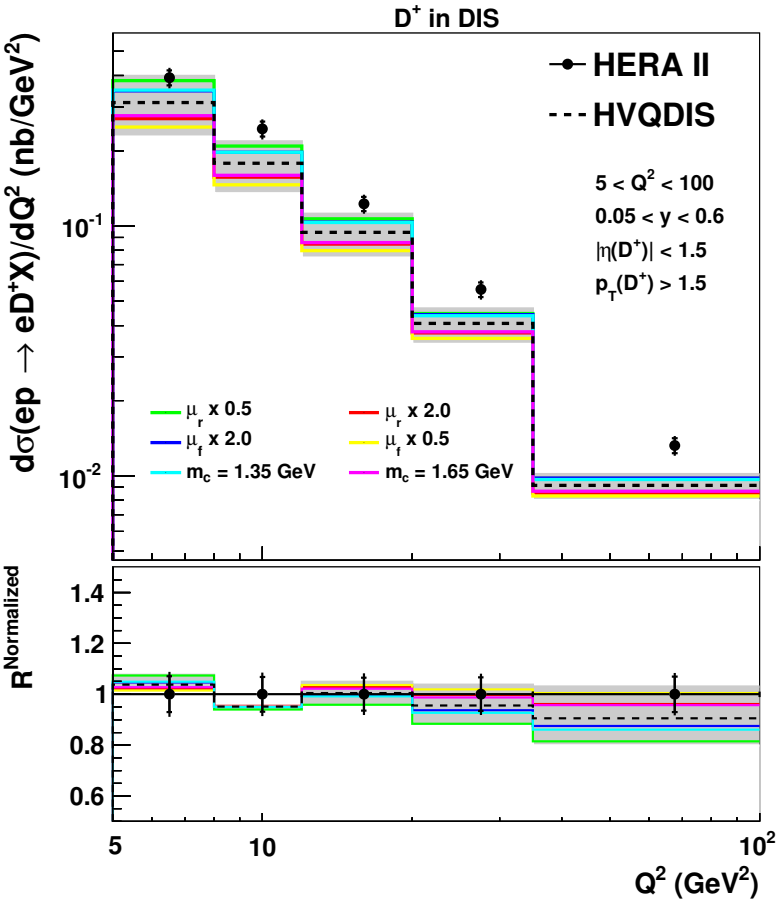

Figure 9.8: Single differential cross section as function of Q^2 in the visible range (cf. table 9.1). The measurements are given as black circles. The measurement is compared to the next-to-leading order calculations of HVQDIS.

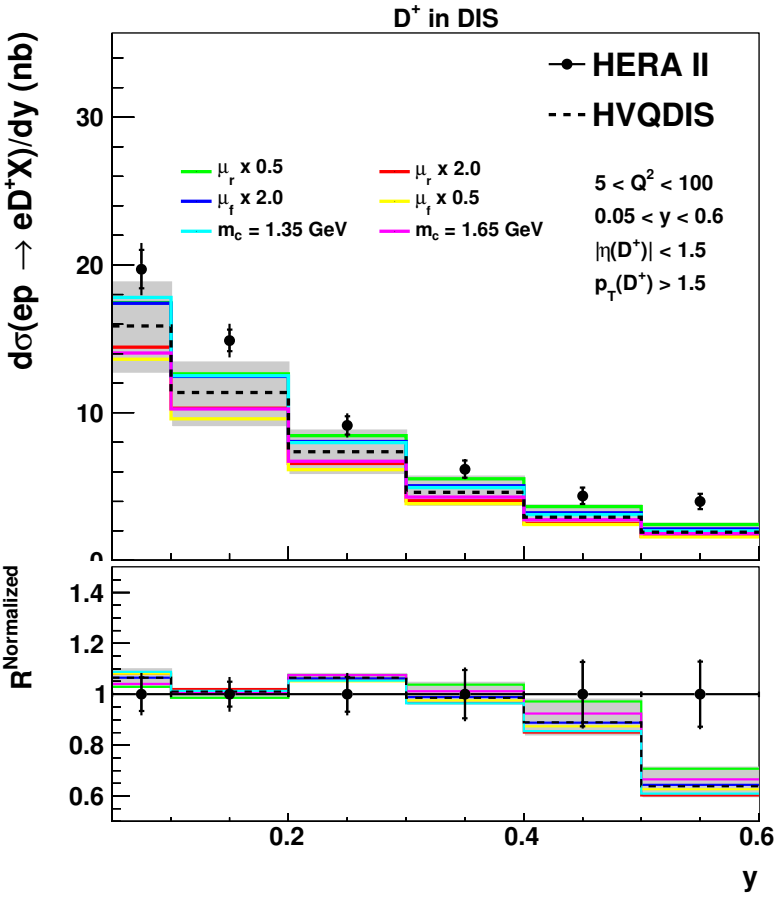

Figure 9.9: Single differential cross section as function of inelasticity y in the visible range (cf. table 9.1). The measurements are given as black circles. The measurement is compared to the next-to-leading order calculations of HVQDIS.

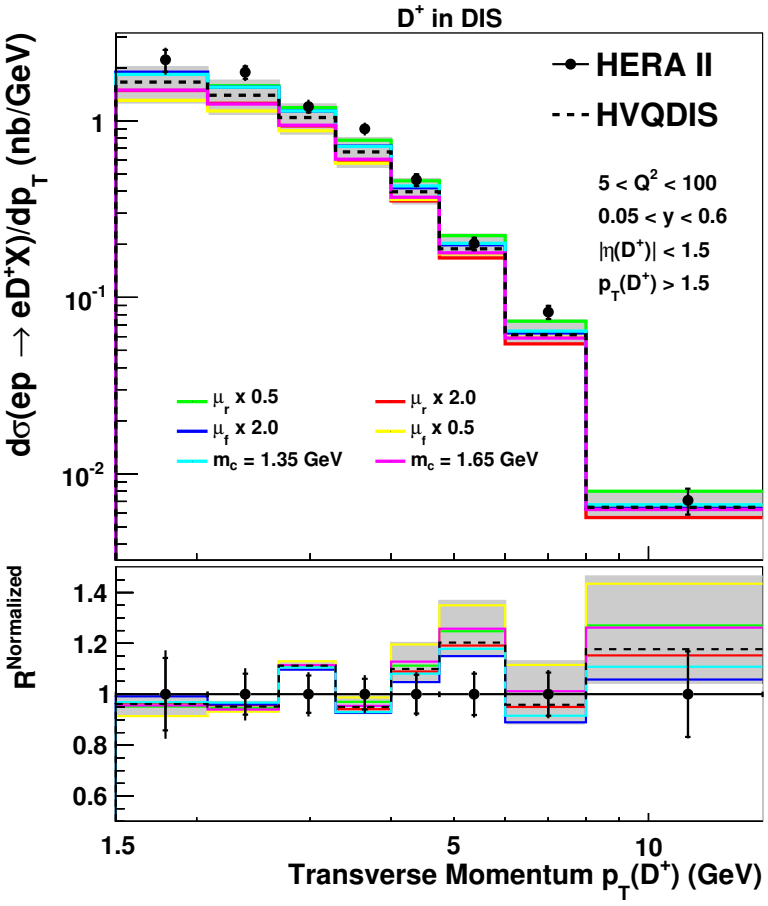

Figure 9.10: Single differential cross section as function of $p_{\mathrm{T}}(D^{\pm})$ in the visible range (cf. table 9.1). The measurements are given as black circles. The measurement is compared to the next-to-leading order calculations of HVQDIS.

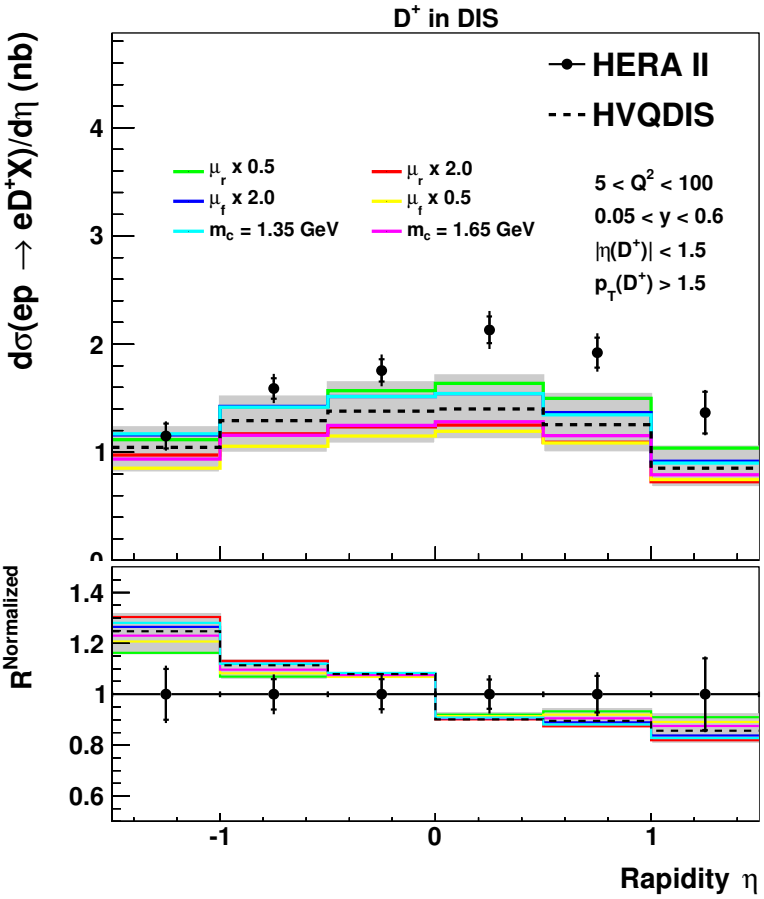

Figure 9.11: Single differential cross section as function of rapidity η in the visible range (cf. table 9.1). The measurements are given as black circles. The measurement is compared to the next-to-leading order calculations of HVQDIS.

distribution falls towards higher values of Q^2 more steeply than the data. Even for the predictions with varied model parameter the data is well described, except for the last Q^2 bin above $35\,\mathrm{GeV}^2$. In this range the predictions for decreased μ_r, increased μ_f and reduced charm mass show a worse description of the data, whereas for an increased μ_r and increased charm mass the predictions are improved. For a decreased factorization scale μ_f the prediction shows an excellent description of the measurement.

The prediction for the cross section measurement as function of y shows a very good description, except for the last bin, which corresponds to a y range of 0.5 to 0.6. The NLO calculation drops for large values of y and is significantly lower in the data for high y. For the y distribution the changes after the variation of the model parameters are less significant compared to one observed for the Q^2 distribution. The distribution of the NLO calculation with a reduced renormalization scale gives the best description of the data.

The NLO prediction describes the cross section as function of the transverse momentum $p_\mathrm{T}(D^\pm)$ within the uncertainty of the measurement. In the p_T range of 4.75 to 6 GeV the prediction overshoots the data. The calculation with an increased factorization scale gives the best approximation of the measurement.

The prediction of the differential cross section as function of the rapidity $\eta(D^\pm)$ overshoots the measurement in the backward region and falls off towards higher values of η too steeply. In the forward region it then undershoots the data. The NLO calculation with the reduced value of the renormalization scale gives a better description of the data and describes the measurement within its uncertainty.

Figure 9.12 displays the double differential cross section as function of Q^2 and y compared to NLO calculations. Taking into account the too low value of the total visible cross section the distributions are overall well described within the experimental and theoretical uncertainties. The description of the shape by

the NLO QCD prediction is better compared to the prediction from the MC event generators. The agreement of the NLO calculations to data is even improved for a smaller value of the renormalization scale, which corresponds to a larger value of the strong coupling constant α_s. The NLO calculations with a smaller value of μ_r also give better descriptions for the y and p_{T} distributions.

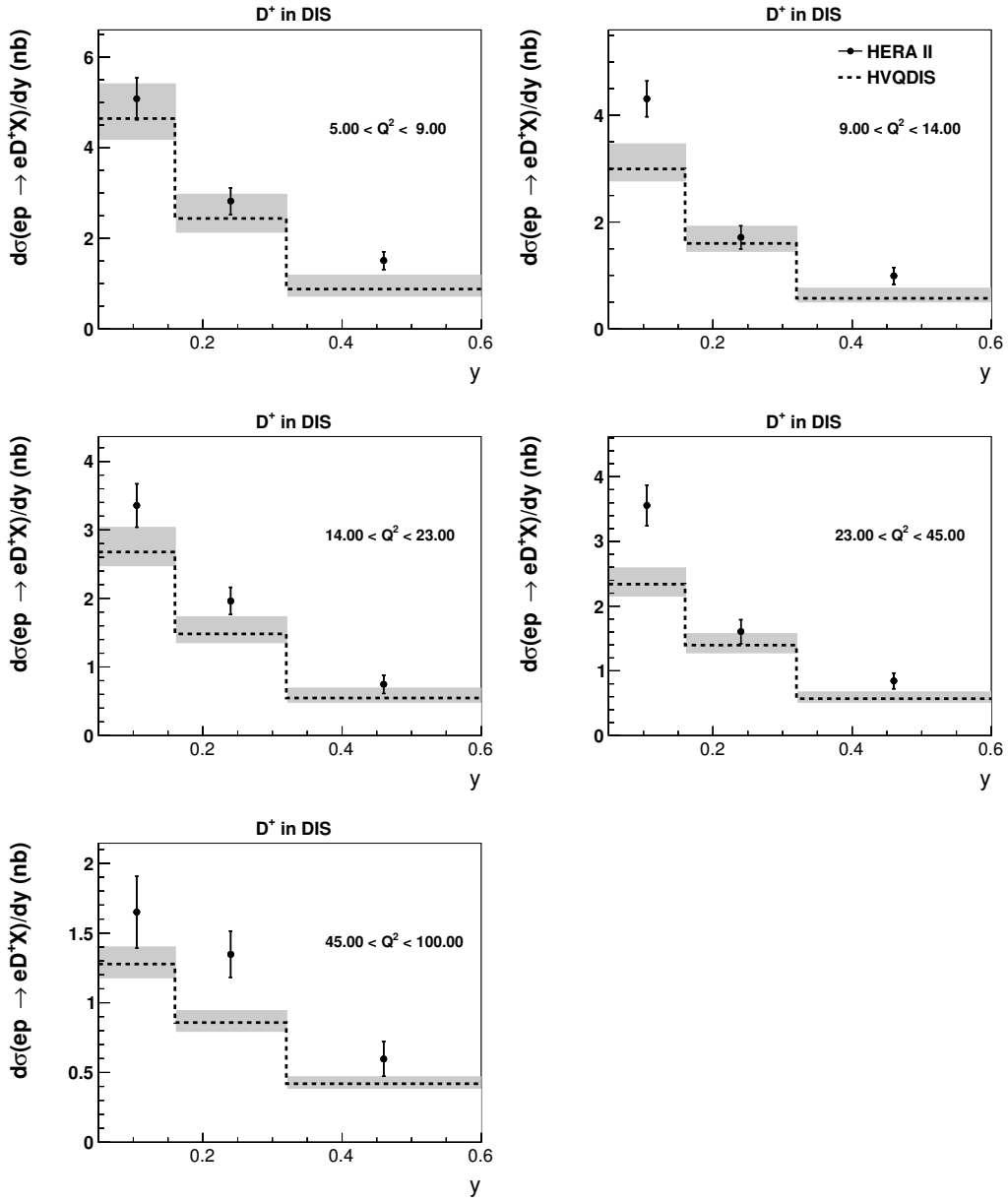

Figure 9.12: The double differential cross section as function of inelasticity y and photon virtuality Q^2 in the visible range (cf. table 9.1). The measurements are given as black circles. The measurement is compared to the next-to-leading order calculations of HVQDIS. The error band corresponds to the total uncertainty derived from the single contributions as described in section 3.2.

9.5 Comparison to Other Measurements

Comparison to the H1 D^* measurement. The results are compared to the D^* production cross section as measured by H1 [3]. The comparison is valid because the fragmentation fractions for $D^\pm$ and D^* as discussed in section 3.2 differ by only 2%. A direct comparison of the differential cross section is not possible due to different phase space regions of the measurements. The measurement of the double differential cross section as function of Q^2 and y allows the summation of the results of corresponding bins in order to obtain a total cross section with a phase space similar to the phase space of this analysis. The most similar phase space for which the total cross section can be calculated corresponds to $5 < Q^2 < 100\,\mathrm{GeV}^2$ and $0.05 < y < 0.7$. The p_T and $\eta(D^\pm)$ ranges are equal to the ranges of this analysis. The contribution to the total cross section due to the difference in the visible phase space at high y is considered small. The result of the total D^* production cross section in this phase space region is 4.65 ± 0.22 nb. This result is compatible with the total cross section from this analysis.

Furthermore the measured differential cross section as function of the rapidity η also shows an excess in the forward direction and is displayed in figure 9.13.

Comparison to the ZEUS measurements The ZEUS experiment has measured the $D^\pm$ and $D^{*\pm}$ production cross section. In the first part of this section the result of the $D^\pm$ measurement from the ZEUS dissertation [57] is discussed. It has shown a precise description of the production cross section by the `HVQDIS` NLO QCD calculations. The visible kinematic range corresponds to $0.02 < y < 0.7$, $5 < Q^2 < 1000\,\mathrm{GeV}^2$, $1.5 < p_\mathrm{T}(D^\pm) < 15\,\mathrm{GeV}$ and $|\eta(D^\pm)| < 1.6$. This allows an indirect comparison between the measurement and the results of this analysis. Unfortunately a direct comparison is not possible due to the differences in the phase spaces. The total cross section is derived by the same method as explained

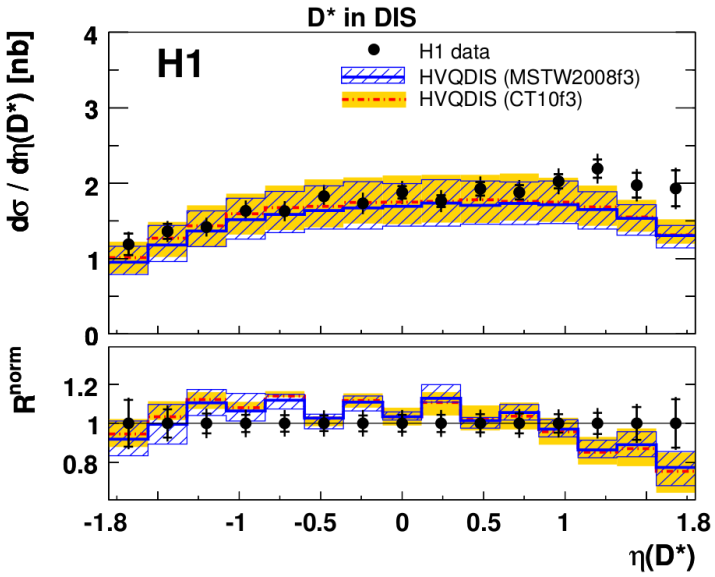

Figure 9.13: The D^* production cross section as function of the rapidity η measured by H1.

in the preceding paragraph in case of the H1 D^* measurement. It is derived by the summation over an appropriate subset of bins of the double differential cross section in order to retrieve a total cross section in a visible phase space, which is similar to the phase space of this analysis. Since in the case of the ZEUS measurement the phase space starts at inelasticities y of 0.02 the phase space which approximates the phase space best corresponds to $0.02 < y < 0.7$. The Q^2, p_T and $\eta(D^{\pm})$ ranges correspond to this analysis. The result of the total cross section with this definition of the visible phase space is 4.36 ± 0.2 nb. In order to estimate the contribution to the cross section in the y-range of $[0.02 - 0.05]$ the fractional contribution is retrieved from the aforementioned H1 D^* measurement, which provides the necessary subdivided bins of y. The contribution of the cross section restricted to a y range of $[0.02 - 0.05]$ to the total visible cross sections amounts to 13%. The difference due to y values above 0.6 are considered small. Considering the contribution for low y, the result of the ZEUS $D^{\pm}$ measurement

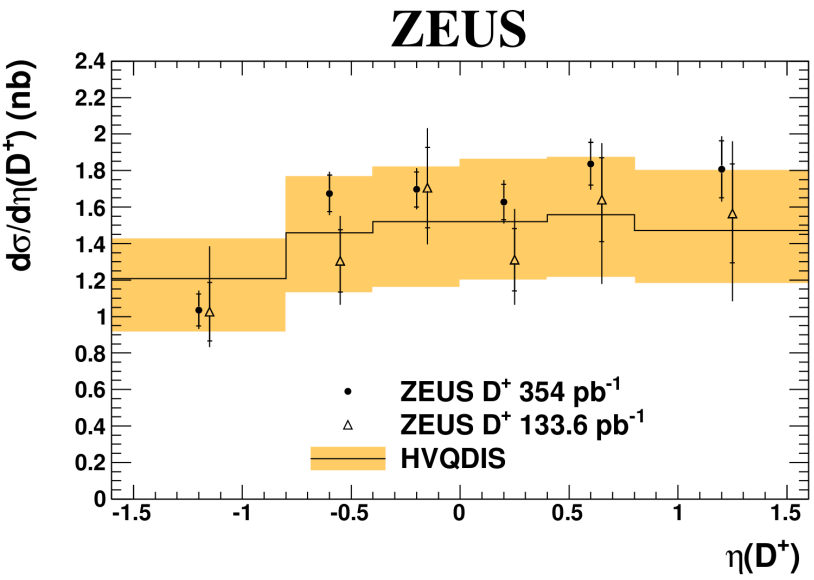

Figure 9.14: The published cross sections as function of the rapidity η measured by ZEUS.

with a phase space similar to the phase space of this measurement amounts to 3.79 nb. This result is in agreement with the HVQDIS prediction, which amounts to 3.61 nb. On the other hand the results published by the ZEUS collaboration are higher. The total $D^{\pm}$ production cross section is 4.88 ± 0.19 nb [7] and the D^{*} production cross section amounts to 5.05 ± 0.112 nb [5]. Both results have been been obtained for the previously used y range of $0.05 < y < 0.7$. The two published ZEUS results are compatible with each other and the H1 measurements. This suggests that the result derived in [57] tends to be too low.

Figure 9.14 depicts the differential $D^{\pm}$ cross section as function of the rapidity $\eta(D^{\pm})$ as published in [7]. Also in this case the model prediction overshoots the data for small values of $\eta(D^{\pm})$ and underestimates the measurement towards higher values.

Chapter 10

Conclusions

The visible inclusive production cross section of $D^{\pm}$ mesons in NC DIS ep scattering at HERA has been studied. The measurement is based on data taken with the H1 detector during the high energy data taking period at center of mass energy of $\sqrt{s} = 318\,\text{GeV}$ in the years 2006 and 2007, which corresponds to an integrated luminosity of $202.6\,\text{pb}^{-1}$. The visible phase space of the neutral current process is defined by $5 < Q^2 < 100\,\text{GeV}^2$, $0.05 < y < 0.6$, $1.5 < p_T(D^{\pm})$ and $-1.5 < \eta(D^{\pm}) < 1.5$. Charm production events are identified by the reconstruction of the $D^{\pm} \to K^{\mp}\pi^{\pm}\pi^{\pm}$ decay channel. The sample is enhanced by the application of a multi-variate analysis technique using a multilayer perceptron based classifier. The input variables of the classifier are based on the specific energy loss of the kaon and the reconstructed decay length of the $D^{\pm}$ meson. A detailed investigation of systematic uncertainties has been done. Especially a convolution of the uncertainties of the input variables of the multilayer perceptron has been performed. The resulting uncertainties on the reconstruction efficiency are relatively small in most regimes of the phase space. The largest contribution to the systematic uncertainty arises from the uncertainty of the decay length error for small transverse momenta of the $D^{\pm}$ meson.

The total $D^{\pm}$ production cross section in the visible range is measured to be

$$\sigma_{vis}^{tot}(ep \to eD^{\pm}X) = 4.82 \pm 0.15(\text{stat.}) \pm 0.28(\text{syst.})\,\text{nb}.$$

The comparison of the LO MC predictions by RAPGAP and DJANGOH show a good description of the data. DJANGOH slightly undershoots the total visible cross section by 13%. The total visible cross section is in good agreement with the published measurements of the $D^{\pm}$ and D^{*} cross sections by ZEUS and the D^{*} measurement by H1.

The single differential cross sections are well described by the LO MC generators for the kinematic variables Q^2 and y and as function of the transverse momentum of the $D^{\pm}$ meson. The description of the distribution of the rapidity $\eta(D^{\pm})$ shows a discrepancy to the measurement, which has also been observed by the H1 D^{*} and ZEUS $D^{\pm}$ measurement.

The results are also compared to NLO QCD predictions calculated by HVQDIS, using the Kartvelishvili fragmentation function. The calculation is sensitive to the treatment of the heavy quark mass in the PDF and in the matrix element. It is found that the NLO prediction for the total visible cross section is 25% below the measurement. Nevertheless, the shapes of the single differential distributions are compared to the data and the shapes are in good agreement for Q^2, y, and p_{T}. The description of the rapidity distribution is improved in comparison to the predictions from LO MC generators. The NLO calculations are performed with different values for the charm mass, factorization scale and renormalization scale and compared to the nominal values and the measurement. The result with a smaller value of the factorization scale improves the description of the rapidity distribution.

Compared to the previous H1 measurement of the $D^{\pm}$ production cross section, which took place during the HERA I period, the available luminosity is in-

creased by a factor of four. The phase space has been extended towards smaller transverse momenta of the $D^{\pm}$ meson from 2.5 to 1.5 GeV. The number of reconstructed $D^{\pm}$ mesons has been increased from about 350 to 14.000 particles. The statistical and systematic uncertainties are reduced by two third. For the first time at H1 the $D^{\pm}$ cross sections have been measured double differentially. Although not the full HERA II data was available because of technical problems of the vertex detector during the data acquisition in 2005 the analysis achieves a high precision due to the improved analysis technique.

Chapter 11

Appendix

11.1 Double Differential Efficiency Systematics

The figures shown in this section contain the double differential efficiency systematics as function of the kinematic variables Q^2 and y and as function of the $D^{\pm}$ meson properties $p_{\mathrm{T}}(D^{\pm})$ and $\eta(D^{\pm})$ (8.1). The title of the figures indicates the variable which has been shifted in order to calculate the systematic uncertainty.

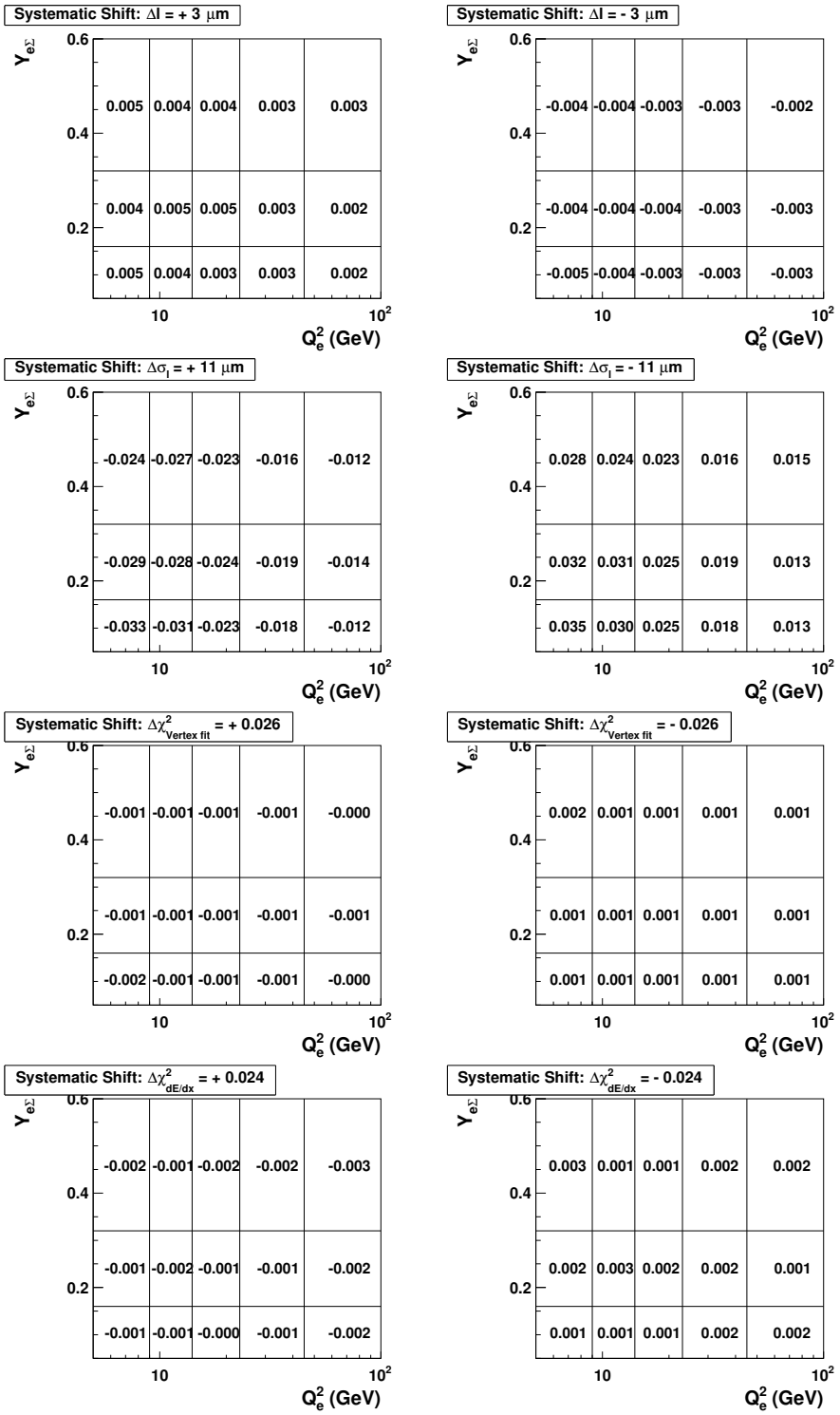

Figure 11.1: Double differential reconstruction efficiency uncertainty for Q^2 and y.

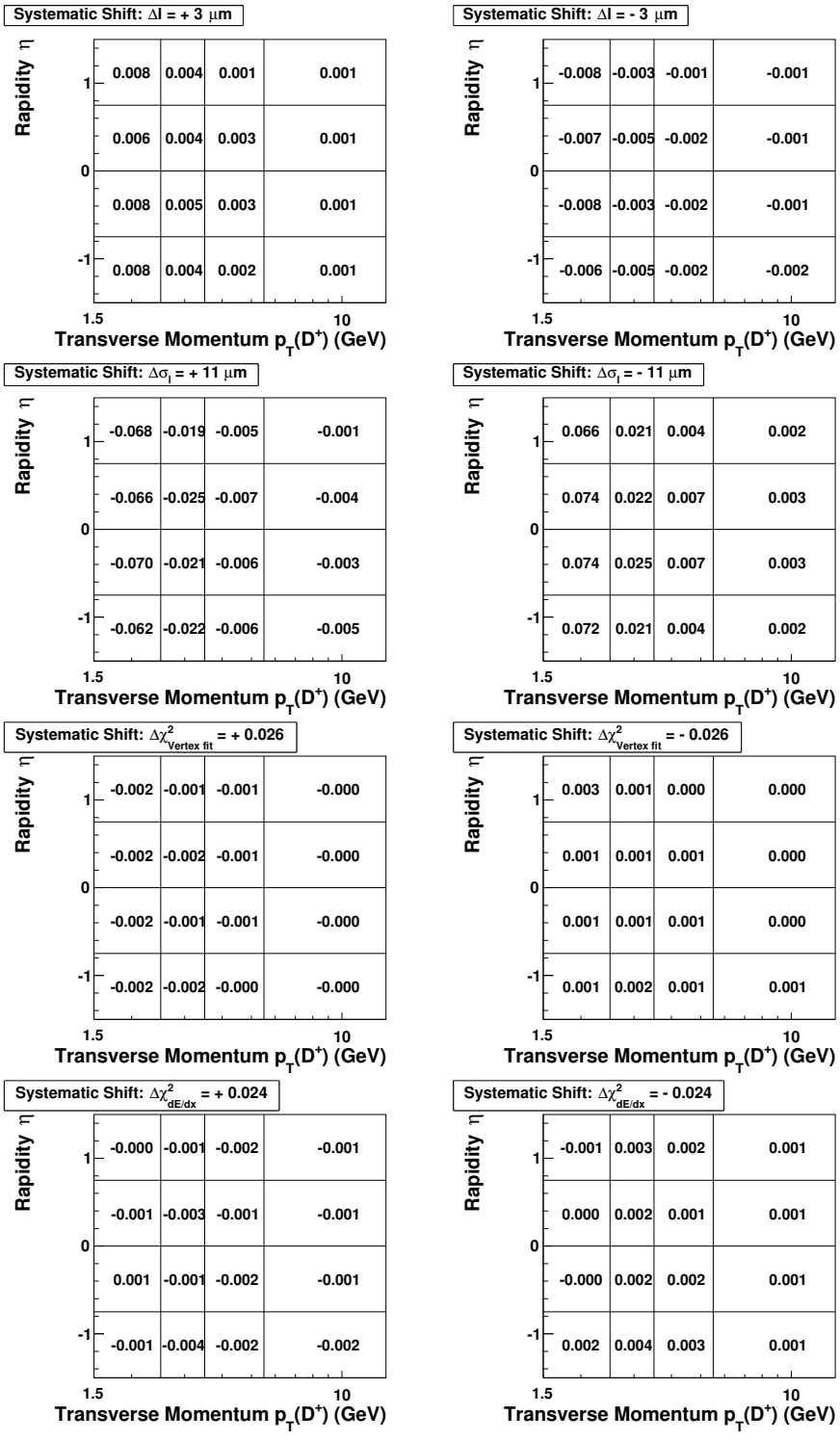

Figure 11.2: Double differential reconstruction efficiency uncertainty for p_{T} and rapidity.

11.2 Mass Distributions

In this section the mass distribution which have been used for the derivation of the cross sections are shown. The distributions for the right charged candidates are located on the left, the distributions for the wrong charge candidates are on the right. The solid lines indicate the result of the fit of the model parameter to the distribution. The fit result is used to derive the number of $D^{\pm}$ mesons (section 6.6).

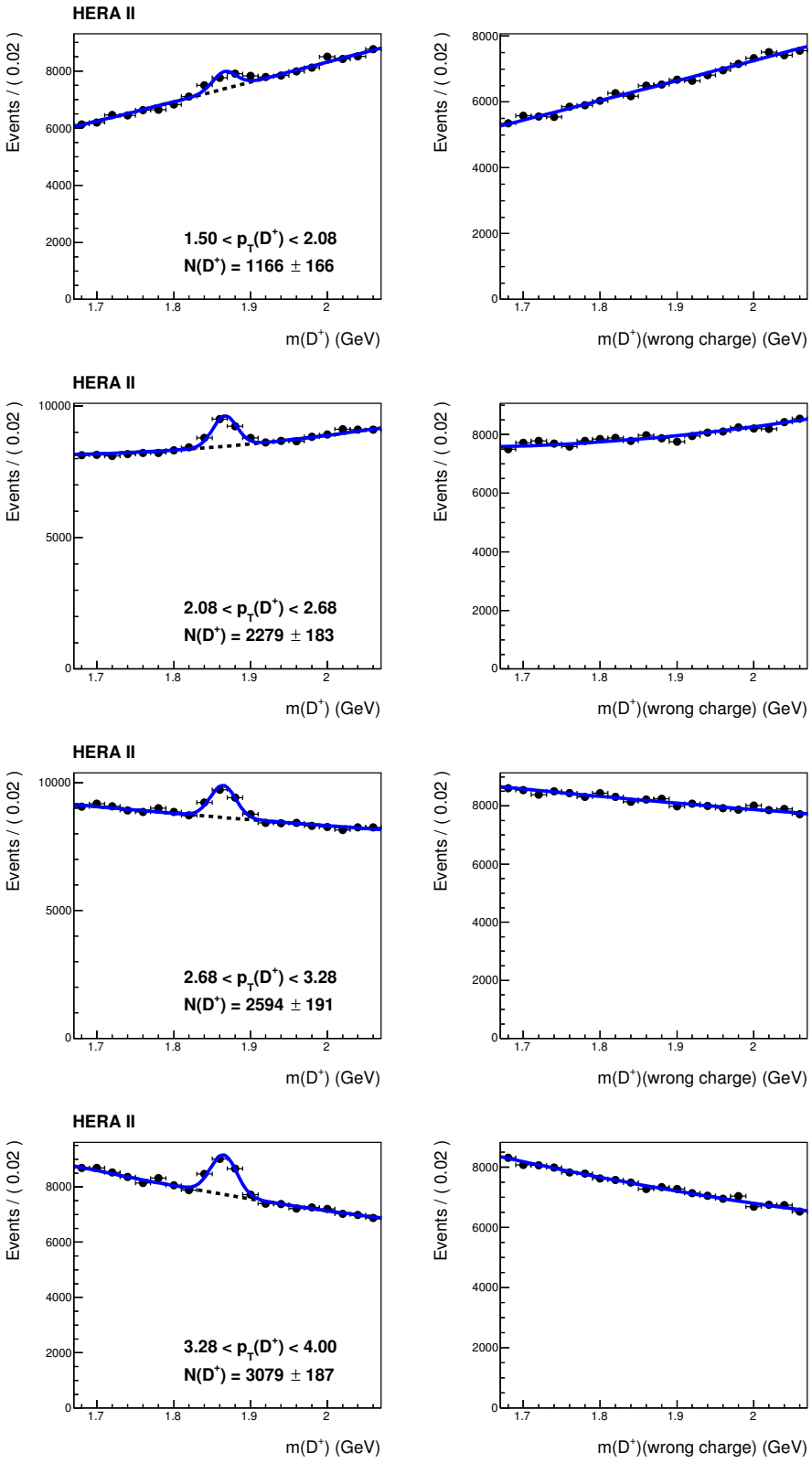

Figure 11.3: $D^{\pm}$ Mass Distributions in bins of the transverse momentum in the range $1.5\,\text{GeV} < p_{\text{T}}(D^{\pm}) < 4.0\,\text{GeV}$.

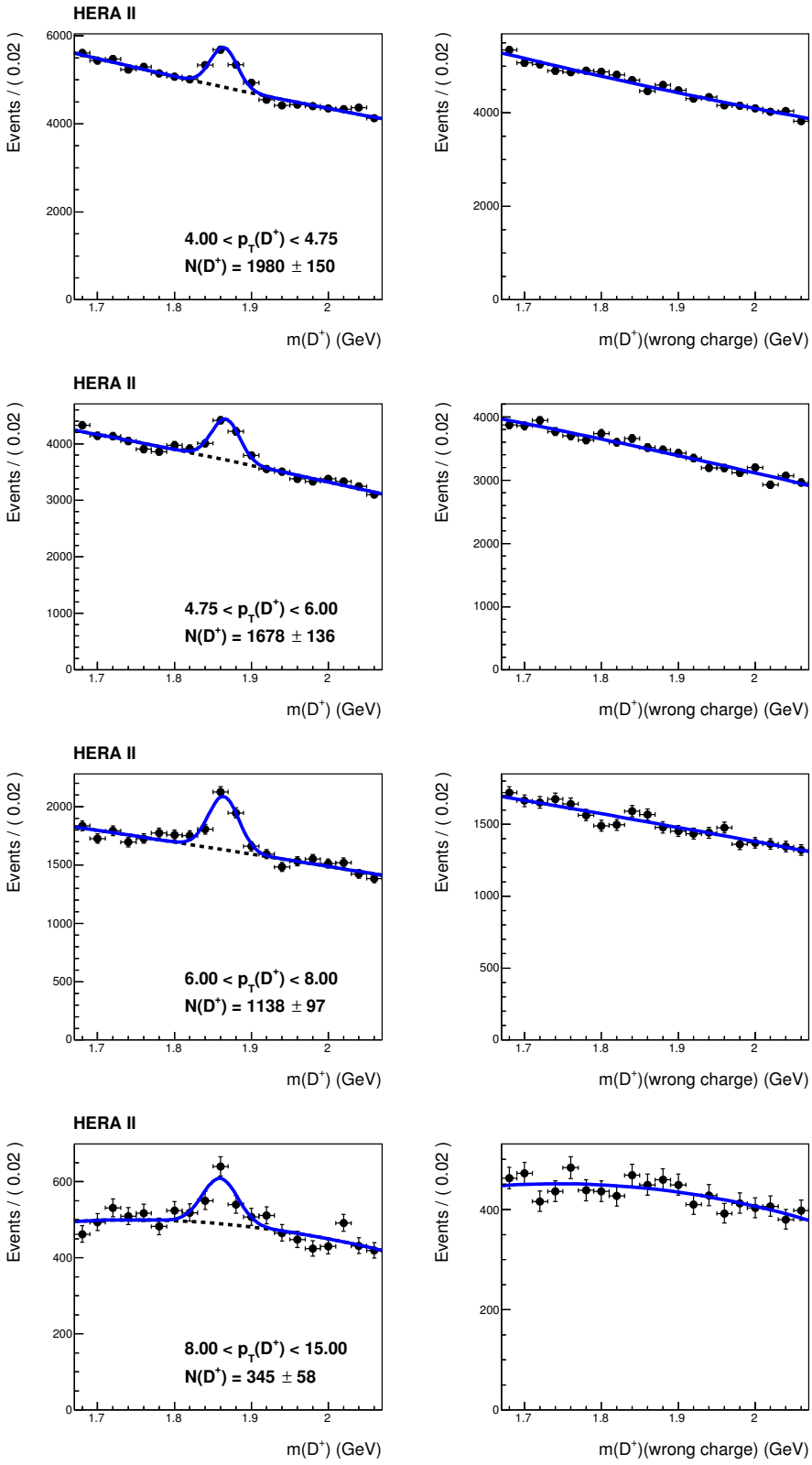

Figure 11.4: $D^{\pm}$ Mass Distributions in bins of the transverse momentum in the range $4.0\,\mathrm{GeV} < p_{\mathrm{T}}(D^{\pm}) < 14.0\,\mathrm{GeV}$.

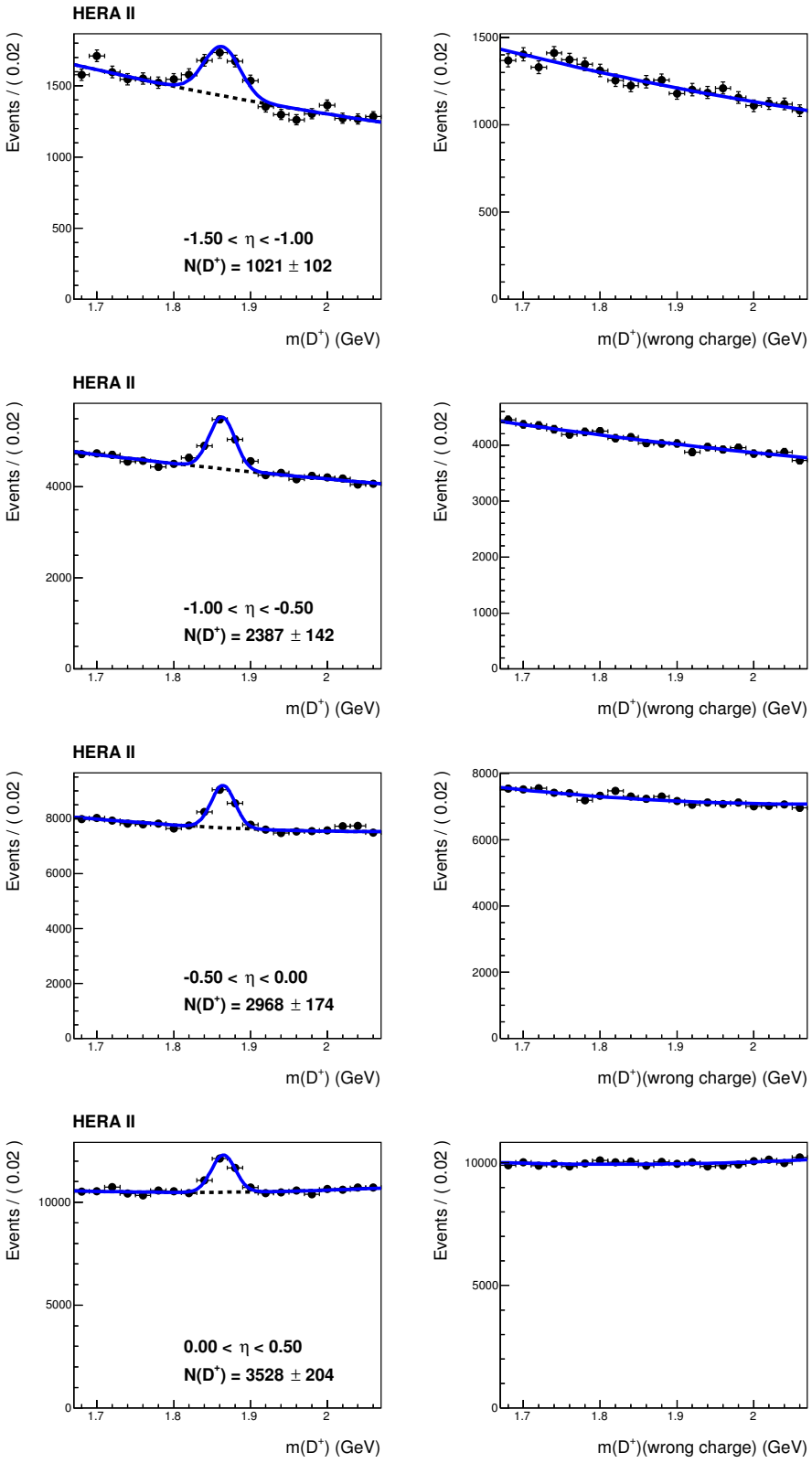

Figure 11.5: $D^{\pm}$ Mass Distributions in bins of the rapidity in the range $-1.5 < \eta(D^{\pm})(D^{\pm}) < 0.5$.

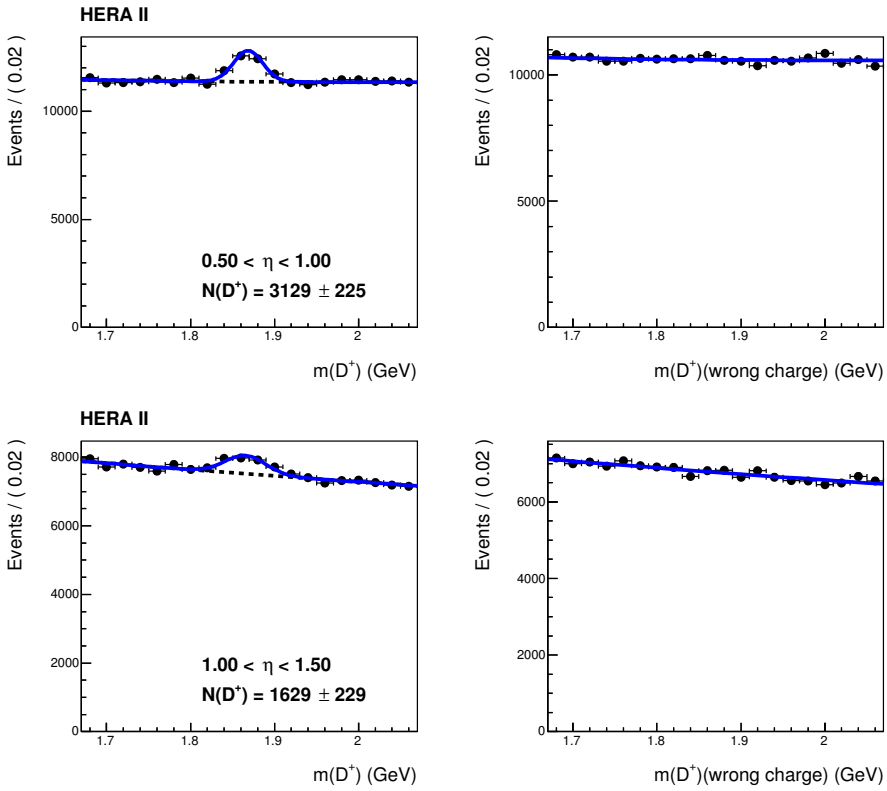

Figure 11.6: $D^{\pm}$ Mass Distributions in bins of the rapidity in the range $0.5 < \eta(D^{\pm})(D^{\pm}) < 1.5$.

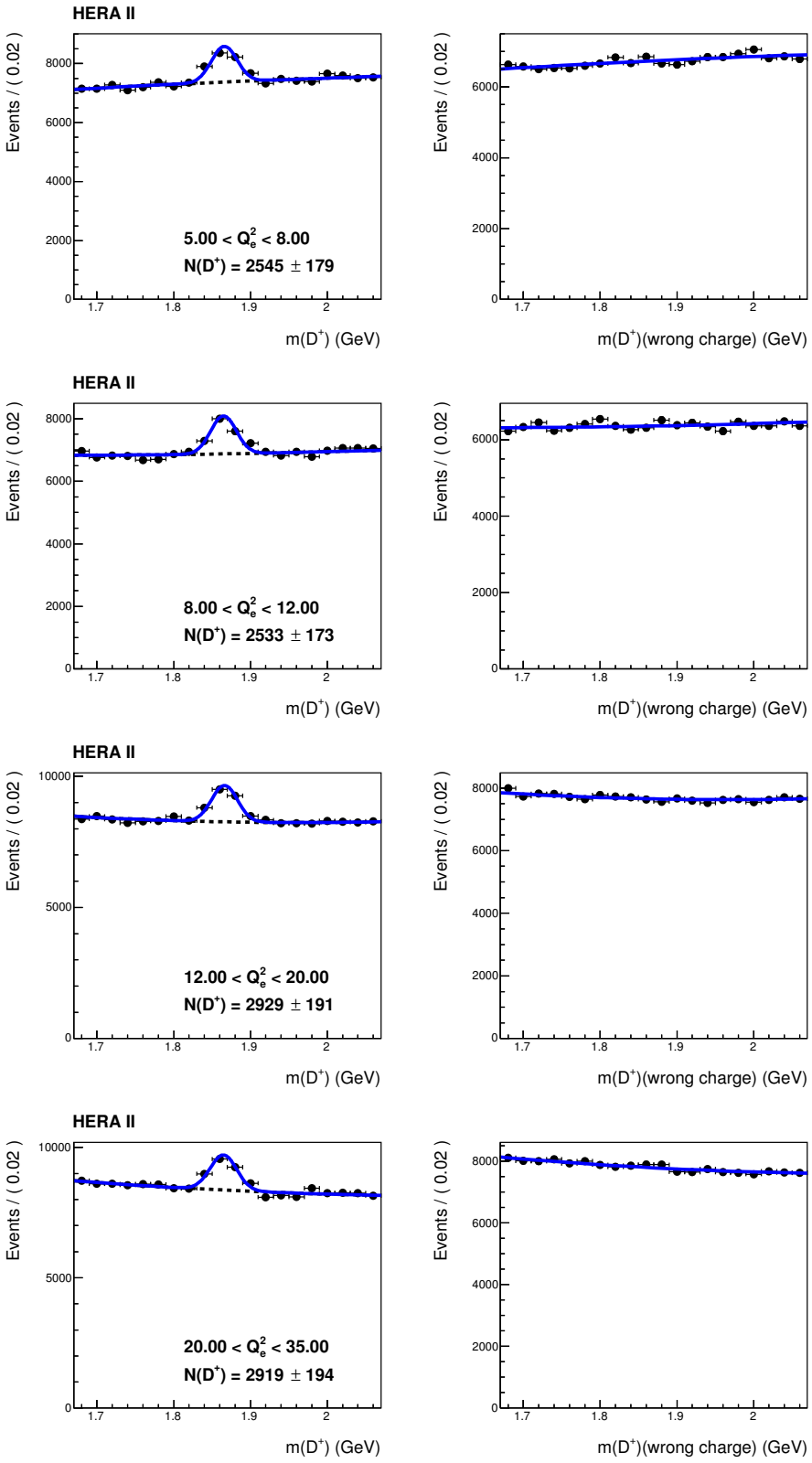

Figure 11.7: $D^{\pm}$ Mass Distributions in bins of Q^2 in the range $5\,\mathrm{GeV}^2 < Q^2 < 35\,\mathrm{GeV}^2$.

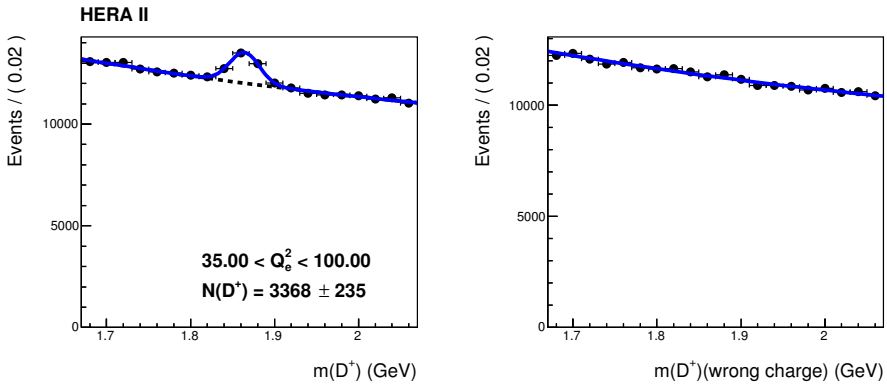

Figure 11.8: $D^{\pm}$ Mass Distributions in bins of Q^2 in the range $35\,\mathrm{GeV}^2 < Q^2 < 100\,\mathrm{GeV}^2$.

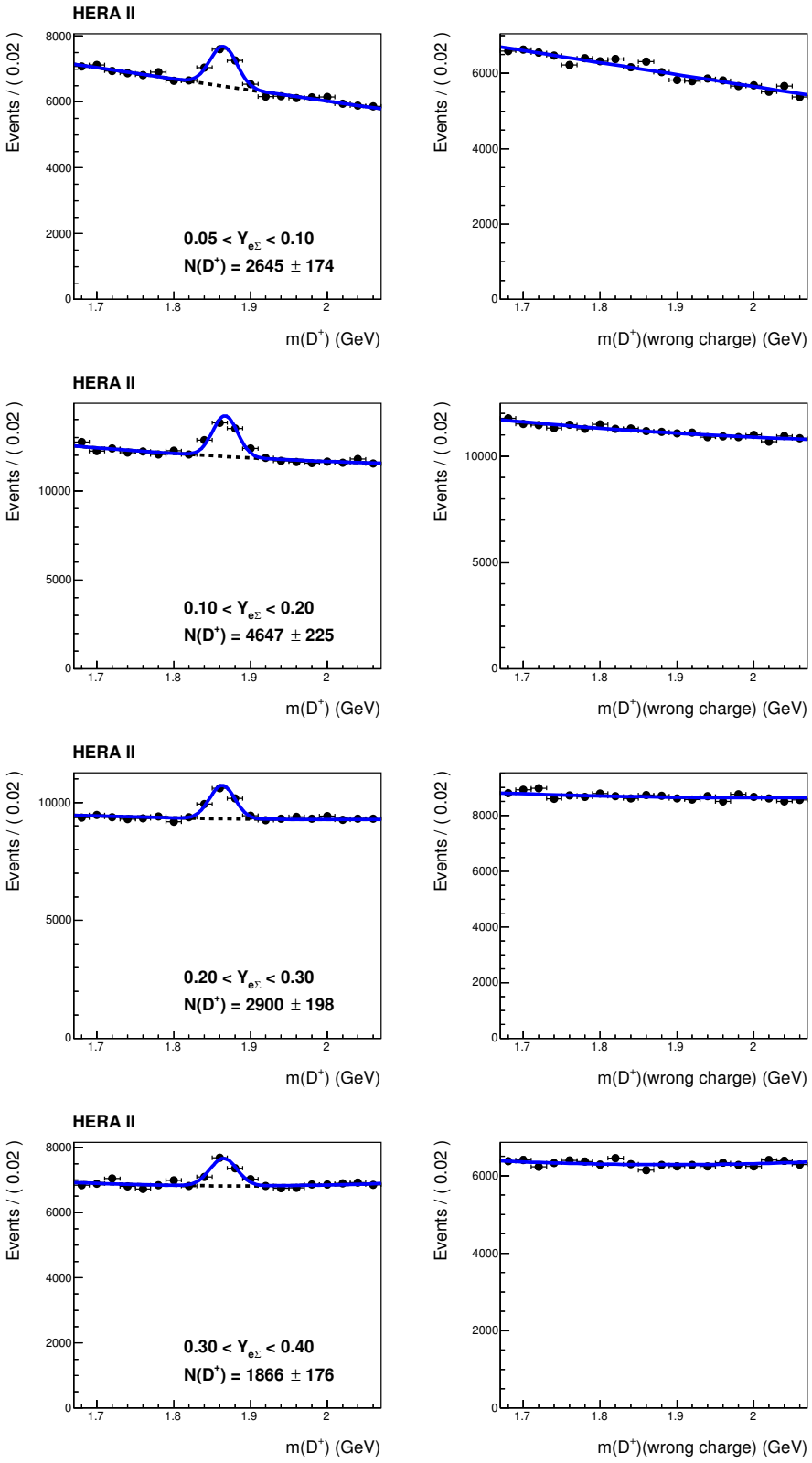

Figure 11.9: $D^{\pm}$ Mass Distributions in bins of the inelasticity y in the range $0.05 < y < 0.4$.

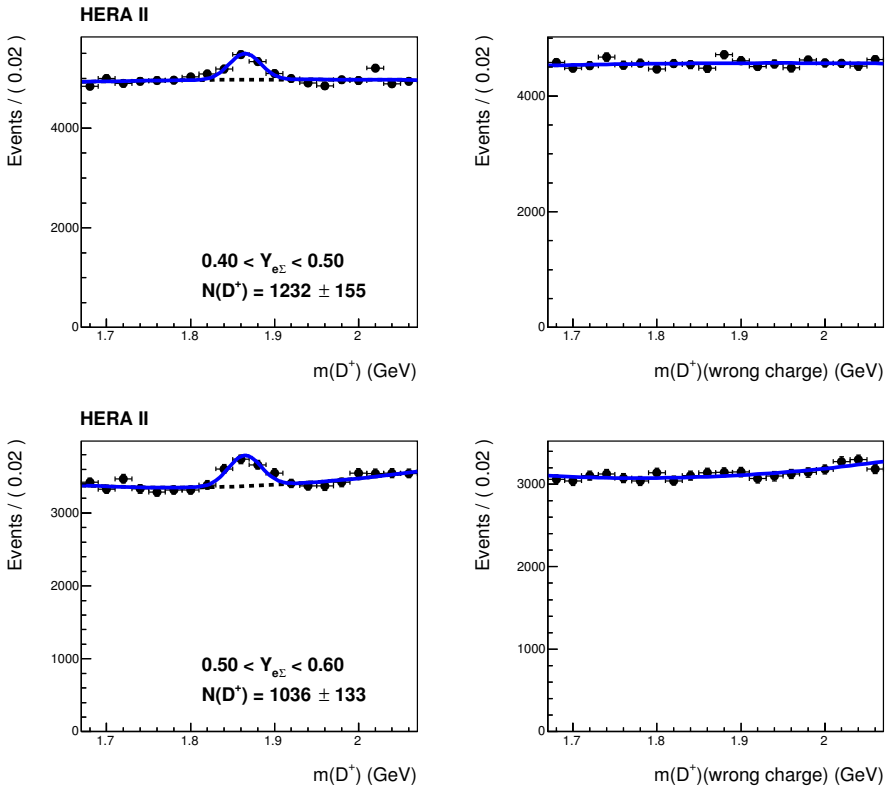

Figure 11.10: $D^{\pm}$ Mass Distributions in bins of the inelasticity y in the range $0.4 < y < 0.6$.

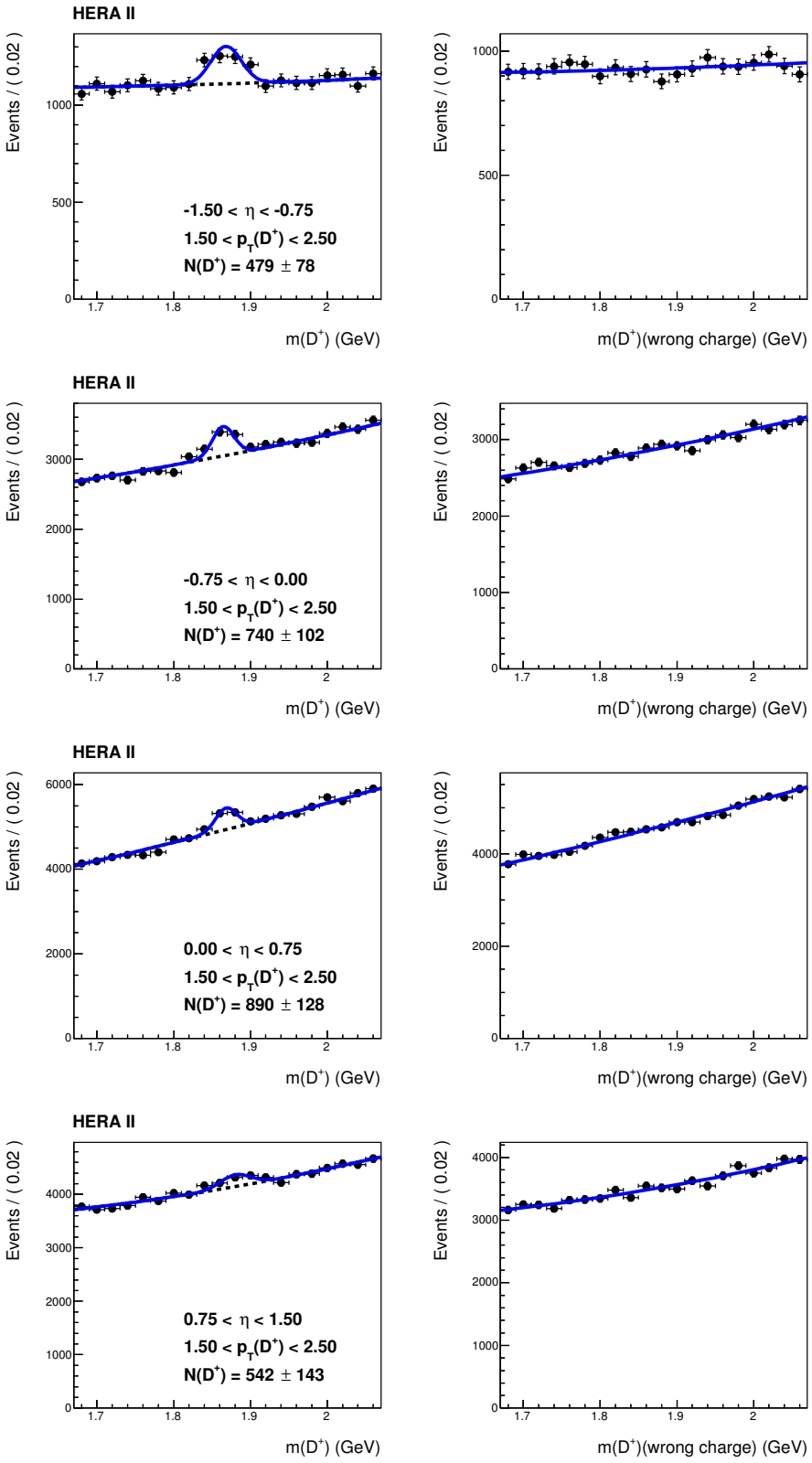

Figure 11.11: $D^{\pm}$ Mass Distributions in bins of the rapidity in the range $-1.5 < \eta(D^{\pm}) < 1.5$ for transverse momenta $1.5\,\mathrm{GeV} < \mathrm{p_T(D^{\pm})} < 2.5\,\mathrm{GeV}$.

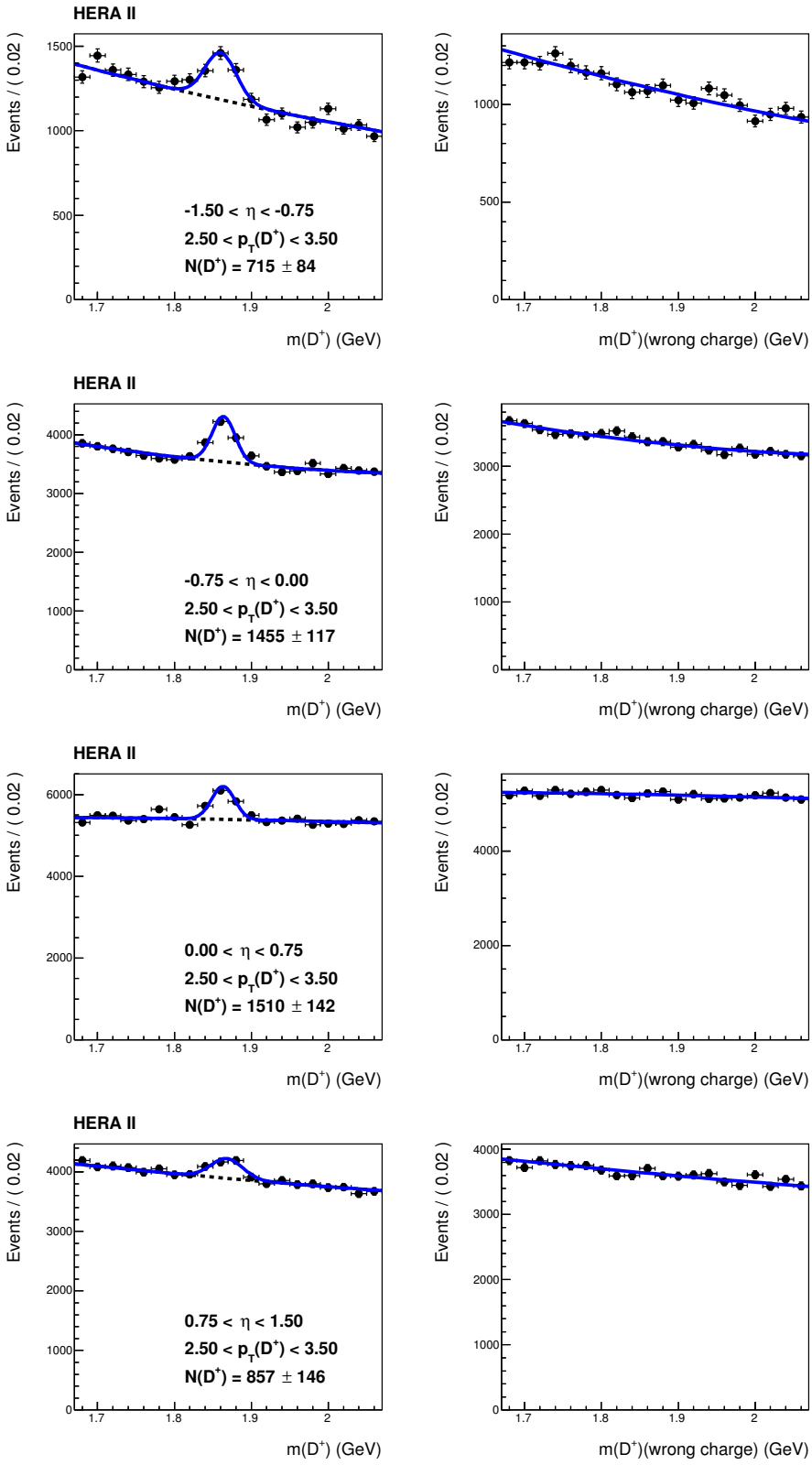

Figure 11.12: $D^{\pm}$ Mass Distributions in bins of the rapidity in the range $-1.5 < \eta(D^{\pm}) < 1.5$ for transverse momenta $2.5\,\mathrm{GeV} < \mathrm{p_T(D^{\pm})} < 3.5\,\mathrm{GeV}$.

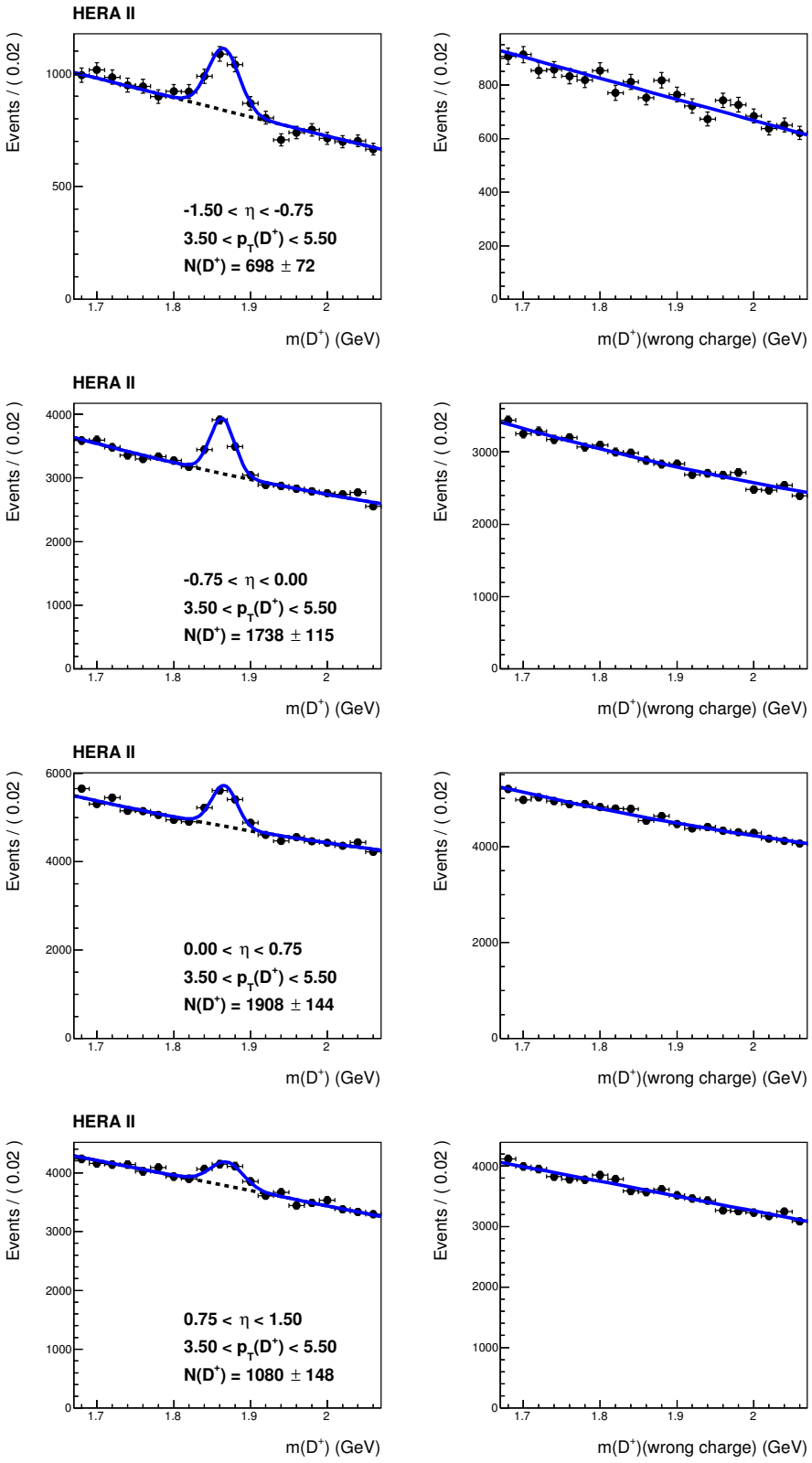

Figure 11.13: $D^{\pm}$ Mass Distributions in bins of the rapidity in the range $-1.5 < \eta(D^{\pm}) < 1.5$ for transverse momenta $3.5\,\mathrm{GeV} < \mathrm{p_T(D^{\pm})} < 5.5\,\mathrm{GeV}$.

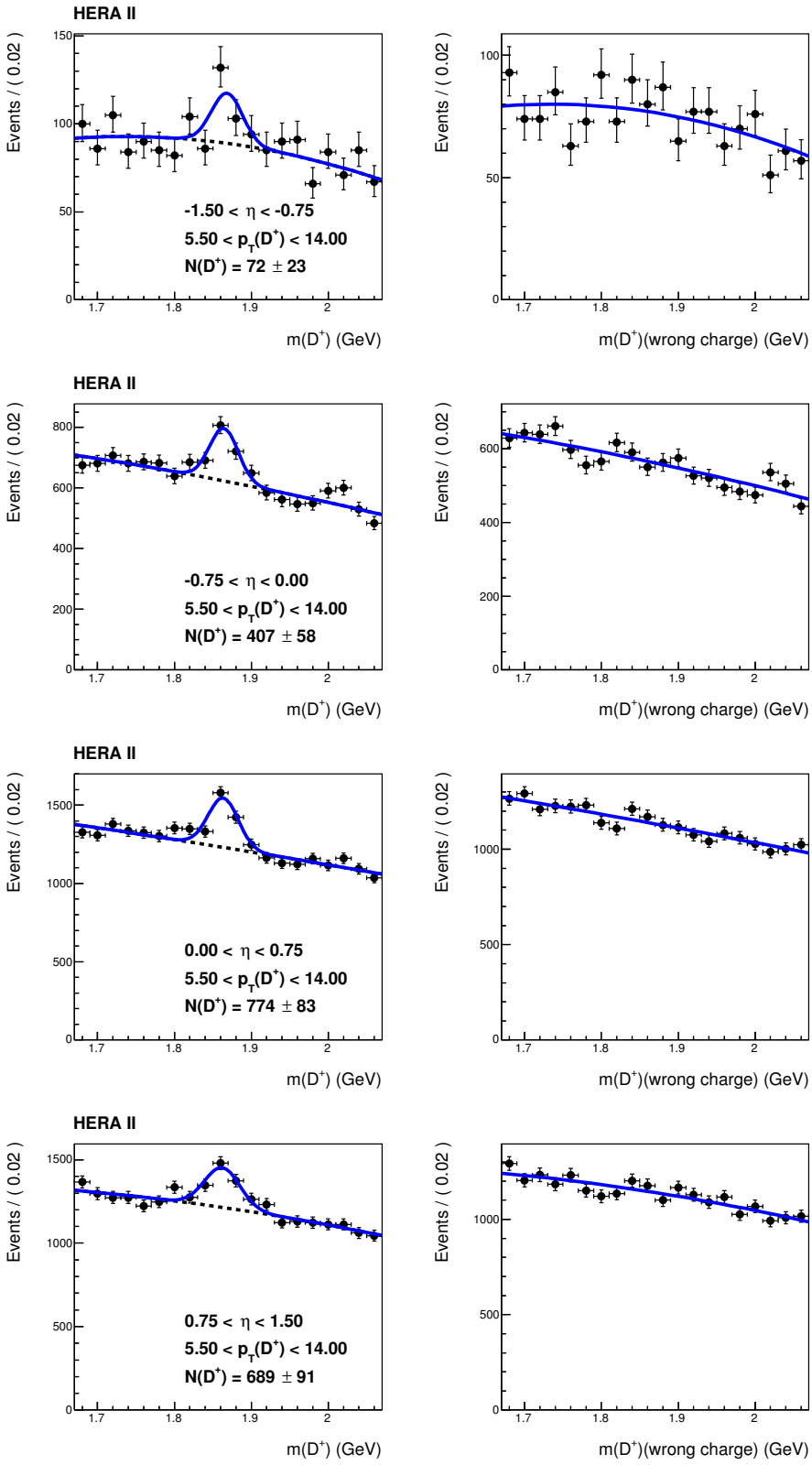

Figure 11.14: $D^{\pm}$ Mass Distributions in bins of the rapidity in the range $-1.5 < \eta(D^{\pm}) < 1.5$ for transverse momenta $5.5\,\mathrm{GeV} < \mathrm{p_T(D^{\pm})} < 14\,\mathrm{GeV}$.

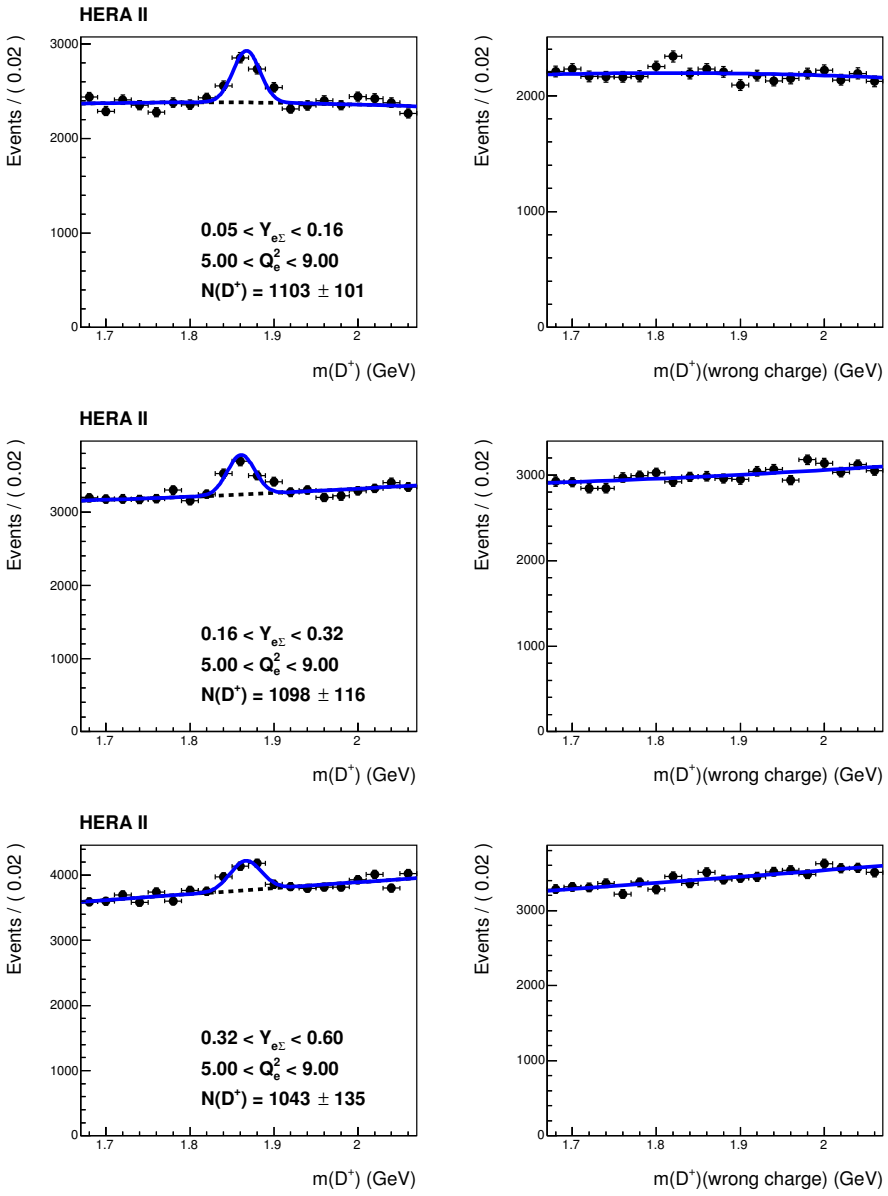

Figure 11.15: $D^{\pm}$ Mass Distributions in bins of the inelasticity y in the range $0.05 < y < 0.6$ and $5\,\mathrm{GeV}^2 < Q^2 < 9\,\mathrm{GeV}^2$.

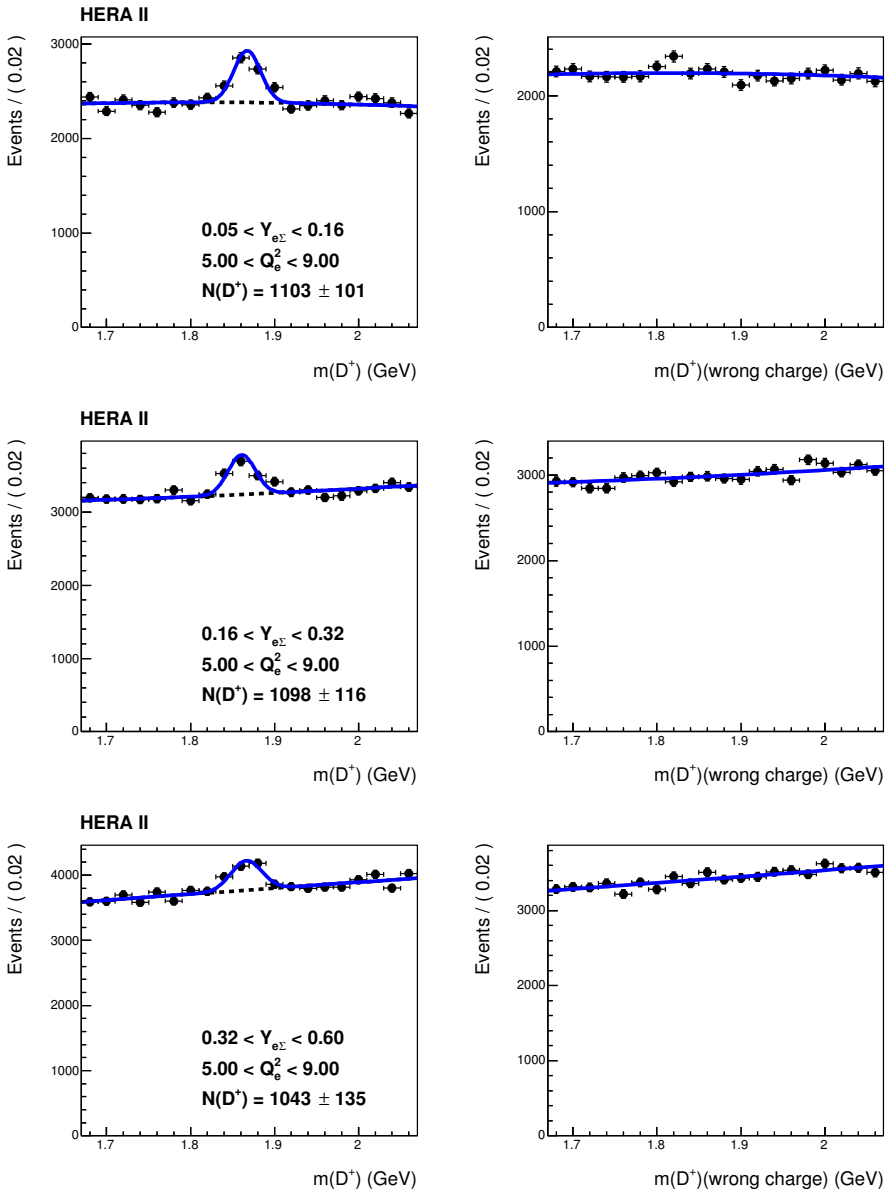

Figure 11.16: $D^{\pm}$ Mass Distributions in bins of the inelasticity y in the range $0.05 < y < 0.6$ and $9\,\mathrm{GeV}^2 < Q^2 < 14\,\mathrm{GeV}^2$.

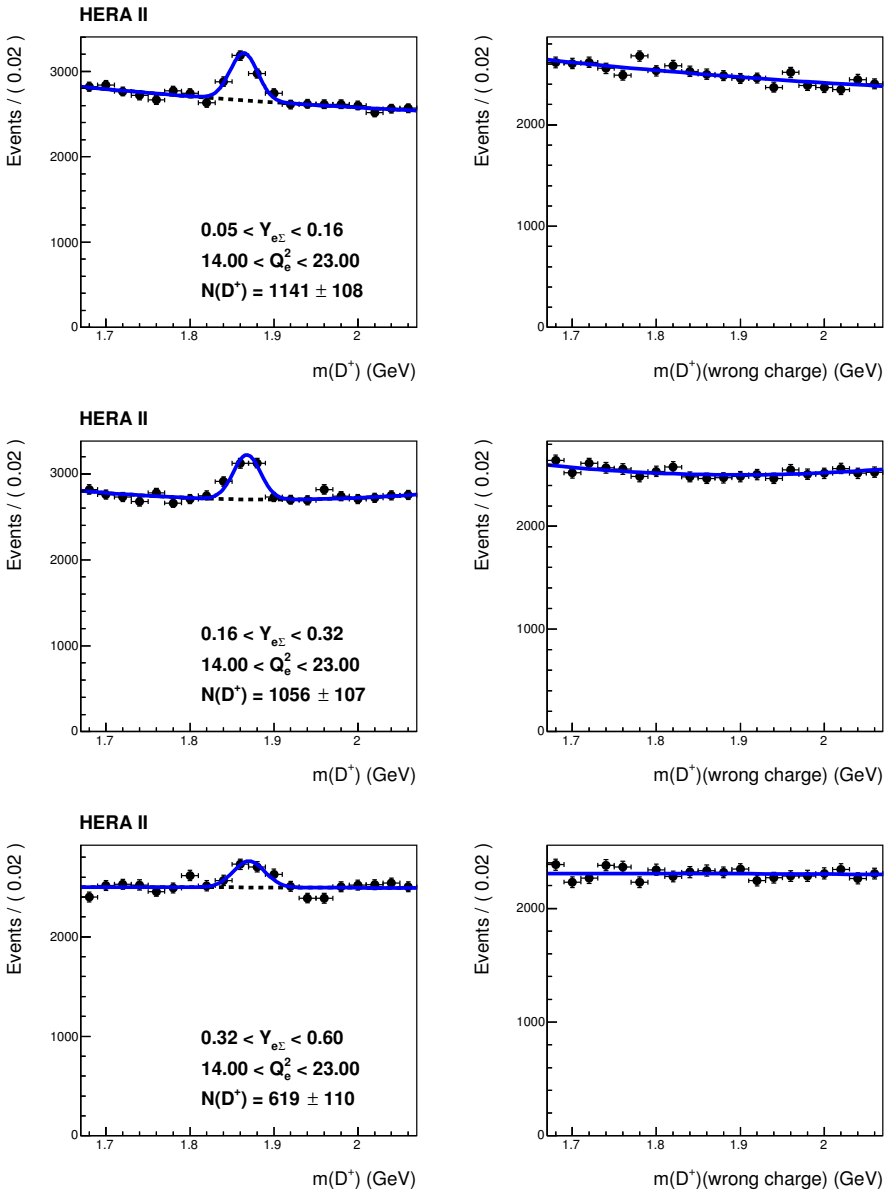

Figure 11.17: $D^{\pm}$ Mass Distributions in bins of the inelasticity y in the range $0.05 < y < 0.6$ and $14\,\mathrm{GeV}^2 < Q^2 < 23\,\mathrm{GeV}^2$.

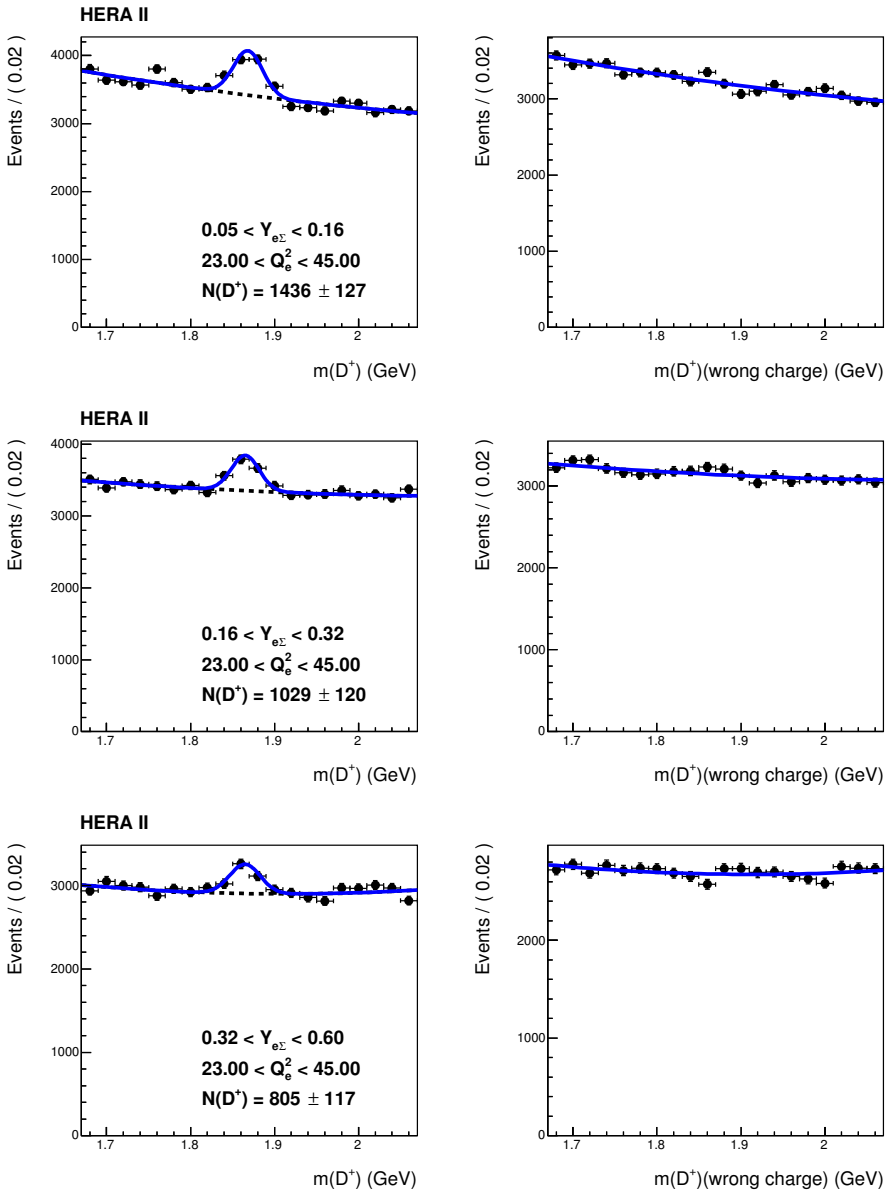

Figure 11.18: $D^{\pm}$ Mass Distributions in bins of the inelasticity y in the range $0.05 < y < 0.6$ and $23\,\mathrm{GeV}^2 < Q^2 < 45\,\mathrm{GeV}^2$.

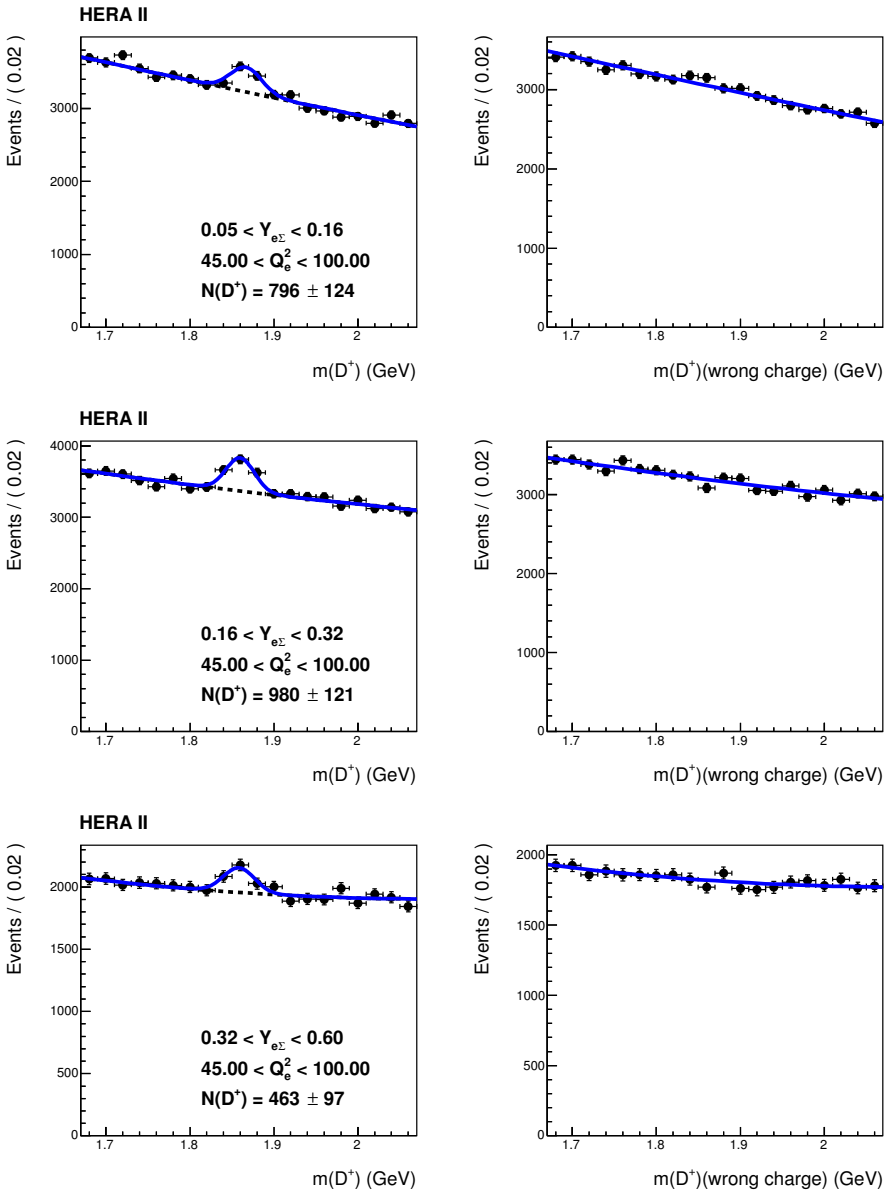

Figure 11.19: $D^{\pm}$ Mass Distributions in bins of the inelasticity y in the range $0.05 < y < 0.6$ and $45\,\mathrm{GeV}^2 < Q^2 < 100\,\mathrm{GeV}^2$.

11.3 Cross Section Tables

$p_T(D^{\pm})$ $[GeV]$	$d\sigma/dp_T$ $[nb/GeV]$	δ(stat.) [%]	δ(syst.) [%]	$\delta(l)$ [%]	$\delta(\sigma_l)$ [%]	$\delta(\chi^2_{\text{Fit}})$ [%]	$\delta(\chi^2_{\text{dEdx}})$ [%]	$\delta(E_{e'})$ [%]	$\delta(\Theta_{e'})$ [%]	δ(Model) [%]
1.50 - 2.08	2.216	14.2	+10.3	0.8	8.7	0.2	0.1	0.1	1.2	0.0
			−10.7	0.8	9.1	0.1	0.1	0.2	1.1	0.0
2.08 - 2.68	1.885	8.0	+7.1	0.6	4.5	0.2	0.1	0.0	0.9	0.1
			−7.3	0.6	4.9	0.1	0.1	0.0	0.7	0.1
2.68 - 3.28	1.207	7.3	+5.8	0.4	2.1	0.1	0.2	0.3	0.5	0.1
			−5.8	0.4	2.2	0.1	0.3	0.1	0.7	0.1
3.28 - 4.00	0.903	6.1	+5.5	0.3	1.0	0.1	0.2	0.1	0.6	0.2
			−5.5	0.3	1.1	0.1	0.3	0.2	0.5	0.2
4.00 - 4.75	0.464	7.6	+5.4	0.2	0.6	0.1	0.2	0.2	0.4	0.3
			−5.4	0.2	0.5	0.1	0.2	0.0	0.4	0.3
4.75 - 6.00	0.202	8.1	+5.4	0.1	0.4	0.0	0.2	0.0	0.2	0.1
			−5.4	0.2	0.3	0.1	0.1	0.2	0.3	0.1
6.00 - 8.00	0.083	8.5	+5.4	0.1	0.2	0.0	0.0	0.2	0.2	0.3
			−5.4	0.1	0.2	0.0	0.1	0.2	0.2	0.3
8.00 - 15.00	0.007	16.8	+5.5	0.0	0.4	0.0	0.2	0.3	0.1	1.3
			−5.6	0.1	0.4	0.0	0.1	0.6	0.4	1.3

Table 11.1: The differential $D^{\pm}$ meson production cross section as a function of the transverse momentum p_T. The total systematic uncertainty includes contributions from other sources not listed in the table (cf. 8.4)

Rapidity	$d\sigma/d\eta$ $[nb]$	δ(stat.) [%]	δ(syst.) [%]	$\delta(l)$ [%]	$\delta(\sigma_l)$ [%]	$\delta(\chi^2_{\text{Fit}})$ [%]	$\delta(\chi^2_{\text{dEdx}})$ [%]	$\delta(E_{e'})$ [%]	$\delta(\Theta_{e'})$ [%]	δ(Model) [%]
-1.50 - -1.00	1.149	10.0	+6.3	0.4	2.5	0.1	0.2	2.0	1.0	0.1
			−6.3	0.4	2.5	0.2	0.2	1.8	1.1	0.1
-1.00 - -0.50	1.591	5.9	+6.0	0.4	2.4	0.1	0.1	0.8	0.8	0.0
			−6.1	0.4	2.7	0.1	0.2	0.8	0.8	0.0
-0.50 - 0.00	1.756	5.9	+5.9	0.4	2.4	0.1	0.1	0.5	0.6	0.0
			−6.0	0.3	2.5	0.1	0.1	0.4	0.7	0.0
0.00 - 0.50	2.131	5.8	+5.9	0.3	2.4	0.1	0.1	0.1	0.4	0.1
			−5.9	0.4	2.4	0.1	0.1	0.1	0.4	0.1
0.50 - 1.00	1.921	7.2	+5.8	0.3	2.0	0.1	0.2	0.7	0.4	0.1
			−5.8	0.4	2.0	0.1	0.2	0.7	0.3	0.1
1.00 - 1.50	1.366	14.1	+5.9	0.3	1.5	0.0	0.1	2.0	0.4	0.3
			−5.9	0.2	1.6	0.1	0.2	1.9	0.2	0.3

Table 11.2: The differential $D^{\pm}$ meson production cross section as a function of the rapidity $\eta(D^{\pm})$. The total systematic uncertainty includes contributions from other sources not listed in the table (cf. 8.4)

Q^2 $[GeV^2]$	$d\sigma/dQ^2$ $[nb/GeV^2]$	δ(stat.) [%]	δ(syst.) [%]	$\delta(l)$ [%]	$\delta(\sigma_l)$ [%]	$\delta(\chi^2_{\text{Fit}})$ [%]	$\delta(\chi^2_{\text{dEdx}})$ [%]	$\delta(E_{e'})$ [%]	$\delta(\Theta_{e'})$ [%]	δ(Model) [%]
5.00 - 8.00	0.392	7.0	$+6.2$	0.5	2.9	0.2	0.1	1.0	0.5	0.3
			-6.4	0.4	3.3	0.1	0.2	0.8	0.7	0.3
8.00 - 12.00	0.245	6.8	$+6.1$	0.4	2.9	0.1	0.1	0.3	0.6	0.0
			-6.2	0.4	3.0	0.1	0.2	0.1	1.2	0.0
12.00 - 20.00	0.123	6.5	$+6.0$	0.4	2.5	0.1	0.1	0.1	0.8	0.1
			-6.0	0.4	2.5	0.1	0.2	0.2	0.7	0.1
20.00 - 35.00	0.056	6.6	$+5.7$	0.3	1.9	0.1	0.1	0.2	0.6	0.2
			-5.8	0.3	2.0	0.1	0.1	0.1	0.8	0.2
35.00 - 100.00	0.013	7.0	$+5.7$	0.3	1.4	0.1	0.2	0.9	1.0	0.0
			-5.7	0.3	1.4	0.1	0.2	1.0	0.8	0.0

Table 11.3: The differential $D^{\pm}$ meson production cross section as a function of the photon virtuality Q^2. The total systematic uncertainty includes contributions from other sources not listed in the table (cf. 8.4)

y	$d\sigma/dy$ $[nb]$	δ(stat.) [%]	δ(syst.) [%]	$\delta(l)$ [%]	$\delta(\sigma_l)$ [%]	$\delta(\chi^2_{\mathrm{Fit}})$ [%]	$\delta(\chi^2_{\mathrm{dEdx}})$ [%]	$\delta(E_{e'})$ [%]	$\delta(\Theta_{e'})$ [%]	δ(Model) [%]
0.05 - 0.10	19.718	6.6	+6.1	0.4	2.4	0.1	0.2	1.7	0.4	0.0
			−6.1	0.3	2.5	0.1	0.2	1.2	0.3	0.0
0.10 - 0.20	14.890	4.8	+5.9	0.4	2.3	0.1	0.1	0.6	0.5	0.0
			−6.0	0.4	2.4	0.1	0.1	0.8	0.4	0.0
0.20 - 0.30	9.137	6.8	+5.9	0.4	2.3	0.1	0.1	0.2	0.5	0.0
			−5.9	0.3	2.4	0.1	0.2	0.5	0.7	0.0
0.30 - 0.40	6.180	9.4	+5.8	0.5	2.1	0.1	0.2	0.4	0.7	0.2
			−5.9	0.3	2.3	0.1	0.2	0.6	0.9	0.2
0.40 - 0.50	4.369	12.6	+6.3	0.3	2.1	0.1	0.2	2.5	0.9	0.1
			−5.9	0.3	2.1	0.1	0.2	1.1	0.6	0.1
0.50 - 0.60	3.989	12.8	+5.8	0.3	1.8	0.1	0.2	0.7	1.1	0.1
			−5.9	0.3	2.0	0.1	0.1	1.4	0.9	0.1

Table 11.4: The differential $D^{\pm}$ meson production cross section as a function of the inelasticity y. The total systematic uncertainty includes contributions from other sources not listed in the table (cf. 8.4)

$p_T(D^{\pm})$ [GeV]	Rapidity	$\frac{d^2\sigma}{dp_T\eta}$ [nb/GeV]	δ(stat.) [%]	δ(syst.) [%]	$\delta(l)$ [%]	$\delta(\sigma_l)$ [%]	$\delta(\chi^2_{\text{Fit}})$ [%]	$\delta(\chi^2_{\text{dEdx}})$ [%]	$\delta(E_{e'})$ [%]	$\delta(\Theta_{e'})$ [%]	δ(Model) [%]
1.5 - 2.5	-1.50 - -0.75	0.634	16.4	+8.5	0.8	6.2	0.2	0.1	1.4	1.5	0.1
				−9.2	0.6	7.2	0.1	0.2	1.5	1.3	0.1
1.5 - 2.5	-0.75 - 0.00	0.657	13.8	+9.0	0.8	7.0	0.2	0.1	0.8	1.0	0.2
				−9.2	0.8	7.4	0.1	0.0	0.6	0.9	0.2
1.5 - 2.5	0.00 - 0.75	0.819	14.4	+8.6	0.6	6.6	0.2	0.1	0.5	1.0	0.1
				−9.1	0.7	7.4	0.1	0.0	0.3	0.7	0.1
1.5 - 2.5	0.75 - 1.50	0.904	26.4	+9.0	0.8	6.8	0.2	0.0	2.1	0.9	0.1
				−8.7	0.8	6.6	0.3	0.1	1.9	0.4	0.1
2.5 - 3.5	-1.50 - -0.75	0.345	11.7	+6.1	0.4	2.2	0.2	0.4	1.6	0.8	0.0
				−6.0	0.5	2.1	0.2	0.4	1.2	1.2	0.0
2.5 - 3.5	-0.75 - 0.00	0.486	8.1	+5.8	0.5	2.1	0.1	0.1	0.4	0.7	0.0
				−6.0	0.3	2.5	0.1	0.2	0.6	0.8	0.0
2.5 - 3.5	0.00 - 0.75	0.518	9.4	+5.9	0.4	2.5	0.2	0.3	0.2	0.2	0.0
				−5.8	0.5	2.2	0.1	0.2	0.1	0.5	0.0
2.5 - 3.5	0.75 - 1.50	0.437	17.0	+6.1	0.4	1.9	0.1	0.1	2.2	0.5	0.0
				−6.1	0.3	2.1	0.1	0.3	1.9	0.4	0.0
3.5 - 5.5	-1.50 - -0.75	0.220	10.2	+5.6	0.2	0.6	0.0	0.2	1.2	0.5	0.5
				−5.5	0.2	0.4	0.1	0.3	0.9	0.6	0.5
3.5 - 5.5	-0.75 - 0.00	0.406	6.6	+5.4	0.3	0.6	0.1	0.2	0.4	0.5	0.0
				−5.4	0.2	0.7	0.1	0.2	0.4	0.5	0.0
3.5 - 5.5	0.00 - 0.75	0.419	7.6	+5.4	0.3	0.7	0.1	0.1	0.0	0.3	0.3
				−5.4	0.2	0.7	0.1	0.1	0.1	0.1	0.3
3.5 - 5.5	0.75 - 1.50	0.320	13.7	+5.5	0.1	0.5	0.1	0.2	1.2	0.4	0.4
				−5.6	0.1	0.4	0.0	0.2	1.5	0.2	0.4
5.5 - 14.0	-1.50 - -0.75	0.021	31.6	+6.0	0.1	0.5	0.0	0.2	2.1	0.7	1.6
				−6.3	0.2	0.2	0.1	0.1	2.8	0.7	1.6
5.5 - 14.0	-0.75 - 0.00	0.080	14.1	+5.5	0.1	0.3	0.0	0.1	0.9	0.3	1.0
				−5.5	0.1	0.3	0.0	0.1	0.7	0.5	1.0
5.5 - 14.0	0.00 - 0.75	0.119	10.7	+5.4	0.1	0.4	0.0	0.1	0.1	0.1	0.1
				−5.4	0.1	0.3	0.0	0.1	0.0	0.4	0.1
5.5 - 14.0	0.75 - 1.50	0.127	13.2	+5.5	0.1	0.1	0.0	0.1	1.2	0.1	0.1
				−5.5	0.1	0.2	0.0	0.1	1.0	0.1	0.1

Table 11.5: The double differential $D^{\pm}$ meson production cross section as a function of transverse momentum p_T and rapidity η. The total systematic uncertainty includes contributions from other sources not listed in the table (cf. 8.4)

Q^2 $[GeV^2]$	y	$\frac{d^2\sigma}{dQ^2y}$ $[nb/GeV^2]$	δ(stat.) [%]	δ(syst.) [%]	$\delta(l)$ [%]	$\delta(\sigma_l)$ [%]	$\delta(\chi^2_{\text{Fit}})$ [%]	$\delta(\chi^2_{\text{dEdx}})$ [%]	$\delta(E_{e'})$ [%]	$\delta(\Theta_{e'})$ [%]	δ(Model) [%]
5.0 - 9.0	0.05 - 0.16	5.081	9.2	+6.4	0.5	3.3	0.2	0.1	1.0	0.9	0.0
				−6.8	0.5	3.5	0.1	0.1	0.3	2.2	0.0
5.0 - 9.0	0.16 - 0.32	2.819	10.6	+6.1	0.4	2.9	0.1	0.1	0.3	0.7	0.2
				−6.3	0.4	3.2	0.1	0.2	0.7	0.2	0.2
5.0 - 9.0	0.32 - 0.60	1.507	12.9	+6.1	0.5	2.4	0.1	0.2	1.5	0.8	0.6
				−6.4	0.4	2.8	0.2	0.3	1.8	0.8	0.6
9.0 - 14.0	0.05 - 0.16	4.441	7.7	+6.4	0.4	3.1	0.1	0.1	1.8	0.0	0.0
				−6.3	0.4	3.0	0.1	0.1	0.3	1.3	0.0
9.0 - 14.0	0.16 - 0.32	1.692	12.6	+6.3	0.5	2.8	0.1	0.2	1.1	1.5	0.0
				−6.2	0.4	3.1	0.1	0.3	0.3	0.6	0.0
9.0 - 14.0	0.32 - 0.60	1.007	15.8	+6.1	0.4	2.7	0.1	0.1	1.0	0.2	0.0
				−6.2	0.4	2.4	0.1	0.1	1.9	0.8	0.0
14.0 - 23.0	0.05 - 0.16	3.576	9.4	+6.1	0.3	2.3	0.1	0.0	1.3	1.1	0.0
				−6.1	0.3	2.5	0.1	0.1	0.8	0.9	0.0
14.0 - 23.0	0.16 - 0.32	1.954	10.1	+5.9	0.5	2.4	0.1	0.1	0.7	0.4	0.0
				−6.1	0.4	2.5	0.1	0.2	0.5	1.3	0.0
14.0 - 23.0	0.32 - 0.60	0.770	17.8	+6.3	0.4	2.3	0.1	0.2	1.8	1.5	0.3
				−5.9	0.3	2.3	0.1	0.1	0.0	0.9	0.3
23.0 - 45.0	0.05 - 0.16	3.748	8.8	+6.1	0.3	1.8	0.1	0.1	2.0	1.0	0.0
				−6.0	0.3	1.8	0.1	0.2	1.6	1.3	0.0
23.0 - 45.0	0.16 - 0.32	1.520	11.6	+5.7	0.3	1.9	0.1	0.1	0.4	0.6	0.1
				−5.8	0.3	1.9	0.1	0.2	0.1	1.0	0.1
23.0 - 45.0	0.32 - 0.60	0.905	14.6	+5.9	0.3	1.6	0.1	0.2	1.8	0.4	0.9
				−6.0	0.3	1.6	0.1	0.2	1.8	0.4	0.9
45.0 - 100.0	0.05 - 0.16	1.730	15.6	+6.0	0.2	1.2	0.0	0.2	2.3	0.9	0.0
				−6.2	0.3	1.3	0.1	0.2	2.7	0.6	0.0
45.0 - 100.0	0.16 - 0.32	1.480	12.3	+5.6	0.2	1.4	0.1	0.2	0.0	1.1	0.2
				−5.7	0.3	1.3	0.1	0.1	1.6	0.2	0.2
45.0 - 100.0	0.32 - 0.60	0.638	21.0	+5.7	0.3	1.2	0.0	0.3	0.0	1.3	0.9
				−5.9	0.2	1.5	0.1	0.2	1.2	1.3	0.9

Table 11.6: The double differential $D^{\pm}$ meson production cross section as a function of photon virtuality Q^2 and inelasticity y. The total systematic uncertainty includes contributions from other sources not listed in the table (cf. 8.4)

Bibliography

[1] F. Aaron, C. Alexa, V. Andreev, B. Antunovic, S. Aplin, et al. Measurement of the Inclusive ep Scattering Cross Section at Low Q^2 and x at HERA. *Eur. Phys. J.*, C63:625–678, 2009.

[2] F. Aaron et al. Combined Measurement and QCD Analysis of the Inclusive $e^{\pm}p$ Scattering Cross Sections at HERA. *JHEP*, 1001:109, 2010.

[3] F. Aaron et al. Measurement of $D^{*\pm}$ Meson Production and Determination of $F_2^{c\bar{c}}$ at low Q2 in Deep-Inelastic Scattering at HERA. *Eur. Phys. J.*, C71:1769, 2011.

[4] F. Aaron et al. Determination of the Integrated Luminosity at HERA using Elastic QED Compton Events. *Eur. Phys. J.*, C72:2163, 2012.

[5] H. Abramowicz et al. Measurement of $D^{*\pm}$ production in deep inelastic scattering at HERA. *JHEP*, 1305:097, 2013.

[6] I. Abt et al. The H1 detector at HERA. *Nucl. Instrum. Meth.*, A386:310–347, 1997.

[7] I. Abt et al. Measurement of $D^{\pm}$ production in deep inelastic ep scattering with the ZEUS detector at HERA. *JHEP*, 1305:023, 2013.

[8] C. Adloff et al. Measurement and QCD analysis of neutral and charged current cross-sections at HERA. *Eur. Phys. J.*, C30:1–32, 2003.

[9] A. Aktas et al. Tests of QCD factorisation in the diffractive production of dijets in deep-inelastic scattering and photoproduction at HERA. *Eur. Phys. J.*, C51:549–568, 2007.

[10] G. Altarelli and G. Parisi. Asymptotic Freedom in Parton Language. *Nucl. Phys.*, B126:298, 1977.

[11] B. Andersson, G. Gustafson, G. Ingelman, and T. Sjostrand. Parton Fragmentation and String Dynamics. *Phys. Rept.*, 97:31–145, 1983.

[12] B. Andersson, G. Gustafson, L. Lonnblad, and U. Pettersson. Coherence Effects in Deep Inelastic Scattering. *Z. Phys.*, C43:625, 1989.

[13] R. Appuhn et al. Hadronic response and e / pi separation with the H1 lead / fiber calorimeter. *Nucl. Instrum. Meth.*, A382:395–412, 1996.

[14] X. Artru and G. Mennessier. String model and multiproduction. *Nucl. Phys.*, B70:93–115, 1974.

[15] J. Binnewies, B. A. Kniehl, and G. Kramer. Predictions for $D^{*\pm}$ Photoproduction at DESY HERA with new Fragmentation Functions from CERN LEP1. *Phys. Rev. D*, 58:014014, Jun 1998.

[16] J. Bizot and D. Hoffmann. Strategy Studies for the H1 Topological L2-Trigger (L2TT). *note interne, H1-01/97-508*, 1997.

[17] J. Bjorken. Asymptotic Sum Rules at Infinite Momentum. *Phys. Rev.*, 179:1547–1553, 1969.

[18] V. Blobel. An Unfolding method for high-energy physics experiments. *Report number: DESY-02-078, arxiv:hep-ex/0208022*, 2002.

[19] V. Blobel. Central Track Reconstruction. *Talk at H1 tracking group meeting, March 11*, 2004.

[20] M.-O. Boenig. Messung des D^*-Meson-Produktionsquerschnitts in tiefinelastischer Streuung mit dem H1-Experiment. Dissertation, Universität Dortmund, 2007.

[21] M. Bowler. e^+e^- Production of Heavy Quarks in the String Model. *Z. Phys.*, C11:169, 1981.

[22] M. Brinkmann. Measurement of the $D^{*\pm}$ meson production cross section and $F_2^{c\bar{c}}$ at high Q^2 in ep scattering at HERA. Dissertation, Universität Hamburg, 2010. Report number: DESY-THESIS-2010-016.

[23] R. Brun, F. Carminati, S. Giani, et al. Geant detector description and simulation tool. *CERN program library long writeup W*, 5013:1993, 1993.

[24] M. Cacciari and M. Greco. J/ψ production via fragmentation at the Tevatron. *Phys. Rev. Lett.*, 73:1586–1589, 1994.

[25] S. Chekanov et al. A ZEUS next-to-leading-order QCD analysis of data on deep inelastic scattering. *Phys. Rev.*, D67:012007, 2003.

[26] K. Chetyrkin, B. A. Kniehl, and M. Steinhauser. Strong coupling constant with flavor thresholds at four loops in the MS scheme. *Phys. Rev. Lett.*, 79:2184–2187, 1997.

[27] J. C. Collins. Hard scattering factorization with heavy quarks: A General treatment. *Phys. Rev.*, D58:094002, 1998.

[28] J. C. Collins and D. E. Soper. The Theorems of Perturbative QCD. *Ann. Rev. Nucl. Part. Sci.*, 37:383–409, 1987.

[29] R. Devenish and A. Cooper-Sarkar. Deep inelastic scattering. 2004. Published at Oxford university press.

[30] Y. L. Dokshitzer. Calculation of the Structure Functions for Deep Inelastic Scattering and e^+e^- Annihilation by Perturbation Theory in Quantum Chromodynamics. *Sov. Phys. JETP*, 46:641–653, 1977.

[31] E. Elsen. Aspects of the H1 trigger and data acquisition system. Prepared for 2nd Annual Conference on Electronics for Future Colliders, Chestnut Ridge, N.Y., 19-21 May 1992.

[32] D.-J. Fischer. Inclusive neutral current ep cross sections with HERA II and two-dimensional unfolding. 2011. Dissertation, Universität Hamburg, 2011. Report number: DESY-THESIS-2011-020.

[33] D. Fox, C. Chang, K. Chen, A. Kotlewski, P. F. Kunz, et al. Test of Scale Invariance in High-Energy Muon Scattering. *Phys. Rev. Lett.*, 33:1504, 1974.

[34] J. I. Friedman and H. W. Kendall. Deep inelastic electron scattering. *Ann. Rev. Nucl. Part. Sci.*, 22:203–254, 1972.

[35] H. Fritzsch, M. Gell-Mann, and H. Leutwyler. Advantages of the Color Octet Gluon Picture. *Phys. Lett.*, B47:365–368, 1973. Introduces the term 'color'.

[36] J. Gaiser. Charmonium spectroscopy from radiative decays of the J/ψ and ψ'. 1982. Dissertation.

[37] J. Gassner. A Measurement of D-Meson Production at HERA by Decay of Vertex Identification. Dissertation, Swiss Federal Institute of Technology Zurich, 2002.

[38] R. L. Gluckstern. Uncertainties in track momentum and direction, due to multiple scattering and measurement errors. *Nucl. Instrum. Meth.*, 24:381–389, 1963.

[39] P. Granet et al. Inclusive Production Cross-Sections of Resonances in 32-GeV/c K^+ p Interactions. *Nucl. Phys.*, B140:389, 1978.

[40] V. Gribov and L. Lipatov. e^+e^- pair annihilation and deep inelastic e p scattering in perturbation theory. *Sov. J. Nucl. Phys.*, 15:675–684, 1972.

[41] D. Gross and F. Wilczek. Asymptotically Free Gauge Theories. 1. *Phys. Rev.*, D8:3633–3652, 1973.

[42] H. C. T. Group. Trigger rate plots. *H1 internal web resource, https://www-h1.desy.de/h1/iww/itrigger/TrigRates/*, 2006.

[43] G. Gustafson and U. Pettersson. Dipole Formulation of QCD Cascades. *Nucl. Phys.*, B306:746, 1988.

[44] B. Harris and J. Smith. Heavy quark correlations in deep inelastic electroproduction. *Nucl. Phys.*, B452:109–160, 1995.

[45] B. Harris and J. Smith. Charm quark and $D^{*\pm}$ cross-sections in deeply inelastic scattering at HERA. *Phys. Rev.*, D57:2806–2812, 1998.

[46] E. Hennekemper. Measurement of the Inclusive D^* Meson Cross Section in Photoproduction at HERA. Dissertation, Universität Heidelberg, 2011.

[47] A. Hoecker, P. Speckmayer, J. Stelzer, J. Therhaag, E. von Toerne, H. Voss, M. Backes, T. Carli, O. Cohen, A. Christov, et al. Tmva-toolkit for multivariate data analysis. *arXiv preprint physics/0703039*, 2007.

[48] G. Ingelman, A. Edin, and J. Rathsman. LEPTO 6.5: A Monte Carlo generator for deep inelastic lepton - nucleon scattering. *Comput. Phys. Commun.*, 101:108–134, 1997.

[49] A. W. Jung. Measurement of the $D^{*\pm}$ meson cross section and extraction of the charm contribution $F_c^2(x,Q^2)$ to the proton structure in deep inelastic ep scattering with the H1 detector at HERA. Dissertation, Universität Heidelberg, Report number: DESY-THESIS-2009-001, 2009.

[50] H. Jung. Hard diffractive scattering in high-energy *ep* collisions and the Monte Carlo generator RAPGAP. *Comput. Phys. Commun.*, 86:147–161, 1995.

[51] V. Kartvelishvili, A. Likhoded, and V. Petrov. On the Fragmentation Functions of Heavy Quarks Into Hadrons. *Phys. Lett.*, B78:615, 1978.

[52] C. Kleinwort. Energy loss measurement with the H1 Central Jet Chamber. *H1 internal note*, 2008.

[53] I. Knowles, T. Sjostrand, A. Blondel, A. Boehrer, C. Buchanan, et al. QCD event generators. 1995. arxiv:hep-ph/9601212.

[54] R. Kogler. Measurement of jet production in deep-inelastic *ep* scattering at HERA. Dissertation, Universität Hamburg, Report number: DESY-THESIS-2011-003, 2011.

[55] J. Kohne, J. Fent, W. Frochtenicht, F. Gaede, A. Gruber, et al. Realization of a second level neural network trigger for the H1 experiment at HERA. *Nucl. Instrum. Meth.*, A389:128–133, 1997.

[56] A. Kwiatkowski, H. Spiesberger, and H. Mohring. HERACLES: An event

generator for ep interactions at HERA energies including radiative processes. Version 1.0. *Comput. Phys. Commun.*, 69:155–172, 1992.

[57] M. Lisovyi. Measurement of charm production in deep inelastic scattering using lifetime tagging for $D^{\pm}$ meson decays with the ZEUS detector at HERA. Dissertation, Universität Hamburg, Report number: DESY-THESIS-2011-033, 2011.

[58] B. List. The H1 silicon tracker. *Nucl. Instrum. Meth.*, A549:33–36, 2005.

[59] E. Lohrmann. Summary of charm fractions. *unpublished, ZEUS and H1 internal*, 2011.

[60] K. Lohwasser. Optimisation of the selection capability of the H1 fast track trigger. Diploma thesis, Universität Dortmund, 2006.

[61] K. Nakamura et al. Review of particle physics. *J. Phys. G*, G37:075021, 2010.

[62] T. Nicholls et al. Performance of an electromagnetic lead / scintillating fiber calorimeter for the H1 detector. *Nucl. Instrum. Meth.*, A374:149–156, 1996.

[63] M. Nozicka. The forward and backward silicon trackers of H1. *Nucl. Instrum. Meth.*, A501:54–59, 2003.

[64] P. Pahl. Measurement of $D^{\pm}$ meson lifetime using the H1 silicon vertex detector at HERA. Diploma thesis, Universität Hamburg, 2008.

[65] C. Peterson, D. Schlatter, I. Schmitt, and P. M. Zerwas. Scaling Violations in Inclusive e^+e^- Annihilation Spectra. *Phys. Rev.*, D27:105, 1983.

[66] D. Pitzl. Tracking group report, Dec. 16. 2009.

[67] D. Pitzl. Tracking Group Report: *DST7*, Talk at H1 software plenary, June 10. 2009.

[68] J. Pumplin, D. Stump, J. Huston, H. Lai, P. M. Nadolsky, et al. New generation of parton distributions with uncertainties from global QCD analysis. *JHEP*, 0207:012, 2002.

[69] G. Schuler and H. Spiesberger. DJANGO: The Interface for the event generators HERACLES and LEPTO. In *Proceedings of the workshop\ Physics at HERA*, volume 3, page 1419, 1991.

[70] T. Sjostrand, P. Eden, C. Friberg, L. Lonnblad, G. Miu, et al. High-energy physics event generation with PYTHIA 6.1. *Comput. Phys. Commun.*, 135:238–259, 2001.

[71] D. E. Soper. Basics of QCD perturbation theory. *arxiv:ep-ph/9702203*, 1996.

[72] G. 't Hooft. Dimensional regularization and the renormalization group. *Nucl. Phys.*, B61:455–468, 1973.

[73] W. Verkerke and D. P. Kirkby. The RooFit toolkit for data modeling. *arxiv:physics/0306116*, 2003.

[74] S. Weinberg. Current algebra and gauge theories. 2. NonAbelian gluons. *Phys. Rev.*, D8:4482–4498, 1973.

[75] C. Wissing et al. Proc. of the 14th IEEE - NPSS Real time Conference 2005, pp 233-236. 2005.